Research on Ternary Semiconductor Metal Oxide Sensor for Cooked Rice Quality Detection at Room Temperature

Thesis submitted for the degree of Doctor in Sciences

Zichen ZHENG

Supervisors:

Prof. C. Bittencourt (Promoteur), UMONS, Material Science Department
Prof. C. Zhang (Co-promoteur), YZU, College of Mechanical Engineering

Jury:

Prof. Jerome Cornil, UMONS, Chemistry Department
Prof. Marc Debliquy, UMONS, Polytechnic Faculty
Prof. Dayu Li, YZU, College of Mechanical Engineering
Prof. Eduard Llobet, University of Rovira i Virgili, Electrical and Automation Department
Prof. Damien Thiry, UMONS, Chemistry Department

2026

Acknowledgments

Time flies so fast, and I think it’s time to say goodbye. When I first arrived at Mons on May 28th, 2024, I thought Mons was a very quiet and pleasant town, and my subsequent life gradually confirmed this. The people are very friendly, and the environment is very beautiful. I have had a very fulfilling and happy time completing my doctoral dissertation.

At first, I would like to thank my supervisor, Carla Bittencourt, at the University of Mons in Belgium. She not only guided my research patiently and effectively but also made every effort to allow me to participate in academic exchanges abroad, which greatly broadened my horizons. She also gave me a lot of help and advice in life. At the same time, she is also a very good friend of mine, and she hopes that I can go further and do better.

Then, I would like to thank my Chinese supervisor, Professor Chao Zhang. As my supervisor during my master’s and doctoral studies, he provided strong guidance and assistance with scientific research and served as my research guide. During my doctoral studies, he provided me with ample financial support, which enabled me to conduct extensive scientific research. At the same time, he gave me the opportunity to attend joint training in Belgium and helped me apply for the CSC scholarship. Such an opportunity is very rare.

Next, I would like to express my sincere gratitude to all the professors on my doctoral dissertation review committee: Prof. Jérôme Cornil, Prof. Marc Debliquy, Prof. Dayu Li, Prof. Eduard Llobet, and Prof. Damien Thiry. Their valuable suggestions have made the dissertation's structure more complete and its argumentation more rigorous, significantly improving the quality of the research.

Once again, I would like to thank the teachers who guided me in research and work, and gave me help: Changlong Wang, Liangchao Guo, Guodong Sun, Yifu Zhang, Jiwei Qu, Feng Liang, Yangjie Shi, Yifan Luo, Kaidi Wu, Jinyong Xu, Heming Wei, Min Zhang, Hui Su, Min Guo, Zhe Ma, and Shaohong Wang.

Finally, I want to thank the University of Mons and Yangzhou University. It is precisely because of such excellent platforms that I am able to conduct scientific research and exploration effectively. I would also like to thank the China Scholarship Council for funding my joint training studies in Belgium.

Without the support of my family and friends, I would not have been able to complete my

doctoral dissertation.

Firstly, I am very grateful to my parents. They are always my strong support.

I want to thank my very important friend and comrade, Kewei Liu. She often gives me effective advice when my research stalls. Whether in experiments or in completing papers, she spares no effort to help me. We have come this far, supporting and understanding each other along the way. When I landed in Belgium, she went to the airport to pick me up. During my subsequent life abroad, her help spared me a lot of unnecessary trouble.

I am deeply grateful to three fellow Chinese PhD students in Mons, Yipeng Yao, Yuan Tian, and Jieqing Zheng, and to Yakun Xu, Yanting Zhou, Shiyuan Du, and Xuliang Qu of the Royal Conservatory of Mons. Their generous help and thoughtful advice were invaluable to me, and their companionship made a foreign place feel like home.

I would also like to thank my colleagues at the University of Mons laboratory, Rony Snyders, Dany Cornelissen, Sabine Bouchez, Driss Lahem, Ahmadou Ly, Philippe Smet, Daniele de Campos, Nayara Balaba, Julia De Oliveira Primo, Arleth Gualle Brito, Federico Apolloni, Assan Abdirakhmanov, Ravikant Adalati, France-Emmanuelle Bol, Alexandre Culot, Robin Dantinne, Suyog Asaram Raut, Pierre Mathieu, and Geneviève Brenda Bena Bodiong. Their enthusiastic help deeply touched me.

During my joint training period, there were many research tasks and other documents that needed to be completed with my University in China. Here, I am very grateful to my junior fellow students and good friends at Yangzhou University, Yiwen Zhou, Zicong Zhang, Xudong Nie, Xintong Wang, Minyue Sun, Jiayue He, Mengjie Han, Kaichun Xu, and Xiaoxi He for their help with many issues. I hope you all have a bright future.

I want to express my gratitude to my colleagues and friends who have consistently provided me with support and assistance: Yongbin Qin, Yu Wang, Zhi Ding, Weigang Liu, Shu Ji, Yao Chen, Wei Gu, Jiani Wang, Guifang Liu, Yuchun Huan, Haizi Zheng, Yuwen Zhang, Jingwen Man, Dehui Tan, Boxuan Li, and Xiaofan Luo. Thank you for your unwavering encouragement and support on my journey forward. Your help and companionship have been indispensable in completing this journey.

Finally, I would like to thank myself. It is my persistent effort that has propelled me forward step by step, allowing me to improve in body, mind, and ability continuously, and to gain opportunities to showcase myself on different stages.

Looking back on this doctoral period, there have been hardships, pressures, as well as countless moments of warmth and inspiration. All experiences, all encounters, and all assistance

will become the strength for me to continue moving forward. May we all, in our respective paths, move forward firmly, live up to our efforts, and live up to our encounters in the future.

Abstract

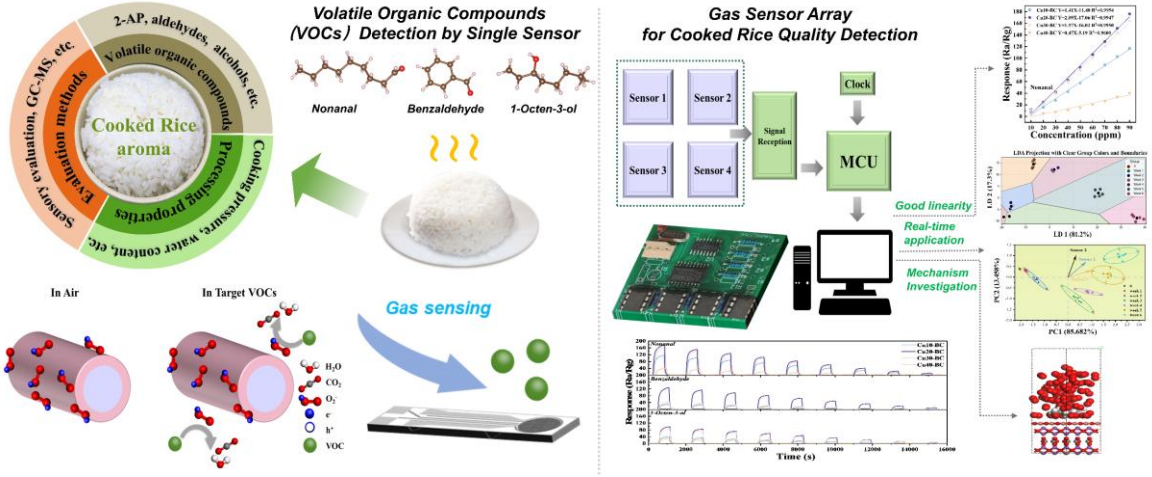

Rice, as a major staple grain in China, garners significant attention for its flavor and quality. The identified volatile organic compounds (VOCs) in cooked rice include aldehydes, ketones, acids, esters, alcohols, hydrocarbons, and heterocyclic compounds, with aldehydes and alcohols comprising the majority of the flavor profile. Various factors, including rice variety, storage time and temperature, degree of milling, amylose content, soaking time, and cooking method, influence the VOC components in cooked rice. Clarifying the correlation between the VOCs released and the quality of cooked rice can have profound implications for ensuring food security and optimizing strategic stockpiles. Traditional methods for testing cooked rice quality, such as sensory analysis and physical or chemical evaluations, have notable limitations. These include their subjective nature, complex procedures, time-consuming processes, reliance on large equipment, and the need for skilled professionals. Consequently, current technologies fall short in delivering objective, real-time, low-cost, and rapid testing solutions. With the growth of the agricultural economy and advancements in science and technology, intelligent detection is emerging as a key trend in the monitoring of the edible agricultural products industry. This underscores the urgent need to develop rapid, effective alternative technologies for assessing the freshness of cooked rice under varying conditions. In this framework, gas sensor technology is gaining prominence in the qualitative and quantitative assessment of agricultural products. Among these, ternary semiconductor metal oxide (TSMOX) sensors are particularly promising

due to their low cost, compact size, ease of integration, and high sensitivity. However, the application of TSMOX sensors for detecting cooked rice quality still faces challenges, including high operating temperatures, insufficient detection limits, performance drift, and low accuracy. To address these issues, this thesis investigates VOCs emitted during cooked rice storage and identifies three characteristic VOCs for evaluation the cooked rice quality. It further designs and develops three innovative room-temperature TSMOX-based gas sensors, explores their working mechanisms, and validates their feasibility.

By linking the odor characteristics of cooked rice (specific VOCs) to changes in sensor resistance signals, the study seeks to develop a reliable method for evaluating cooked rice quality through effective data analysis. Furthermore, it demonstrates the effectiveness of the room-temperature semiconductor gas sensor array. The ultimate objective is to establish a scientific foundation for the rapid, non-destructive testing of cooked rice quality. The specific research focuses are:

(1) Flavor generation mechanism and characteristic odor information extraction of cooked rice during storage:

We explore the mechanisms of flavor generation and extract characteristic odor information of cooked rice at different stages of freshness during storage. It briefly describes the main causes of cooked rice spoilage, considering factors such as rice variety, environmental conditions, and other contributing elements. The types of VOCs detectable in cooked rice, ranging from freshness indicators to spoilage markers, were summarized along with their biochemical production mechanisms. Specifically, 1-octen-3-ol, benzaldehyde, and nonanal were identified as the key indicators of cooked rice quality. This provides a foundational basis for designing room-temperature TSMOX gas sensors and sensor arrays for quality detection.

(2) Design and fabrication of a new room-temperature semiconductor nonanal sensor.

La-decorated $Bi_2O_2CO_3$ (BCO-La) microspheres were synthesized via a facile wet-chemical strategy for low-concentration nonanal sensing at room temperature. The BCO-6La sensor demonstrated significantly higher sensitivity compared to the pure BCO sensor, achieving a response of 174.6 to 30 ppm nonanal. It also exhibited faster response time (36 s) when exposed to 18 ppm of nonanal. Additionally, the sensor showed superior selectivity for nonanal gas detection (approximately 4-24 times higher) compared to interfering gases, including 1-octanol, geranyl acetone, linalool, hexanal, 2-pentyfuran, and 1-octen-3-ol, during cooked rice quality

detection. The gas sensing mechanism and the factors contributing to the enhanced sensing performance of the BCO-La microspheres were demonstrated in a realistic detection scenario.

(3) Design and fabrication of a new room-temperature semiconductor benzaldehyde sensor.

The carbon-functionalized cladding bismuth tungstate-based benzaldehyde sensors are produced. A 3D twisted micro-flower structure was obtained, and a uniform carbon cladding was applied using a one-pot hydrothermal strategy. The $C_{0.75}/WO_3/Bi_2WO_6$ sensor exhibits excellent benzaldehyde sensing performance across a wide concentration range, with remarkable sensitivity (33.7 @ 50 ppm), stability for over 15 days, and robust selectivity, all at room temperature. Even under high-humidity conditions, the response value showed minimal degradation, decreasing by only 8.96% compared to the dry-condition performance. Density functional theory (DFT) calculations revealed that the $C_x/WO_3/Bi_2WO_6$ sensor exhibited higher benzaldehyde adsorption energy and stronger anti-humidity performance than WO_3/Bi_2WO_6, thereby contributing to its enhanced gas-sensing efficacy.

(4) Defect engineering strategy for 1-octen-3-ol detection using $NiWO_4$ microstructures:

A defect-engineering strategy was employed to modify the electronic and surface properties of $NiWO_4$ microstructures through controlled hydrogen reduction for 1-octen-3-ol detection. Systematic annealing protocols induced a high density of oxygen vacancy (O_V) via selective oxygen removal, as confirmed by structural and spectroscopic characterization. The engineered O_V enhanced bulk electron transport by improving conductivity and boosted surface reactivity by optimizing adsorption sites. The optimized $NiWO_4$ sensor demonstrated exceptional performance for 1-octen-3-ol detection at 40 ppm, with a high response value (R_a/R_g = 20.6), a fast response time (22 s), and strong resilience to relative humidity (19.7% response drift across 20-80% RH). The enhanced sensing performance was explained using an oxygen adsorption model and molecular dynamics (MD) simulations.

(5) Development of a gas sensor array system for cooked rice quality evaluation:

A high-sensitivity, highly selective gas sensor array was developed to evaluate the quality of cooked rice accurately. $CuO/Bi_2O_2CO_3$ (Cu-BC) p-n heterostructure micro-flowers are used as sensing materials to create a four-channel gas sensor array that converts voltage signals into

resistance. Individual Cux-BC sensors (x = 10, 20, 30, and 40) exhibited strong responses to nonanal, benzaldehyde, and 1-octen-3-ol, with detection specificity confirmed through principal component analysis (PCA) and linear discriminant analysis (LDA). This integrated gas sensor array effectively identified and distinguished the quality of cooked rice, ranging from freshly prepared rice to rice stored for 1 to 6 weeks. The sensing mechanism relies on increased O_V and improved electron mobility. Additionally, MD simulations were used to explore the adsorption and diffusion mechanisms of target gas molecules and oxygen on the materials' surfaces.

The comprehensive research of this thesis lays the groundwork for developing advanced gas-sensing technologies that enable rapid, non-destructive evaluation of cooked rice quality.

Résumé

Le riz, en tant que denrée de base majeure en Chine, suscite une attention considérable en raison de son arôme et de sa qualité. Les composés organiques volatils (COV) identifiés dans le riz cuit comprennent des aldéhydes, des cétones, des acides, des esters, des alcools, des hydrocarbures et des composés hétérocycliques, les aldéhydes et les alcools constituant la majeure partie du profil aromatique. Divers facteurs, notamment la variété du riz, la durée et la température de stockage, le degré de mouture, la teneur en amylose, le temps de trempage et le mode de cuisson, influencent la composition des COV du riz cuit. Clarifier la corrélation entre les COV libérés et la qualité du riz cuit revêt une importance majeure pour garantir la sécurité alimentaire et optimiser les réserves stratégiques.

Les méthodes traditionnelles d'évaluation de la qualité du riz cuit, telles que l'analyse sensorielle et les évaluations physiques ou chimiques, présentent des limites notables. Celles-ci incluent leur caractère subjectif, des procédures complexes, des analyses chronophages, une dépendance à l'égard d'équipements volumineux, ainsi que la nécessité de faire appel à des professionnels qualifiés. Par conséquent, les technologies actuelles ne permettent pas encore d'assurer une évaluation objective, en temps réel, à faible coût et rapidement. Avec le développement de l'économie agricole et les progrès des sciences et des technologies, la détection intelligente s'impose comme une tendance majeure dans la surveillance des produits agricoles destinés à l'alimentation. Cela souligne l'urgence de développer des technologies alternatives, rapides et efficaces pour évaluer la fraîcheur du riz cuit dans diverses conditions.

Dans ce contexte, la technologie des capteurs de gaz occupe une place de plus en plus importante dans l'évaluation qualitative et quantitative des produits agricoles. Parmi eux, les capteurs à base d'oxydes métalliques semi-conducteurs ternaires (TSMOX) apparaissent particulièrement prometteurs en raison de leur faible coût, de leur taille compacte, de leur facilité d'intégration et de leur haute sensibilité. Cependant, l'application des capteurs TSMOX à la détection de la qualité du riz cuit se heurte encore à plusieurs défis, notamment des températures de fonctionnement élevées, des limites de détection insuffisantes, une dégradation des performances et une faible précision. Pour répondre à ces problèmes, cette thèse étudie les COV émis lors du stockage du riz cuit et identifie trois COV caractéristiques pour évaluer la qualité du riz. Elle conçoit et développe en outre trois capteurs de gaz innovants à base de

TSMOX, fonctionnant à température ambiante, en explorant les mécanismes de fonctionnement et en validant leur faisabilité.

En reliant les caractéristiques olfactives du riz cuit (COV spécifiques) aux variations des signaux de résistance des capteurs, cette étude vise à développer une méthode fiable d'évaluation de la qualité du riz cuit, fondée sur une analyse efficace des données. Par ailleurs, elle démontre l'efficacité d'un réseau de capteurs de gaz semi-conducteurs fonctionnant à température ambiante. L'objectif ultime est d'établir une base scientifique pour un contrôle rapide et non destructif de la qualité du riz cuit. Les axes spécifiques de cette recherche sont les suivants :

(1) Mécanisme de génération des arômes et extraction des informations olfactives caractéristiques du riz cuit pendant le stockage :

Nous avons exploré les mécanismes de génération des arômes et extrait les informations olfactives caractéristiques du riz cuit à différents stades de fraîcheur au cours du stockage. Les principales causes d'altération du riz cuit ont été brièvement décrites, en tenant compte de facteurs tels que la variété du riz, les conditions environnementales et d'autres facteurs contributifs. Les types de COV détectables dans le riz cuit, allant des indicateurs de fraîcheur aux marqueurs d'altération, ont été résumés, ainsi que leurs mécanismes biochimiques de formation. Plus précisément, le 1-octène-3-ol, le benzaldéhyde et le nonanal ont été identifiés comme indicateurs clés de la qualité du riz cuit. Cela fournit une base fondamentale pour la conception de capteurs de gaz TSMOX à température ambiante et de réseaux de capteurs destinés à la détection de la qualité.

(2) Conception et fabrication d'un nouveau capteur semi-conducteur de nonanal fonctionnant à température ambiante :

Des microsphères de $Bi_2O_2CO_3$ décorées au La (BCO-La) ont été synthétisées par une stratégie simple et humide pour la détection de faibles concentrations de nonanal à température ambiante. Le capteur BCO-6La a montré une sensibilité significativement supérieure à celle du capteur BCO pur, atteignant une réponse de 174,6 à 30 ppm de nonanal. Il a également présenté un temps de réponse plus court (36 s) lorsqu'il était exposé à 18 ppm de nonanal. De plus, le capteur a montré une excellente sélectivité pour la détection du nonanal, avec une réponse environ 4 à 24 fois plus élevée que pour des gaz interférents, notamment le 1-octanol, la

géranylacétone, le linalol, l'hexanal, le 2-pentylfurane et le 1-octène-3-ol, dans le cadre de la détection de la qualité du riz cuit. Le mécanisme de détection gazeuse, ainsi que les facteurs responsables de l'amélioration des performances de détection des microsphères BCO-La, ont été démontrés dans un scénario de détection réaliste.

(3) Conception et fabrication d'un nouveau capteur semi-conducteur de benzaldéhyde fonctionnant à température ambiante :

Des capteurs de benzaldéhyde à base de tungstate de bismuth revêtus de carbone ont été élaborés. Une structure tridimensionnelle en microfleurs torsadées a été obtenue, et un revêtement carboné uniforme a été obtenu par une stratégie hydrothermale en une seule étape. Le capteur $C_{0.75}/WO_3/Bi_2WO_6$ présente d'excellentes performances de détection du benzaldéhyde sur une large gamme de concentrations, avec une sensibilité remarquable (33,7 à 50 ppm), une stabilité supérieure à 15 jours et une sélectivité robuste, le tout à température ambiante. Même dans des conditions d'humidité élevée, la valeur de réponse n'a montré qu'une faible dégradation, diminuant de seulement 8,96 % par rapport aux performances observées en conditions sèches. Les calculs de théorie de la fonctionnelle de la densité (DFT) ont révélé que le capteur $C_x/WO_3/Bi_2WO_6$ présentait une énergie d'adsorption du benzaldéhyde plus élevée et de meilleures performances anti-humidité que WO_3/Bi_2WO_6, ce qui a contribué à améliorer son efficacité de détection gazeuse.

(4) Stratégie d'ingénierie des défauts pour la détection du 1-octène-3-ol à l'aide de microstructures de $NiWO_4$:

Une stratégie d'ingénierie des défauts a été adoptée pour modifier les propriétés électroniques et de surface des microstructures de $NiWO_4$ par réduction contrôlée à l'hydrogène, en vue de la détection du 1-octène-3-ol. Des protocoles systématiques de recuit ont induit une forte densité de lacunes en oxygène par élimination sélective de l'oxygène, comme l'ont confirmé les caractérisations structurales et spectroscopiques. Ces lacunes en oxygène ont amélioré le transport électronique dans le volume en augmentant la conductivité, tout en renforçant la réactivité de surface par l'optimisation des sites d'adsorption. Le capteur $NiWO_4$ optimisé a démontré des performances exceptionnelles pour la détection du 1-octène-3-ol à 40 ppm, avec une valeur de réponse élevée (R_a/R_g = 20,6), un temps de réponse rapide (22 s) et une forte résistance à l'humidité relative (19,7 % de dérive de réponse entre 20 et 80 % HR). L'amélioration des performances de détection a été expliquée à l'aide d'un modèle d'adsorption

de l’oxygène et de simulations de dynamique moléculaire (MD).

(5) Développement d’un système de réseau de capteurs de gaz pour l’évaluation de la qualité du riz cuit :

Un réseau de capteurs de gaz à haute sensibilité et haute sélectivité a été développé pour évaluer avec précision la qualité du riz cuit. Des microfleurs à hétérojonction p-n $CuO/Bi_2O_2CO_3$ (Cu-BC) ont été utilisées comme matériaux sensibles afin de créer un réseau de capteurs de gaz à quatre canaux convertissant les signaux de tension en résistance. Les capteurs individuels Cux-BC (x = 10, 20, 30 et 40) ont présenté de fortes réponses au nonanal, au benzaldéhyde et au 1-octène-3-ol, et la spécificité de détection a été confirmée par l’analyse en composantes principales (PCA) et l’analyse discriminante linéaire (LDA). Ce réseau intégré de capteurs de gaz a permis d’identifier et de distinguer efficacement la qualité du riz, du riz fraîchement préparé au riz stocké pendant 1 à 6 semaines. Le mécanisme de détection repose sur l’augmentation des lacunes en oxygène et sur l’amélioration de la mobilité électronique. En outre, des simulations de dynamique moléculaire ont été utilisées pour explorer les mécanismes d’adsorption et de diffusion des molécules gazeuses cibles, ainsi que de l’oxygène, à la surface des matériaux.

Les recherches approfondies menées dans cette thèse jettent les bases du développement de technologies avancées de détection gazeuse permettant une évaluation rapide et non destructive de la qualité du riz cuit.

Table of contents

Chapter 1: Context **1**

Chapter 2: Theoretical background **5**

2.1 Theoretical basis of cooked rice quality gas analysis 5

2.1.1 VOCs for cooked rice flavor 5

2.1.2 Cooked rice flavor detection method 19

2.2 Processing properties for cooked rice flavor 28

2.2.1 Pressure 29

2.2.2 Water content 30

2.2.3 Temperature 31

2.3 State of the art of Semiconductor Metal Oxide-based Gas Sensor for Cooked Rice Quality Detection 31

2.3.1 Generalities on semiconductor metal oxide gas sensors 32

2.3.2 Constitution, working principle, and testing procedure of SMOX gas sensors 34

2.3.3 Criteria of SMOX gas sensor evaluation 37

2.3.4 General sensing mechanism of SMOX gas sensors 41

2.3.5 Performance enhancement mechanisms of ternary semiconductor metal oxide for VOC detection 43

2.4 Characterization Techniques 46

2.5 Challenges faced by TSMOX gas sensor technology and objectives of the thesis 48

2.6 Strategy for this PhD. thesis 50

Chapter 3: La-Decorated $Bi_2O_2CO_3$ Sensor for Nonanal Detection **54**

3.1 Synthesis of La-decorating $Bi_2O_2CO_3$ microspheres 57

3.2 Results and discussion 58

3.2.1 Characterization results 58

3.2.2. Gas sensing performance 68

3.2.3 Gas sensing mechanism 73

3.3 Practical detection scenario 77

3.4 Conclusions 78

Chapter 4: Carbon functionalized cladding bismuth tungstate-based 3D twisted micro-flowers for benzaldehyde detection under ultraviolet light excitation 80

4.1 Synthesis process..... 84

4.2 Results and discussion..... 85

4.2.1. Characterization results 85

4.2.2 Gas sensing properties..... 109

4.2.3 Gas sensing mechanism 123

4.3 Practical detection scenario 126

4.4 Conclusions 130

Chapter 5: Defect-Engineered Nickel Tungstate Micro-flowers for 1-Octen-3-ol Detection 131

5.1 Synthesis of defect-rich $NiWO_4$ micro-flowers 134

5.2 Results and discussion..... 135

5.2.1 Characterization results 135

5.2.2 Gas sensing performance 145

5.2.3 Gas sensing mechanism 151

5.3 Conclusions 157

Chapter 6: CuO-Decorated Bismuth Subcarbonate Gas Sensor Arrays for Cooked Rice Quality Assessment.....158

6.1 Synthesis of CuOx-BC Micro-structures 160

6.2 Results and discussion..... 161

6.2.1 Characterization results 161

6.2.2 Gas sensing performance 171

6.2.3 Gas sensing mechanism 174

6.2.4 Sensor arrays detection..... 178

6.3 Conclusions 180

Chapter 7: Conclusions And Perspectives.....182

APPENDICES 185

Appendix A1: Cooked rice quality evaluation 185
Appendix A2: Specific description of the representation characterization methods. 186
REFERENCES 193
SCIENTIFIC CONTRIBUTIONS.....238
Peer-reviewed publications 238
Congress proceedings..... 241
Project..... 241
Awards..... 242

Chapter 1: Context

Rice is a crucial staple food that feeds more than 4 billion people [1, 2]. By steaming or boiling, rice can be transformed into cooked rice, a daily essential for most Asians [3]. As a complex carbohydrate rich in protein, sugar, calcium, vitamins, and containing the amino acids necessary for human beings, the edible and cooking quality of cooked rice has always been the most crucial factor sought by consumers [4]. The degree to which various nutrients are retained in rice grains depends on the post-harvest processing methods, including hulling, milling, and cooking. The importance of cooked rice to human beings is self-evident. The detection and exploration of the quality of cooked rice taste are of great significance for promoting healthy competition in the rice market and agricultural economic development. Figure 1-1 summarizes the multidimensional origins and regulatory factors of cooked rice aroma, including: (1) volatile organic compounds (VOCs); (2) processing conditions; and (3) evaluation methods.

The aroma of cooked rice largely determines its taste quality. Among the numerous VOCs, 2-acetyl-1-pyrroline (2-AP) stands out as a principal volatile constituent and key indicator in cooked rice, drawing significant attention from researchers. This key indicator has been detected in both raw and cooked rice, contributing a characteristic popcorn-like aroma [5, 6]. In recent years, a large number of researchers have studied the characteristic VOCs and inner formation mechanism of cooked rice aroma, as well as the specific factors affecting the flavor of cooked rice, including temperature [7], steam pressure [8], and fragmentation degree [9], among others. The aroma quality of cooked rice is highly complex due to the complex interactions among a large number of VOCs and the influence of numerous factors in storage and processing conditions. Before the development of molecular technology, the genetic basis of cooked rice aroma, particularly 2-AP, was investigated using genetic and molecular mapping techniques. Rice aroma has been identified as a highly heritable trait [10]. Repeated genetic analyses of different rice cultivars have

demonstrated that the major aroma traits in rice are controlled by recessive single-gene inheritance, independent of cytoplasmic genes [11, 12]. Genetic factors are major contributors to cooked rice aroma, and the same cultivar may produce distinct cooked rice flavors under diverse planting, processing, and storage conditions. Hence, monitoring the gases released during the storage of cooked rice has emerged as a promising nondestructive approach, characterized by simple operation, rapid response, and high sensitivity in assessing cooked rice quality. Therefore, the development of rapid and efficient techniques for detecting and evaluating the quality of cooked rice under varying storage conditions and durations remains essential.

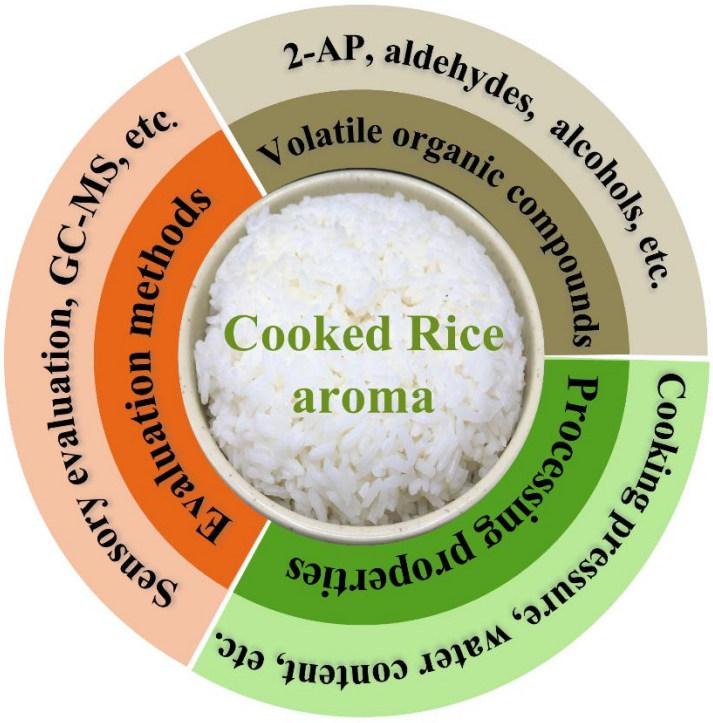

Figure 1-1 The multidimensional origins and regulatory factors of cooked rice aroma.

Traditional methods for VOC analysis, such as sensory evaluation panels, headspace solid-phase microextraction (HS-SPME), and gas chromatography–mass spectrometry (GC-MS), have been widely employed [13]. While these techniques provide accurate and detailed chemical information, they suffer from limitations including high operational costs, labor-intensive procedures, long analysis times, and

the need for specialized expertise. Moreover, they are unsuitable for real-time, on-site monitoring of cooked rice quality during storage and distribution. These constraints have created a pressing demand for alternative detection approaches that are rapid, nondestructive, cost-effective, and adaptable to practical scenarios. Chemiresistive gas sensors (CGSs) have garnered considerable attention across various fields due to their cost-effectiveness, ease of miniaturization, and environmental sustainability. These attributes render CGSs particularly valuable for applications in public security, environmental monitoring, and healthcare diagnostics [14-17]. CGSs based on semiconductor metal oxide (SMOX) have been widely adopted due to their high sensitivity, low cost, ease of use, and long-term stability. Specifically, SMOX-based CGSs are widely used and recognized for their high sensitivity, affordability, user-friendliness, and long-term stability. Numerous studies have documented the performance of binary SMOX-based CGSs in gas detection, demonstrating both high sensitivity and low detection limits. Ternary semiconductor metal oxide (TSMOX) active layers are a fundamental component of CGSs and are widely used for detecting various gases. Their widespread application is attributed to several advantages, including straightforward preparation methods, cost-effectiveness, and operational convenience for users [18-21]. These sensors have applications in non-invasive disease detection [22], agricultural product testing [23], and wearable devices [24].

This thesis aims to advance high-performance, energy-efficient gas-sensing technology and address core issues in detecting cooked rice quality, including elevated operating temperatures, constrained detection limits, and inadequate accuracy. Therefore, three important VOCs (nonanal, benzaldehyde, and 1-octen-3-ol) in cooked rice were chosen as target gases. Correspondingly, La-decorated $Bi_2O_2CO_3$ microspheres effectively introduced oxygen vacancies, significantly improving adsorption strength and enabling ultrasensitive detection of nonanal. Carbon-functionalized WO_3/Bi_2WO_6 composites enhance benzaldehyde detection under UV-assisted conditions and exhibit excellent humidity resistance. Defect-engineered

$NiWO_4$ microflowers optimized via hydrogen reduction exhibited superior response and humidity tolerance for the detection of 1-octen-3-ol. Finally, voltage-controlled $CuO/Bi_2O_2CO_3$ p-n heterostructures were integrated into multi-channel sensor arrays, enabling selective recognition of VOCs and comprehensive assessment of cooked rice quality across different storage stages. These advances highlight the significant potential of TSMOX-based sensor arrays in food quality monitoring. Compared to single-sensor systems, sensor arrays mimic the biological olfactory system by combining responses from multiple sensing elements, thereby enhancing selectivity and enabling the pattern recognition of complex VOC mixtures. By incorporating statistical and machine learning techniques, such as principal component analysis (PCA) and linear discriminant analysis (LDA), sensor arrays can effectively distinguish subtle differences in the aroma and freshness of cooked rice. The integration of sensor arrays into portable or embedded devices opens the way for intelligent, real-time food quality monitoring, with potential applications extending beyond cooked rice to other agricultural and food products.

This work is supported by UMONS and Yangzhou University. Thanks to the China Scholarship Council (No. 202308320445), I have an opportunity to study at UMONS for two years as a joint Ph.D candidate.

Chapter 2: Theoretical background

2.1 Theoretical basis of cooked rice quality gas analysis

2.1.1 VOCs for cooked rice flavor

It has been identified that there are more than 300 kinds of VOCs in cooked rice, and the main components are aldehydes, alcohols, ketones, acids, hydrocarbons, esters, and heterocyclic compounds [10, 25]. These odor components can be categorized into three parts based on pH: acidic, basic, and neutral. From the perspective of volatile compounds, the aroma of cooked rice can be divided into 2-AP, aldehydes, alcohols, phenols, and heterocyclic compounds, among others. In general, different types of VOCs impart distinct flavor characteristics to cooked rice. Aldehydes imparted a fruity aroma to cooked rice, alcohols a floral aroma, and esters a fruity aroma. For example, nine VOCs, including 2-AP, (E, E)-2,4-decadienal, 4-vinyl-guaiacol, nonanal, (E)-2-nonenal, octanal, decanal, hexanal, and 4-vinylphenol in cooked rice were identified by Buttery et al. These VOCs are classified as significant contributors to the aroma intensity of cooked rice in the 20^{th} century [26]. Protein, starches, and lipids are the three main substances in cooked rice. Although lipids are less abundant in cooked rice than starches and proteins, they positively relate to the palatability of cooked rice [27]. As a kind of starch, amylose can generate complexes with multiple aroma compound ligands. VOCs produced by the main components of cooked rice are presented in Table 2-1.

Table 2-1 The flavors produced by the main cooked rice components

rice components	mainly produced substances	common compounds	literature
protein	aldehydes and ketones, furans, pyrrole, and sulfurous compounds	2-phenyl ethanol, phenylacetic acid, 6-methyl-5-heptene-2-ketone, 1-pyrroline, 2-methyl-3-furanthiol and dimethyl sulfide	[27-35]
lipids	aldehydes, ketones, furans, alcohols, acids, and hydrocarbons	hexanal, valeraldehyde, (E)-2-octenal, (E, E)-2, 4-decdienal, 3-pentene-2-ketone, 2-pentylfuran, amyl alcohol, oleic acid, linoleic acid and heptadecane	
starch	aldehydes and ketones, furans and pyrrole	nonanal, butanedione, furfural, 2-acetyl-1-pyrroline	
maillard-derived volatiles	pyrazines, Strecker aldehydes, etc	2-methoxy-3,5-dimethylpyrazine, 2-isobutyl-3-methoxypyrazine, benzeneacetaldehyde, 3-methylbutanal, 2-methylbutanal, etc	

Ma et al. studied the relationship between five aromatic compounds (hexaldehyde, 1-octen-3-ol, γ-decalactone, 2-AP, 2,3-butanedione) and amylose in cooked rice. Experimental results showed that, except for 2,3-butanedione, the other four aroma components can interact with amylose to form V-type crystal complexes, confirming the effect of amylose on aroma release [36]. Table 2-2 summarizes some VOCs released from cooked rice. In general, there are many kinds of VOCs in cooked rice, but only a few of them affect the overall flavor of cooked rice [37].

Table 2-2 Volatile organic compounds in cooked rice

volatile organic compounds	odor description	extraction method	cooked rice types	[c]RI				literature
				DB-WAX	ZB-5	Capillary GC	FFAP	
Hexanal	leaf-like	SDE, DHS	cooked Korean non-aromatic rice	1078				[38]
	green	SPME GC–O, GC–PFPD	jasmine rice (khao dawk mali 105)	1086	799			[39]
	-	GC-O/GC-MS	japonica cooked rice			1081		[40]
	green	HRGC-O/HRGC-MS	cooked brown rice				1089	[35]
Unknown	earthy, sulfury	SDE	cooked Korean non-aromatic rice	1096				[38]
2-Pentylfuran	green bean	SDE, DHS	cooked Korean non-aromatic rice	1224				[38]
	-	GC-O/GC-MS	japonica cooked rice			1227		[40]
2-Methyl-3-furanthiol	vitamin, meaty, cooked rice	SDE, DHS	cooked Korean non-aromatic rice	1297				[38]
	meaty	SPME GC–O, GC–PFPD	jasmine rice (khao dawk mali 105)	1313	873			[39]
	meaty, sulfurous	HRGC-O/HRGC-MS	cooked brown rice				1319	[35]
2-Acetyl-1-pyrroline	popcorn	SDE, DHS	cooked Korean non-aromatic rice	1340				[38]
	cooked jasmine rice	SPME GC–O, GC–PFPD	jasmine rice (khao dawk mali 105)	1342				[38]
	popcorn, toasted grain, nuty	HS-SPME-GC-MS/MS	[b]ten cooked rice samples	1354				[41]

volatile organic compounds	odor description	extraction method	cooked rice types	[c]RI				literature
				DB-WAX	ZB-5	Capillary GC	FFAP	
Nonanal	-	GC-O/GC-MS	japonica cooked rice			1353		[40]
	popcorn-like	HRGC-O/HRGC-MS	cooked brown rice				1330	[35]
	tallowy	SDE, DHS	cooked Korean non-aromatic rice	1401				[38]
	green, citrusy, soapy	SPME GC–O, GC–PFPD	jasmine rice (khao dawk mali 105)	1396	1106			[39]
	green, fatty, citrus	HS-SPME-GC-MS/MS	[b]ten cooked rice samples	1401				[41]
(E)-2-Octenal	-	GC-O/GC-MS	japonica cooked rice			1396		[40]
	fatty	SDE	cooked Korean non-aromatic rice	1427				[38]
	green, nutty	SPME GC–O, GC–PFPD	jasmine rice (khao dawk mali 105)	1435	1062			[39]
	-	GC-O/GC-MS	japonica cooked rice			1435		[40]
1-Octen-3-ol	mushroom-like	SDE	cooked Korean non-aromatic rice	1445				[38]
	green, mushroom, earthy, oily	HS-SPME-GC-MS/MS	[b]ten cooked rice samples	1455				[41]
Methional	baked potato	SDE, DHS	cooked Korean non-aromatic rice	1451				[38]
	cooked potato	SPME GC–O, GC–PFPD	jasmine rice (khao dawk mali 105)	1456	910			[39]
Decanal	flowery	SDE, DHS	cooked Korean non-aromatic rice	1504				[38]

volatile organic compounds	odor description	extraction method	cooked rice types	[c]RI				literature
				DB-WAX	ZB-5	Capillary GC	FFAP	
	fatty, citrusy	SPME GC–O, GC–PFPD	jasmine rice (khao dawk mali 105)	1506	1202			[39]
Benzaldehyde	-	GC-O/GC-MS	japonica cooked rice			1531		[40]
	almond, nutty	HS-SPME/GC-MS	cooked Chinese japonica rice	1541.46				[42]
(E)-2-Nonenal	tallowy, green	SDE, DHS	cooked Korean non-aromatic rice	1545				[38]
	metallic	SPME GC–O, GC–PFPD	jasmine rice (khao dawk mali 105)	1540	1161			[39]
Unknown	earthy	SDE	cooked Korean non-aromatic rice	1626				[38]
(E,Z)-2,4-Decadienal	waxy, fatty	SDE	cooked Korean non-aromatic rice	1767				[38]
	-	GC-O/GC-MS	japonica cooked rice			1769		[40]
(E,E)-2,4-Decadienal	waxy, fatty	SDE, DHS	cooked Korean non-aromatic rice	1777				[38]
	fatty, metallic	SPME GC–O, GC–PFPD	jasmine rice (khao dawk mali 105)	1820	1318			[39]
	-	GC-O/GC-MS	japonica cooked rice			1824		[40]
Unknown	vitamin, meaty, cooked rice	SDE, DHS	cooked Korean non-aromatic rice	1897				[38]
4-Vinylguaiacol	clove	SDE	cooked Korean non-aromatic rice	2196				[38]
Dimethyl sulphide	cooked, sulfury	SPME GC–O, GC–PFPD	jasmine rice (khao dawk mali 105)	760	690			[39]

volatile organic compounds	odor description	extraction method	cooked rice types	[c]RI				literature
				DB-WAX	ZB-5	Capillary GC	FFAP	
3-Methyl-2-butene-1-thiol	nutty, sulfury	SPME GC–O, GC–PFPD	jasmine rice (khao dawk mali 105)	1093	824			[39]
	citrusy	SPME GC–O, GC–PFPD	jasmine rice (khao dawk mali 105)	1290	999			[39]
Octanal	citrus-like	HRGC-O/HRGC-MS	cooked brown rice				1284	[35]
	-	GC-O/GC-MS	japonica cooked rice			1295		[40]
1-Octen-3-one	mushroom	SPME GC–O, GC–PFPD	jasmine rice (khao dawk mali 105)	1303	980			[39]
	mushroom-like	HRGC-O/HRGC-MS	cooked brown rice				1300	[35]
Hexanol	green	SPME GC–O, GC–PFPD	jasmine rice (khao dawk mali 105)	1376	869			[39]
Dimethyl trisulfide	sulfury, cabbage-like	SPME GC–O, GC–PFPD	jasmine rice (khao dawk mali 105)	1384	979			[39]
Unknown	musty	SPME GC–O, GC–PFPD	jasmine rice (khao dawk mali 105)	1439	-			[39]
	fatty, metallic	SPME GC–O, GC–PFPD	jasmine rice (khao dawk mali 105)	1575	-			[39]
1-Octanol	waxy, green citrus	HS-SPME-GC-MS/MS	[b]ten cooked rice samples	1564				[41]
	-	GC-O/GC-MS	japonica cooked rice			1575		[40]
(E,Z)-2,6-Nonadienal	green, metallic	SPME GC–O, GC–PFPD	jasmine rice (khao dawk mali 105)	1593	1157			[39]
Unknown	roasted, nutty	SPME GC–O, GC–PFPD	jasmine rice (khao dawk mali 105)	1635	-			[39]

volatile organic compounds	odor description	extraction method	cooked rice types	[c]RI				literature
				DB-WAX	ZB-5	Capillary GC	FFAP	
(E)-2-Decenal	green herbal geranium	SPME GC–O, GC–PFPD	jasmine rice (khao dawk mali 105)	1656	1275			[39]
(E,E)-2,4-Nonadienal	fatty, metallic	SPME GC–O, GC–PFPD	jasmine rice (khao dawk mali 105)	1711	1218			[39]
Dodecanal	minty, soapy	SPME GC–O, GC–PFPD	jasmine rice (khao dawk mali 105)	1727	1419			[39]
2-Acetyl-2-thiazoline	cooked jasmine rice	SPME GC–O, GC–PFPD	jasmine rice (khao dawk mali 105)	1766	1112			[39]
Geranyl acetate	floral	SPME GC–O, GC–PFPD	jasmine rice (khao dawk mali 105)	1780	1382			[39]
β-Damascone	sweet honey	SPME GC–O, GC–PFPD	jasmine rice (khao dawk mali 105)	1828	1425			[39]
β-Damascenone	sweet honey	SPME GC–O, GC–PFPD	jasmine rice (khao dawk mali 105)	1833	1395			[39]
α-Ionone	floral	SPME GC–O, GC–PFPD	jasmine rice (khao dawk mali 105)	1861	1459			[39]
Unknown	medicine	SPME GC–O, GC–PFPD	jasmine rice (khao dawk mali 105)	1867	-			[39]
2-Phenylethanol	floral	SPME GC–O, GC–PFPD	jasmine rice (khao dawk mali 105)	1907	1106			[39]
β-Ionone	raspberry, floral	SPME GC–O, GC–PFPD	jasmine rice (khao dawk mali 105)	1952	1496			[39]
Ethyl butyrate	fruity, green, apple, fatty	HS-SPME-GC-MS/MS	[b]ten cooked rice samples	1046				[41]

volatile organic compounds	odor description	extraction method	cooked rice types	[c]RI				literature
				DB-WAX	ZB-5	Capillary GC	FFAP	
Ethyl 3-methylbutanoate	fruity, sweet apple, pineapple	HS-SPME-GC-MS/MS	[b]ten cooked rice samples	1077				[41]
Ethyl hexanoate	fruity, apple peel	HS-SPME-GC-MS/MS	[b]ten cooked rice samples	1242				[41]
(E)-2-Heptenal	fruity, green, fatty	HS-SPME-GC-MS/MS	[b]ten cooked rice samples	1338				[41]
1-Hexanol	green, herbaceous, woody, sweet	HS-SPME-GC-MS/MS	[b]ten cooked rice samples	1361				[41]
	-	GC-O/GC-MS	japonica cooked rice			1383		[40]
Ethyl octanoate	fruity, fatty, brandy	HS-SPME-GC-MS/MS	[b]ten cooked rice samples	1444				[41]
Ethyl 3-hydroxybutyrate	green, fruity, waxy, apple skin	HS-SPME-GC-MS/MS	[b]ten cooked rice samples	1529				[41]
2,3-Butanediol	creamy, fruity, buttery	HS-SPME-GC-MS/MS	[b]ten cooked rice samples	1548				[41]
2-Undecanone	waxy, fruity creamy, fatty, floral	HS-SPME-GC-MS/MS	[b]ten cooked rice samples	1606				[41]
Ethyl benzoate	sweet, fruity, wintergreen, medicinal,	HS-SPME-GC-MS/MS	[b]ten cooked rice samples	1682				[41]
Naphthalene	pungent, tarry	HS-SPME-GC-MS/MS	[b]ten cooked rice samples	1764				[41]
	-	GC-O/GC-MS	japonica cooked rice			1713		[40]

volatile organic compounds	odor description	extraction method	cooked rice types	[c]RI				literature
				DB-WAX	ZB-5	Capillary GC	FFAP	
Ethyl benzeneacetate	-	HS-SPME-GC-MS/MS	[b]ten cooked rice samples	1798				[41]
2-Methylnaphthalene	sweet, floral, woody	HS-SPME-GC-MS/MS	[b]ten cooked rice samples	1878				[41]
1-Methylnaph-thalene	naphthyl, medicinal	HS-SPME-GC-MS/MS	[b]ten cooked rice samples	1916				[41]
Phenylethyl Alcohol	floral, sweet, rosey, honey	HS-SPME-GC-MS/MS	[b]ten cooked rice samples	1929				[41]
Ethyl 9-hexadecenoate	-	HS-SPME-GC-MS/MS	[b]ten cooked rice samples	2267				[41]
Indole	animal, floral, mothball	HS-SPME-GC-MS/MS	[b]ten cooked rice samples	2475				[41]
	-	GC-O/GC-MS	japonica cooked rice			2441		[40]
1-Butanol	-	GC-O/GC-MS	japonica cooked rice			1135		[40]
Pyridine	-	GC-O/GC-MS	japonica cooked rice			-		[40]
Acetophenone	-	GC-O/GC-MS	japonica cooked rice			1615		[40]
2-Undecenal	-	GC-O/GC-MS	japonica cooked rice			1748		[40]

volatile organic compounds	odor description	extraction method	cooked rice types	[c]RI				literature
				DB-WAX	ZB-5	Capillary GC	FFAP	
Hexanoic acid	-	GC-O/GC-MS	japonica cooked rice			1855		[40]
Benzyl alcohol	-	GC-O/GC-MS	japonica cooked rice			1855		[40]
Heptanoic acid	-	GC-O/GC-MS	japonica cooked rice			1885		[40]
Benzothiazole	-	GC-O/GC-MS	japonica cooked rice			1938		[40]
1-Dodecanol	-	GC-O/GC-MS	japonica cooked rice			1965		[40]
Phenol	-	GC-O/GC-MS	japonica cooked rice			1998		[40]
2-Pentadecanone	-	GC-O/GC-MS	japonica cooked rice			2016		[40]
2-Pyrrolidinone	-	GC-O/GC-MS	japonica cooked rice			2029		[40]
Octanoic acid	-	GC-O/GC-MS	japonica cooked rice			2088		[40]
6,10,14-Trimethyl-2-pentadecanone	-	GC-O/GC-MS	japonica cooked rice			2116		[40]
2-Methoxy-4-vinylphenol	-	GC-O/GC-MS	japonica cooked rice			2173		[40]

volatile organic compounds	odor description	extraction method	cooked rice types	[c]RI				literature
				DB-WAX	ZB-5	Capillary GC	FFAP	
Nonanoic acid	-	GC-O/GC-MS	japonica cooked rice			2183		[40]
Methyl palmitate	-	GC-O/GC-MS	japonica cooked rice			-		[40]
Decanoic acid	-	GC-O/GC-MS	japonica cooked rice			-		[40]
2-Tetradecanone	-	GC-O/GC-MS	japonica cooked rice			-		[40]
Ethyl palmitate	-	GC-O/GC-MS	japonica cooked rice			-		[40]
4-Methyl-5-thiazoleethanol	-	GC-O/GC-MS	japonica cooked rice			2299		[40]
2,4-Di-tert-butylphenol	-	GC-O/GC-MS	japonica cooked rice			2337		[40]
2,3-Dihydrobenzofuran	-	GC-O/GC-MS	japonica cooked rice			2398		[40]
Dodecanoic acid	-	GC-O/GC-MS	japonica cooked rice			2513		[40]
Tridecanoic acid	-	GC-O/GC-MS	japonica cooked rice			-		[40]
Vanillin	-	GC-O/GC-MS	japonica cooked rice			2538		[40]
Butan-2,3-dione	buttery	HRGC-O/HRGC-MS	cooked brown rice				985	[35]

volatile organic compounds	odor description	extraction method	cooked rice types	[c]RI				literature
				DB-WAX	ZB-5	Capillary GC	FFAP	
2-Methoxy-3,5-Dimethylpyrazine	earthy	HRGC-O/HRGC-MS	cooked brown rice				1423	[35]
2-Isobutyl-3-methoxypyrazine	earthy, green bell pepper	HRGC-O/HRGC-MS	cooked brown rice				1514	[35]
Benzeneacetaldehyde		HSSE/GC/MS	cooked jasmine rice	1045				[34]
3-Methyl-butanal		HSSE/GC/MS	cooked jasmine rice	652				[34]
2-Methyl-butanal		HSSE/GC/MS	cooked jasmine rice	660				[34]

[a]Abbreviations: FFAP, Free fatty acid phase; SDE, Steam distillation and solvent extraction; DHS, Dynamic headspace sampling; SPME GC-O, solid phase microextraction gas chromatography-olfactometry; GC-PFPD, gas chromatography-pulsed flame photometric detector; HS-SPME, Headspace solid-phase micro-extraction; HS-SPME-GC-MS/MS headspace solidphase microextraction with gas chromatography-tandem mass spectrometry; HRGC/O, High-Resolution Gas Chromatography-Olfactometry; HRGC/MS, High-Resolution Gas Chromatography-Mass Spectrometry; HSSE/GC/MS, Headspace sorptive extraction Gas Chromatography-Mass Spectrometer; [b]Ten cooked rice samples: IR-64, Pusa Basmati-1, Pusa Basmati-1509, and Pusa 1652 (Improved Kala Namak), Jeera 32, Govind Bhog, Kala Jeera, Kala Nuniya, Kala Namak-1, and Kala Namak-2; [c]RI: Retention index.

2.1.1.1 Aldehydes

The aldehydes (hexanal, nonanal, decanal, octanal, Methional, etc.) are thought to decompose primarily through lipid oxidation, which accounts for the largest proportion of cooked rice flavor content (Table 2-2). Nonanal, with the RI (Retention Index) of 1401 and concentration of 34.8 ± 0.7 ng/g in cooked rice Pusa Basmati-1509, mainly contributes to tallowy green, citrusy, soapy, and fatty flavor for cooked rice [41]. Meanwhile, hexanal contributes a leaf-like and green for cooked rice, and the odor intensity is 9.96 for Basmati cooked rice [38, 39]. After cooking, non-fragrant rice contains significantly more nonanal content than fragrant rice, so that cooking can distinguish the two kinds of rice [38]. Benzaldehyde, characterized by its almond and nut-like aroma [43], has been recognized as a key and abundant VOC widely distributed in traditional rice cultivars [44]. Using a metabolomics approach based on headspace solid-phase microextraction coupled with GC-MS, Zhao et al. investigated the differentiation of japonica rice varieties from various regions of China in both raw and cooked states. Their findings revealed that benzaldehyde concentrations showed little variation among raw rice samples but differed markedly after cooking. Specifically, the study concluded that cooked rice samples from southern China, which contained higher amounts of lipid oxidation products, contained the highest levels of benzaldehyde, whereas samples from the northeastern region exhibited the lowest concentrations of benzaldehyde [42].

The odor of cooked rice left over for an extended period may be due to aldehyde formation. Therefore, Tsuchida et al. developed a chemical analysis method to determine the flavor composition of cooked rice by comparing the chemical composition of fresh cooked rice with that of cooked rice stored for a period. The bamboo charcoal was used to enhance the flavor of the cooked rice, and a subsequent chemical evaluation was conducted. GC-MS analysis revealed that the aroma of the stored rice was associated with the generation of aldehydes, including hexanal, heptanal, nonanal, and octanal, during storage. These aldehydes were present in the steam before, during, and after cooking the rice. Fourier Transform InfraRed (FT-IR) measurements showed an obvious ester-based peak before cooking, but it was absent after the rice had been left for some time. This peak arose from the formation of a new aldehyde group, indicating partial hydrolysis and oxidation of the esters, which were converted to

aldehydes. The findings suggested that the odor of cooked rice was closely bound up with aldehydes. Bamboo charcoal could adsorb aldehyde compounds during cooking and reduce the odor of aged cooked rice, consistent with the results of the sensory analysis report [45]. A small portion of aldehydes can impart a pleasant, fruity flavor to cooked rice. As storage time increases, cooked rice produces many aldehydes, which leads to odor formation. In addition, Strecker aldehydes (2-methylpropanal, 2-methylbutanal, 3-methylbutanal, etc.) at parts-per-million threshold produced through the Maillard reaction primarily contribute malty aroma characteristics to cooked rice [34, 46, 47]. Therefore, attention should be paid to controlling the content of aldehydes in cooked rice processing.

2.1.1.2 Alcohols and Heterocyclic Compounds

Heterocyclic compounds, which consist of monoheterocyclic and gelled heterocyclic compounds (furan, Thiazole, pyridine, quinoline, etc.), are identified in Table 2-2. Specifically, the degradation of starch occurs primarily through retroaldol reactions, which generate small reactive fragments, such as hydroxylated carbonyl compounds and α-diketo compounds, that act on α-amino acids to form labile intermediates. Most of the labile intermediates undergo a specific condensation or degradation reaction, resulting in heterocyclic substances that exhibit profound flavor properties. Meanwhile, the heterocyclic flavors of cooked rice, found in Maillard flavor compounds, include pyridines, thiazoles, pyrazines, furans, oxazoles, and pyrroles, as well as their derivatives. [48]. Dihydrobenzofuran, 2-pentylfuran, 2-acetyl-2-thiazoline, etc., were produced by lipid reaction and Maillard reaction, and have less overall content in cooked rice [49]. In furans, 2-alkyl furans with long side chains are usually formed by oxidation of lipids. 2-pentylfuran probably comes from the secondary oxidation products of monohydroperoxides, which typically give cooked rice its nutty and bean flavor [43]. 2-pentylfuran has also been found in diverse thermally processed foods and juices [50], and it can be detected using deuterated analogs [51]. The presence of specific lipid oxidation products, e.g., 2-pentylfuran and indole, can reduce the aromaticity of cooked rice, thereby negatively affecting consumers' acceptance. Excellent rice varieties usually possess a high level of 2-AP and a low concentration of lipid-oxidizing compounds.

As shown in Table 2-2, alcohols (1-octen-3-ol, hexanol, 1-octanol, etc.) have a

higher odor threshold, and they are considered to be the most abundant compounds except for aldehydes [33]. Meanwhile, the floral and fruity aroma of cooked rice is contributed by alcohols [43]. In addition, among all alcohols, 1-octen-3-ol is thought to be produced during lipid oxidation; it has a high content and a low threshold for the smell of wild mushrooms, contributing most to cooked rice aroma [9].

2.1.2 Cooked rice flavor detection method

The key to detecting the quality of cooked rice lies in identifying its volatile flavor. The detection methods for cooked rice flavor can be divided into sensory evaluation methods and instrumental analysis methods (e.g., gas chromatography (GC), electronic nose (E-nose)). The detection results include qualitative analysis and quantitative comparison. From the qualitative analysis, classes of various VOCs can be identified, and different rice varieties can be distinguished. The concentration of specific VOCs can be obtained from quantitative analysis.

2.1.2.1 Sensor evaluation method

Sensory evaluation with human noses as detectors provides direct, intuitive, unique, and subjective information about the flavor of cooked rice. This method offers the ultimate human sense, while the theoretical odor detection limit of the human nose is around 10^{-19} mol [52]. For the detection of cooked rice flavor, sensory evaluation is usually carried out while eating cooked rice [53, 54]. The sensory evaluation method enables the subjective assessment of the taste characteristics of cooked rice, typically conducted by a trained panel of several members. They will be asked to assess sensory information on the taste, aroma, and overall quality of the cooked rice. During the sample assessment, each panelist will consume some specific food (such as natural mineral water and saltless crackers) to maintain a clean taste. The final sensory scores are statistically analyzed to ensure the accuracy of the experiment [55].

Honma et al. employed quantitative descriptive analysis (QDA) to study the sensory properties of 10 cooked brown rice samples. Eight technical panelists selected 94 sensory-descriptive terms to evaluate four samples using an open-ended sensory evaluation mode. Preliminary sensory testing identified 18 kinds of evaluation criteria (Aroma: 3; Appearance: 4; Taste: 4; Taste: 1; Texture: 6), as the aroma includes “the

smell of green grass after mowing", "the aroma of freshly cooked white rice", and the aroma of sweet boiled red beans". After multiple comparisons, 18 attributes showed evident differences ($p < 0.05$) among ten cooked brown rice samples [56].

Lapchareonsuk and Sirisomboon et al. proposed exploiting visible light and shortwave near-infrared spectroscopy (NIRS) techniques to analyze the aroma quality of cooked rice. Four distinct cultivars of polished rice were utilized in this research: cooked rice, white rice, fresh jasmine rice, and aged jasmine rice. The organoleptic quality of the rice, including stickiness, firmness, dryness, whiteness, and aroma, was evaluated by a sensory team, which revealed that these sensory properties were correlated with visible light and shortwave NIRS data. Data analysis: visible- and shortwave-NIRS models were built using partial least squares regression to predict the sensory quality of cooked rice. The R^2_{val} values of the sensory quality prediction results all varied from 0.837 to 0.918, among which the cooked rice aroma had the maximum R^2_{val} value of 0.918 [53].

2.1.2.2 Instrumental analysis method

The GC method is a common method for VOCs identification in cooked rice [43, 57]. It consists of two important steps: sample pretreatment and final identification. Generally, solvent extraction and headspace (HS) methods are used for pretreating cooked rice samples. The cooked rice aroma is usually subjected to isotopic dilution with the combination of GC-MS, and the detection standards of each VOC are individually set to quantify the detected substances accurately [51].

Shi et al. employed a combined sensory evaluation technique, incorporating gas chromatography-tandem mass spectrometry (GC-MS/MS) and scanning electron microscopy (SEM) to study the variation in aromatic constituents and microstructure of cooked brown rice during roasting. Roasting, a powerful processing technique for increasing the content of aromatic compounds in grains, has been extensively applied in rice and cereal products in recent years [58]. GC-MS analysis detected 11 VOCs in cooked brown rice samples, and roasting increased the content of heterocyclic compounds and decreased the concentrations of hydrocarbons and benzene derivatives [59]. The primary flavor substances in roasted brown rice are mainly Maillard-derived volatiles, including furfural, 5-methylfurfural, 2,5-dimethylpyrazine, 2-methylpyrazine, 2-ethyl-6-methylpyrazine, and 2-ethyl-3,5-dimethylpyrazine. In addition, roasting can

lead to an uneven surface of cooked brown rice, increase the space between particles, and promote the production and distribution of aromatic components. Such microstructural variation increases the spillover pathways of aromatic compounds. Qi et al. studied the impacts of various processing methods on the fluidity, solubility, nutritional components, composition, color, and aroma components of four types of ready-to-eat brown rice. GC-MS methods provided quantitative analysis of 18 VOCs, including 13 aldehydes, 2 heterocyclic furans, 1 each of ketones, olefins, and acids, and no alcohols or esters were detected [60].

Dias et al. studied the VOCs produced from fragrant cooked rice (IAC 500) to identify compounds that play a pivotal part in cooked rice flavor. The aroma of IAC 500 rice was mainly described via a carefully selected professional sensory panel, and the VOCs of cooked rice extracted by SPME were identified by olfactometry (OSME) and GC-MS. 80 volatiles in total were identified through OSME, and 65 compounds in total were detected via chromatographic analysis, of which 44 had a certain odor, and 36 did not. The detected compounds were mainly aldehydes, alkanes, carboxylic acids, alcohols, and ketones [61]. The study by Maraval et al. aimed to complete the analysis of flavor VOCs released by two fragrant rice samples (Aychade and Fidji) from the Camargue region and to compare them with those of a well-known Asian fragrant rice cultivar (Thai). In addition, non-aromatic varieties from the Camargue region were compared with aromatic varieties. The gas chromatography-olfactometry (GC-O) technique was employed to research the odor profile [62] of cooked rice samples, as it allows the selection and analysis of odorant-active compounds in complex mixtures [63, 64], and the working principle is shown in Figure 2-1. In addition, it was more accurate to combine with GC-MS to detect various cooked rice flavor compounds [65].

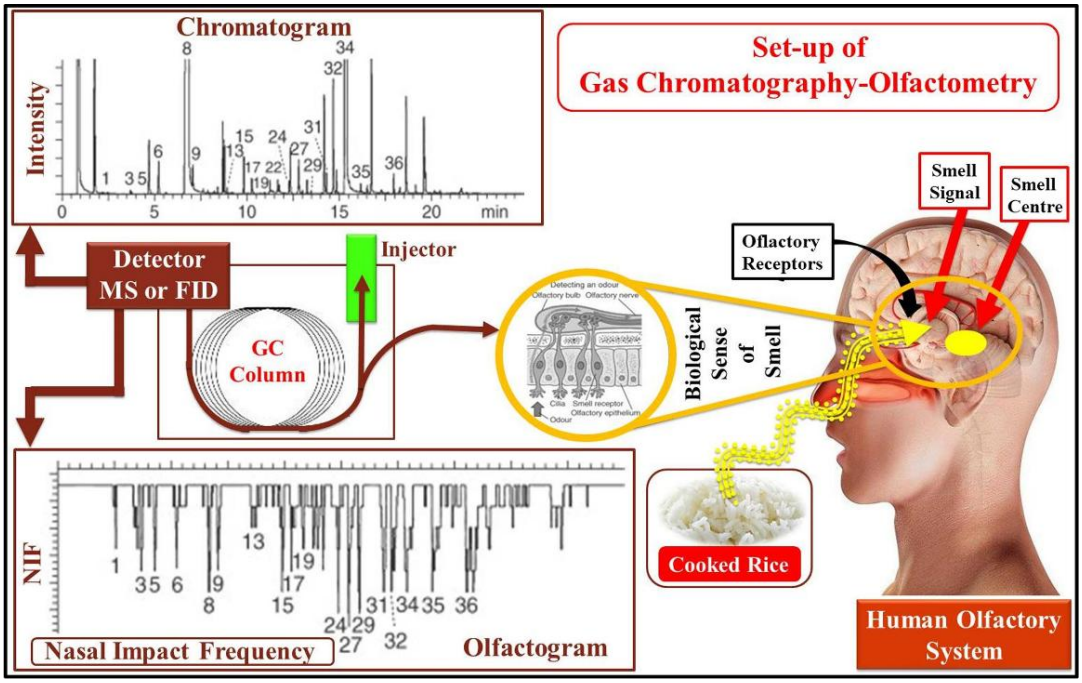

Figure 2-1 Schematic diagram of GC-O system [66].

Furthermore, Gas Chromatography-Olfactometry-Mass Spectrometry (GC-O-MS) integrates the virtues of sensory description analysis and GC-MS. GC-O-MS plays a crucial role in identifying pivotal, aromatic, and vigorous compounds in cooked rice, providing not only minute sensory evaluation of flavor quality but also quantitative and qualitative analyses of compounds. Steam distillation and solvent extraction (SDE) are widely used for the identification of cooked rice flavor. However, it is time-consuming and tedious, and its reproducibility is poor, so it is easy to lead to errors in the analysis process and loss of some compounds [38].

Zeng et al. used an improved HS-SPME method to directly extract aroma volatile compounds from 3 Japanese rice varieties, namely Nihonbare, Koshihikari, and Akitakomachi, during the cooking process, and GC-MS was used to analyze them. 46 VOCs in total were detected, incorporating aldehydes, ketones, alcohols, heterocyclic compounds, fatty acid esters, phenolic compounds, and hydrocarbons. As the cooking time was prolonged, the number of significant odor compounds added increased, while the quantity of volatiles with low boiling points decreased. Guo et al. used headspace-gas chromatography-time-of-flight mass spectrometry (HS-GC-TOF MS) combined with headspace-solid phase microextraction-gas chromatography-time-of-flight mass spectrometry (HS-SPME-GC-TOF MS) for precise and rapid quantification of 2-AP in cooked rice [67]. Aseptic-packaged cooked rice (APCR) is a type of rice food with a

rapidly expanding market. Compared with rice steamed in electric rice cookers, APCR has a longer shelf life (6 months) and only needs to be microwaved for 2 minutes before eating [68]. Lee et al. used a standard addition method combined with SPME/GC-MS to quantify 2-AP flavor in APCR. The results showed that the content of 2-AP in APCR containing 20% fragrant rice stored at 25℃ for 1 month and 2 months was 15.3 ~ 9.5 ng/g and 6.1 ng/g, respectively, which proved the practicability of the method [69].

An electronic nose is a novel instrument for fast food detection developed in the 1990s. It uses diverse gas sensors and pattern recognition systems to provide overall information quickly about the target sample, and the corresponding data are distinguished accurately [70, 71]. SMOX gas sensor-based E-noses have chemical imaging capabilities and sensor systems with the advantages of excellent cross-sensitivity and fast, stable, and broad-spectrum response, which can be used to analyze VOCs in cooked rice [72, 73]. Jana et al. introduced an aroma-based detection and classification instrument for aromatic rice varieties. It mainly consisted of an odor-processing module, an olfactory-detection module, a water-bath module, and a computing module. The odor processing module mainly transfers the flavor of cooked rice to the olfactory detection module. The olfactory detection module is formed by a printed circuit board assembled with eight gas sensors and a sensor chamber. The water bath module, connected to a heater to facilitate cooking, is used to prepare rice samples. The computational module quantifies the smell messages collected via the sensors. Principal Component Analysis (PCA) enables data acquisition from sensor arrays and clustering. Probabilistic Neural Network (PNN), Back propagation multilayer perceptron (BPMLP), and Linear Discriminant Analysis (LDA) were used to identify and classify rice varieties [74].

Sinelli et al. used an E-nose and near-infrared (NIR) Fourier transform (FT-NIR) technology to explore the optimal cooking time (OCT) of unpolished rice, cooked rice, and instant rice, and compared it with the gelatinization time and the suggested cooking time (SCT) on the packaging label. It was found that the FT-NIR method could accurately confirm the OCT of polished and cooked rice. Moreover, the maximum rate of aromatic flavor change during cooking, as assessed by E-nose, was associated with the SCT of the 3 rice samples. In addition, the combination of the two methods is faster, simpler, and more objective, making it ideal for sensory analysis and for determining rice gelatinization time [75]. Rok et al. used an E-nose comprising 12 gas sensors to

study complex odors emitted by 44 japonica rice varieties and to characterize VOCs emitted from Japonica rice and from cooked Japonica rice. The responses of gas sensors were evaluated using PCA and clustering analysis (CA) [76]. In addition to traditional gas sensors, E-noses are currently combined with mass spectrometry and colorimetric sensors, which enhances their innovation and reliability for cooked rice aroma detection. As discussed above, this section summarizes the evaluation techniques for cooked rice flavor, as shown in Tables 2-3 and 2-4.

Table 2-3 Summary of evaluation methods for identifying VOCs in cooked rice

evaluation method	food type (cooked rice)	the main VOCs	cooking method and instrument	literature
HS-SPME/GC-MS	brown rice	hexanal, nonanal, and 2-pentylfuran	the high-pressure cooking (60, 70, and 105 kpa), the low-pressure cooking (30, 40, and 50 kpa)	[77]
GC	soybean-rice mixture	-	cooked by two types of rice cookers: an erc (lj-mg0402) and an eprc (ljp-sa063e)	[78]
HS-SPME/GC-MS	three japanese rice cultivars, nihonbare, koshihikari, and akitakomachi	indole and 2-acetyl-1-pyrroline	cooked by sra18h automatic electric rice cooker during four stages	[79]
SPME/GC-MS	the akitakomachi cultivar of paddy rice (oryza sativa l.)	n-nonanal and hexadecanoic acid	cooked by sra18h automatic electric rice cooker during four stages	[80]
GC-MS/FT-IR	koshihikari (polished rice)	hexanal, heptanal, octanal, nonanal	cooked by ih rice cooker (sr-spx104, panasonic)	[45]
Sensory evaluation/E-nose/ HS-SPME/(GC-MS/MS)/SEM	brown rice (japonica rice)	furans and pyrazines	roasted by different time and temperature	[59]
E-nose	kaminibhog, radhunipagal, govindobhog, sitabhog et al	-	cooked at 100^{o}C for 20 minutes	[74]
HS-GC-TOF MS/ HS-SPME-GC-TOF MS/ Sensory evaluation	eight types of rice samples (zhongzao 39, yuexiuyou 376, nanjingxiangzhan et al)	2-acetyl-1-pyrroline	cooked according to the agricultural industry standard of china ny/t 596–2002 “aromatic rice” with some modification	[67]
OSME/GC-O/ SPME/GC-MS	aromatic rice iac 500	2-acetyl-1-pyrroline	cooked in an electric pan (mondial, são paulo, Brazil) with water at a ratio of 1:2.5 (100 g rice/250 ml water)	[61]
FGC E-Nose/HS-SPME-GC-MS	rice produced by yihai kerry co., ltd. (wuchang, heilongjiang, china)	2-acetyl-1-pyrroline and aldehydes	cooked using an automatic rice cooker (cfxb50fc8055-75, zhejiang supor limited by share ltd., hangzhou, zhejiang, China)	[7]
GC-MS/GC-O	three scented cultivars (aychade, fidji, and giano) and a common nonscented cultivar (ruille)	2-acetyl-1-pyrroline, hexan-1-ol, indole and phenol	rice (5 g) and mineral water (volvic, 10 ml) were cooked in open steam for 20 min	[65]

evaluation method	food type (cooked rice)	the main VOCs	cooking method and instrument	literature
Sensory evaluation /QDA	brown rice	-	cooked using an ih rice cooker (sr-fd106, panasonic corporation) without soaking	[56]
FT-NIR spectroscopy/E-nose	milled, parboiled and quick-cooking rice (oryza sativa l. japonica)	-	soaked in 1650 ml of water and cooked in a rice cooker for times up to 1320, 1200 and 900 s, respectively.	[75]
HS-SPME/GC-MS	aseptic-packaged cooked rice	2-acetyl-1-pyrroline	microwaved (model kr-g20ew; daewoo electronics co., south korea) for 120 s at 700 w	[69]
Sensory evaluation/Shortwave NIR	jasmine rice	-	home electronic rice cookers (rc-10 mm; toshiba, thailand)	[53]
SDE/GC/GC-MS	rice (oryza sativa l. japonica) harvested in niigata prefecture, japan	-	cooked in an aluminium cup by an automatic electric rice cooker (toshiba model rc-4b)	[81]
GC-O/GC-MS	twenty-six japonica rice varieties	2-acetyl-1-pyrroline	cooked according to a national standard method gb/t 15682-2008	[40]
SDE/DHS/GC-MS	korean non-aromatic rice	2-methyl-3-furanthiol and 2-acetyl-1-pyrroline	boiling by adding 200 ml deodorized distilled water	[38]
HS-SPME-GC-MS/MS	ten cooked rice samples	2-acetyl-1-pyrroline, ethyl butyrate, ethyl 3-methylbutanoate, ethyl benzoate and 2-methylnaphthalene	boiling by adding 0.25 ml of ultra-pure water with 1 g rice grain sample	[41]
SPME GC–O, GC–PFPD	jasmine rice (khao dawk mali 105)	2-acetyl-1-pyrroline	cooked in a rice cooker (black & decker, model no. rc3406) at 100°C, for 18 min	[39]

[a]Abbreviations: GC, Gas chromatography; GC-MS/MS, Gas chromatography-tandem mass spectrometer, SEM, Scanning electron microscope; HS-GC-TOF MS, Headspace-gas chromatography-time-of-flight mass spectrometry; HS-SPME-GC-TOF MS, Headspace-solid phase micro-extraction-gas chromatography-time-of-flight mass spectrometry; OSME, Olfactometry; GC-O, GC olfactometry technique; GC-FID, Gas chromatograph-flame ionization detector; FGC E-Nose, Flash gas chromatography electronic nose; HS-SPME-GC-MS, Headspace solid-phase micro-extraction method combined with gas chromatography-mass spectrometry; QDA, Quantitative Descriptive Analysis; FT-NIR, Fourier transformation near infra-red; NIR, Near-Infrared Spectroscopy.

Table 2-4 Overview of detection methods of characteristic flavor in cooked rice

Detection Method	Advantage	Disadvantage	Reference
GC-MS	high sensitivity, strong qualitative ability and convenient daily maintenance	relative high cost for purchase and restriction for widely use as the operation temperature limit[82, 83]	[45, 50, 77, 79]
HS-SPME	low detection limit, relative high sensitivity, simplicity, speed, wider compound coverage, and higher throughput, simple operation and fast test speed, basically no solvent, little environmental pollution, and less sample consumption	Sulfur and sulfide compounds cannot be detected[84]	[50, 79]
E-nose	low cost, accurate, fast, reliable, and portable	Data collection is tedious and labor-intensive. Data collection from different sources, the e-nose performance is highly affected by temperature modulation[85, 86]	[74, 87]
GC-O-MS	identification of key aroma-active compounds accurately, capable of illustrate relationship between odorants and sensory properties	limited scope of application, need to train professionals to operate[88]	[89]
Sensory evaluation	with subjective characteristics	low reproducibility and poor accuracy	[7, 67]

[a]Abbreviations: GC-O-MS, Gas Chromatography-Olfactometry-Mass Spectrometry.

2.2 Processing properties for cooked rice flavor

The whole cooking process is usually broken down into 4 phases: (I) 25 minutes from the beginning of heating until the steam comes out; (II) the steam starts to come out of the pot and ends 13 minutes later; (III) the remaining steam overflows from the rice cooker until it stops automatically 10 minutes of heating; (IV) 30 minutes of heat preservation starting from automatic stop heating [79]. In addition, rice cooking is a gelatinization process: the starch absorbs water. It expands when heated, and then the starch is released from the cell wall, destroying the previous crystal structure and forming a gel. The difference in the starch of cooked rice can affect the volatilization of aroma compounds [90]. A proper cooking process can minimize the nutrient loss of food and improve the edible characteristics and quality [91]If the cooking methods are inappropriate, the excessive nutrients may be lost, and the edible quality of cooked rice could decrease. Cooking rice usually requires five steps: washing rice, adding water, flooding, heating, and heat preservation. The purpose of each step in cooking rice is shown in Table 2-5, and the last three steps require more attention in the research. Different processing properties of cooked rice greatly impact the VOCs produced, as shown in Figure 2-2.

Table 2-5 The purpose of each step of cooking

steps	purpose	literature
wash rise	remove impurities and odors from rice grains, reduce potential arsenic or toxic metal contaminants	[92, 93]
add water	provides water for starch gelatinization	
flooding	make rice grain water absorption uniform, conducive to heating gelatinization	
heating	provides the energy needed for starch gelatinization	
heat preservation	use the remaining temperature in the pot to balance the water between rice grains, and make the starch gelatinize evenly	

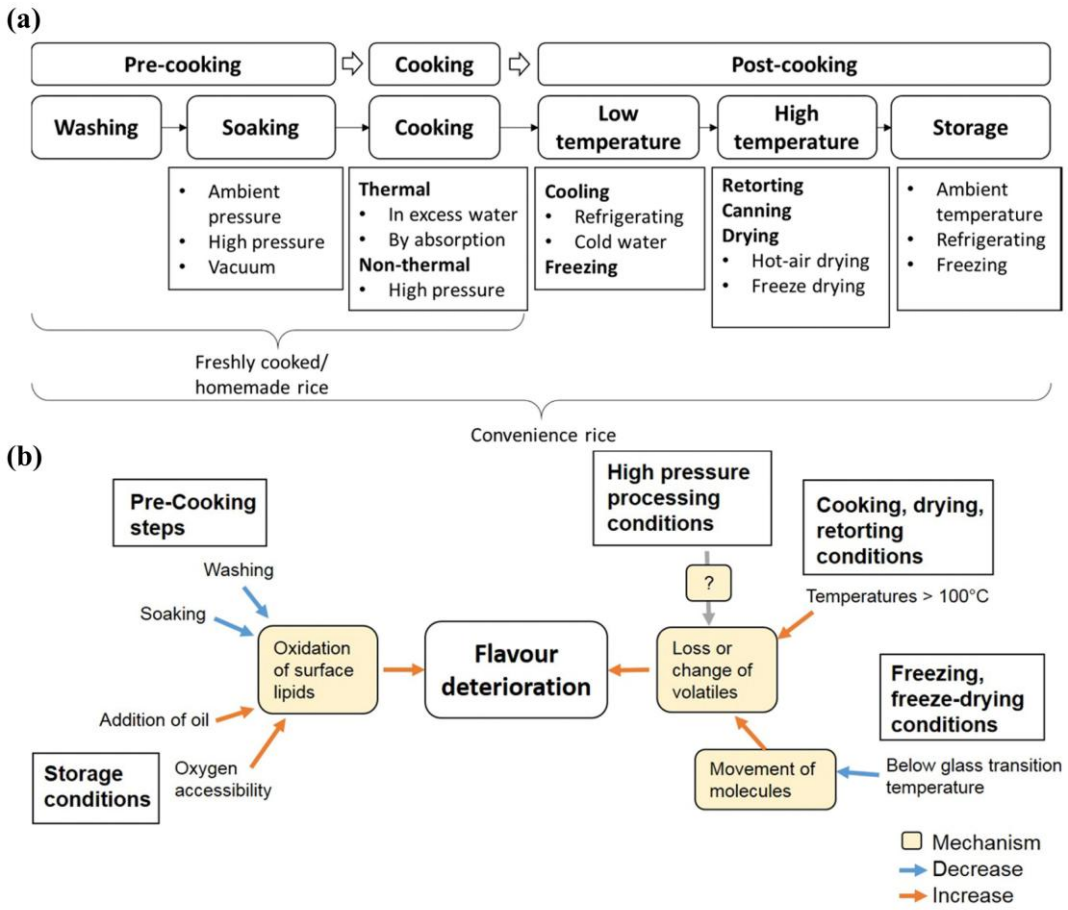

Figure 2-2 (a) Pre-cooking, cooking and post-cooking technologies with different classifications to produce freshly cooked and convenience rice; (b) Effects of processing conditions on cooked rice flavor deterioration, measured by sensory analysis and/or instruments [94].

The aroma of cooked rice is affected by the type of rice, pre-harvest conditions, post-harvest conditions, and processing properties [37], as we focus on the effects of some vital processing properties (cooking pressure, water content, temperature, etc. [95]) on the cooked rice aroma in this section.

2.2.1 Pressure

Among most Chinese, ordinary and pressure cooking are the universal home processing methods, while pressure cooking can bring better taste [78]. Xu et al. analysed the aroma of cooked rice using high-pressure steam (HPS) at different levels. The results showed that HPS cooking significantly affected the flavor characteristics of cooked rice. As the cooking pressure gradually increased from 0 MPa to 0.18 MPa, the

aldehyde content increased, and the alcohols and some heterocyclic compounds initially increased and then decreased. For example, the content of nonanal rose from 5.789% (0 Mpa) to 7.009% (0.18 Mpa), and 2-pentylfuran's level went from 3.819% to 10.106%, then down to 8.800% [8].

2.2.2 Water content

Depending on the different cultural backgrounds, rice varieties, and cooking methods, there are two main ways to make cooked rice at home [94]: (1) steaming with adsorbed pre-determined doses of water; (2) cooking with extra water at a specific temperature (higher than gelatinization temperature). The former method is more prone to result in insufficient water diffusion through the rice grain, and the starch in the center of the granule may not be completely gelatinized during cooking, which will generate a harder texture [96]. The larger food industry usually uses excess water to cook rice because this continuous cooking process keeps the rice particles fully saturated with moisture and uniformly distributed. Additionally, there are two mechanisms in rice cooking: (1) the water is absorbed asymptotically from the surface to the inside of the rice; (2) the textural composition of grains is changed by heating with water [97]. As for rice aroma, 11 rice varieties were soaked in water for 30 min, and a negative effect on flavor and sweetness indicates that soaking water could lose a small amount of flavor-active metabolites, while the flavor changing was not related to the change of grain structure [37, 98]. By adjusting the rice-cooking mechanism, the cooking method can be improved and the flavor quality of rice further enhanced.

Moisture also affects the flavor quality of instant-cooked rice. Dehydrated rice and non-dehydrated rice are the two main categories of instant cooked rice. Among them, dehydrated rice (α-rice) is widely popular due to its convenience, low moisture content, long shelf life, and straightforward production process. However, processed instant-cooked rice loses too much flavor and reduces taste quality. The high quality of the finished instant cooked rice can be determined by its taste character, and it needs to be enhanced [99, 100]. It is crucial to explore the impacts of different cooking methods on changes in flavor compounds and the quality of instant-cooked rice after rehydration.

2.2.3 Temperature

Temperature can indirectly affect the flavor of cooked rice by changing the degree of lipid oxidation. Through reducing the temperature, rapid cooling helps reduce starch degradation during the storage of cooked rice [101], which can add much freshness to the cooked rice.

Ma et al. investigated the relationship between cooling rates (CR) (0.19, 1.27, 1.74, and 2.88°C/min) and cooked rice flavor during storage. The experimental results of flash gas chromatography electronic nose (FGC E-nose) and sensory analysis indicated that the faster the cooling rate, the longer the aroma retention time of the rice. In contrast, the slower the cooling rate, the faster the acceptability of the cooked rice flavor degrades. In the experiment with 17 cooked rice samples in total, the control group (freshly boiled rice) had the highest total score, significantly higher than the other samples ($p < 0.05$). The scores for each sample showed significant discrepancies ($p < 0.05$) across storage times. With prolonged storage, the flavor of the samples deteriorated, and consumer acceptability decreased [7]. The half-boiling method is a hydrothermal method widely used in rice cooking. It causes variation in the physicochemical and nutritional features of rice particles, which has a huge impact on sensory and other taste qualities. Electrostatic interactions, including van der Waals forces, hydrogen bonds, and disulfide bonds, primarily mediate the binding between proteins and flavor substances in cooked rice. High temperature may weaken or disappear these forces, leading to a change in flavor substances [102]. Therefore, hydrothermal processing methods during half-boiling can not only passivate lipases in cooked rice but also inhibit off-flavor production, which significantly enhances the taste quality of cooked rice.

2.3 State of the art of Semiconductor Metal Oxide-based Gas Sensor for Cooked Rice Quality Detection

Cooked rice quality is governed by texture, aroma, and taste, and directly influences consumer acceptance and grading in both domestic and industrial contexts. Among these attributes, aroma is particularly critical, since it reflects complex profiles

of volatile organic compounds (VOCs) that are highly sensitive to rice variety, processing, and storage history, and therefore provides an informative fingerprint of cooked rice quality [103-106]. Conventional evaluation relies on trained sensory panels in combination with chromatographic techniques such as GC-MS and GC-O, which offer accurate characterization of key odorants but are time-consuming, destructive, and instrument-intensive, and difficult to deploy for online or at-line quality control of cooked rice [104, 107]. Recent studies have demonstrated that the headspace gas above cooked rice encodes rich information about eating quality, staling, and off-flavors, and that electronic nose systems based on arrays of low-cost gas sensors can already discriminate among varieties, storage conditions, and quality grades in both raw and cooked rice [108-110]. In general, gas sensors consist of an active sensing layer integrated with a transducer and operate by converting chemical interactions with target analytes into measurable electrical signals, such as changes in resistance, frequency, current, or voltage [111-113]. Within this broader family, semiconductor metal oxide (SMOX) chemoresistive gas sensors provide a particularly attractive platform for cooked rice quality detection, since they combine high sensitivity to trace VOCs with low cost, robustness, miniaturization, and straightforward integration into electronic nose architectures and embedded measurement systems that enable non-destructive, real-time monitoring of food quality [114-119]. Against this background, a focused analysis of SMOX-based gas sensors for cooked rice quality detection is timely. It can guide the design of future sensor systems for continuous monitoring of the palatability and safety of cooked rice throughout the rice supply chain. [117-119]

2.3.1 Generalities on semiconductor metal oxide gas sensors

In contemporary society, the ubiquitous presence of toxic, flammable, and explosive gases represents one of the most persistent and deleterious sources of atmospheric contamination. These hazardous gases not only accelerate the deterioration of ecological systems but also impose profound risks to human health and the survival of other living organisms. The deleterious consequences of such emissions have thus galvanized intense global efforts to develop highly sophisticated gas-sensing technologies. In particular, gas sensors capable of detecting trace-level analytes at concentrations well below the threshold of the human respiratory system have emerged

as indispensable tools across diverse disciplines, including environmental monitoring, agricultural management, industrial process control, and biomedical diagnostics [113, 120-122].

Fundamentally, a gas sensor comprises two principal components: a transducer and an active sensing layer. Functioning as a subset of chemical detectors, gas sensors transduce molecular interactions at the sensing interface into quantifiable electrical outputs. These measurable signals typically manifest as variations in electrical resistance, current, frequency, or potential, which serve as proxies for the concentration and identity of the target gases [123, 124]. To rigorously assess their efficacy, the performance of gas sensors is generally benchmarked against a suite of critical parameters, such as sensitivity, detection limit, selectivity, reproducibility, long-term stability, operating temperature range, resistance to ambient humidity, as well as rapidity of response and recovery dynamics [125, 126].

To enhance sensing capabilities, a range of advanced strategies has been systematically explored. These include rational heterojunction engineering [127], surface morphology modulation [128], defect state engineering [129], catalytic doping and surface functionalization [130, 131], physicochemical environment tailoring such as pH regulation [132], and the incorporation of highly porous and tunable metal organic frameworks (MOFs) [133, 134]. Notably, SMOX-based sensors, especially those operating on chemoresistive mechanisms, have demonstrated remarkable versatility and adaptability [135, 136]. Their applications now span from real-time medical diagnostics and health monitoring [137, 138], to industrial hazard prevention [121], crop diseases and insect pests detection [139], and food quality detection [140, 141]. The exceptional sensing attributes of SMOXs, including high signal-to-noise ratios, robustness under fluctuating environmental conditions, and the ability to be miniaturized and integrated into flexible or wearable platforms, position them as pivotal candidates for next-generation gas-sensing devices [142, 143]. Taken together, the rapid advances in material design and sensor engineering underscore the transformative potential of SMOX-based chemoresistive gas sensors. Their convergence with emerging paradigms such as artificial intelligence (AI), machine-learning-driven signal analysis, and the Internet of Things (IoT) promises to usher in a new era of intelligent, autonomous, and adaptive gas-sensing networks. These developments not only address the pressing global demand for real-time air quality surveillance but also lay the

foundation for future innovations in environmental protection, sustainable agriculture, industrial safety, and personalized healthcare.

2.3.2 Constitution, working principle, and testing procedure of SMOX gas sensors

Semiconductor metal oxide (SMOX) gas sensors are typically fabricated on insulating substrates, commonly made of alumina, silica, or flexible organic materials. These substrates are integrated with interdigitated metallic electrodes (most often gold or platinum) and heating elements, usually composed of platinum or nickel-chromium alloys. The active sensing layer, consisting of an SMOX, is deposited onto the substrate. While the electrodes enable precise measurement of electrical conductivity, the integrated heater regulates the operating temperature, thereby providing the activation energy required for gas adsorption and desorption, ultimately optimizing sensing performance.

The sensor electrodes (Figure 2-3(a)) specifically used in this thesis were fabricated using an alumina substrate with dimensions of 6 by 30 mm. The substrates were screen-printed with platinum paste to form a heater and measurement electrodes. A 0.42 mm gap was maintained between the electrodes for gear shaping. Prior to the deposition of the sensing film, the sensor substrates underwent a cleaning procedure involving sonication in deionized water and absolute alcohol. Specifically, a fixed milligram of synthetic gas-sensitive powder material was dispersed in deionized water or absolute alcohol to form a homogeneous slurry, which was then uniformly drop-coated onto the substrates (Figure 2-3(b)). The coated substrates were dried and thermally treated in an electric heating forced-air oven to obtain stable sensor elements suitable for subsequent gas-sensing measurements.

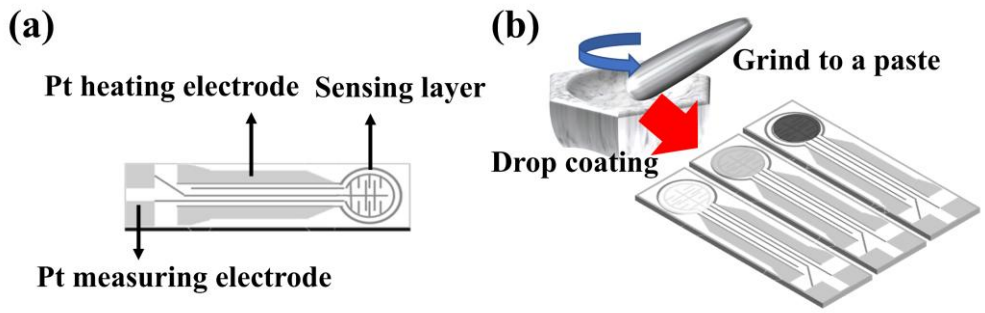

Figure 2-3 (a) The schematic diagram of sensor electrode and (b) sensing material drop coating process.

The experimental setup shown in Figure 2-4 allows the study of gas-sensing behavior of the sensors in contact with a specific gas or a gas mixture. Gas-sensing tests were performed using a four-channel gas sensing tester as shown in Figure 2-5. The testing apparatus consists of two main components: an air intake system and a detection unit. Synthetic dry air (79% N_2 + 21% O_2) was sourced from Nanjing Special Gas Factory Co., Ltd. The four-channel gas-sensing tester was acquired from Wuhan Huachuang Ruike Technology Co., Ltd. To adjust the concentration of the target gas, Bronkhorst mass flow controllers in Germany were used to vary the flow rates of synthetic dry air. This instrument measures changes in electrical resistance in both high-purity air and specific VOCs over time, detailing the resistance variation patterns. All tests were performed at room temperature (25 ± 2 °C), and the mean relative humidity was approximately 15-20% without any additional moisture control. A desktop computer was used to collect response data, equipped with an analog-to-digital (A/D) data acquisition board that measures electrical resistance values for the corresponding channels, using a laboratory DC power supply (GPS-3303C) with 12 V and 4 A. In detail, the data logger supplies a steady voltage of 2.5 V (V_{EX}). This voltage is distributed between the reference resistor (R_{ref}), which has a known, constant resistance, and the IDA-CR, whose resistance varies with the detected VOC concentration. The voltage is relatively distributed according to the resistance of the two circuit components. Therefore, given the voltage between V_{EX} and ground (GND), the voltage between V_{meas} and GND is measurable, and from their ratio, the IDA-CR resistance can be calculated, as described in Equation (2-1).

$$\frac{V_{meas}}{V_{EX}} = \frac{R_{CR}}{R_{CR}+R_{ref}} \rightarrow R_{CR} = \frac{R_{ref}\cdot(\frac{V_{meas}}{V_{EX}})}{1-(\frac{V_{meas}}{V_{EX}})} \quad (2\text{-}1)$$

The target gas vapor at a specified concentration was obtained using a simple dynamic gas distribution method. The saturated vapor pressures of nonanal, 1-octen-3-ol, and benzaldehyde liquids are 0.26 mmHg, 0.75 mmHg, and 0.975 mmHg (25 ± 2°C). The flow (x, unit: sccm) of standard nonanal, 1-octen-3-ol, and benzaldehyde with the concentration of 342 ppm, 1090 ppm, and 1283 ppm was calculated by Equation (2-2) [144] and controlled by the mass flow controllers. The flows of dry air (y, in sccm) and humid air (z, in sccm) from high-purity mixed air were controlled using two mass flow controllers. Relative humidity was regulated using two distinct flow meters; one for dry

air (flow rate: A sccm) and another for fully humidified air (flow rate: B sccm). The relative humidity was determined by the formula B/(A+B)*100%.

Concentration of VOCs (ppm) =(vapor pressure of VOCs (mmHg)/760)×10^6 (2-2)

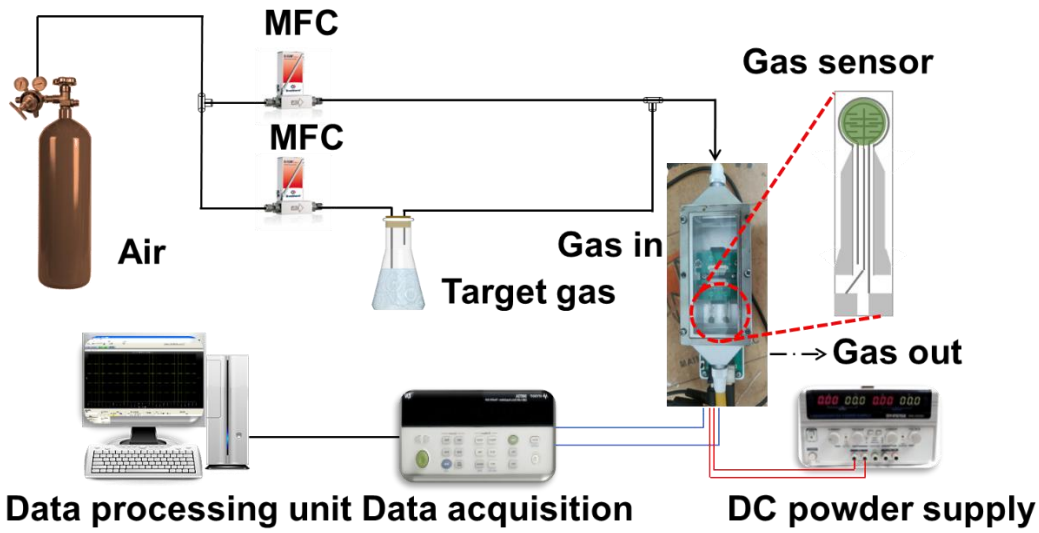

Figure 2-4 The schematic diagram of the gas sensing test systems.

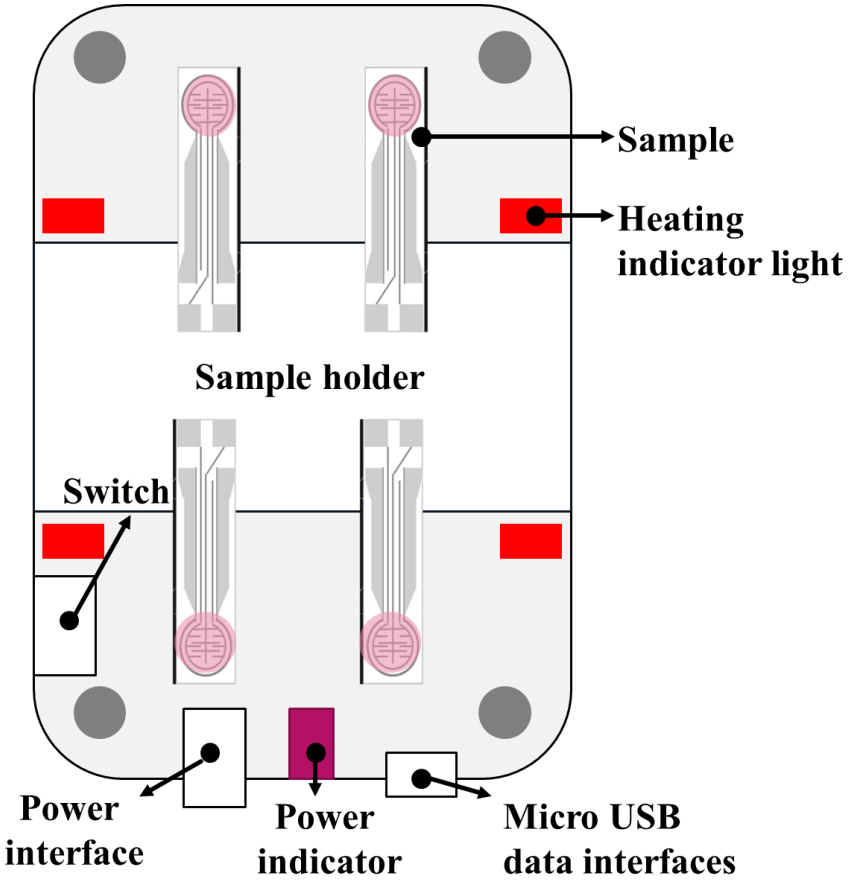

Figure 2-5 The schematic diagram of the sensor testing chamber.

The sensing mechanism is governed by the chemisorption of gas molecules onto the semiconductor surface, leading to electron transfer processes that modulate the material's conductivity. The extent of conductivity variation directly correlates with both the nature and concentration of the analyte gas, enabling selective and quantitative detection. In practice, SMOX-based gas sensing systems are often implemented in static configurations, incorporating valve assemblies, flow controllers, gas chambers, power supplies, and signal acquisition units [145, 146]. For sensor fabrication, artificial analyte samples containing a controlled amount of deionized water are typically ground in a mortar to produce a homogeneous mixture, followed by preparation of a paste. This paste is uniformly deposited onto the sensor substrate and subsequently aged under specific conditions to yield the functional sensing device. The sensor is then mounted within a test chamber for performance evaluation. Under controlled operating conditions, high-purity air is first introduced to establish a stable baseline resistance, after which the target gas is injected for sensing measurements. Upon achieving a steady resistance state, the chamber is purged again with high-purity air to restore the baseline. Throughout this process, the testing chamber is maintained as a contamination-free environment with well-regulated relative humidity and temperature, ensuring reproducible raw sensing data and reliable extraction of key performance metrics. Moreover, SMOX sensors can be engineered into diverse device architectures, including ceramic tube configurations or planar designs fabricated on alumina substrates, offering flexibility in structural design and application adaptability.

2.3.3 Criteria of SMOX gas sensor evaluation

The performance of SMOX-based gas sensors is commonly assessed by a comprehensive set of criteria, including optimum operating temperature, gas response (sensitivity), response and recovery dynamics, selectivity and anti-interference capability, limit of detection (LoD), long-term stability, reproducibility, moisture resistance, and the influence of gas flow rate [147-149], as shown in Figure 2-6. These

criteria collectively provide a holistic framework for evaluating the feasibility and practical applicability of gas sensors across diverse environments, including environmental surveillance, industrial safety monitoring, and biomedical diagnostics. The following subsections provide an in-depth analysis of these parameters.

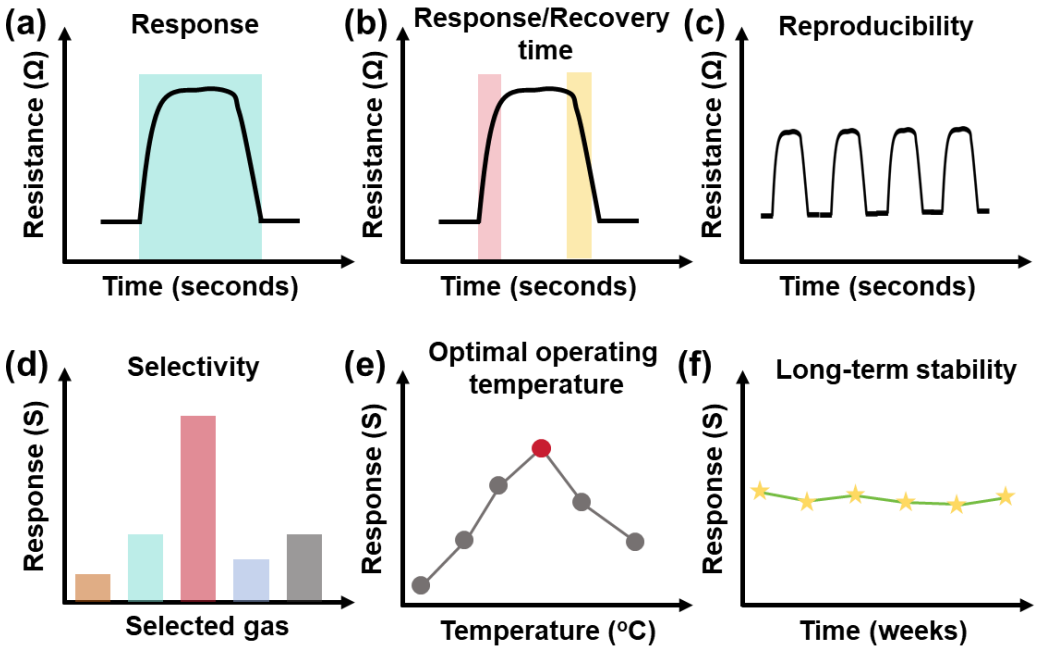

Figure 2-6 Schematic demonstration of evaluation parameters for the performance of a gas sensor.

(1) Optimum operating temperature

Operating temperature profoundly influences the sensing mechanism, as it governs the kinetics of chemical interactions between target gas molecules and the SMOX surface. While elevated temperatures typically accelerate adsorption-desorption processes and enhance sensor response, they also pose considerable drawbacks, including excessive power consumption, incompatibility with flexible or wearable devices, challenges in sensor miniaturization and integrated circuit compatibility, and compromised long-term stability and safety. Consequently, substantial research efforts have been directed towards developing sensors that operate efficiently at room temperature or even subzero temperatures, thereby offering greater sustainability and application potential.

(2) Gas response

Gas response, often equated with sensitivity, is a pivotal parameter that quantifies the relative change in electrical signal output as a function of target analyte concentration. It essentially reflects the strength of physicochemical interactions between gas molecules and the sensing material. For oxidizing gases, the response is typically defined as R_a/R_g, where R_a and R_g denote the resistance values in air and in the target gas, respectively. For reducing gases, the response is expressed as R_g/R_a [149, 150]. An alternative expression utilizes the relative resistance variation, $\Delta R/R_a$ [148, 151]. A higher response value is usually indicative of superior sensing performance and is considered a benchmark for advanced gas sensor design.

(3) Response and recovery time

The response time is defined as the interval during which the sensor resistance undergoes 90% of its total change upon exposure to the target gas, whereas the recovery time represents the duration required for the resistance to return 90% towards its baseline upon removal of the analyte [152]. These kinetic parameters provide a direct measure of adsorption–desorption processes at the gas–solid interface. Sensors with rapid response and recovery are essential for real-time monitoring applications, especially in dynamic or hazardous environments.

(4) Selectivity and Anti-Interference Performance

Selectivity represents the ability of a sensor to preferentially detect a target gas while minimizing cross-sensitivity to interfering species, including environmental humidity [153]. However, due to the chemically resistive nature of SMOX sensors, complete elimination of cross-selectivity is inherently challenging. To overcome this limitation, hybrid approaches have been adopted, such as electronic nose (E-nose) systems based on SMOX arrays coupled with advanced pattern recognition algorithms. Additionally, kinetic modeling approaches, such as the Eley-Rideal mechanism, have

been integrated to improve discrimination performance in multi-analyte scenarios [115, 154, 155].

(5) Limit of Detection (LoD)

The lowest detectable concentration of the target gas, discernible against the background signal at a signal-to-noise ratio of three, is a critical parameter. Optimizing the lower detection limit is essential in specific domains, such as microenvironmental monitoring and medical diagnostics. Achieving ultra-low detection limits is pivotal for expanding the applicability of gas sensors, particularly given the current paucity of sensors operating at the ppb and ppt levels [156]. The theoretical LoD could be calculated as:

$$\mathrm{LoD(ppm)} = 3\frac{\sigma}{k} \tag{2-3}$$

$$\sigma = \sqrt{\frac{\sum(y-y_i)^2}{N}} \tag{2-4}$$

where k is the slope of the linear calibration curve of response value vs. gas concentration (ppm), σ is the sensor noise. y, y_i, N are the baseline data point (100), the average, and the number of data points, respectively.

(6) Stability

Stability is a multidimensional concept encompassing both reproducibility and long-term operational reliability. Reproducibility refers to the consistency of sensor responses across repeated dynamic response-recovery cycles under identical conditions, while long-term stability assesses sensitivity fluctuations over extended periods (≥15 days) [157]. Stability directly impacts the reliability, durability, and service lifetime of sensors, making it one of the most decisive parameters for practical deployment.

(7) Resistance to Humidity Interference

Water vapor in the ambient environment competes with target gas molecules for adsorption sites on the sensing surface, often leading to baseline resistance drift and attenuated sensitivity. The impact of humidity is particularly detrimental in real-world

applications where relative humidity fluctuates widely [158, 159]. Consequently, strategies such as surface hydrophobic functionalization, nanocomposite integration, and heterostructure engineering are actively employed to enhance moisture tolerance, thereby improving overall reliability.

(8) Gas flow rate

Accurate control of gas flow rate is indispensable for reliable sensing. Deviations in flow rate can significantly alter diffusion profiles, residence times, and effective analyte concentrations at the sensor surface, thereby impacting response values. On one hand, statistical methods can be used to decouple sensitivity from flow-related artifacts. On the other hand, material engineering approaches, such as designing stable and porous gas-sensitive matrices, can mitigate the impact of excessive or insufficient flow rates at the fundamental level.

In summary, the aforementioned criteria collectively define the operational boundaries and performance potential of SMOX gas sensors. Optimization of these parameters is not only crucial for laboratory-scale evaluations but also determines the feasibility of real-world applications in environmental monitoring, industrial safety, and healthcare diagnostics. The synergistic consideration of thermal management, sensitivity enhancement, dynamic response tuning, and robustness against environmental perturbations will pave the way for the next generation of high-performance, reliable, and multifunctional SMOX-based sensing platforms.

2.3.4 General sensing mechanism of SMOX gas sensors

The adsorbed oxygen model is widely employed to interpret gas-sensing responses in SMOX. In this framework, the sensing signal originates from surface redox reactions between oxygen species pre-adsorbed on the oxide surface and incoming target gas molecules, which modulate the near-surface charge distribution and thereby alter the

electrical conductivity. Under an oxidative atmosphere (air) and at elevated operating temperatures, oxygen molecules are first adsorbed on the SMOX surface and subsequently extract electrons from the semiconductor, yielding negatively charged chemisorbed oxygen species whose dominant form depends on temperature (O_2^-, O^-, O^{2-}) [125, 160-162]:

$$O_{2(gas)} \rightarrow O_{2(ads)} \quad (2\text{-}5)$$

$$O_{2(ads)} + e^- \rightarrow O^-_{(ads)} \quad T < 150℃ \quad (2\text{-}6)$$

$$O_2^-{}_{(ads)} + e^- \rightarrow 2O^-_{(ads)} \quad 150℃ < T < 400℃ \quad (2\text{-}7)$$

$$O^-_{(ads)} + e^- \rightarrow O^{2-}_{(ads)} \quad T > 400℃ \quad (2\text{-}8)$$

In detail, the sensing mechanism for reducing VOCs by SMOX follows a unified mechanistic framework, as illustrated in Figure 2-7. The process sequentially includes surface reactions, the establishment of a space charge layer, the modulation of interfacial barriers and conductive channels, and ultimately manifests as a measurable electrical readout [162]. Within a suitable operating temperature range, ambient oxygen molecules are first adsorbed and activated into surface-active oxygen species, which capture charge carriers and establish a surface charge layer and band bending, making polycrystalline grain boundaries and device interfaces extremely sensitive to surface charge. n-type SMOX materials form an electron depletion layer in air, resulting in a high baseline resistance. Upon exposure to reducing VOCs, the surface oxidation reaction returns electrons to the semiconductor materials, causing the depletion layer to shrink. This reduces grain-boundary and contact barriers, which macroscopically manifests as a decrease in resistance. p-type SMOX materials form a hole accumulation layer in air, resulting in a low baseline resistance. Upon contact with reducing gases, electrons are released and recombine with holes, thereby relaxing the hole accumulation layer. As a result, the effective conduction channels are limited, leading to an increase in resistance [163].

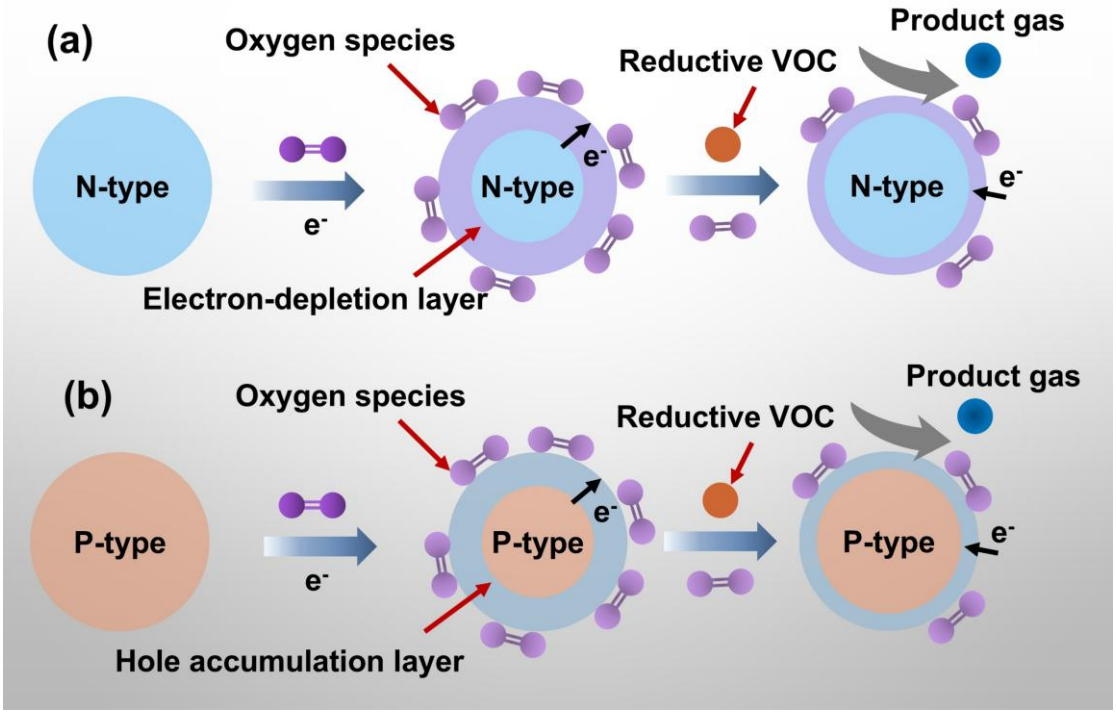

Figure 2-7 The sensing mechanism of (a) n-type and (b) p-type SMOX in the presence of reducing VOCs.

2.3.5 Performance enhancement mechanisms of ternary semiconductor metal oxide for VOC detection

In this thesis, ternary semiconductor metal oxide resistive (TSMOX) was selected among SMOX. TSMOX expands the design space beyond binary limits by enabling simultaneous control of A/B-site chemistry, valence distribution, oxygen-vacancy populations, and heterointerface density [164-166]. These degrees of freedom can modulate band alignment, carrier density, the acidity and basicity of the surface, and catalytic activity, which together govern adsorption, activation barriers, and transduction efficiency [167, 168]. Multiphase and heterojunction architectures (p-n, p-p, n-n) further introduce depletion regions and interfacial polarization, thereby amplifying signals at lower temperatures [169, 170]. As a result, TSMOX can deliver enhanced selectivity (via site/acid-based matching and molecular sieving), improved humidity tolerance (via hydrophobic microstructures and tuned hydroxyl chemistry),

and reduced power consumption (via photoactivation or spillover-assisted low-temperature operation). These characteristics make TSMOX more suitable for detecting VOCs with higher molecular weights. The performance enhancement method of TSMOX for VOC detection is listed below.

2.3.5.1 Surface Modification and Catalytic Promoters

Surface modification and catalytic promoters provide the "last-mile" in enabling selective switching and low-temperature activation in TSMOX. Noble-metal nanodots and single-atom sites (Pt, Pd, Au, Ag) facilitate $H^*/O^*/OH^*$ spillover and accelerate key steps, such as α-C-H activation in acetone and dehydrogenation/C-C scission in ethanol, while engaging in synergy with the host's reversible redox couples [171-173]. Transition-metal promoters (Cu, Co, Ni, Mn, Mo) or porphyrin/phthalocyanine sites can bias pre-activation of aromatic VOCs, delivering high signal-to-noise at 80-120°C [174, 175]. Tuning acid/base sites enables chemoselective adsorption among alcohols/ketones/aromatics; fluorinated/silanized hydrophobic coatings mitigate water competition without impeding target VOC transport, thereby improving selectivity and baseline stability under high humidity. Promoter loading must balance dispersion, sintering resistance, and low cross-talk, as mesopore or micropore confinement and defect or step anchoring may enhance anti-agglomeration and tolerance to sulfur or chlorine poisoning [176-178].

2.3.5.2 Interface and Grain-Boundary Engineering

Interface and grain-boundary engineering govern baseline resistance and response amplitude in polycrystalline and heterostructured ternary semiconductor metal oxide (TSMOX). TSMOX often exhibits dual grain/grain-boundary conduction, such as space-charge layers and band bending at boundaries that are dynamically modulated by adsorbate-induced surface charge redistribution, yielding a "gate-like" amplification of VOC responses [179, 180]. Preferentially oriented growth, controlled sintering necks, and boundary-site-targeted dopants enable fine-tuning of barrier heights and stabilization of contact type (ohmic vs Schottky) [181, 182]. In ternary/ternary or

ternary/binary composites (e.g., $ZnFe_2O_4/ZnSnO_3$ [23], $LaFeO_3@TiO_2$ [183], $NiFe_2O_4@NiO$ [184]), interface cleanliness and interdiffusion control dictate reproducibility and aging. Conformal atomic-layer-deposited interlayers can suppress trap-assisted tunneling, set band offsets, and tailor selective permeability [185, 186]. Guided by this framework, device geometry and bias strategies can be optimized to shorten response/recovery times and reduce drift.

2.3.5.3 Defect Engineering

In TSMOX, aimed at VOC detection (e.g., perovskite-type ABO_3, spinel-type AB_2O_4, and mixed nickelates/cobaltates), defect engineering is the primary method that enhances low-temperature activation and selectivity. Oxygen vacancies, cation vacancies, and aliovalent dopants co-modulate carrier density, surface chemisorption strength, and reaction pathways [187-189]. In systems such as $LaFeO_3$, $NiFe_2O_4$, or $CoMn_2O_4$, the reversible redox couples on the B-site transition metals correlate strongly with the formation of reactive surface oxygen species (O^-/O_2^-), thereby lowering the onset barriers for oxidizing alcohols (ethanol, isopropanol), ketones (acetone, methyl ethyl ketone), and aromatics (toluene, xylene) [190-193]. Reducing or oxidizing anneals, cooling rate, and dopant concentration set the amount and spatial distribution of equilibrium defects. When the oxygen-vacancy density lies within a “response-power” compromise window, one can simultaneously achieve high sensitivity and a low operating temperature (≤150°C, even at room temperature with photo/thermal assistance). It is recommended to combine XPS, EPR, steady-state or time-resolved PL to detect defect levels, and thermogravimetric oxygen non-stoichiometry measurements, complemented by temperature-dependent conductivity or Seebeck analyses to extract small-polaron hopping barriers. These tools define an “optimal defect window” that maximizes signal gain per unit power while maintaining stability across varying humidity and time conditions.

2.4 Characterization Techniques

Crystal structures and phases of the samples were characterized using X-ray diffraction (XRD, Bruker D8 Advance), and the micromorphology was analyzed using a field emission-scanning electron microscope (FE-SEM, model S4800) and transmission electron microscopy (TEM, Tecnai model). Infrared spectral data were acquired using Fourier transform infrared (FTIR) spectroscopy on an Agilent 660-IR. The UV-Vis absorption spectra and bandgap were obtained via a UV-Vis-NIR spectrophotometer (Cary 5000, Varian, USA). Chemical states of relevant elements and their distribution uniformity were observed using X-ray photoelectron spectroscopy (XPS, Thermo Fisher ESCALAB250Xi) and high-angle annular dark-field scanning transmission electron microscopy (HAADFSTEM) with energy-dispersive spectroscopy (EDS), respectively. Calibration of the spectrometer was based on the C 1s peak at 284.8 eV. Electron paramagnetic resonance (EPR, Bruker A300-10/12) was employed to verify the presence of surface oxygen vacancies. At the same time, rotational and vibrational modes and Raman mapping images were analyzed by a laser confocal Raman spectrometer (Renishaw in Via) and a microscopic Raman imaging spectrometer (DXRxi, Thermofisher, USA). Brunauer–Emmett–Teller (BET) surface area, pore-size distribution, and N_2 adsorption/desorption isotherms were investigated using a specific surface and aperture analyzer (Autosorb IQ3, Quantachrome Instruments). The mass variation as a function of temperature during the heating process was studied through Thermogravimetric (TGA) analysis (Pyris 1 TGA, PerkinElmer, USA). Water contact angle (WCA) measurements were conducted using a LAUDA Scientific GmbH LAUDA OSA 100 system to assess surface hydrophobicity. The metal content in the samples was determined using inductively coupled plasma mass spectrometry (ICP-MS, Optima 7300 DV, PerkinElmer, USA) and a flame atomic absorption spectrophotometer (FLAA, PinAAcle 900F, PerkinElmer, USA). The in-Situ FT-IR spectra were recorded using a Bruker INVENIO S infrared spectrometer with a 0.4 cm-1 resolution, equipped with a DTGS detector and a liquid nitrogen-cooled MCT detector. Volatile compounds were extracted by headspace solid-phase microextraction (HS-SPME) and analyzed by a gas chromatograph coupled with a mass spectrometer (Trace ISQ, Thermo Fisher, USA). The SPME device contained a fused-

silica fiber (Supelco, Bellefonte, PA, USA) coated with DVB/CAR/PDMS (Divinylbenzene/Carboxen/Polydimethylsiloxane, 50/30 μm thickness, 10 mm length). The cooked rice samples (20 g) were weighed and placed into 20 mL headspace vials (sealed with a PTFE silicone septum). The vials were maintained at 50°C for 60 min to equilibrate the absorption of volatile compounds onto the SPME fiber. Then the fiber was desorbed at the GC-MS injection port for 5 min at 250°C. The volatiles were separated by a DB-5MS capillary column (30 m × 0.25 mm × 0.25 μm) at a column velocity of 6 PSI. The injection port was in a splitless mode. The temperature program was firstly set at 40°C for 5 min, raised to 125°C at a rate of 8°C/min, and kept for 3 min, then raised to 165°C at a rate of 4°C/min, and kept for 3 min, then raised to 250°C at a rate of 3°C/min, and kept for 2 min. The MS detector conditions were as follows: mass spectra were acquired in the electron ionization mode with an electron energy of 70 eV, the ion source temperature was 250°C, the multiplier voltage was 1000 V, and the mass range was from 20 to 400 m/z. Compounds were identified by comparing their mass spectra with those in the mass spectral libraries (NIST 11, WILEY 07), calculating their linear retention index (RI) relative to standard n-alkanes (C7-C40), and matching them with literature data.

XRD with a Cu-Kα anode source (λ=0.15406 nm) was operated at 40 kV and 40 mA, with a scanning step of 5 °/min. HRTEM and SAED were operated at an accelerating voltage of 200 kV, and interplanar spacings were analyzed using the Gatan Digital Micrograph software. All of the binding energies of XPS analysis with monochromatic Al-Kα radiation were calibrated by the signal of the carbon C 1s peak with a binding energy of 284.8 eV. FTIR spectra were recorded using the KBr pellet method on an infrared spectrophotometer with a resolution of 0.1 cm^{-1} in the range of 4000-400 cm^{-1}. The BET and pore size distributions were obtained from nitrogen physisorption isotherms acquired at 77 K. The TGA analysis was performed from 30 °C to 800 °C in N_2 with a heating rate of 10 °C/min.

A detailed description of the techniques used to characterize the materials is presented in the Appendix.

2.5 Challenges faced by TSMOX gas sensor technology and objectives of the thesis

(1) The biggest challenge in TSMOX gas sensor technology is their poor selectivity and cross-sensitivity in complex atmospheric environments. Due to the intrinsic chemoresistive mechanism, oxygen adsorption-desorption processes on the sensor surface are easily disturbed by multiple coexisting gases and fluctuating humidity. This results in difficulties in discriminating target VOCs, such as nonanal, benzaldehyde, and 1-octen-3-ol, which are critical key indicators for assessing cooked rice. To overcome this limitation, integration of different TSMOX materials into array platforms, combined with advanced data analysis methods such as principal component analysis (PCA), linear discriminant analysis (LDA), and machine learning algorithms, provides a promising approach to enhance selectivity and improve recognition accuracy in complex environments.

(2) Another persistent bottleneck lies in the high working temperature and power consumption of conventional TSMOX sensors. Most TSMOX-based devices require elevated temperatures (200-400°C) to generate oxygen species, leading to prolonged response/recovery times, rapid material degradation, and incompatibility with wearable or portable devices. In this regard, rational material design strategies-such as oxygen vacancy engineering, heterojunction construction, noble metal decoration, and carbon cladding-are effective in lowering activation barriers and enabling room-temperature operation.

For instance, engineered oxygen vacancies in $NiWO_4$ microflowers or La-decoration in $Bi_2O_2CO_3$ microspheres can significantly enhance electron transport and adsorption reactivity, thereby improving response values and lowering detection limits under mild conditions. These strategies not only reduce power consumption but also prolong sensor lifetime and broaden practical applicability.

(3) Beyond selectivity and power issues, real-world applications of TSMOX gas

sensors face further challenges related to stability, repeatability, and environmental tolerance. Agricultural quality detection, environmental monitoring, and medical diagnostics demand sensors capable of long-term, reliable operation under varying humidity, temperature, and chemical backgrounds. However, TSMOX sensors often suffer from signal drift, poor anti-humidity performance, and insufficient durability, which limit their industrial translation. In particular, moisture competition with oxygen adsorption sites substantially deteriorates sensitivity. At the same time, low VOC volatility and interference from complex sample matrices hinder accurate assessment of food products such as cooked rice.

Therefore, new material systems and device structures are required to ensure robustness, high reproducibility, and resistance against environmental perturbations. In this context, the purpose of this thesis is to design TSMOX gas sensors with superior sensitivity, selectivity, stability, and environmental adaptability for detecting VOCs released during the storage of cooked rice. Accordingly, the main objectives of this thesis are as follows:

(1) To design and synthesize advanced nanostructured SMOX-based sensing layers (e.g., La-decorated $Bi_2O_2CO_3$, carbon-functionalized WO_3/Bi_2WO_6, defect-engineered $NiWO_4$, $CuO/Bi_2O_2CO_3$ heterostructures) with enriched oxygen vacancies, heterojunction interfaces, and high surface reactivity, enabling low-temperature or room-temperature operation with enhanced anti-humidity features.

(2) To elucidate the fundamental gas-sensing mechanisms of these engineered nanomaterials by combining in-situ spectroscopic characterization, density functional theory (DFT) calculations, and molecular dynamics (MD) simulations, thereby clarifying the interplay between oxygen vacancy chemistry, electron transport, and VOC adsorption–desorption dynamics.

(3) To construct multi-channel TSMOX sensor arrays integrated with pattern recognition algorithms, enabling discrimination of multiple cooked rice-related VOC key indicators (nonanal, benzaldehyde, and 1-octen-3-ol) in simulated cooked rice storage environments, and to correlate sensor responses with cooked rice quality degree

for early-warning applications.

(4) To explore the practical applicability of the proposed TSMOX sensors in food safety and agricultural storage monitoring by assessing their sensitivity, selectivity, and stability in complex environments, thereby providing new strategies for the development of intelligent, low-power, and environmentally robust sensing systems.

2.6 Strategy for this PhD. thesis

This thesis aims to establish an integrated strategy for developing efficient, low-power, and highly selective semiconductor gas sensors to address critical challenges in agricultural product storage and quality evaluation, particularly in detecting cooked rice quality. The overall goal is to overcome the inherent limitations of conventional TSMOX sensors, including high operating temperature, instability under humidity, limited selectivity, and insufficient sensitivity at trace VOC concentrations.

(1) To target ultra-low concentrations of nonanal under room-temperature and food-compatible conditions, $Bi_2O_2CO_3$ is first selected because it is an environmentally benign bismuth-based oxide with an Aurivillius-type layered structure, abundant exposed Bi-O active sites, and a moderate band gap that allows efficient surface charge transfer. In particular, its layered framework can readily host aliovalent rare-earth dopants, thereby facilitating the creation and control of oxygen vacancies, which are crucial for aldehyde adsorption and reaction. Building on these advantages, the research begins by designing La-decorated $Bi_2O_2CO_3$ microspheres to detect ultra-low concentrations of nonanal, a key volatile aldehyde associated with cooked rice flavor. Decoration-induced oxygen vacancy engineering enhances surface activity, thereby achieving room-temperature operation with high sensitivity, rapid response, and improved selectivity.

(2) For selective benzaldehyde sensing under ultraviolet excitation, the

WO_3/Bi_2WO_6 system is chosen because both components are chemically stable tungstate semiconductors with compatible crystal structures, strong UV photo-response, and staggered band alignment that favors interfacial charge separation. At the same time, WO_3 and Bi_2WO_6-based materials have shown promising photocatalytic activity toward aromatic compounds, yet their use in gas sensing of benzaldehyde under high humidity remains insufficiently explored. To exploit the strong UV photo-response and favorable band alignment of the WO_3/Bi_2WO_6 system for aromatic aldehyde sensing, the strategy next advances to carbon-cladded WO_3/Bi_2WO_6 heterostructures, tailored for benzaldehyde detection under ultraviolet excitation. The introduction of carbon cladding improves electron transport, enhances photocatalytic activity, and significantly reduces interference from humidity, enabling robust detection performance in realistic environments.

(3) To further clarify and optimize the role of defect chemistry and surface oxygen species in alcohol sensing, $NiWO_4$ is selected as a model tungstate because it possesses a relatively narrow band gap, a high density of surface hydroxyl and chemisorbed oxygen species, and a robust microcrystalline framework that can tolerate controlled reduction without structural collapse. The flower-like morphology that $NiWO_4$ readily forms also offers a high specific surface area and abundant accessible active sites, which are advantageous for interaction with 1-octen-3-ol. In view of the narrow band gap, abundant surface chemisorbed oxygen species, and good chemical stability of $NiWO_4$ toward alcohol vapors, the work then develops defect-engineered $NiWO_4$ micro-flowers through controlled hydrogen reduction. This defect-engineering strategy optimizes oxygen vacancy density, thereby enhancing both conductivity and surface reactivity. The resulting sensors exhibit superior detection of 1-octen-3-ol, a critical key indicator in cooked rice quality, while maintaining stability across varying humidity conditions. Molecular dynamics (MD) simulations further elucidate the adsorption and diffusion processes, strengthening the mechanistic understanding of sensing behavior.

(4) To move from single-material optimization toward a practical platform for comprehensive quality evaluation of cooked rice, CuO-decorated $Bi_2O_2CO_3$ is selected as the basis for constructing a sensor array. CuO is a prototypical p-type oxide that exhibits strong responses to VOCs, and its coupling with n-type Bi2O2CO3 forms a well-defined p-n heterostructure with tunable junction properties. At the same time, both components are low-cost, non-toxic, and compatible with scalable fabrication. On this basis, a CuO-decorated $Bi_2O_2CO_3$ p-n heterostructured sensor array is finally established. By integrating four individual sensors into a voltage-controlled array, this system achieves multidimensional detection of aldehydes and alcohols (nonanal, benzaldehyde, and 1-octen-3-ol). Coupled with PCA and LDA, the array enables the precise classification of cooked rice made from rice with varying storage times, providing a validated platform for quality assessment in agricultural applications.

Collectively, this thesis develops a systematic material engineering framework, ranging from surface decoration, carbon cladding, and defect engineering to heterostructure array integration, to construct a new generation of room-temperature semiconductor gas sensors and related sensor arrays. The outcomes provide both theoretical insights and practical solutions for agricultural storage monitoring, food safety evaluation, and VOC key indicator detection. The overall strategy of the PhD thesis is summarized in Figure 2-8.

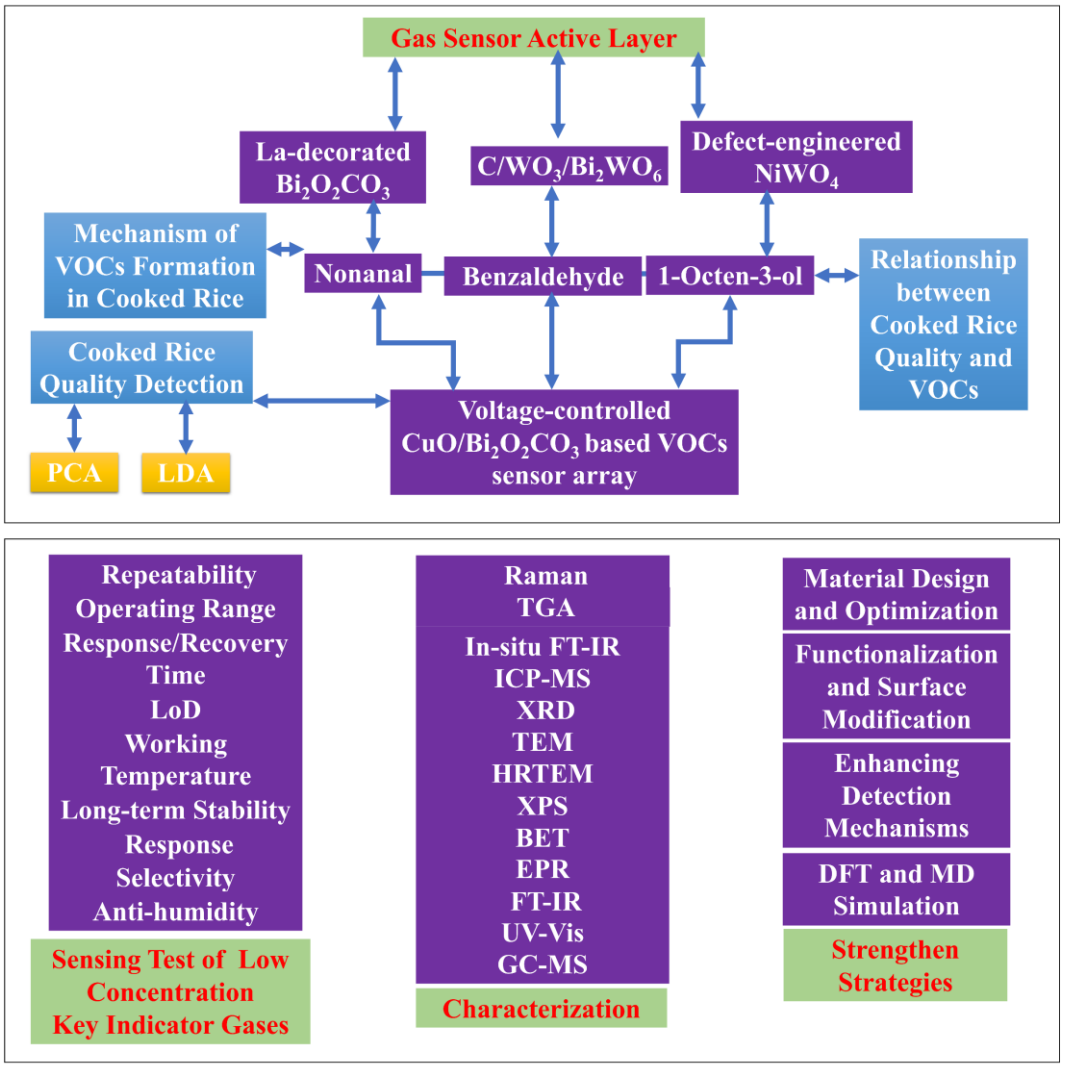

Figure 2-8 The strategy of the PhD thesis.

Chapter 3: La-Decorated $Bi_2O_2CO_3$ Sensor for Nonanal Detection

In this chapter, we proposed a novel one-step hydrothermal method for the synthesis of La-decorated bismuth subcarbonate ($Bi_2O_2CO_3$) microspheres, achieved by controlling reaction kinetics using urea as a stabilizer and trisodium citrate as a precipitant. The resulting material, optimized for nonanal detection, exhibited a spherical morphology with an average diameter of 3.5 μm and a highly permeable lamellar structure composed of 2D nanosheets. The gas-sensing tests demonstrated that sensors with 6 at% La-decorated BCO active layers exhibited exceptional detection capabilities for nonanal, achieving a sensitivity of 174.6 towards 30 ppm of nonanal at room temperature, a rapid response time of 36 s at 18 ppm, and good long-term stability.

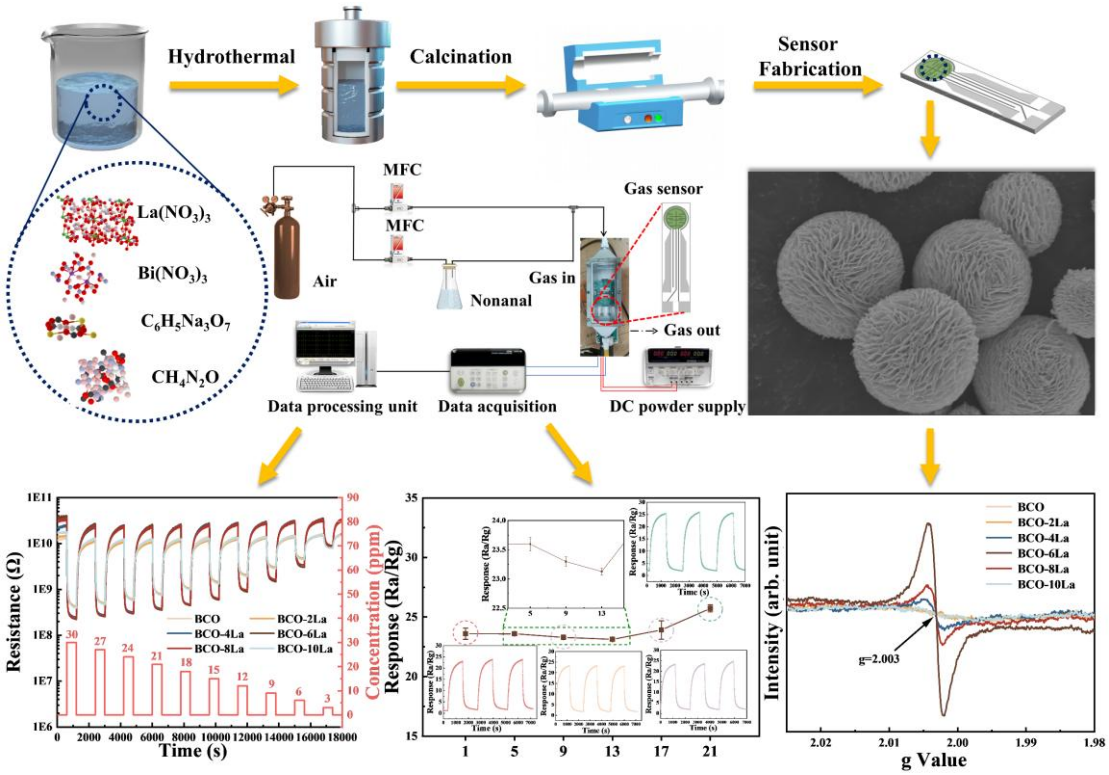

Schematic diagram 3-1 Graphical abstract of this chapter.

As the target VOC in this chapter, nonanal ($C_9H_{18}O$) is primarily produced through the reduction of the carboxyl group in nonanoic acid ($C_9H_{18}O_2$). Nonanal has been

reported to play a crucial role in influencing the flavor characteristics of cooked rice and other agricultural products [13, 33, 194]. A subtle aroma in rice is associated with low aldehyde concentrations, whereas elevated levels contribute to a pronounced, fatty flavor [80]. Secondly, it has been identified as a metabolite in cancer cell metabolism and serves as a biomarker in breath analysis for COVID-19 [195, 196]. The concentration of nonanal in the exhaled breath of lung cancer patients is significantly elevated compared to that of healthy individuals [197, 198]. The Cancer Odor Database also indicates that nonanal levels are markedly higher in biological samples from patients with colorectal, breast, ovarian, gastric, and esophageal cancers compared with healthy controls [199].

A significant limitation of TSMOX-based CGSs is their requirement for elevated operating temperatures, typically exceeding 250°C, which constrains their practical applications [143]. To address this limitation, our research focuses on $Bi_2O_2CO_3$, a TSMOX, as the active layer material for the detection of nonanal at room temperature. $Bi_2O_2CO_3$ (BCO) is classified as an n-type TSMOX with a structure related to the Aurivillius/Sillén phases, and it has attracted considerable interest as a functional semiconductor material. Huang et al. synthesized $Bi_2O_2CO_3$ nanosheets coated with $In(OH)_3 \cdot xH_2O$ nanocomposites via a two-step hydrothermal method for the engineering of sensing layers for real-time detection of isopropanol. These sensors exhibited an extraordinary response value of 20.39 at 100 ppm, with detection capabilities spanning 1-1000 ppm, operating at a reduced temperature of 100 °C [200]. To enhance the photocatalytic stability of oxygen vacancies (O_V) in BCO, Chen et al. developed an effective method for preparing Bi-metal nanoparticle-modified BCO nanosheets, which exhibited high photocatalytic activity and stability. The synergistic interaction between Bi-metal nanoparticles and induced O_V suppresses the formation of poisonous intermediate (NO_2), facilitating the conversion to the final product, NO_3^- [201]. Zai et al. reported that I^- can partially substitute CO_3^{2-} in BCO, resulting in a reduced bandgap and increased visible light absorption, leading to the synthesis of rose-like I-doped BCO microstructures via a hydrothermal strategy. Photoelectrochemical testing confirmed that I^- doping reduces the bandgap by introducing intermediate energy levels within the bandgap. Optimized I-doped microspheres exhibited superior photocatalytic performance, degrading Rhodamine B in 6 minutes and reducing Cr(VI) by approximately 90% in 25 minutes under visible light ($\lambda > 400$ nm) [202]. Notably,

BCO-based materials have demonstrated exceptional catalytic performance. Given the similarity between catalytic reactions and gas-sensing mechanisms, which involve the chemical interaction of target molecules with the sensor active-layer material, BCO presents substantial potential for diverse gas-sensing technologies. The structural characteristics of BCO, comprising alternating layers of $[Bi_2O_2]^{2+}$ and CO_3^{2-}, facilitate the formation of two-dimensional nanosheet structures [203, 204]. However, these densely packed nanosheet structures may not provide sufficient active sites for effective interactions between the active layer surface and target molecules. Consequently, it is imperative to explore the engineering of BCO-based materials with three-dimensional porous structures enhanced by the addition of transition metal atoms to improve their functional performance.

Among various strategies to improve the performance of sensing materials, the incorporation of transition metal atoms is used to optimize grain size, create OV, and modify surface states, thereby enhancing the interaction between the material surface and target molecules and, consequently, the catalytic activity. In particular, lanthanide (La) has been identified as an efficient catalyst for achieving the requisite selectivity and sensibility for practical applications, in addition to reported improvements in the physicochemical properties of SMOX [205-207]. Gao et al. synthesized La-doped cadmium tin oxide microcubes via coprecipitation and annealing, exhibiting excellent ethanol gas-sensing properties. The La@$CdSnO_3$ sensor exhibited a response value of 115.2 to 100 ppm ethanol, approximately 19 times higher than that of pure $CdSnO_3$ at an optimal working temperature of 300°C, alongside rapid response-recovery rates and good stability [208]. Shingange et al. investigated the H2S-sensing potential of ZnO nanofibers (NFs) synthesized via electrospinning, followed by La doping and post-calcination treatments at different doping concentrations. Their comparative analysis demonstrated that La-doped ZnO NF-based sensors exhibited enhanced response and faster response/recovery times while exhibiting high selectivity towards H_2S [209]. Additionally, Wang et al. reported that carboxylated graphene oxide decorated with La particles displayed enhanced antibacterial properties [210]. Furthermore, Yuksel et al. investigated H_2 adsorption and sensing on La-doped/decorated carbon nanotube and graphene structures, revealing that La modification significantly enhances H_2 interactions in both materials [211].

3.1 Synthesis of La-decorating $Bi_2O_2CO_3$ microspheres

All the reagents employed in this study were of analytical grade and used without further purification. The following chemicals were purchased from Aladdin Biochemical Technology Co., Ltd., China: Bismuth nitrate pentahydrate ($Bi(NO_3)_3 \cdot 5H_2O$) (AR grade, CAS: 10035-06-0), lanthanum nitrate hexahydrate ($La(NO_3)_3 \cdot 6H_2O$) (AR grade, CAS: 10277-43-7), urea (CH_4N_2O) (AR grade, CAS: 57-13-6), trisodium citrate dihydrate ($C_6H_5Na_3O_7 \cdot 2H_2O$) (AR grade, CAS: 6132-04-3), and nonanal ($C_9H_{18}O$) (AR grade, CAS: 124-19-6). The synthesis of $Bi_2O_2CO_3$ microspheres was performed following the procedure reported by Huang et al. [212]. As shown in Figure 3-1, 0.97 g of $Bi(NO_3)_3 \cdot 5H_2O$ and varying quantities of $La(NO_3)_3 \cdot 6H_2O$ (0 g, 0.018 g, 0.036 g, 0.052 g, 0.070 g, and 0.866 g) were individually and uniformly dispersed in 70 mL of deionized water in separate containers. Subsequently, 0.30 g of CH_4N_2O and 1 g of $C_6H_5Na_3O_7 \cdot 2H_2O$ were added to each solution. The ratio of La with respect to Bi was adjusted to obtain x% (La/Bi = 2 at%, 4 at%, 6 at%, 8 at%, and 10 at%). Following sonication for 5 minutes and magnetic stirring for 60 minutes to ensure homogeneity, the resulting solution was transferred to a 100 mL Teflon-lined stainless-steel autoclave and heated at 180°C for 20 hours. After undergoing six washes through centrifugation with ethanol and deionized water, the samples were collected and dried at 70°C. The obtained precursor was then subsequently calcined at 300°C for 30 minutes under atmospheric conditions, with a heating rate of 2°C per minute. The resulting products, including pure BCO and La-decorating BCO variants, were labeled as BCO, BCO-2La, BCO-4La, BCO-6La, BCO-8La, and BCO-10La, respectively.

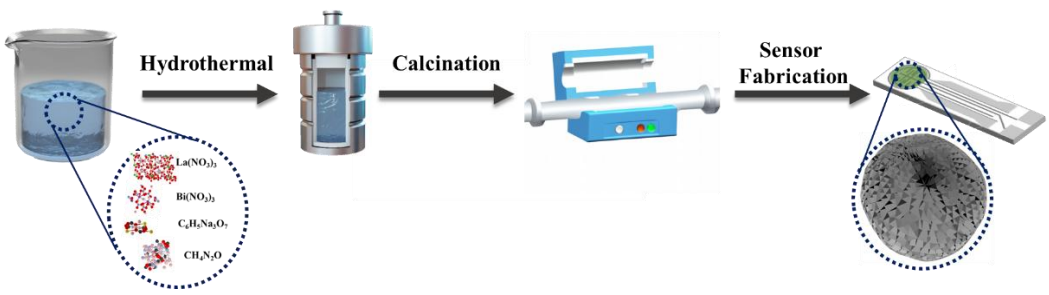

Figure 3-1 Schematic illustration for fabricating La-decorating $Bi_2O_2CO_3$ microspheres.

3.2 Results and discussion

3.2.1 Characterization results

XRD analysis was used to determine the crystal structures of the samples. As depicted in Figure 3-2, the XRD patterns of the samples exhibited a high degree of correlation with the orthorhombic $Bi_2O_2CO_3$ phase (JCPDS Card No. 84-1752) [213], thereby confirming their high purity, consistent with TEM results. With an increase in La decoration, the characteristic peaks gradually broaden, particularly in the BCO-8La and BCO-10La samples, indicating reduced crystalline quality and a tendency towards atomic disorder.

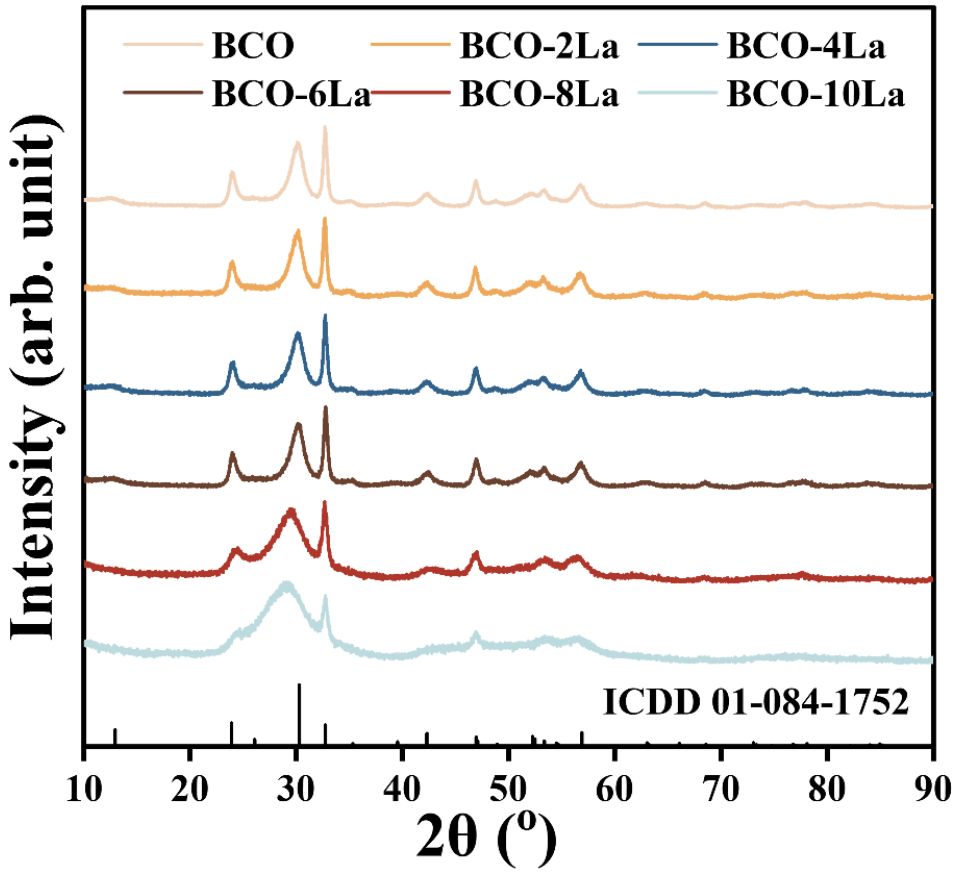

Figure 3-2 XRD patterns of all samples.

To further understand the crystal structure of the samples and their correlation with gas-sensing performance, we calculated the crystallite sizes for all samples, as detailed in Tables 3-1 to 3-6.

Table 3-1 XRD parameters of BCO.

Peak	2υ (°)	β (°)	D (nm)	$\delta\times10^{-3}$ (nm^{-2})	$\varepsilon\times10^{-3}$
1	12.69023	1.44401	5.535455953	32.63572022	56.66177971
2	24.02729	0.7192	11.29335447	7.84068634	14.74633987
3	30.07053	1.42166	5.786117186	29.86933473	23.09365054
4	32.73249	0.43114	19.20439923	2.711430948	6.405710598
5	35.14151	0.45604	18.27267206	2.994993471	6.28392844
6	42.32227	1.29602	6.572981512	23.14595895	14.60872581
7	46.92176	0.66093	13.10306731	5.824438398	6.644806747
8	48.64232	1.06312	8.200392049	14.87067795	10.26355355
9	51.99659	1.62754	5.43071328	33.9067568	14.56129747
10	53.38077	0.88625	10.03298356	9.934357833	7.69187939
11	56.76314	1.10159	8.196913333	14.88330266	8.896446676

In Tables 3-1 to 3-6, 2υ is the peak position, and β is the corresponding FWHM. From XRD data, D (nm) is the crystallite size calculated through the Scherer equation ($D = \frac{k\lambda}{\beta cos\upsilon}$). δ ($nm^{-2}$) is the dislocation density calculated through $\delta = \frac{1}{D^2}$ equation. ε is the microstrain calculated by $\varepsilon = \frac{\beta}{4\,tan\upsilon}$.

Table 3-2 XRD parameters of BCO-2La.

Peak	2υ (°)	β (°)	D (nm)	$\delta\times10^{-3}$ (nm^{-2})	$\varepsilon\times10^{-3}$
1	12.65575	1.03541	7.719634421	16.78056317	40.74024737
2	23.99391	0.79293	10.24261589	9.531872548	16.28138009
3	30.02862	1.39182	5.909588798	28.63422772	22.64197531
4	32.69429	0.4213	19.65101979	2.589582872	6.26723858
5	35.05813	0.51904	16.05107892	3.881428046	7.170150378
6	42.28197	1.36942	6.219827731	25.84897267	15.45223004
7	46.87816	0.65501	13.21931128	5.722454412	6.592155376
8	48.39075	1.41252	6.165845557	26.30357117	13.71688383
9	51.98088	1.47633	5.986542473	27.90280499	13.21304718

Peak	2υ (°)	β (°)	D (nm)	$\delta\times10^{-3}$ (nm^{-2})	$\varepsilon\times10^{-3}$
10	53.32824	0.89423	9.941160431	10.11872598	7.770012412
11	56.73578	1.06525	8.47545023	13.92112856	8.607878397

Table 3-3 XRD parameters of BCO-4La.

Peak	2υ (°)	β (°)	D (nm)	$\delta\times10^{-3}$ (nm^{-2})	$\varepsilon\times10^{-3}$
1	12.66555	1.15146	6.941676228	20.75254159	45.27112057
2	24.0309	0.76278	10.6482013	8.819571684	15.63747611
3	30.07621	1.4251	5.772227136	30.01326036	23.14495116
4	32.7378	0.43396	19.07986305	2.746942026	6.44650414
5	35.06466	0.66998	12.43515026	6.466926499	9.253437834
6	42.3154	1.40955	6.043430758	27.37996564	15.89126487
7	46.91862	0.60109	14.40733882	4.817619111	6.043645446
8	48.81045	0.45446	19.19595814	2.71381608	4.370342439
9	51.9963	1.58584	5.573508161	32.19161145	14.18830647
10	53.34656	0.90427	9.831574357	10.34555666	7.854119223
11	56.7736	1.03744	8.704197964	13.19904411	8.376542519

Table 3-4 XRD parameters of BCO-6La.

Peak	2υ (°)	β (°)	D (nm)	$\delta\times10^{-3}$ (nm^{-2})	$\varepsilon\times10^{-3}$
1	12.56939	1.41952	5.630298272	31.54548395	56.24069263
2	24.07105	0.78365	10.36539429	9.307399304	16.03772504
3	30.11184	1.41764	5.803087178	29.69489611	22.99525744
4	32.77612	0.43908	18.8592311	2.811590292	6.514504692
5	35.146	0.61979	13.44515524	5.531824048	8.539132146
6	42.37022	1.26365	6.742449494	21.99705781	14.22616603
7	46.95964	0.62035	13.96220419	5.129700744	6.231185814
8	48.83795	0.40817	21.37527355	2.188651618	3.92268966

Peak	2υ (°)	β (°)	D (nm)	$\delta\times10^{-3}$ (nm^{-2})	$\varepsilon\times10^{-3}$
9	52.02679	1.52305	5.804037674	29.68517096	13.61733485
10	53.39904	0.90116	9.867775487	10.26978805	7.818178894
11	56.80025	1.06366	8.490700419	13.87116585	8.583475851

Table 3-5 XRD parameters of BCO-8La.

Peak	2υ (°)	β (°)	D (nm)	$\delta\times10^{-3}$ (nm^{-2})	$\varepsilon\times10^{-3}$
1	24.34566	1.09432	7.426545155	18.13119163	22.13547036
2	29.33996	2.48899	3.299328375	91.86475391	41.48542167
3	32.70133	0.51104	16.20053977	3.810140853	7.600477576
4	42.71274	2.01033	4.243092563	55.54372321	22.43305869
5	46.88054	0.89147	9.713012275	10.59966464	8.971426886
6	53.36292	1.26441	7.031766209	20.22419081	10.97824032
7	56.4755	1.53065	5.891246797	28.81280677	12.43607972

Table 3-6 XRD parameters of BCO-10La.

Peak	2υ (°)	β (°)	D (nm)	$\delta\times10^{-3}$ (nm^{-2})	$\varepsilon\times10^{-3}$
1	29.14384	5.07344	1.617902196	382.0282431	85.1565443
2	31.30176	1.53261	5.383090099	34.50934388	23.86926359
3	46.93435	0.97755	8.859519504	12.74030024	9.825060463
4	53.48595	2.4501	3.630807061	75.85664962	21.21618975
5	56.55071	2.68359	3.361399628	88.50334897	21.76908749

The average crystallite sizes were determined to be 10.15 nm for BCO, 9.96 nm for BCO-2La, 10.78 nm for BCO-4La, 10.94 nm for BCO-6La, 7.69 nm for BCO-8La, and 4.57 nm for BCO-10La, with BCO-6La exhibiting the largest crystallite size. Given its superior response to nonanal, it can be suggested that the increased crystallite size facilitates the continuity of the conductive pathways, thereby enhancing sensitivity and conferring improved stability and selectivity.

The FESEM images of BCO-6La, a representative sample, reveal the presence of non-aggregated spherical particles (Figure 3-3a), indicating a homogeneous dispersion of particles without agglomeration. Statistical analysis indicates an average diameter of 3.49 μm, as shown in Figure 3-4. Detailed SEM images at higher magnification reveal that each microsphere exhibits a highly permeable, layered microstructure consisting of loosely stacked two-dimensional nanosheets (Figure 3-3b and Figure 3-3c). HRTEM and high-resolution SEM characterization confirm that the loose stacking of nanosheets (with a spacing of ≈ 150 nm) within individual microspheres forms a lamellar structure, enhancing the permeability of BCO-6La (Figure 3-3d and Figure 3-5). As shown in Figure 3-3e and Figure 3-3f, some evenly distributed La nanoparticles can be observed on the surface of bismuth subcarbonate. Additionally, the examination of BCO decorated with varying La concentrations (2-10 at%) indicates that La decorating did not significantly alter the layered structure (Figure 3-6). Distinct lattice fringes were observed for BCO-6La, with lattice spacings of 0.270 nm and 0.195 nm corresponding to the (002) and (202) planes of BCO, respectively (Figure 3-3g). HAADF and EDS mapping of BCO-6La demonstrate a uniform distribution of Bi, C, O, and La, confirming effective decorating (Figure 3-3h to Figure 3-3l).

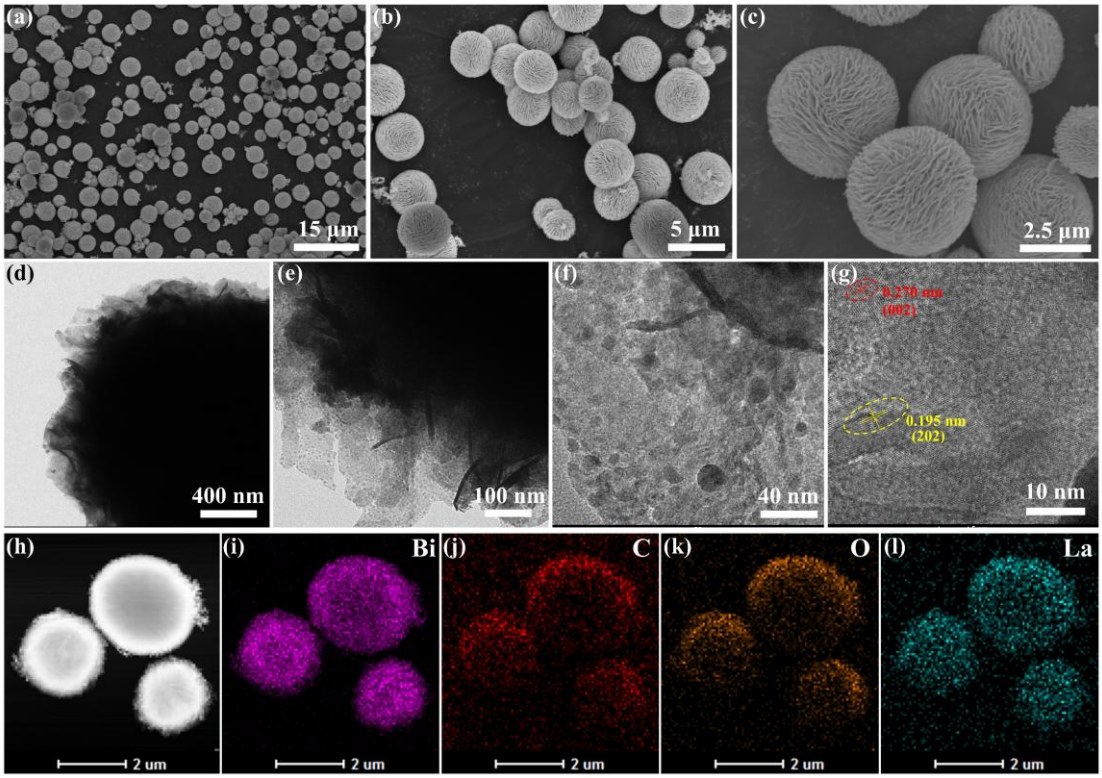

Figure 3-3 (a-c) FESEM image of BCO-6La, (d-g) high-resolution TEM images of BCO-6La, (h-l) EDS elemental mapping results of BCO-6La.

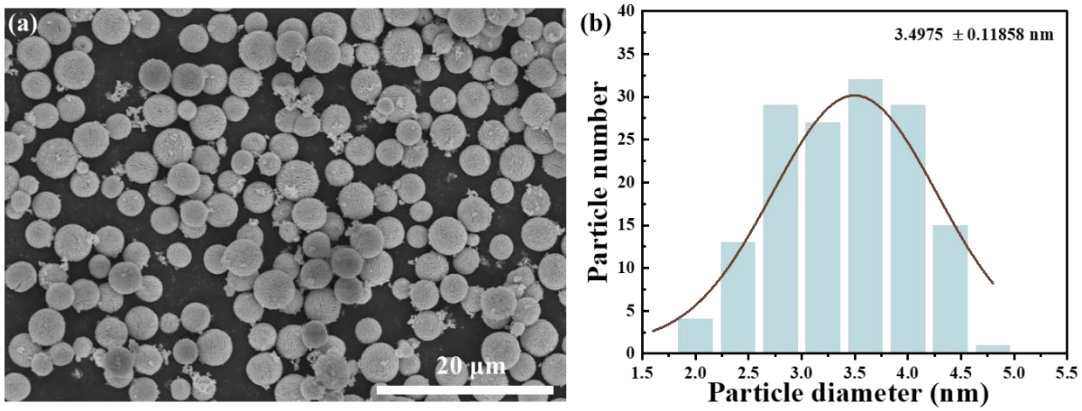

Figure 3-4 FESEM image of (a) BCO-6La, (b) the particle size distribution of BCO-6La.

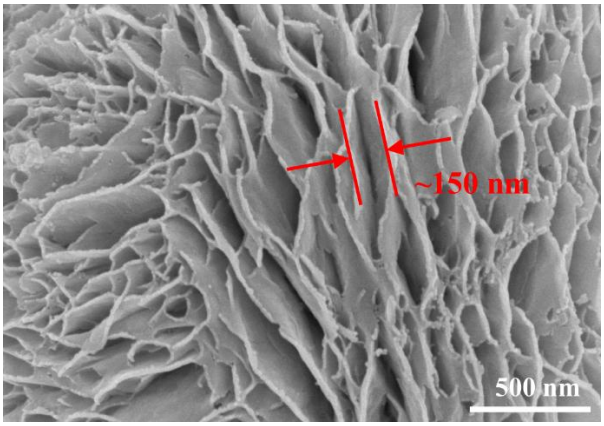

Figure 3-5 FESEM image of BCO-6La.

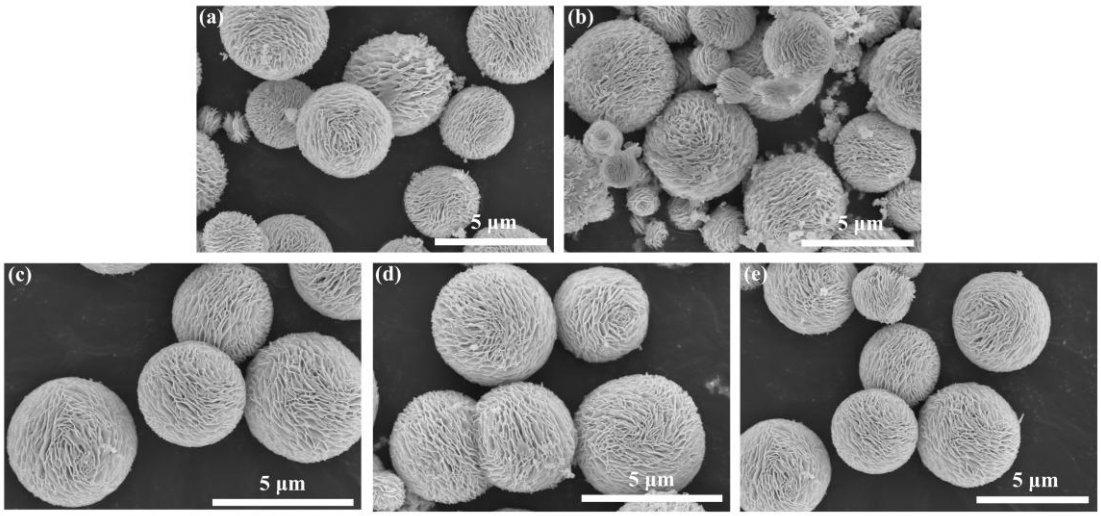

Figure 3-6 FESEM image of (a) BCO, (b) BCO-2La, (c) BCO-4La, (d) BCO-8La, and (e) BCO-10La.

XPS analysis was used to determine the chemical states of elements present in the sample. The XPS spectra of BCO-6La (Figure 3-7) exhibited peaks corresponding to Bi 4f, C 1s, O 1s, and La 3d, indicating the presence of these elements, in agreement with EDS analysis.

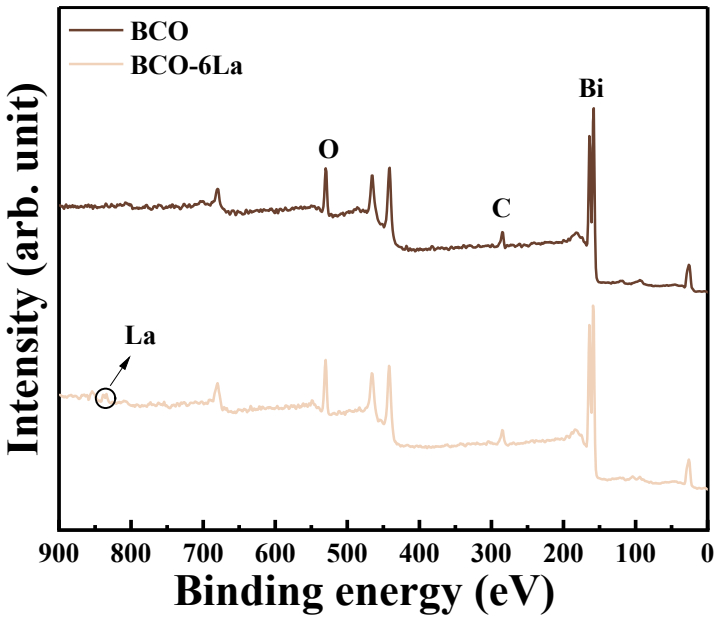

Figure 3-7 XPS survey spectrum of BCO and BCO-6La.

The fitting analysis of the O 1s spectra in Figure 3-8a shows three components: lattice oxygen (O_L), O_V, and chemisorbed oxygen (O_C). Specifically, O_L refers to oxygen atoms that occupy lattice positions within the crystal structure of solid materials, while O_V refers to oxygen vacancies, which are characterized by the absence or displacement of oxygen atoms from their positions within the crystal structure. This defect manifests as the absence of one or more oxygen atoms in the lattice. The presence of oxygen vacancies may lead to a lower binding energy peak due to the reduced oxidation state of surrounding metal ions. O_C denotes molecular oxygen or oxygen atoms that are adsorbed onto the surface or interface of a material [214-216]. For BCO-6La, these components are centered at 529.3 eV, 530.7 eV, and 531.5 eV, respectively, while for BCO, the corresponding values are 529.3 eV, 530.6 eV, and 531.6 eV, respectively. From this analysis, the amount of O_V in BCO-6La was 32.4 %, higher than that in the BCO sample (29.3 %). The higher O_V content can be linked to enhanced gas sensitivity [115, 217]. Furthermore, in Figure 3-8b, the La 3d spectrum of BCO-6La exhibits the spin-orbit components ($3d_{3/2}$ and $3d_{5/2}$) accompanied by their multiplet splitting, with the La $3d_{5/2}$ peak at 834.2 eV indicating the presence of La in La-O bonds, suggesting the successful decorating of $Bi_2O_2CO_3$ with La^{3+} ions [208, 218]. Figure 3-8c presents the high-resolution Bi 4f spectra for both BCO and BCO-6La samples. The components of the Bi 4f doublet, in the BCO spectrum, are located at 158.4 eV (Bi $4f_{7/2}$) and 163.7 eV (Bi $4f_{5/2}$). These components are shifted by 0.2 eV towards higher binding

energy in the BCO-6La spectrum, indicating successful La decoration in the BCO lattice [219]. The C 1s spectrum of BCO-6La (Figure 3-8d) was fitted with three components. The one centered at 284.6 eV was attributed to adventitious carbon (AC) species, while the components at 286.0 eV and 288.3 eV were attributed to ether and ester groups, respectively, consistent with the C 1s recorded on the BCO sample [220, 221].

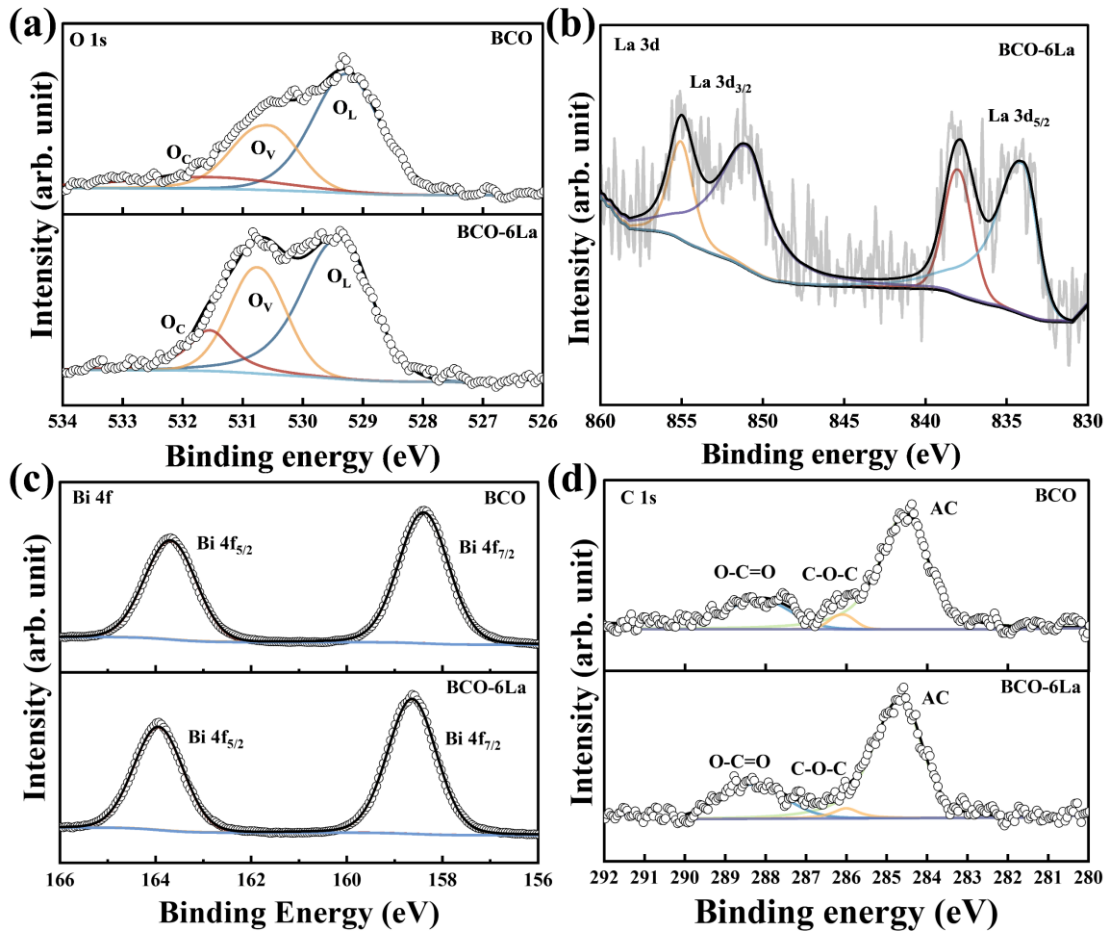

Figure 3-8 High-resolution XPS spectrum of BCO and BCO-6La for (a) O 1s, (b) La 3d, (c) Bi 4f, and (d) C 1s.

UV-Vis analysis demonstrates that La decorating enhances light absorption within the 500-675 nm range (see Figure 3-9a inset). The band gap of the samples was determined to be 2.35 eV for BCO, 1.93 eV for BCO-2La, 1.73 eV for BCO-4La, 0.92 eV for BCO-6La, 1.49 eV for BCO-8La, and 2.06 eV for BCO-10La [202]. Figure 3-9a indicates that La-decorating significantly affects the UV-visible absorption characteristics. Therefore, the improved sensing performance of BCO-6La is primarily

due to its high O_V concentration (as determined by XPS) and narrow band gaps, which facilitate oxygen adsorption and carrier transfer. During synthesis, decorating La particles on the surface of BCO can enhance the OV in the material, mainly by promoting oxygen diffusion and migration. The electronic structure and chemical environment at the interface between La metal particles and BCO can reduce the diffusion energy barrier for oxygen ions, making it easier for them to escape from the lattice and thereby form O_V. Furthermore, the presence of La metal particles can introduce local stress or generate local structure distortions on the surface of BCO. Such stress and distortions can alter the material's lattice energy, reduce the formation energy of OV, and make it easier to generate O_V. The abundance of O_V in BCO-6La promotes charge spacing and the formation of an electron depletion layer, thereby enhancing sensing capabilities [222-224].

EPR spectroscopy was used to evaluate the O_V. As illustrated in Figure 3-9b, BCO-6La exhibits a distinct peak (g = 2.003), significantly more intense than that of BCO, suggesting that La decorating induces more O_V in $Bi_2O_2CO_3$ microspheres, which is in agreement with XPS results [208]. FT-IR measurement (Figure 3-9c) shows absorption bands at 848 cm^{-1} corresponding to CO_3^{2-} bending modes. Bands at 1380 and 1534 cm^{-1} are associated with CO_3^{2-} antisymmetric vibration modes [225]. Additionally, the broad absorption bands at around 3342 cm^{-1} are assigned to O-H vibrations [226]. These findings, supported by XRD, XPS, EPR, and FT-IR analyses, confirm the successful synthesis and La-decorating of BCO.

The N_2 adsorption-desorption isotherms observed for BCO and BCO-6La in Figures 1-9d and 1-9e fall under type IV-H3, indicating the synthesis of mesoporous materials characterized by slit pore structures resulting from the stacking of particles. Calculations demonstrate specific surface areas of 18.154 m^2/g for BCO and 31.303 m^2/g for BCO-6La. A larger specific surface area provides more active sites, which enhances the gas-sensing properties of materials [227]. Additionally, ICP-MS and FLAA analyses were conducted to investigate metal elements in all samples, as shown in Figure 3-9f. These analyses revealed that the La-to-Bi ratio aligns with the initial experimental design, providing further evidence of the successful incorporation of La.

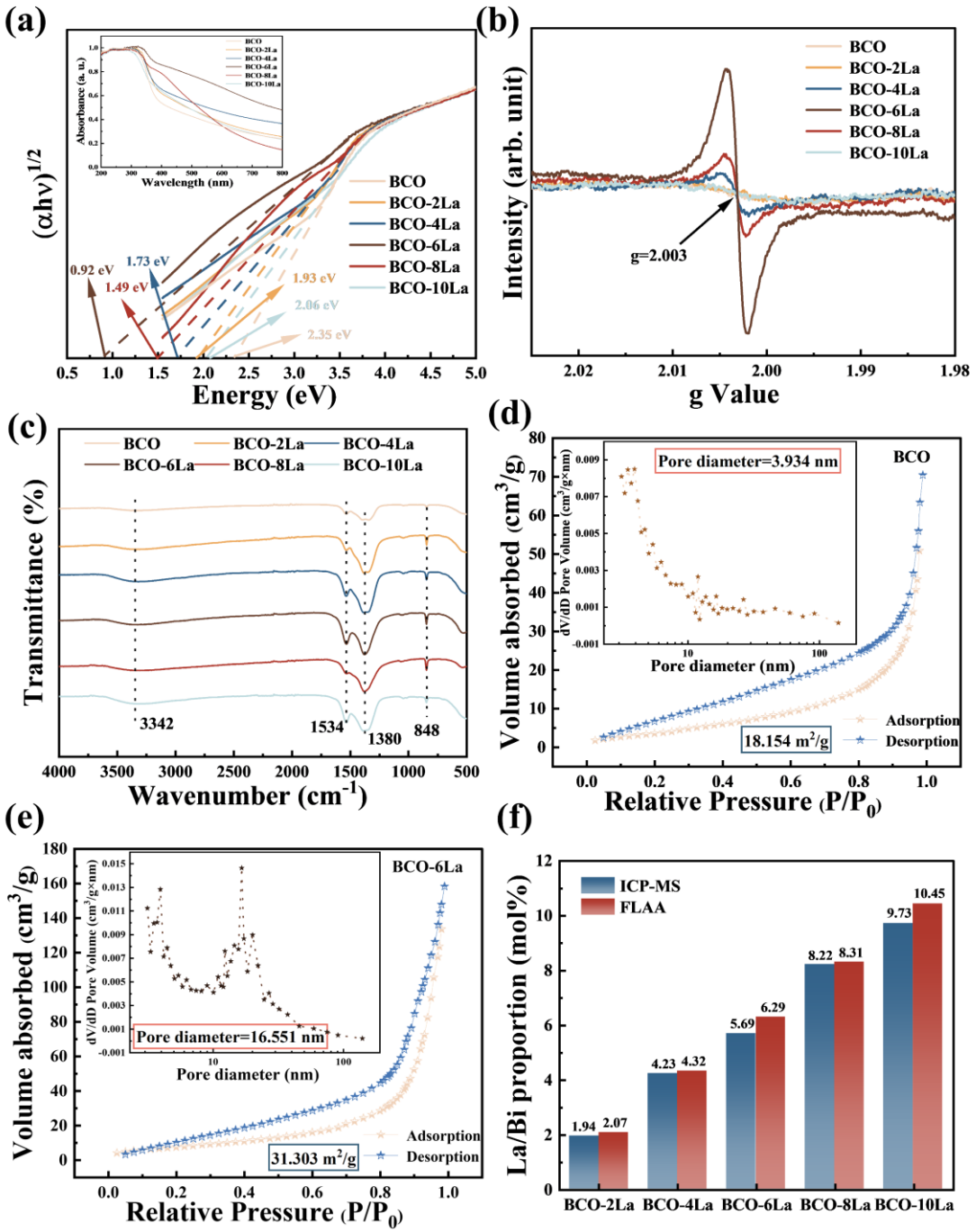

Figure 3-9 (a) Tauc curve (inset: UV-Vis absorption spectrum), (b) EPR spectra, and (c) the FT-IR spectroscopy of all samples, nitrogen sorption isotherms and pore size distributions (inset) of the (d) BCO and (e) BCO-6La. The pore size distributions are determined by the BJH model based on the absorption branches, (f) The La/Bi proportion of all samples analyzed by ICP-MS and FLAA.

3.2.2. Gas sensing performance

In this section, the performance of La-decorated $Bi_2O_2CO_3$ microspheres in nonanal sensing was evaluated. The sensor response value was defined as R_a/R_g, and

the definitions of response and recovery time were consistent with those of Jeong et al. [14]. The transient curves illustrated in Figure 3-10a to 1-10b and Figure 3-10c demonstrate fluctuations in response and resistance, respectively, when the BCO-xLa gas sensors are exposed to different concentrations of nonanal gas (3, 6, 9, 12, 15, 18, 21, 24, 27, and 30 ppm). Sensing for each gas concentration was measured for 6 minutes and 12 minutes, in the presence and absence of gas. Upon exposure to nonanal gas as an electron donor, the electron concentration within BCO-xLa increased, resulting in a decrease in resistance (Figure 3-10c). Consequently, the gas-sensing response of the optimal BCO-6La sensor progressed from a low level (4.9 at 3 ppm) to a high level (174.6 at 30 ppm), with a relatively wide detection range. The measured minimum detection limit of the BCO-6La sensor (4.9 at 3 ppm) enhances sensitivity and accuracy, thereby improving reliability and efficiency in practical applications, particularly in scenarios where high precision and rapid response are required. All the tested sensors' responses demonstrate good linearity, as shown in Figure 3-10d. Furthermore, the limit of detection (LOD) for BCO-6La is estimated to be 117.3 ppb for nonanal.

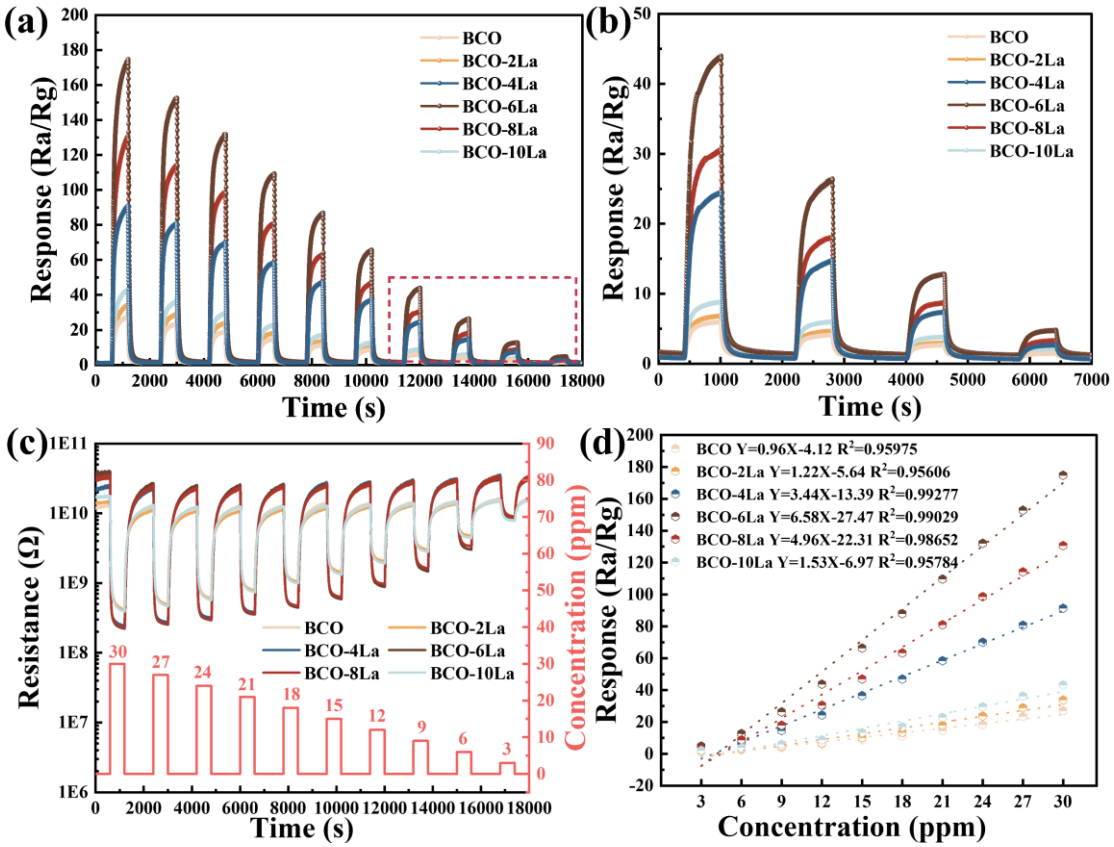

Figure 3-10 (a) Transient response BCO-xLa film to nonanal concentrations of 3-30 ppm at room temperature (25±2°C), (b) magnified area of Figure 3-10a, (c) resistive response of BCO-xLa gas

sensors toward exposure to 3-30 ppm of nonanal at room temperature (25±2°C), (d) linear relationship between response verse nonanal vapor concentrations.

For real-time gas monitoring applications, stable performance is crucial to ensure reliable measurements over extended periods. The BCO-6La sensor demonstrated highly reproducible sensing characteristics even after undergoing twenty repetitive cycles, as illustrated in Figure 3-11. Additionally, the BCO-6La sensor performance was evaluated over a 3-week period at 9 ppm nonanal exposure, as shown in Figure 3-12. The sensor's response remains stable with variations ≤ 5% (standard deviation), which can be attributed to minor environmental fluctuations (such as humidity or temperature) within the gas mixing setup. Notably, the absence of a decrease in sensor performance emphasizes the reversibility of nonanal interaction. The response and recovery times of BCO-6La to 18 ppm nonanal gas were determined, as shown in Figure 3-13. The response time for nonanal gas was 36 seconds, while the recovery time exceeded 1500 seconds, highlighting rapid response capabilities and strong adsorption energy towards nonanal molecules. The swift response time is adequate for periodic nonanal monitoring in critical environments. Furthermore, the detection capabilities of the BCO and BCO-6La sensors were validated by testing their performance against various VOCs that significantly contribute to the flavor of cooked rice, as illustrated in Figure 3-14. The BCO-6La sensor demonstrated enhanced responsiveness to nonanal gas compared to other interfering gases, highlighting improved selectivity over the BCO. This enhanced selectivity may be attributed to the relatively low bond energy of C-H-O in nonanal (approximately 312.8 kJ/mol), making it susceptible to bond cleavage when reacting with oxygen species [228, 229].

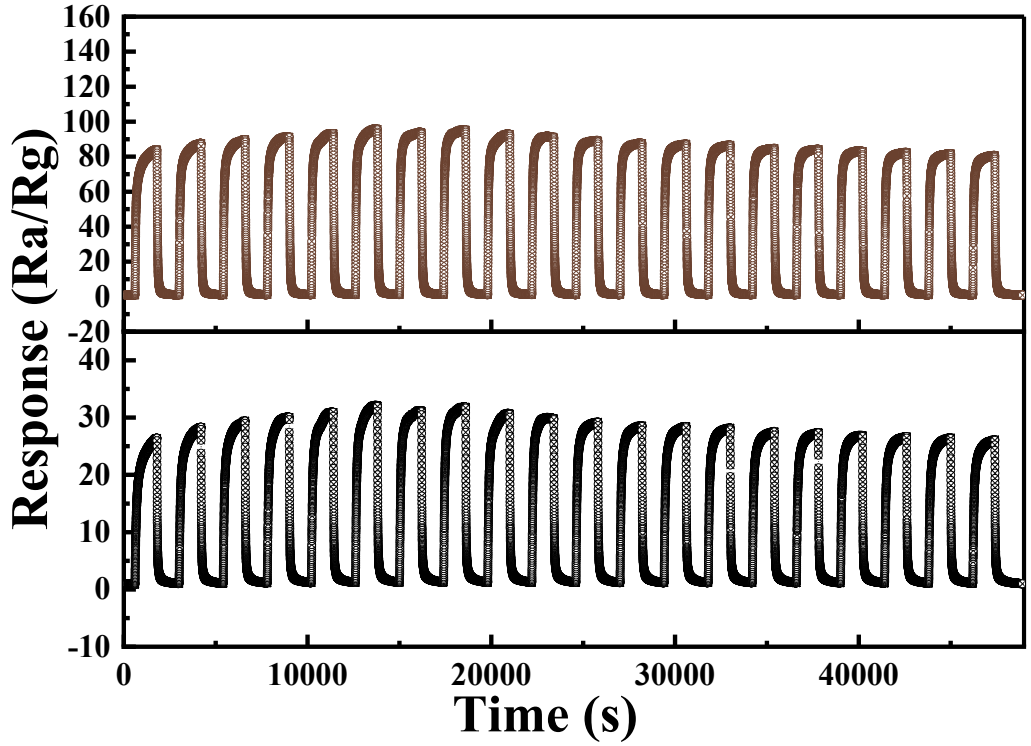

Figure 3-11 Repeatability of the BCO-6La sensor under 9 and 18 ppm nonanal (20 cycles).

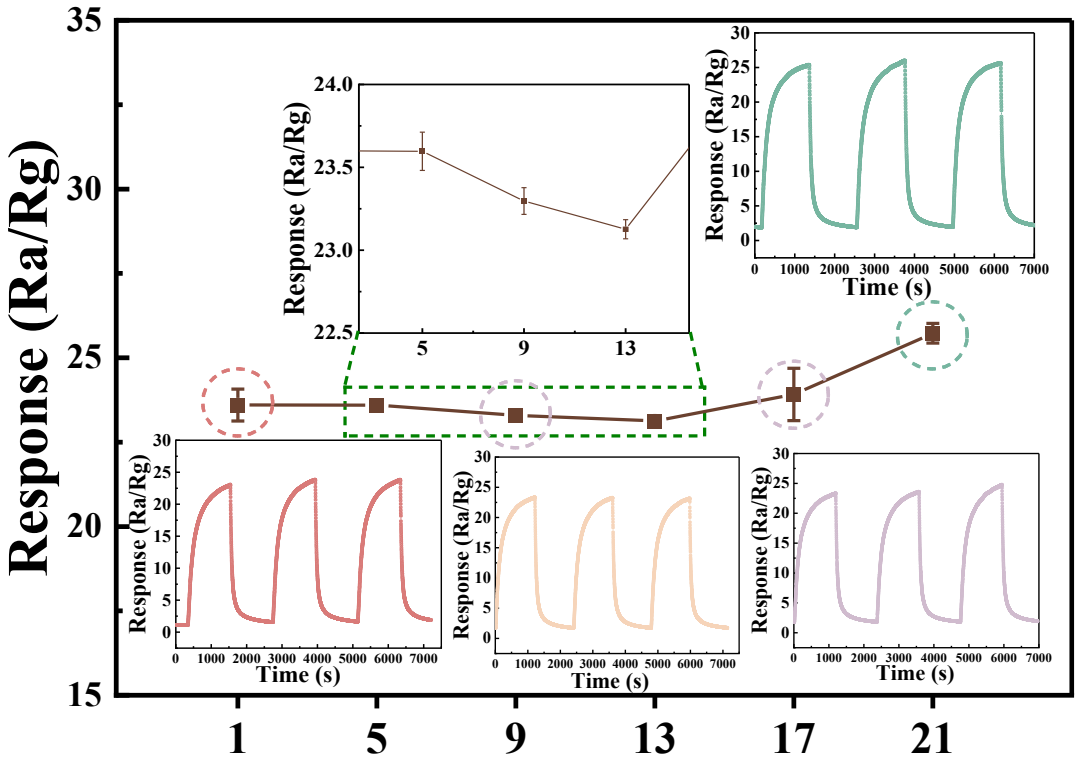

Figure 3-12 Long-term stability of the BCO-6La gas sensor to 9 ppm nonanal at room temperature (25±2°C).

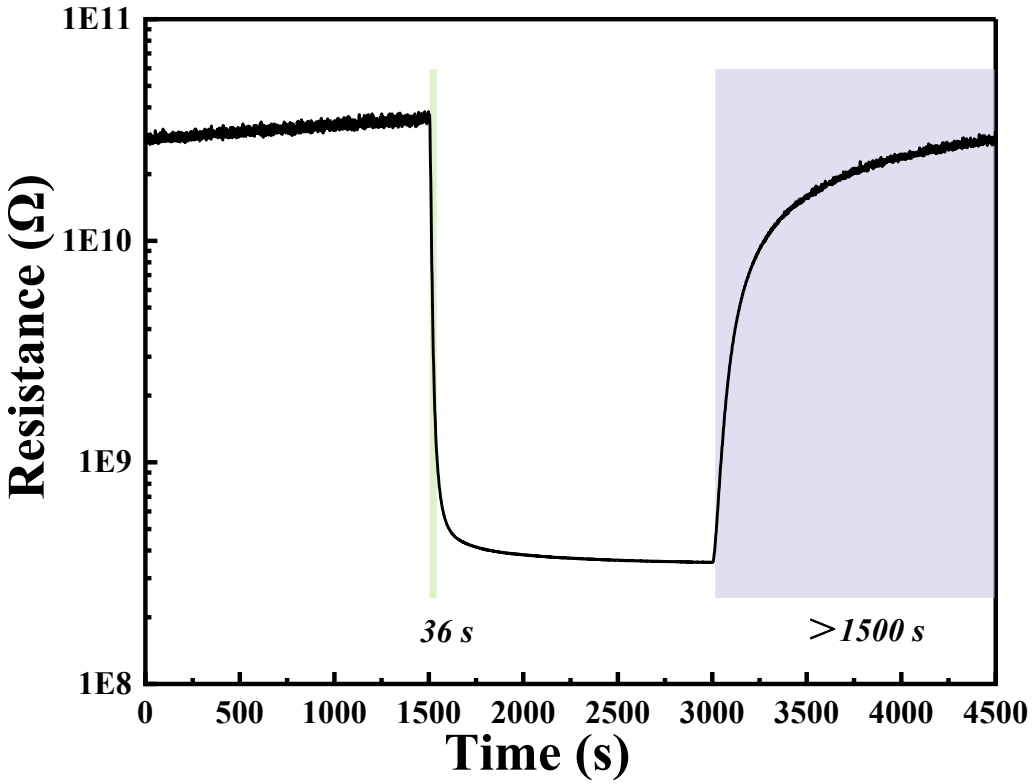

Figure 3-13 Responses/recovery time of BCO-6La to 18 ppm nonanal at room temperature (25±2°C).

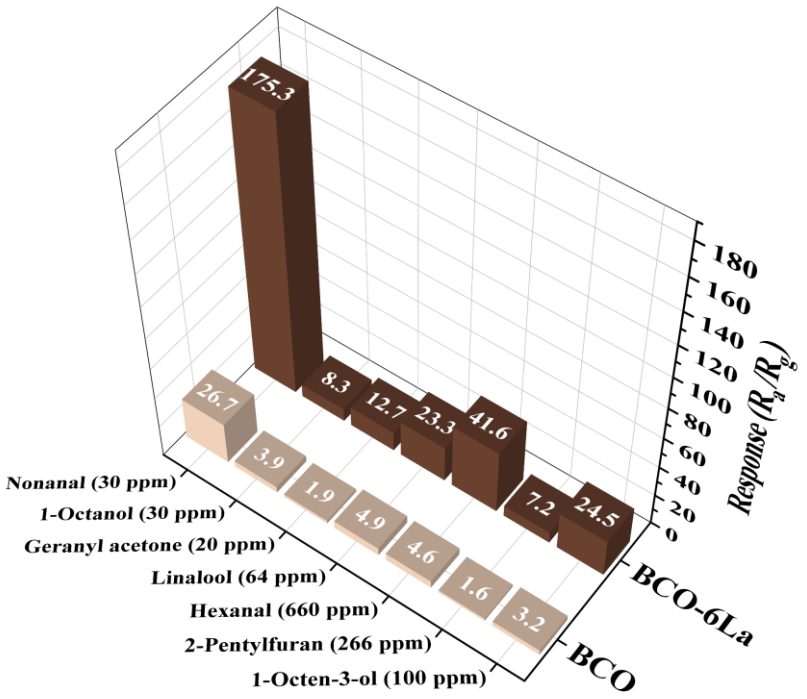

Figure 3-14 Exclusive detection to 30 ppm nonanal and various gases of BCO-6La at room temperature (25±2°C).

3.2.3 Gas sensing mechanism

When BCO-xLa is exposed to air, oxygen molecules adsorb on its surface, capturing electrons and forming oxygen ions. At temperatures below 150°C, oxygen ions predominantly exist as O_2^-. The reaction processes are as follows (Equation (3-1)-(3-2)) [208, 230]:

$$O_2(gas) \rightarrow O_2\ (ads) \quad (3\text{-}1)$$

$$O_2(ads) + e^- \rightarrow O_2^-\ (ads) \quad (3\text{-}2)$$

Upon exposure to nonanal gas, nonanal molecules transfer electrons to the conduction band of La-decorated BCO, thereby reducing the electron depletion layers and the potential energy barrier. The reaction processes follow Equations (3-3) and (3-4) [231-233]. The resistance of the BCO-xLa gas sensor decreases, and $C_9H_{18}O$ combines with O_2^- to form $C_9H_{16}O$, ultimately generating carbon dioxide and water molecules [234, 235], which is shown in Figure 3-15.

$$C_9H_{18}O(g) \rightarrow C_9H_{18}O\ (ads) \quad (3\text{-}3)$$

$$2C_9H_{18}O(ads) + O_2^-(ads) \rightarrow 2C_9H_{16}O(ads) + 2H_2O(g) + e^- \quad (3\text{-}4)$$

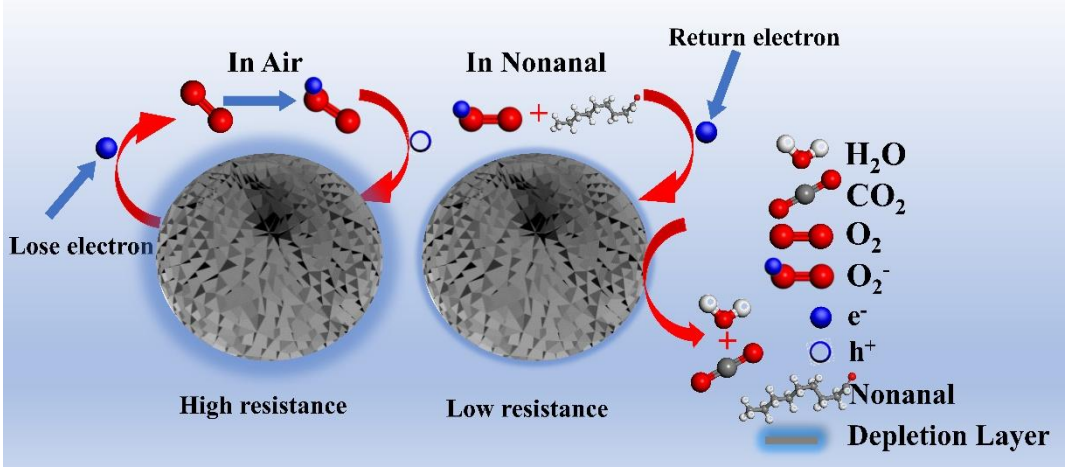

Figure 3-15 Schematic illustration of the nonanal gas-sensing mechanism of La-doped $Bi_2O_2CO_3$ microspheres at room temperature.

To further verify the mechanism, we obtained in situ FT-IR spectra of BCO-6La, as shown in Figure 3-16. During the adsorption process of nonanal on BCO-6La, a distinct strong and broad band around 2350 cm^{-1} was observed, attributed to the C=O stretching vibration in carbon dioxide [236, 237]. Additionally, the broad absorption band at 3389 cm^{-1} corresponds to the O-H stretching vibration absorption peak of water molecules [238]. These results confirm the capability of high-performance nonanal detection at room temperature.

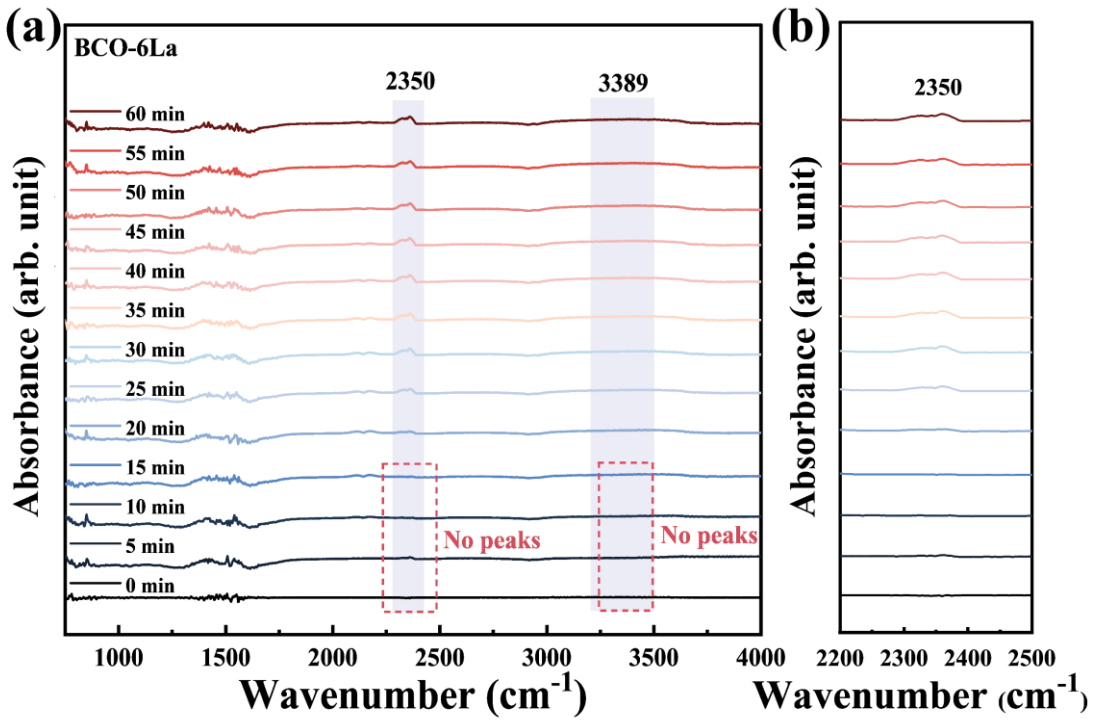

Figure 3-16 (a) In-situ FT-IR spectra of BCO-6La during nonanal adsorption, (b) magnified portion of In-situ FT-IR spectra (2200 cm^{-1}-2500 cm^{-1}).

By introducing O_V into the BCO, the oxygen-ion conductivity of the materials was enhanced, thereby accelerating oxidation-reduction reactions during nonanal detection. The enhancement in oxygen ion conductivity can effectively boost the sensitivity and response speed of gas sensors, enabling faster and more accurate gas detection, as corroborated by the gas sensing results. The response of the sensor can be presented as Equation (3-5) [214]:

$$S_g=\frac{\Gamma_t\, k(T)[O_{ads}^{ion}]^b}{n_o}C_g^b+1 \qquad (3\text{-}5)$$

where Γ_t represents the time constant, $k(T)$ is the reaction rate, $[O_{ads}^{ion}]^b$ is the density

of adsorbed oxygen ions, and n_o is the electron concentration of the sensor at room temperature. Specifically, La decoration enhances the ability of the sensor surface to adsorb oxygen (Figure 3-8a). As a result, there is a significant improvement in the sensor response after La decoration. Notably, the binding energy shift observed between the two components used to reproduce the La $3d_{5/2}$ peak in Figure 3-8b (~3.9 eV) suggests the presence of a small amount of $La(OH)_3$. While a minor amount of La(OH)3 improves the sensor response, excessive amounts may be detrimental, as they could impede carrier migration by surrounding the grain boundaries of $Bi_2O_2CO_3$. As shown in Figure 3-10, the sensor response gradually decreases with increasing La content. Thus, an optimal level of decoration enhances gas-sensing characteristics, whereas excessive decoration can deteriorate them. Additionally, as indicated by Equation (1-5), an increase in the b value correlates with a more rapid increase in response, highlighting the critical role of oxygen adsorption in enhancing gas response. As shown in Figure 3-10d, slope b, which relates sensor sensitivity and target gas concentration, is measured at 0.96, 1.22, 3.44, 6.58, 4.96, and 1.53, respectively, for the BCO, BCO-2La, BCO-4La, BCO-6La, BCO-8La, and BCO-10La sensors. The slope of the BCO-6La sensor is greater than that of BCO, suggesting that the La-decorated BCO sensor contains more oxygen ions, particularly in the BCO-6La samples, which also explains its highest response value. Furthermore, to gain a more comprehensive understanding of the gas-sensing mechanism of La-decorated BCO materials, we performed DFT calculations to investigate the role of La as a guest component. Decoration configurations and the nonanal molecular adsorption behavior were revealed by DFT calculations. All DFT calculations were performed using the CASTEP code in Materials Studio. In the generalized gradient approximation (GGA), the exchange-related potential was described by the Perdew-Burke-Ernzerhof (PBE) functional. The 2×2×1 supercells of the (020) surface $Bi_2O_2CO_3$ were built. When performing geometric optimization, the energy cutoff of plane wave expansion was set to 500 eV, and the energy convergence criterion in geometry optimization was set as 10^{-5} eV. A 15 Å vacuum layer was set between the layers to avoid interactions. The adsorption energy was calculated by Equation (3-6):

$$E_{ads}=E_{surface+gas}-(E_{surface}+E_{gas}) \quad (3\text{-}6)$$

where $E_{surface}$, E_{gas}, and $E_{surface+gas}$ denote the total electronic energies of BCO/BCO-La, nonanal, and their complex, respectively.

We optimized the adsorption configurations of BCO and BCO-La. The calculated adsorption energy of nonanal on BCO-La was -1.56 eV, significantly higher than the -0.23 eV observed for BCO (Figure 3-17). This indicates that the introduction of La atoms enhances the adsorption of nonanal and subsequent catalytic oxidation, further confirming the strong interaction between BCO-La and nonanal, elucidating the excellent selectivity of BCO-La towards nonanal.

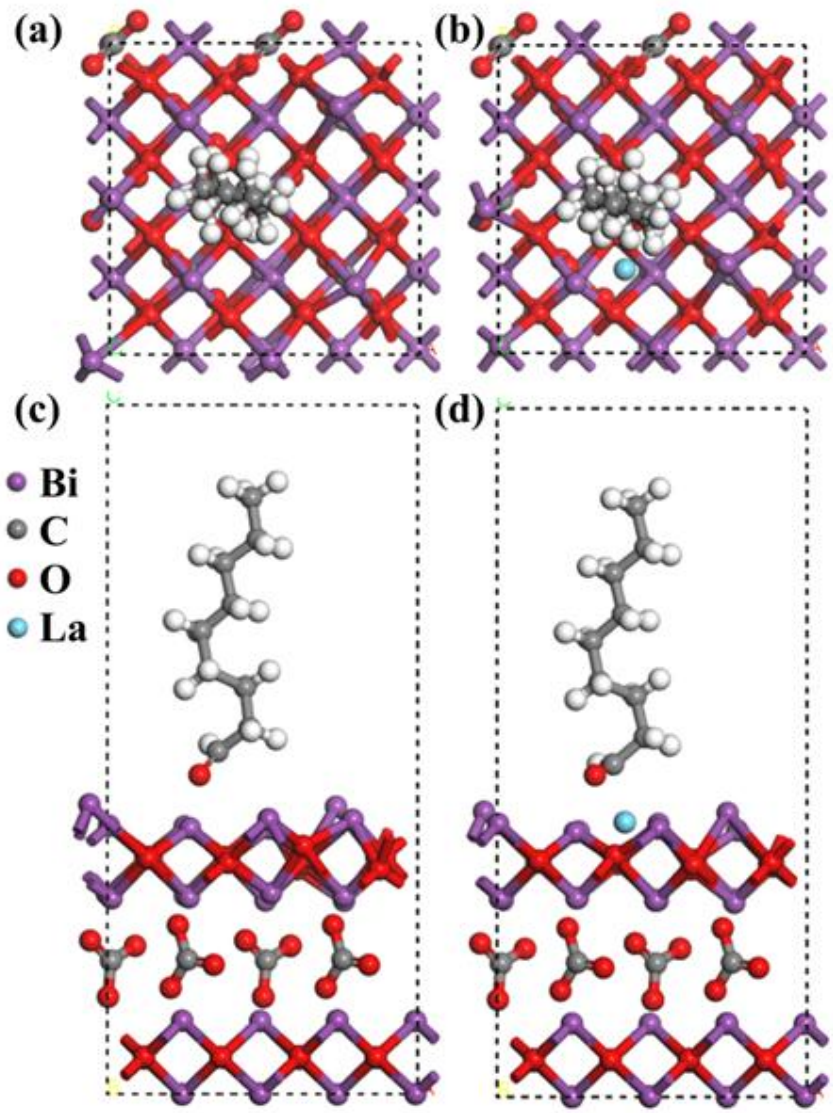

Figure 3-17 (a-b) Optimized adsorption structures of nonanal on the BCO and BCO-6La in the top view, respectively. (c-d) Adsorption configurations of nonanal on the optimum structure of BCO and BCO-6La, respectively.

3.3 Practical detection scenario

Monitoring changes in nonanal gas concentration presents a non-invasive and efficient method for evaluating the quality of cooked rice. The presence of nonanal in cooked rice has been demonstrated using the GC-MS technique (Figure 3-18).

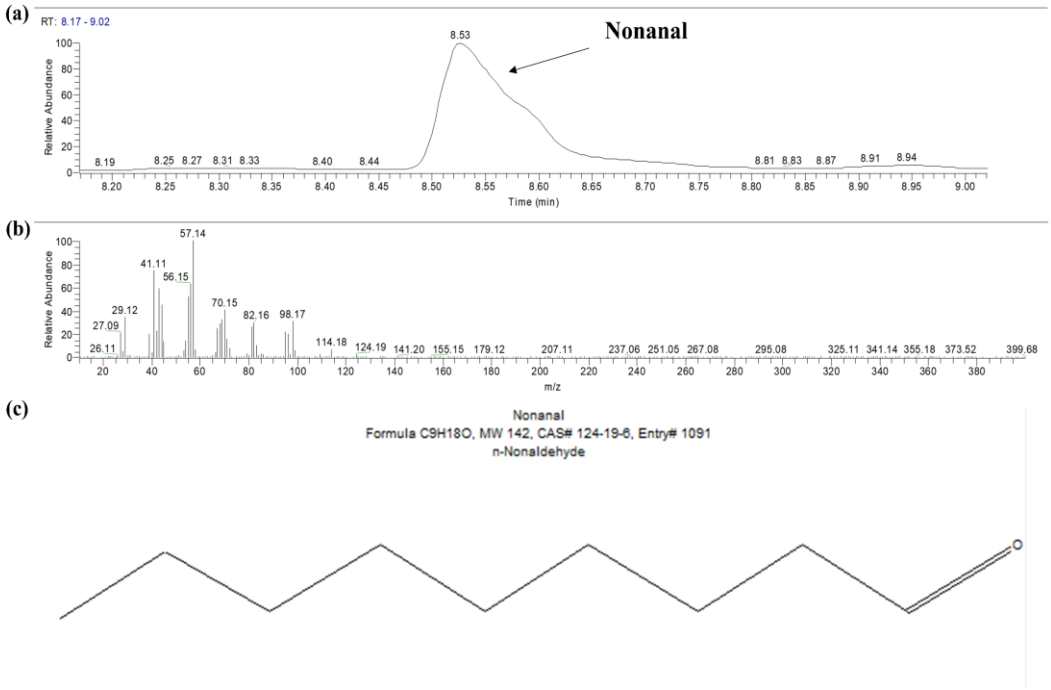

Figure 3-18 Magnified chromatogram of the nonanal region of cooked rice, (b-c) mass spectra of the nonanal in cooked rice.

The BCO-6La gas sensor was used to monitor changes in electrical resistance during rice storage. To minimize the influence of humidity, calcium chloride ($CaCl_2$) was used as a desiccant without affecting nonanal detection. Results demonstrated a significant increase in the sensor response after 6 hours of rice storage compared to the fresh state, indicating a rise in nonanal concentration (Figure 3-19). This observation highlights the sensor's potential to detect changes in nonanal concentration, reflecting the progression of staling in cooked rice. These findings are consistent with previous studies, which suggest that minimizing the oxidation and hydrolysis of lipids and moisture loss during storage can preserve the freshness of cooked rice [7, 104, 239].

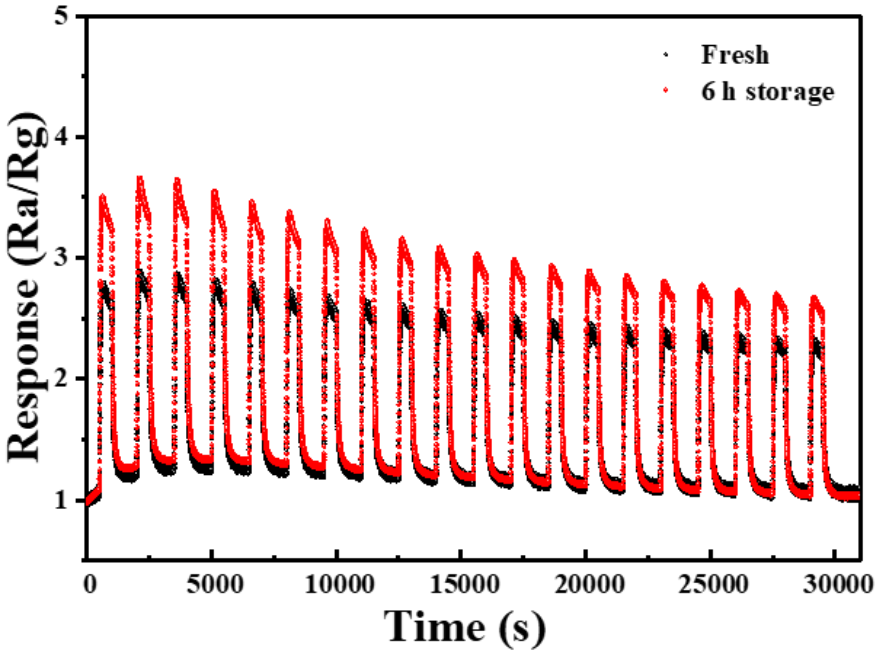

Figure 3-19 Response curves of the BCO-6La sensor as a function of storage time measured at room temperature under exposure to odors from cooked rice.

3.4 Conclusions

In summary, La-decorated BCO microspheres characterized by an abundance of O_V were synthesized. The gas sensor engineered using BCO-6La microspheres as active layer demonstrated exceptional sensitivity for room temperature detection of nonanal at a concentration of 30 ppm. Notably, the sensor exhibited a rapid response time of 36 s, excellent response of 174.6, and good selectivity that was approximately 4 to 24 times greater than that for other target gases. The enhanced sensing performance was attributed to the engineered O_V in the BCO-6La microspheres, which effectively reduces the energy bandgap, thereby facilitating electron transfer enhancing the sensor response to nonanal. Therefore, the incorporation of extrinsic oxygen defects through the La decoration of BCO microspheres is crucial for optimizing the nonanal sensing performance. We anticipate that this research will contribute significantly to advancements in nonanal gas sensors based on $Bi_2O_2CO_3$. The underlying sensing mechanism was identified by in-situ Fourier transform infrared (FT-IR) spectra, revealing that nonanal is initially converted to intermediate gas species that

subsequently decompose into CO_2 and H_2O. DFT calculation indicated that the adsorption energy of the active layer surface increased after La decoration, suggesting enhanced adsorption strength and stability, thereby contributing to enhanced gas sensing performance. Therefore, the rapid response and sensitivity enhancement associated with the La decoration are instrumental in advancing practical applications of nanomaterials-based gas sensors for high-performance online agricultural product inspection.

Chapter 4: Carbon functionalized cladding bismuth tungstate-based 3D twisted micro-flowers for benzaldehyde detection under ultraviolet light excitation

In this chapter, we construct a room-temperature benzaldehyde gas sensor based on carbon-functionalized cladding WO_3/Bi_2WO_6 three-dimensional twisted micro-flowers synthesized by a simple hydrothermal method. Benzaldehyde, a typical VOC widely used in food and agricultural applications, is selected as a target marker for environmental monitoring and cooked rice quality assessment, where conventional detection is often hindered by cross-interference and humidity effects. For the first time, $C/WO_3/Bi_2WO_6$-based gas sensors operated under ultraviolet (UV) excitation are systematically investigated and their sensing mechanism clarified. The sensor achieves a wide detection range with high sensitivity (33.7 at 50 ppm), and stable performance over more than 15 days at room temperature, enabling low-power operation and simple device architecture suitable for e-nose integration. It also exhibits strong anti-humidity and selectivity, with only 8.96% response loss at 90% relative humidity and clear benzaldehyde discrimination by dynamic response and PCA analysis. Finally, tests on cooked rice prepared from rice stored for 1-8 weeks demonstrate its practicality for agricultural product quality inspection.

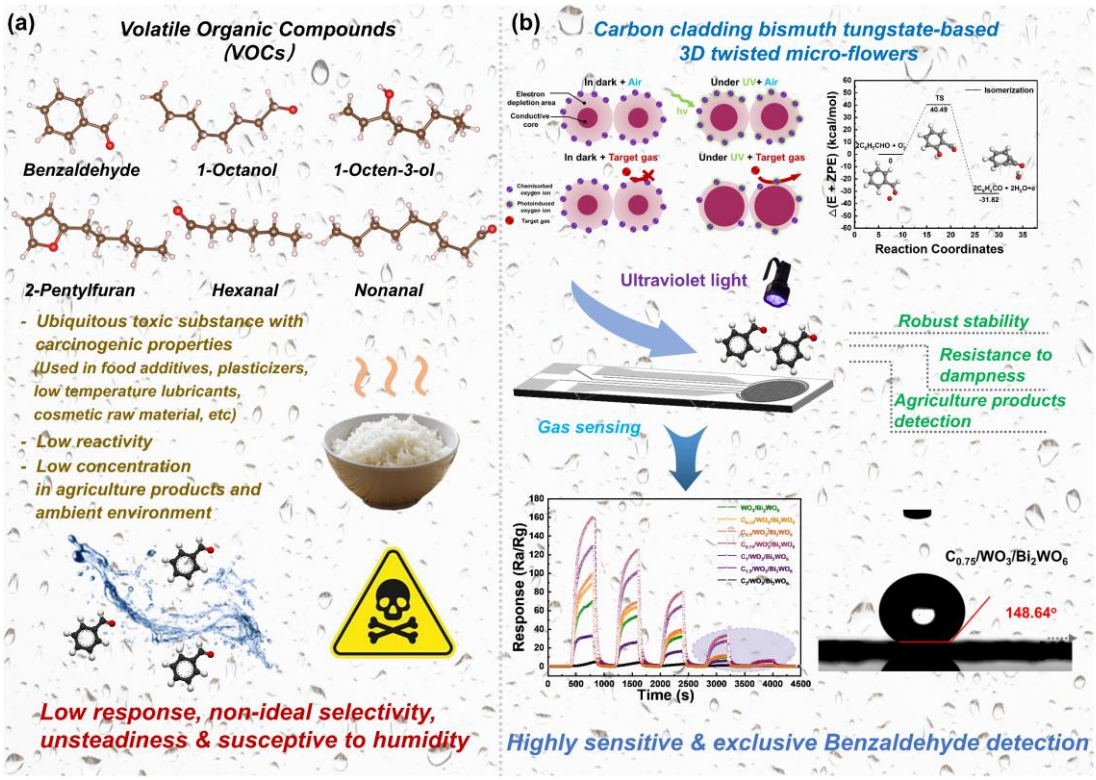

Schematic diagram 4-1 Graphical abstract of this chapter.

Benzaldehyde, in addition to being one of the important VOCs in cooked rice, is also widely used as a food additive, plasticizer, low-temperature lubricant, and cosmetic raw material [240, 241]. Nonetheless, as it is a carcinogenic substance with genetic toxicity, which may also cause atopic dermatitis, benzaldehyde has been identified as a hazardous substance [242]. Therefore, many studies have reported detection and elimination strategies for benzaldehyde, including chemiluminescence [243, 244], chemoresistive [242, 245, 246], fluorescence [241], and surface plasmon resonance immunosensor [247]. Wang et al. synthesized Co_3O_4-ZnO/rGO composites that can detect 3-5 ppm benzaldehyde with response and recovery times of 19/12 s [242]. A novel coralloid SnO_2 gas sensor was fabricated by Fang et al., which exhibited excellent sensitivity, rapid recovery, and a good linear dependence on benzaldehyde concentration [245]. However, they remained susceptible to environmental influences and were constrained by low yield and high power consumption. Hence, the development of highly sensitive and exclusive gas sensors for benzaldehyde detection with moisture-resistant, robust features must be pursued and improved to scrutinize food quality and ensure environmental safety in real-time and on-site.

In the benzaldehyde sensing process, the bulk resistance of SMOX is determined by the oxygen adsorption (O_2^-, O^-, and O^{2-}) model under temperature dominance [23, 248]. In humid environments, chemisorption of water molecules shares the same site on the material's surface as adsorption of oxygen species, and electrons acquired by the adsorbed oxygen in this course are returned to the SMOX, as demonstrated in followed reaction (4-1) [249]:

$$H_2O + 2M_m + O_{ad}^- \leftrightarrow 2\left(M_m^+ - OH\right) + e^- + S \qquad (4\text{-}1)$$

where M refers to metal elements in SMOX; M_m represents the site of M on the surface; O_{ad}^- is related to ion-adsorbed oxygen species; e^- refers to the electron; $\left(M_m^+ - OH\right)$ represents a terminal hydroxyl group, while S is a surface site for chemically adsorbing oxygen.

When facing with rising humidity as detecting target VOCs, the bond between water molecules with gas-sensitive layers will gradually transform from individual chemisorption to a complex physical and chemical adsorption [250], subsequently, the proton hopping manifested, in compliance with the Grotthuss mechanism, where protons are successively relayed along hydrogen-bonded water chains, will greatly decrease the material resistance and the accuracy of sensing [251], resulting in a greater degree of adsorption competition and deterioration of the sensitivity [252]. In terms of the unsatisfactory and inevitable humidity effect, physical isolation [253], surface engineering [254], novel material development [255], algorism compensation [256], working parameter modulation [257], and other mainstream approaches have been adopted to improve the reliability and robustness of ideal sensors. Nonetheless, the predicament is that high sensitivity, exclusive detection, low operating temperature, and stable output from gas sensors cannot be achieved concurrently. For instance, Kim et al. reported that the Pr-doped $Ce_4W_9O_{33}$-based trimethylamine sensor fabricated by the ultrasonic spray pyrolysis method addresses the water-poisoning problem, as the sensitivity was largely independent of ambient humidity, although the preparation process is time-consuming and labor-intensive [258]. Following the idea of loading hydrophobic materials, Sun et al. loaded CuO with strong affinity for the hydroxyl group on In2O3, forming clustered nanospheres to improve moisture resistance in CO

detection, yet the selectivity sensing results demonstrated undesirable performance [259]. Incorporating integrated microheaters with SnO_2/RGOH NO_2 sensors to regulate the operating temperature, Wu et al. revealed that higher temperature leads to greater immunity to humidity interference [260]. However, the appendant microheater limits real-time, portable detection capabilities, and its power consumption is higher. Furthermore, Liu et al. employed 3-aminopropyltriethoxysilane-modified tungsten oxide nanotubes with thin-walled porous features, which can provide abundant hydrophobic groups for NO_2 detection, and the sensitivity merely drops to 80% of the incipient response value even in saturated relative humidity [261]. Nevertheless, the above methods still suffered from a complex preparation process, insufficient selectivity, an intricate detection system, etc. Thus, a breakthrough is urgently needed to develop highly sensitive VOC sensors with reliable sensing performance under high-humidity conditions, as cooked rice also releases a lot of water. In this context, it is desirable to exploit SMOX that are intrinsically humidity-tolerant, can be activated by light rather than external heaters, and are compatible with simple device architectures. Tungsten-based oxides are particularly attractive candidates because of their suitable band structure, rich surface chemistry, and well-documented photocatalytic activity, which are beneficial for room-temperature VOC sensing in moist environments.

Here, we choose WO_3 and Bi_2WO_6 as sensing materials, as they are both n-type semiconductors with an appropriate band gap of 2.7-2.9 eV and high surface activity, effectively adsorbing VOCs in the surrounding environment [262-264]. Furthermore, they both exhibit excellent photocatalytic properties, which enable them to generate electron-hole pairs easily, further enhancing their sensitivity and selectivity towards VOCs under light exposure. The photocatalytic activity also aids in decomposing VOCs adsorbed on the sensor surface, reducing sensor saturation and improving recovery speed [265-267]. Therefore, we introduced D-(+)-Glucose anhydrous as a carbon-functionalized cladding for WO_3/Bi_2WO_6 to achieve highly sensitive and robust benzaldehyde detection at room temperature with UV light assistance. Photoexcitation increased the number of carriers with high mobility and reduced the grain boundary barrier, improving the response to benzaldehyde at room temperature [268]. By combining carbon-based materials and introducing n-n heterojunctions, the optimal sensing material exhibited a stable nanostructure, a high specific surface area, abundant surface oxygen vacancies, and distinct hydrophobicity. The corresponding sensor

exhibited high sensitivity (33.7 at 50 ppm), robust reproducibility, and long-term stability, along with a distinct detection feature.

4.1 Synthesis process

All reagents used were of analytical grade and were used without further purification. Bismuth nitrate pentahydrate ($Bi(NO_3)_3 \cdot 5H_2O$) (AR grade, CAS: 10035-06-0), anhydrous ethanol (AR grade, CAS: 64-17-5), and benzaldehyde (AR grade, CAS: 100-52-7) were acquired from Aladdin Biochemical Technology Co., Ltd. of China. Sodium tungstate dihydrate ($Na_2WO_4 \cdot 2H_2O$) (AR grade, CAS: 10213-10-2) and D-(+)-Glucose anhydrous (AR grade, 50-99-7) were obtained from Sinopharm Chemical Reagent Co., Ltd. Polyvinyl pyrrolidone (K30) (AR grade, CAS: 9003-39-8) were purchased from Merck Chemical Technology (Shanghai) Co., LTD.

Synthesis of C: C was synthesized via a hydrothermal method. Initially, 0.75 g of D-(+)-Glucose anhydrous was dissolved in 60 mL of deionized water. This solution was then transferred to a 100 mL Teflon-lined stainless-steel autoclave following magnetic stirring for 1 hour. The autoclave was heated to 160 °C and maintained at that temperature for 20 hours, then allowed to cool naturally. The resultant material was isolated by centrifugation with absolute ethanol five times. The final product was dried in an oven at 60 °C for 12 hours.

Synthesis of Bi_2WO_6: Bi_2WO_6 was synthesized via a hydrothermal method, which was modified from previous studies [269]. A mixture of 4 mmol of $Bi(NO_3)_3 \cdot 5H_2O$, 2 mmol of $Na_2WO_4 \cdot 2H_2O$, and 0.6 g of PVP (K30) was prepared in 60 mL of deionized water. This mixture was then transferred to a 100 mL Teflon-lined stainless-steel autoclave after stirring magnetically for 1 hour. The autoclave was subsequently heated to 160 °C and maintained at that temperature for 20 hours, then allowed to cool naturally. The products were subjected to centrifugation with absolute ethanol five times. After drying at 60 °C for 12 hours in an oven, the synthesized Bi2WO6 was obtained. The final products are referred to as Bi_2WO_6.

Synthesis of $C_x/WO_3/Bi_2WO_6$*:* $C_x/WO_3/Bi_2WO_6$ were fabricated using an adapted hydrothermal method modified from previous studies [269, 270]. In detail, a mixture containing 4 mmol $Bi(NO_3)_3 \cdot 5H_2O$, 5 mmol $Na_2WO_4 \cdot 2H_2O$, 0.6 g PVP and certain amounts of D-(+)-Glucose anhydrous was prepared in 60 mL of deionized water. This

mixture was stirred for 1 hour before being placed into 100 mL Teflon-lined stainless autoclaves. The autoclaves were subjected at 160°C for 20 hours before being allowed to cool to room temperature naturally. The resulting products were isolated by centrifugation with ethanol and deionized water, then dried at 60°C. The final products synthesized with D-(+)-Glucose anhydrous of 0 g, 0.25g 0.5 g, 0.75g, 1 g, 1.5 g and 2 g are denoted as WO_3/Bi_2WO_6, $C_{0.25}/WO_3/Bi_2WO_6$, $C_{0.5}/WO_3/Bi_2WO_6$, $C_{0.75}/WO_3/Bi_2WO_6$, $C_1/WO_3/Bi_2WO_6$, $C_{1.5}/WO_3/Bi_2WO_6$ and $C_2/WO_3/Bi_2WO_6$.

4.2 Results and discussion

4.2.1. Characterization results

The highly anti-humidity and exclusive $C_x/WO_3/Bi_2WO_6$ chemoresistive sensors were prepared by an elementary, one-step roadmap (Preparation process section and Figure 4-1a). Distinctively, PVP (K30) serves both as a stabilizer and a crystallization inhibitor, preventing ionic aggregation during the reaction and controlling the size and morphology of bismuth tungstate and tungsten oxide, ensuring their uniform shape. Thus, simultaneously under the action of PVP dispersant, D-(+)-Glucose anhydrous can form a uniform carbon coating naturally. All the diffraction peaks of the Bi_2WO_6 pattern were matched to the cubic phase (JCPDS Card No. 39-0256) and the WO_3 was indexed to the cubic phase (JCPDS Card No. 52-8916) (Figure 4-1b, Figure 4-2). As the amount of D-(+)-Glucose anhydrous increases gradually, the color of the samples progressively deepened and the intensity of characteristic peak of WO_3, (002), decreases slowly and eventually disappears (Figure 4-1h), demonstrating an excess of D-(+)-Glucose anhydrous would lead to the destruction of WO_3/Bi_2WO_6 double heterojunction, degrade the positive role of PVP. The texture coefficient values of seven samples were calculated (Table 4-1 and Figure 4-3) [115], and the corresponding value of each crystallographic plane displayed no evident variation, manifesting that the C cladding may not lead to a re-orientation effect. Meanwhile, the pure carbon was synthesized via the one-step hydrothermal strategy above and the C exists in two forms: as nanoparticles and as micrometer-sized spheres (Figure 4-4). To verify the successfully functionalization of caron cladding, we performed TGA characterization on five typical

samples, and the results demonstrated that with the augment of D-(+)-Glucose anhydrous addition, the mass of the samples decreased further correspondingly (From WO_3/Bi_2WO_6 to $C_1/WO_3/Bi_2WO_6$: 3.09 wt%, 21.11 wt%, 24.12 wt%, 34.49 wt%, 50.38 wt%), while carbon will be converted into CO_2 during this process. To gain a more comprehensive insight into the crystal structure of the as-prepared products, XRD Rietveld refinement was carried out, as depicted in Figure 4-1d and Figures 4-5 to 4-11. The analysis of $C_{0.75}/WO_3/Bi_2WO_6$ yielded a notably low weighted residual (R_{wp} = 8.444%), manifesting a high degree of correlation between the refined pattern and the original XRD observations. As shown in Figure 4-1e, we determined that the peak at approximately 719 cm-1 was correlated with the W-O-W bond [271, 272], while the peak at 1618 cm-1 was assigned to the ring C-C stretch [273], which verifies the smooth encapsulation of the carbon. Furthermore, the most intense W-O-W peak was observed in sample $C_{0.75}/WO_3/Bi_2WO_6$, indicating a higher concentration of specific molecules that absorb photons, thereby enhancing sensitivity. Finally, Raman spectra of all samples and Raman mapping of WO3/Bi2WO6 and C0.75/WO3/Bi2WO6 were conducted (Figures 4-1f and 4-1g). Additionally, the relatively weak peak observed at around 1362 cm^{-1} correlates with the defects and disordered structure of the carbon portion (D band), while the relatively strong peak at approximately 1573 cm^{-1} is indicative of the planar vibration mode characteristic of sp^2-hybridized carbon atoms (G band) [274], which further confirms the successful formation of C cladding. As shown in Figure 4-1f, the Raman mapping of G band (1573 cm^{-1}) and D band (1362 cm^{-1}) of $C_{0.75}/WO_3/Bi_2WO_6$ presented high intensity, which verified the uniform distribution of C and the existentially induced defects. Furthermore, the C is in the compressed state in the green region, and the constricted C-C bond is due to the hydrothermal reaction at high temperature [275], thereby verifying its robustness and anti-humidity features, while the procreant defect states will facilitate the absorption of UV light, enhancing gas sensing performance.

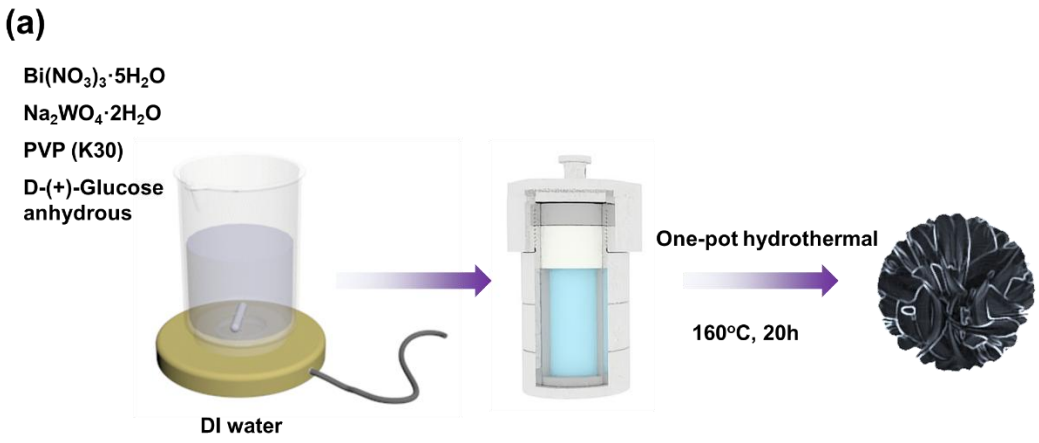

Figure 4-1 (a) Schematic illustration for the fabrication of $C_x/WO_3/Bi_2WO_6$.

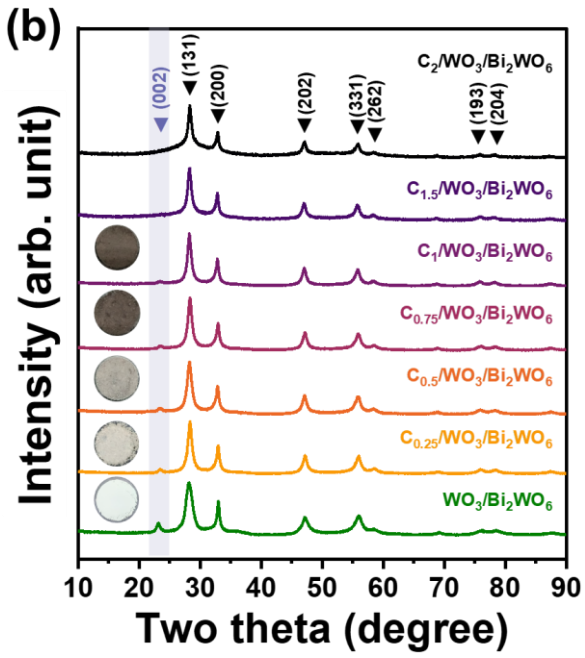

Figure 4-1 (b) XRD pattern of all samples.

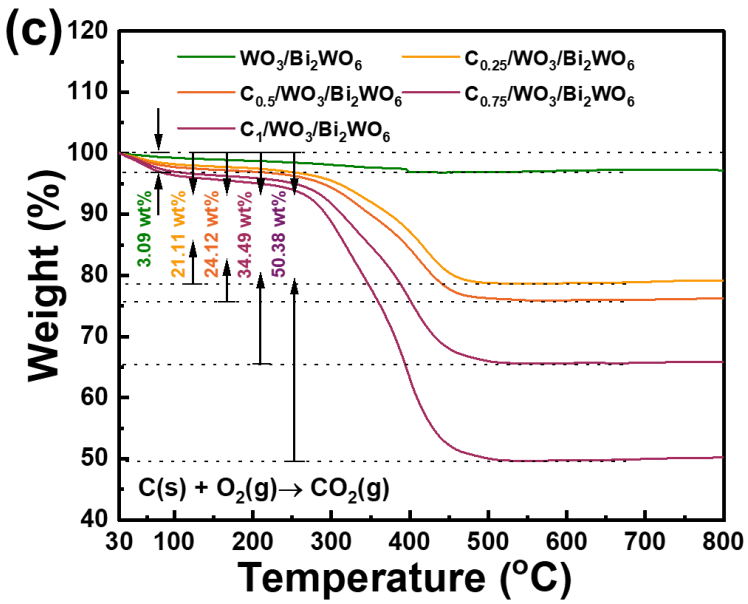

Figure 4-1 (c) Dynamic TGA curves with a heating rate of 10 °C ·min^{-1} of all samples.

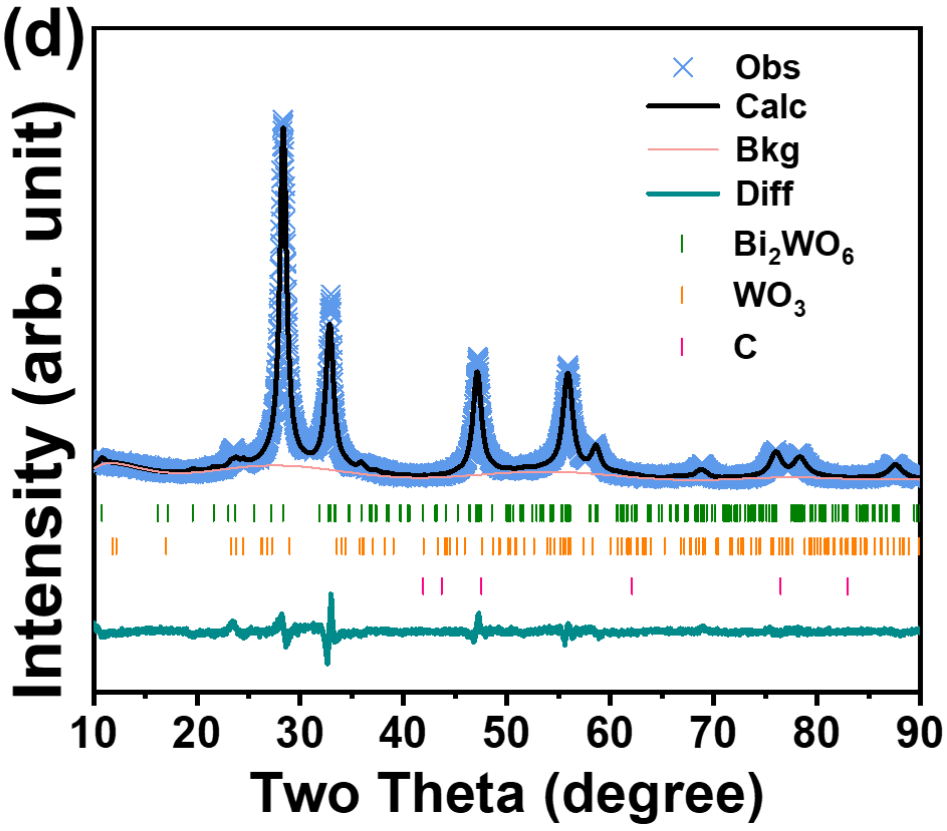

Figure 4-1 (d) Rietveld refinement patterns of $C_{0.75}/WO_3/Bi_2WO_6$.

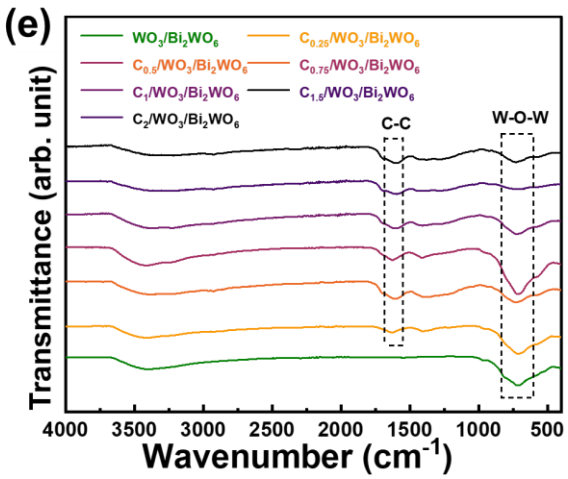

Figure 4-1 (e) FT-IR spectra of all samples.

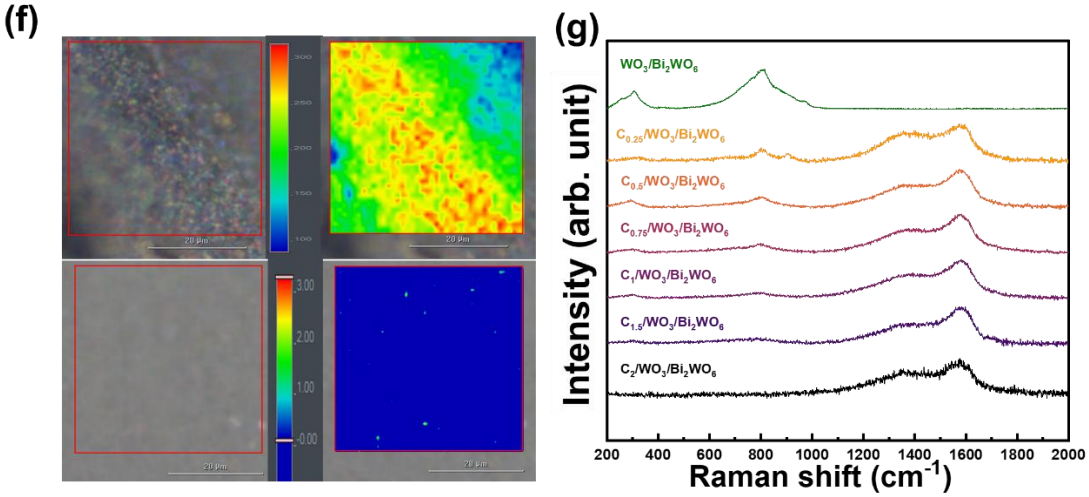

Figure 4-1 (f) Raman mapping of graphitic G bands in a locally laser-irradiated region of pure WO_3/Bi_2WO_6 (under part) and $C_{0.75}/WO_3/Bi_2WO_6$ (upper part), (g) Raman spectra of all samples.

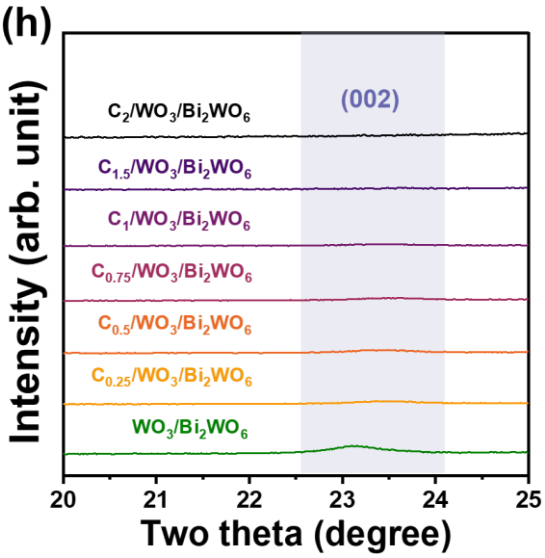

Figure 4-1 (h) Magnified portion of XRD pattern (20°-25°) of all samples.

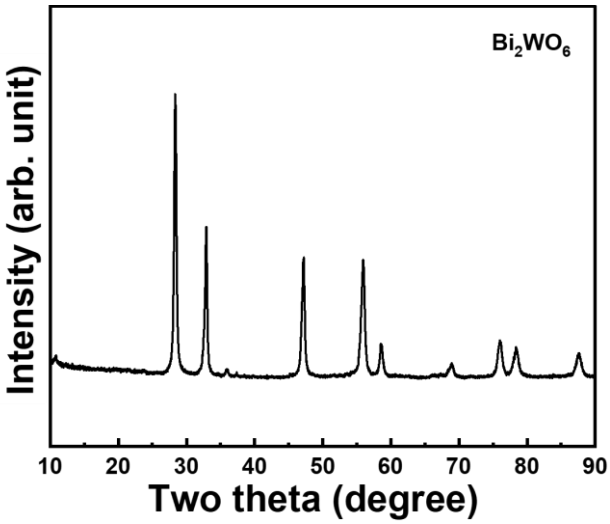

Figure 4-2 XRD patterns of Bi_2WO_6.

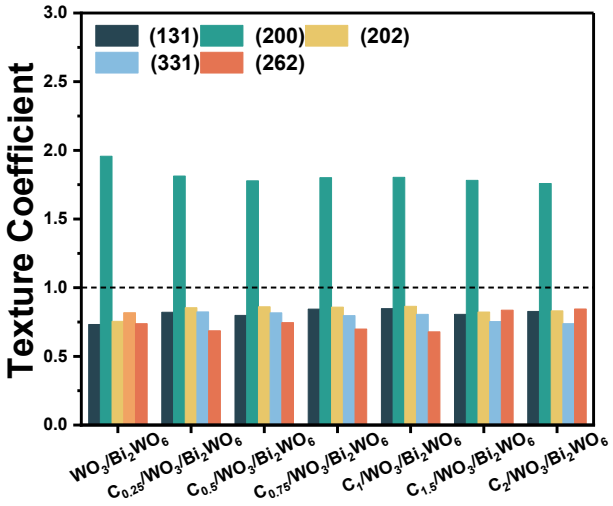

Figure 4-3 Texture coefficient values of all samples.

Table 4-1 TC values of as-synthesized pure WO_3/Bi_2WO_6 and $C_x/WO_3/Bi_2WO_6$ samples.

Sample	TC(131)	TC(200)	TC(202)	TC(331)	TC(262)
WO_3/Bi_2WO_6	0.73176	1.95697	0.75505	0.81783	0.73838
$C_{0.25}/WO_3/Bi_2WO_6$	0.82138	1.8134	0.85455	0.82415	0.68652
$C_{0.5}/WO_3/Bi_2WO_6$	0.79831	1.7783	0.86097	0.81665	0.74577
$C_{0.75}/WO_3/Bi_2WO_6$	0.84424	1.80113	0.85882	0.79649	0.69933
$C_1/WO_3/Bi_2WO_6$	0.84718	1.80361	0.86423	0.80591	0.67907
$C_{1.5}/WO_3/Bi_2WO_6$	0.80583	1.7816	0.8228	0.75364	0.83612
$C_2/WO_3/Bi_2WO_6$	0.82736	1.75869	0.83119	0.73776	0.845

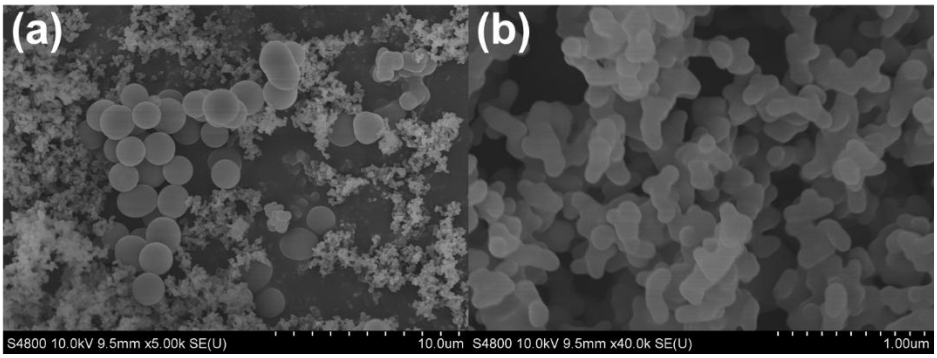

Figure 4-4 The FESEM images of C synthesized via a one-step hydrothermal strategy.

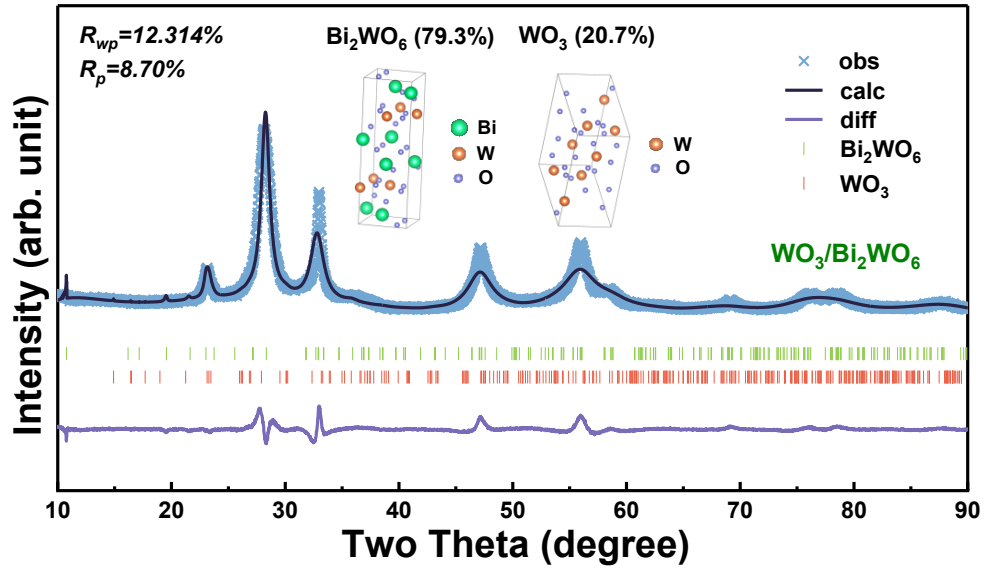

Figure 4-5 Rietveld refinement of the XRD pattern for WO_3/Bi_2WO_6.

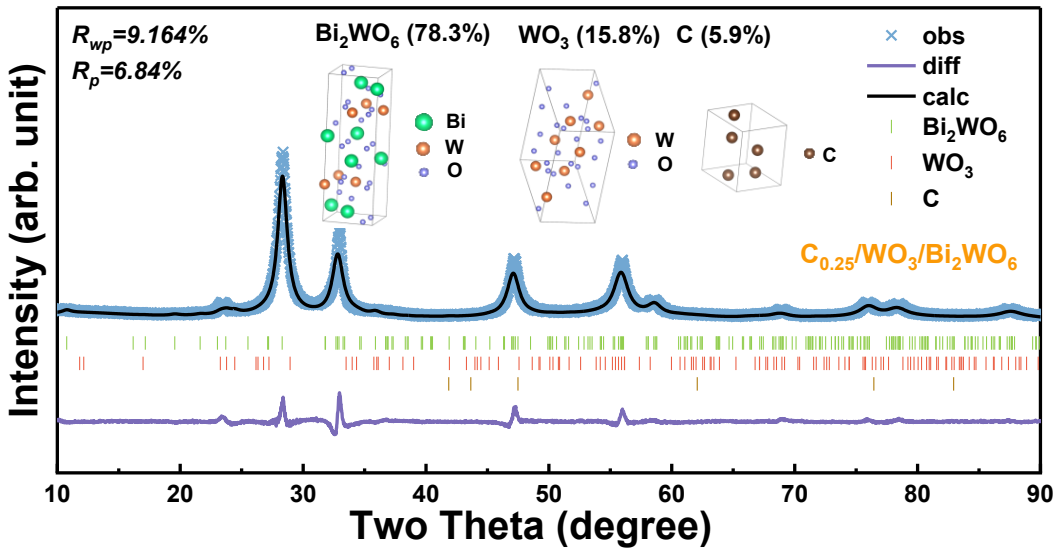

Figure 4-6 Rietveld refinement of the XRD pattern for $C_{0.25}WO_3/Bi_2WO_6$.

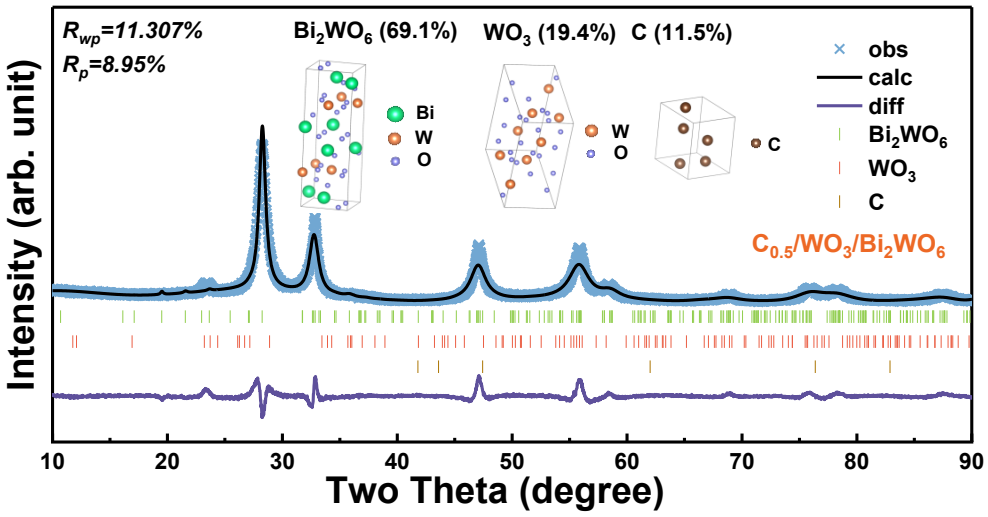

Figure 4-7 Rietveld refinement of the XRD pattern for $C_{0.5}WO_3/Bi_2WO_6$.

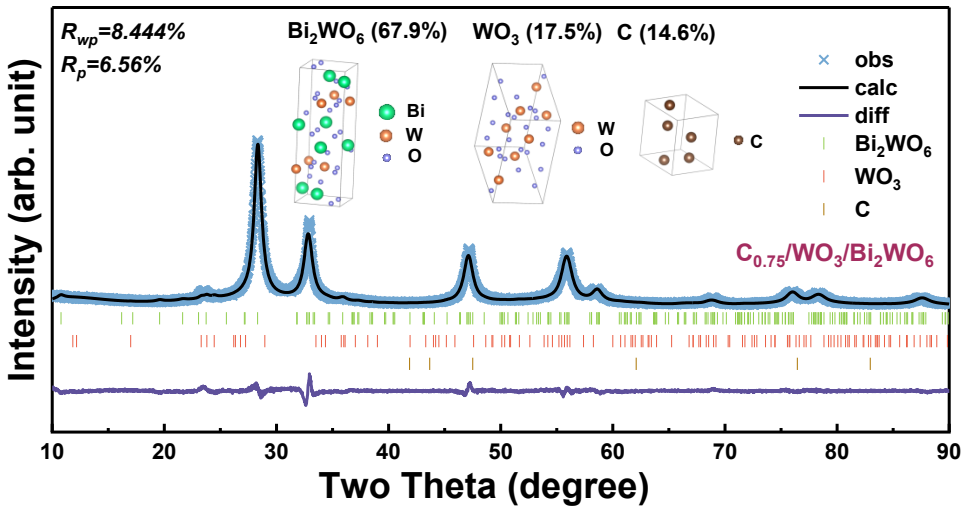

Figure 4-8 Rietveld refinement of the XRD pattern for $C_{0.75}WO_3/Bi_2WO_6$.

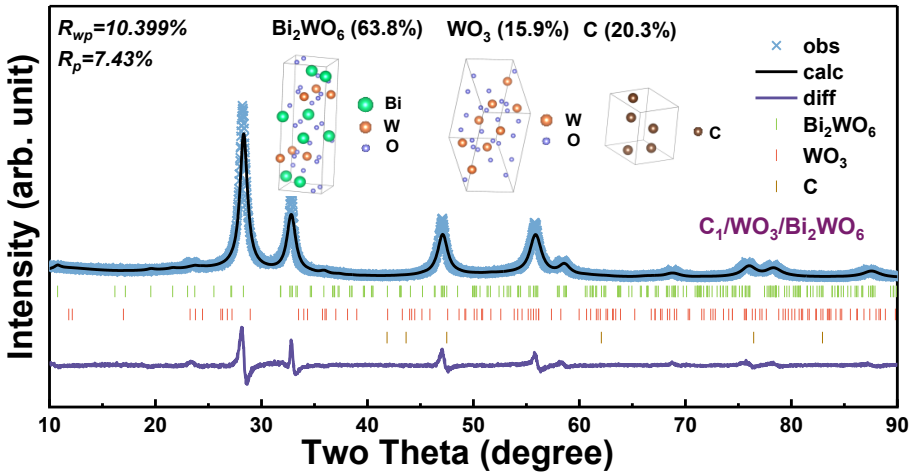

Figure 4-9 Rietveld refinement of the XRD pattern for C_1WO_3/Bi_2WO_6.

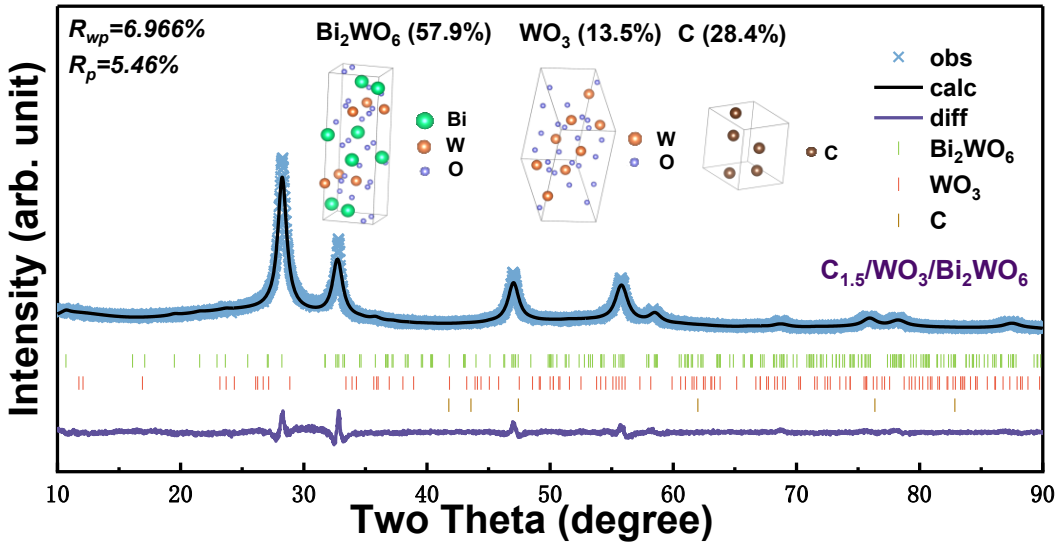

Figure 4-10 Rietveld refinement of the XRD pattern for $C_{1.5}WO_3/Bi_2WO_6$.

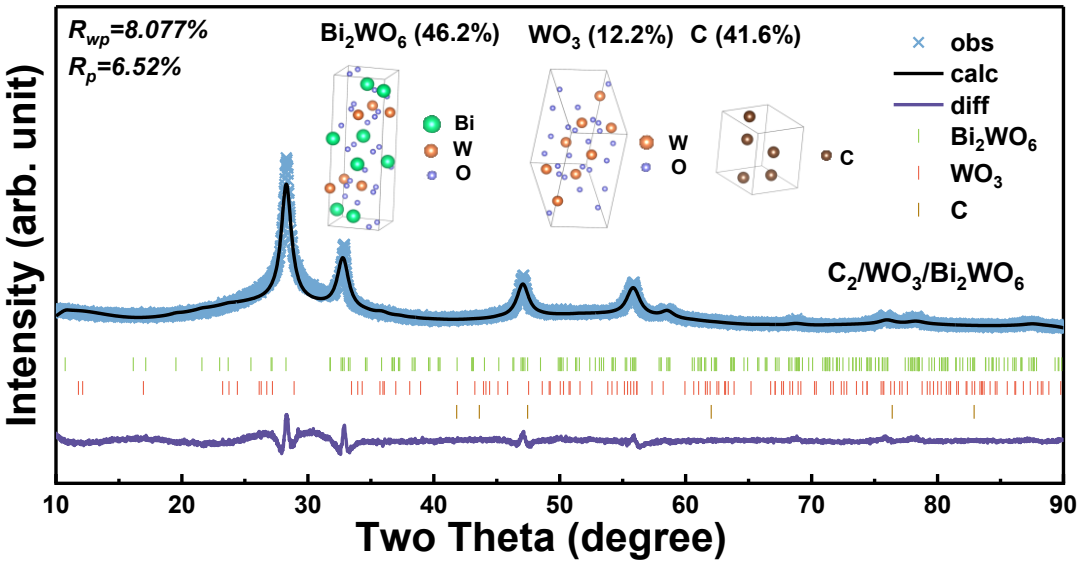

Figure 4-11 Rietveld refinement of the XRD pattern for C_2WO_3/Bi_2WO_6.

Via regulating the amount of D-(+)-Glucose anhydrous, adequate C was clad on the appointed heterojunction, thus $C_{0.75}/WO_3/Bi_2WO_6$ with the 3D twisted micro-flower nature was prepared (Figure 4-12a and Figure 4-12b). In detail, it was assembled from abundant mesoporous WO3/Bi2WO6 with C-cladding branches rotating around a specific axis. PVP acts as a dispersant in the synthesis to prevent the aggregation of bismuth, tungsten, and carbon sources, facilitating the acquisition of uniform $C_{0.75}/WO_3/Bi_2WO_6$ micro-flower. The morphology of other samples was also examined

(Figure 4-13) while the atomic weight ratios and atomic ratios of Bi, W, O, and C in samples through EDS spectra were depicted in Figure 4-14 and Figure 4-15, which illustrate the incremental C content with the increase in D-(+)-Glucose anhydrous content. However, there exists a singular point that the atom ratio of C of $C_{0.75}/WO_3/Bi_2WO_6$ is higher than that of $C_1/WO_3/Bi_2WO_6$, which may be because of the synergistic effect of the appropriate D-(+)-Glucose anhydrous adding content and PVP stabilizer resulting in a slightly higher C content in the $C_{0.75}/WO_3/Bi_2WO_6$ sample. Furthermore, high-resolution TEM (HRTEM) was used to image $C_{0.75}/WO_3/Bi_2WO_6$ (Figures 4-12c and 4-12d) and C1.5/WO3/Bi2WO6 (Figures 4-12e and 4-12f). Bi (Figure 4-12d1), W (Figure 4-12d2), O (Figure 4-12d3), and C (Figure 4-12d4) were distributed uniformly over the whole 3D $C_{0.75}/WO_3/Bi_2WO_6$ twisted micro-flower, while the EDS linear scanning results confirm this viewpoint simultaneously (Figure 4-12g and Figure 4-16). As shown in Figure 4-12c of high-angle annular dark-field images (HAADF) of C0.75/WO3/Bi2WO6, there are bright and dark areas intermingled, indicating a certain hollow property and erythrocyte-like structure. In detail, the thickness of $C_{0.75}/WO_3/Bi_2WO_6$ 3D micro-flowers increases with the augment of the diameter from the axis outward. However, there still leaves a large amount of C in the form of spheres in $C_{1.5}/WO_3/Bi_2WO_6$ samples (Figure 4-12e and Figure 4-12f), indicating the importance of adding an appropriate amount of D-(+)-Glucose anhydrous. Three categories of clear lattice fringes for Bi_2WO_6, WO_3, and C of $C_{0.75}/WO_3/Bi_2WO_6$ were marked thoroughly (Figure 4-12h, Figure 4-17a, and Figure 4-17b). In detail, the lattice spacing of 0.390 nm, 0.301 nm, and 0.218 nm corresponded to the (002), (111), and (220) planes (Figure 4-17c2) of WO_3, respectively. As for Bi_2WO_6, the interplanar spacing between contiguous lattice fringes was 0.314 nm, 0.196 nm, and 0.157 nm, which can be assigned to the (131), (202), and (262) planes, respectively (Figure 4-17c1 and Figure 4-18c). The interplanar spacing of 0.34 nm along two orthogonal directions corresponds with the (020) crystallographic plane of carbon (Figure 4-17c3 and Figure 4-18a) [276]. The post-optimized FFT images of $C_{0.75}/WO_3/Bi_2WO_6$ for Bi_2WO_6 (Figure 4-18d) and C (Figure 4-18b) were obtained,

thereby verifying the accuracy of the measured lattice fringe spacing. Meanwhile, the selected area electron diffraction (SAED) for $C_{0.75}/WO_3/Bi_2WO_6$ was examined (Figure 4-12i), demonstrating the polycrystalline nature, as distinct diffraction rings with a small number of spots are visible, consistent with the XRD analysis. In addition, SAED experiments were carried out for WO_3/Bi_2WO_6 (Figure 4-12j). The monocrystal feature of WO_3/Bi_2WO_6 without C cladding was discerned.

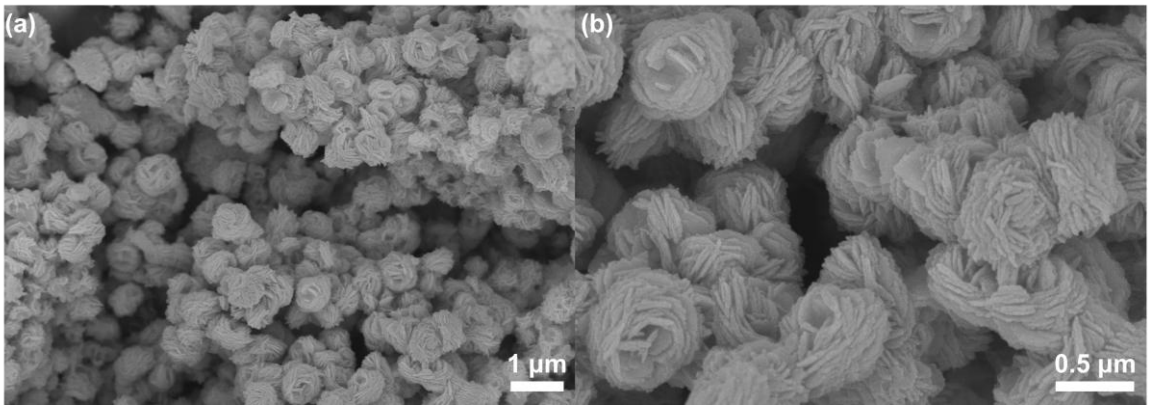

Figure 4-12 (a-b) FESEM image of $C_{0.75}/WO_3/Bi_2WO_6$ shows its 3D twisted micro-flower nature.

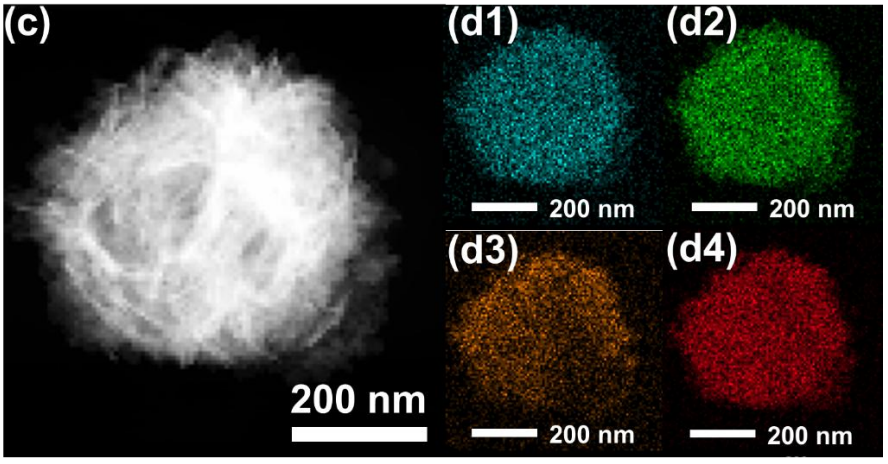

Figure 4-12 (c-d) EDS elemental mapping results of $C_{0.75}/WO_3/Bi_2WO_6$ in two different perspectives (d1: Bi, d2: W, d3: O, d4: C).

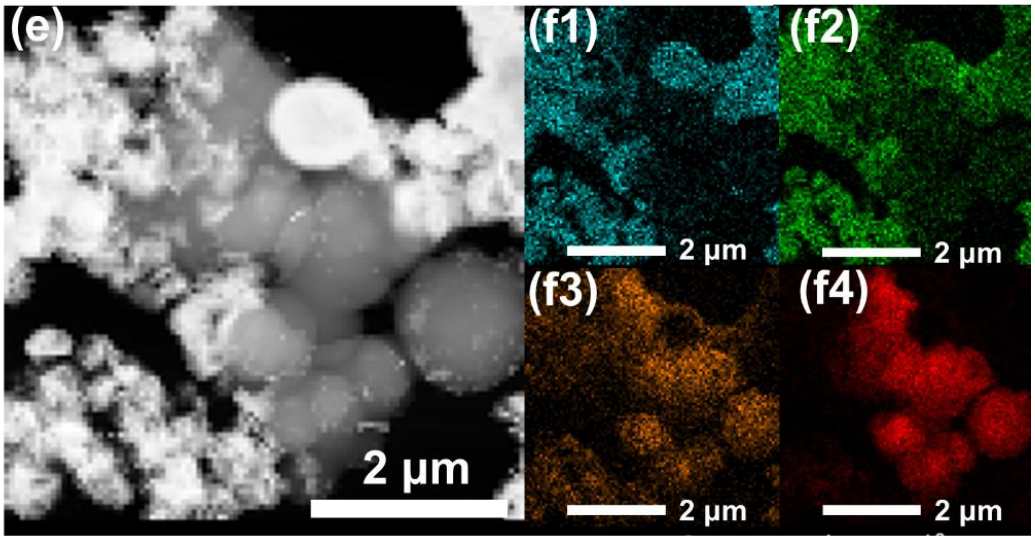

Figure 4-12 (e-f) EDS elemental mapping results of $C_{1.5}/WO_3/Bi_2WO_6$ in two different perspectives (f1: Bi, f2: W, f3: O, f4: C).

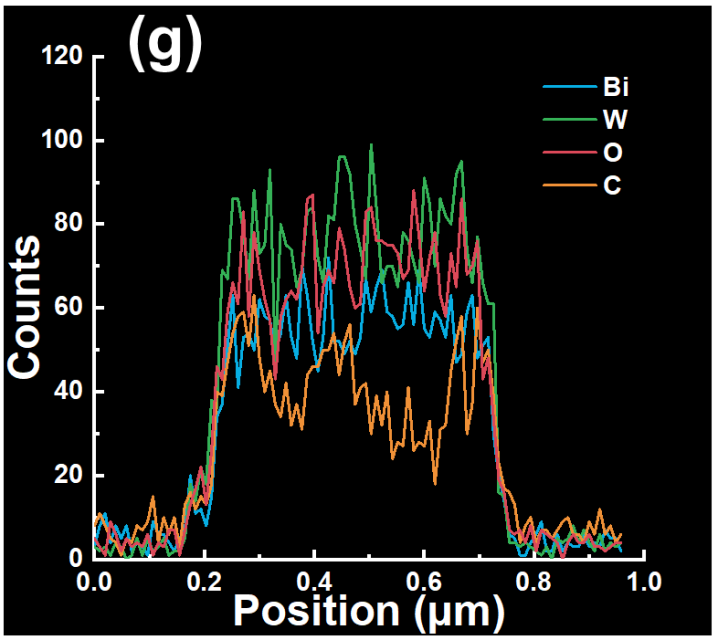

Figure 4-12 (g) EDS linear scanning results of $C_{0.75}/WO_3/Bi_2WO_6$.

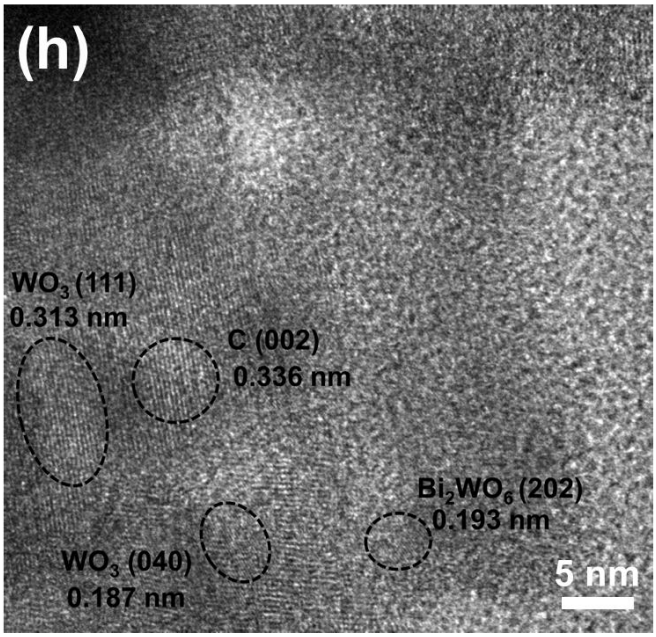

Figure 4-12 (h) High-resolution TEM images of $C_{0.75}/WO_3/Bi_2WO_6$.

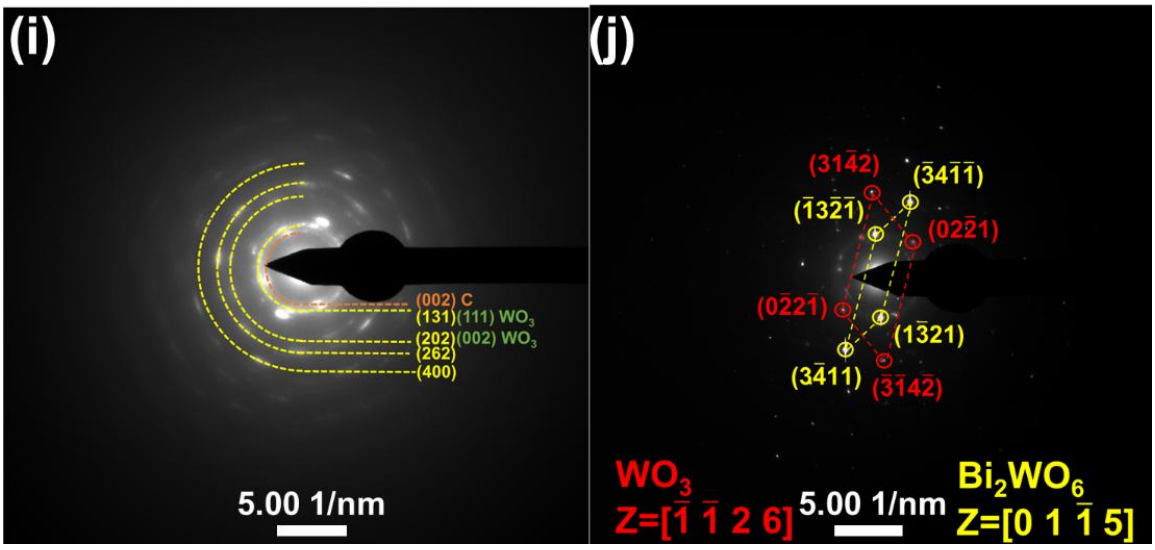

Figure 4-12 SAED analysis of (i) $C_{0.75}/WO_3/Bi_2WO_6$ and (j) WO_3/Bi_2WO_6.

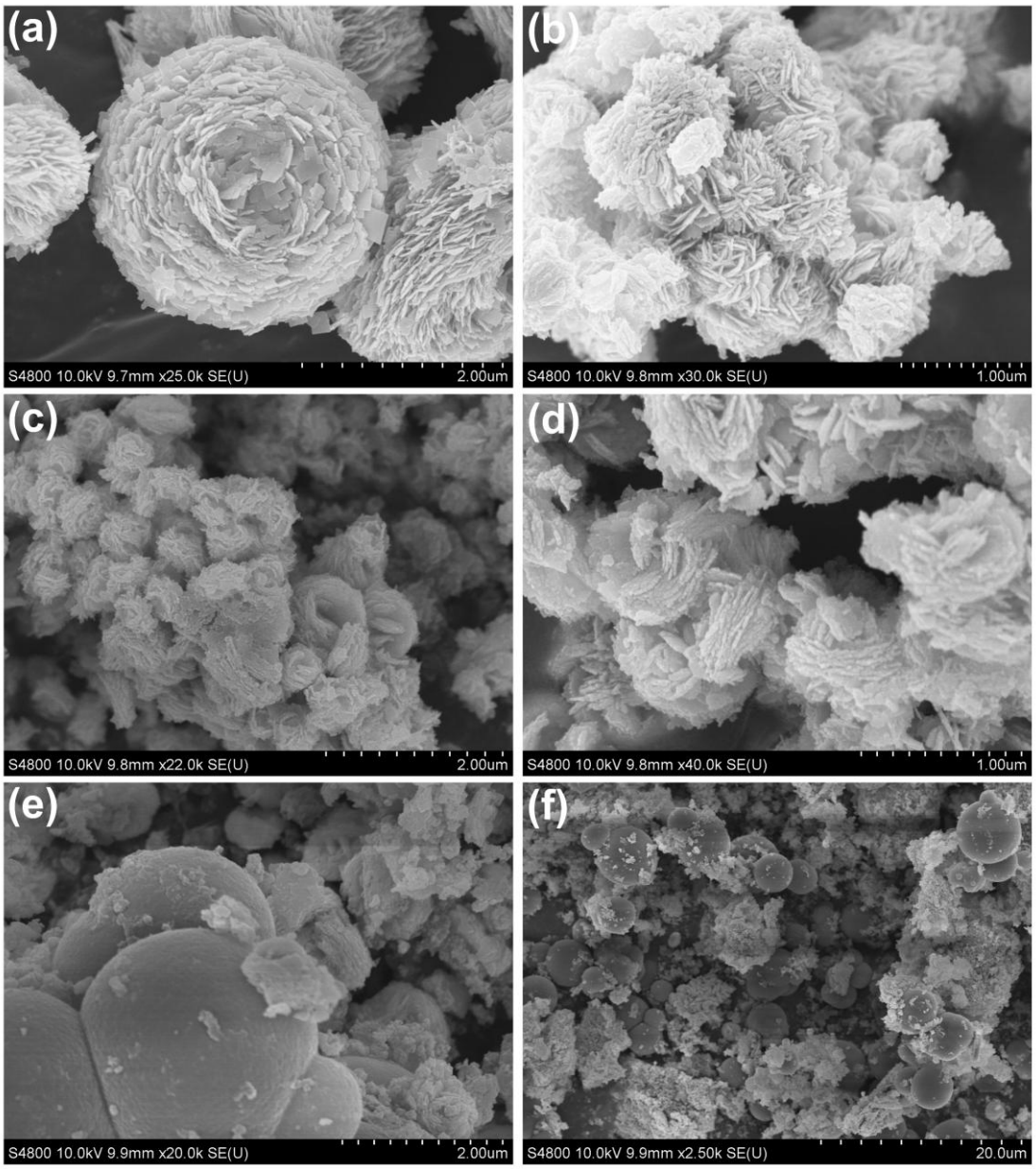

Figure 4-13 The FESEM images of (a) WO_3/Bi_2WO_6, (b) $C_{0.25}/WO_3/Bi_2WO_6$, (c) $C_{0.5}/WO_3/Bi_2WO_6$, (d) $C_1/WO_3/Bi_2WO_6$, (e) $C_{1.5}/WO_3/Bi_2WO_6$ and (f) $C_2/WO_3/Bi_2WO_6$.

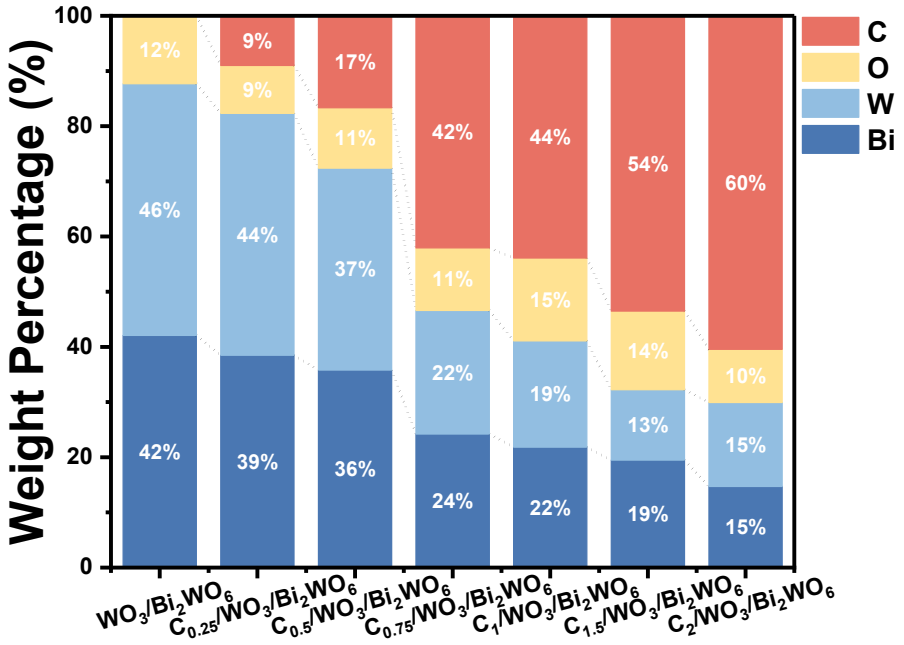

Figure 4-14 Atomic weight ratios of Bi, W, O, and C in samples through EDS spectra.

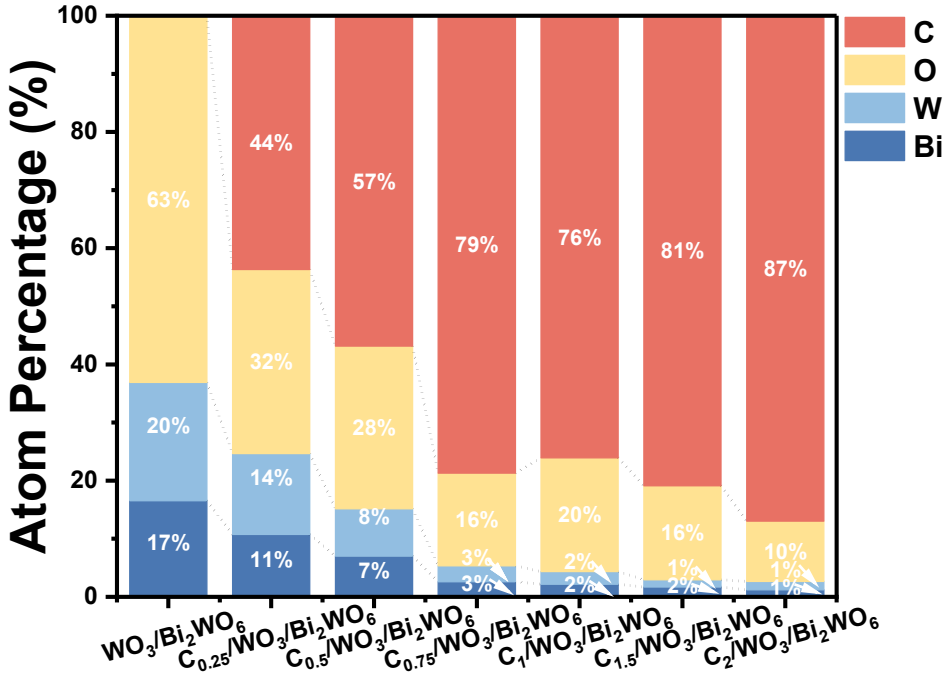

Figure 4-15 Atomic ratios of Bi, W, O, and C in samples through EDS spectra.

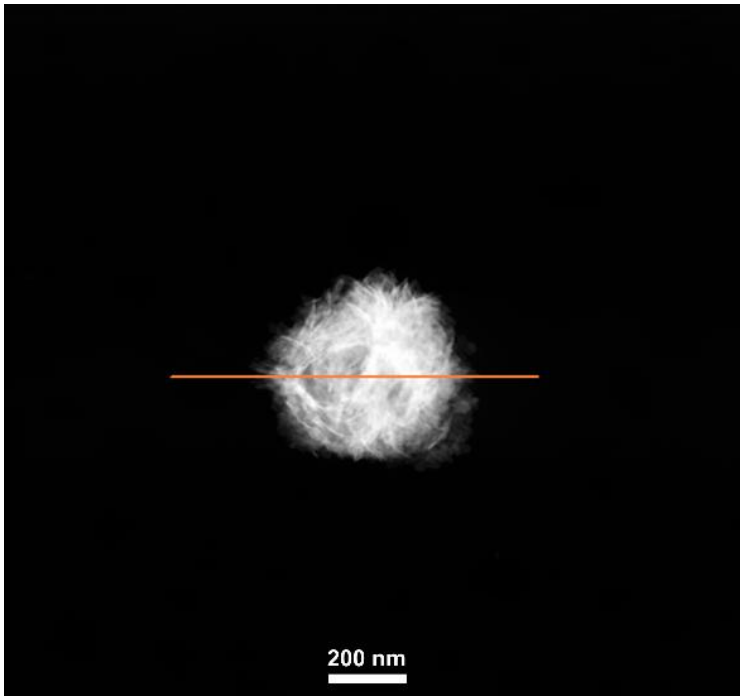

Figure 4-16 EDS linear scanning selected field of $C_{0.75}/WO_3/Bi_2WO_6$.

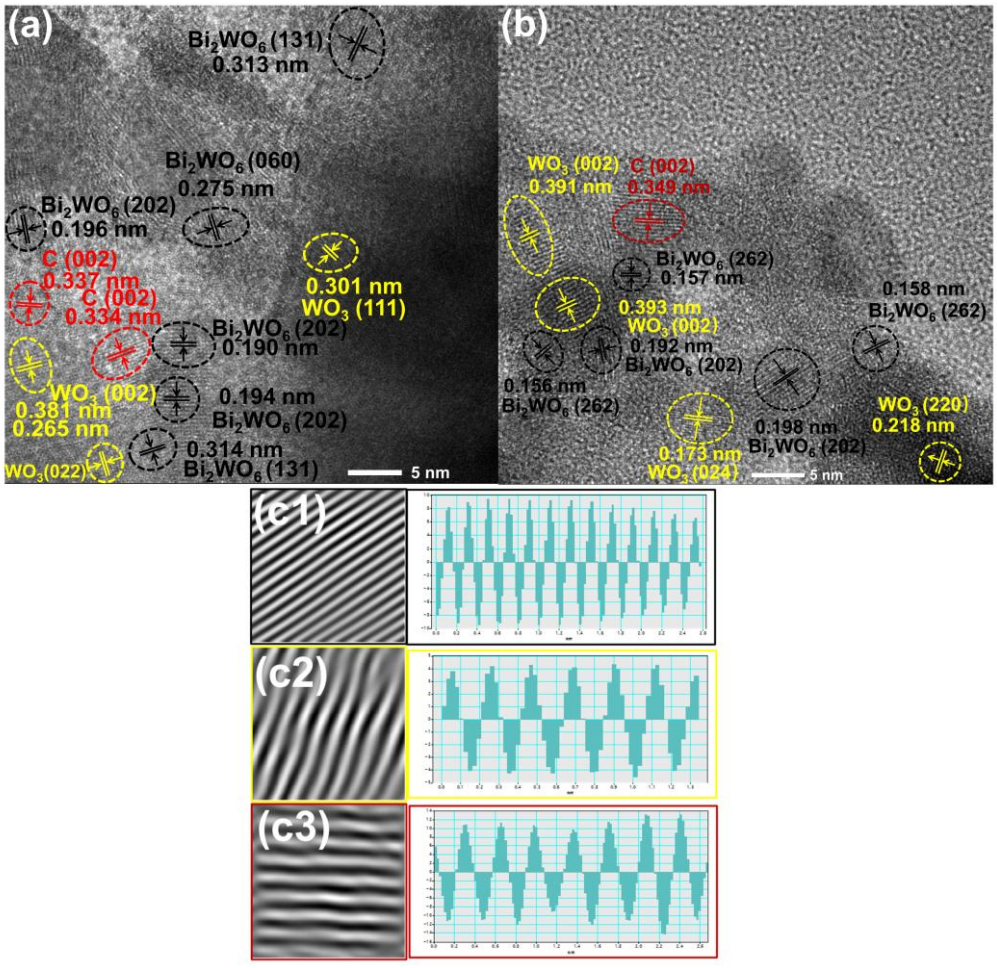

Figure 4-17 (a, b) High-resolution TEM images of $C_{0.75}/WO_3/Bi_2WO_6$, (c) the corresponding IFFT pattern and intensity profiles in Figure 4-17b.

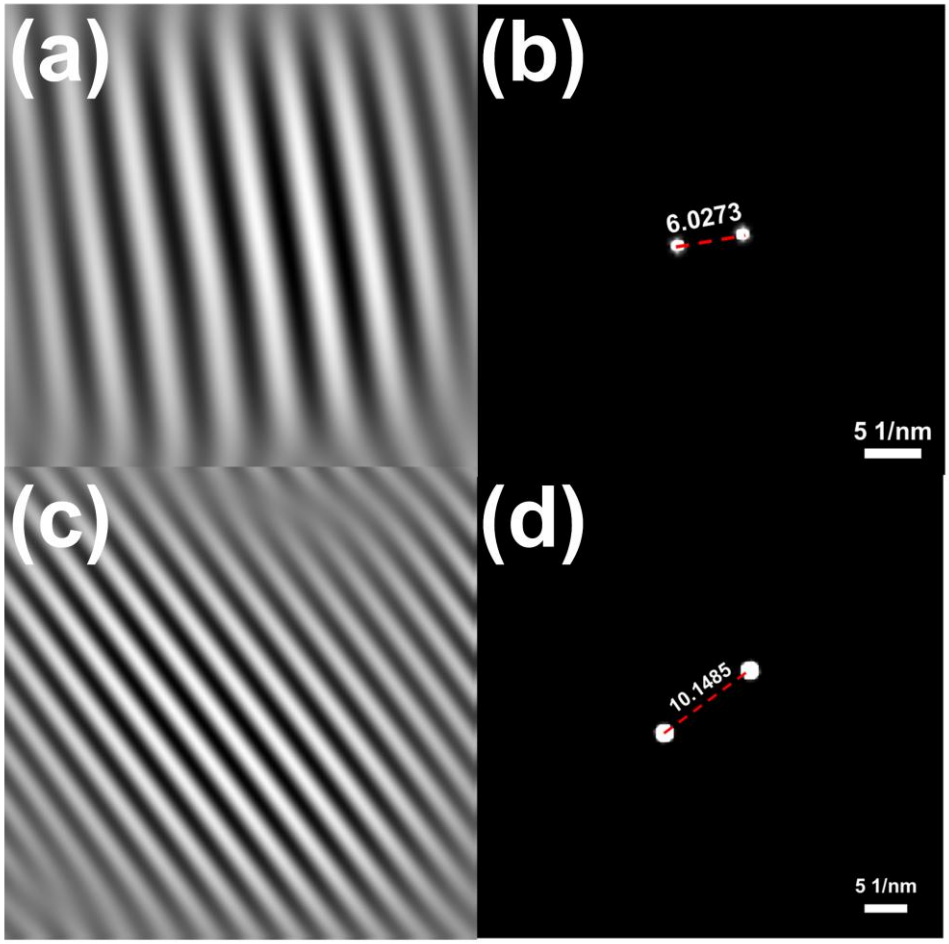

Figure 4-18 The corresponding (a, c) IFFT pattern and (b, d) post-optimized FFT images of Figure 4-12h; (a, b) correspond to the C (002) plane, and (c, d) correspond to the Bi_2WO_6 (202) plane.

X-ray photoelectron spectroscopy (XPS) analysis is employed to determine the surface elemental composition and chemical state of the synthesized samples. Low-resolution survey unveils the core-level peaks of Bi 5d, Bi 4f, Bi 4p, W 4d, W 4f, O 1s, and C 1s of all prepared samples (Figure 4-19a). The C 1s spectra of $C_{0.75}/WO_3/Bi_2WO_6$ can be deconvoluted into four peaks located at 288.44 eV, 286.82 eV, 285.47 eV, and 284.42 eV, which are assigned to O=C-O, C=O, C-O, and C-C, respectively (Figure 4-19b) [277, 278], verifying the fulfillment of C cladding. As depicted in Figure 4-19c, the O 1s spectra of $C_{0.75}/WO_3/Bi_2WO_6$ and WO_3/Bi_2WO_6 were deconvoluted into surface-chemisorbed oxygen (O_C), oxygen vacancies (O_V), and lattice oxygen (O_L). After C cladding, the binding energy of O_V and O_L increased, which can be attributed to the relatively small electronegativity difference between C and O compared to that

between Bi/W and O, leading to the formation of covalent bonds. Consequently, the peaks associated with O_V and O_L were shifted towards higher binding energies due to the bonding of O with both C, BI and W. Furthermore, the highest percentage of O_V (44.25%) and O_C (23.56%) of $C_{0.75}/WO_3/Bi_2WO_6$ was calculated (Figure 4-19f), which enhanced the sensing performance at a deep level, while it is mainly reflected in the regulation of the sensor baseline resistance and O_V distribution [279]. Meanwhile, the higher concentration of O_C increases the oxidation reaction rate and signal output, reduces the noise interference, and comprehensively improves the stability of the $C_{0.75}/WO_3/Bi_2WO_6$ sensor. In the case of W 4f spectra for the $C_{0.75}/WO_3/Bi_2WO_6$ sample (Figure 4-19d), it was deconvoluted into W 4f5/2 and W 4f7/2 centered at 37.5 eV and 35.3 eV, which are 0.2 eV higher than those of WO_3/Bi_2WO_6. Meanwhile, the Bi 4f spectra of $C_{0.75}/WO_3/Bi_2WO_6$ can be divided into Bi $4f_{5/2}$ and Bi $4f_{7/2}$ peaks, which are observed at 164.4 eV and 159.1 eV, while a 0.2 eV enhancement was discerned compared to the sample without C cladding (Figure 4-19e) [262]. The red shift of the W 4f and Bi 4f spectra demonstrated the low binding energy and high electron cloud density of $C_{0.75}/WO_3/Bi_2WO_6$, stimulating the adsorption and desorption rates of oxygen species and target gases.

To investigate the impact of C cladding on the formation of O_V, EPR measurements were conducted on all samples, as shown in Figure 4-19g. All samples displayed a symmetrical EPR signal at g=2.003. The highest signal intensity and intensity ratio (Figure 4-19h) of $C_{0.75}/WO_3/Bi_2WO_6$ illustrated that $C_{0.75}/WO_3/Bi_2WO_6$ possessed the highest concentration and the most evenly distributed O_V [280], which is in excellent agreement with the XPS results.

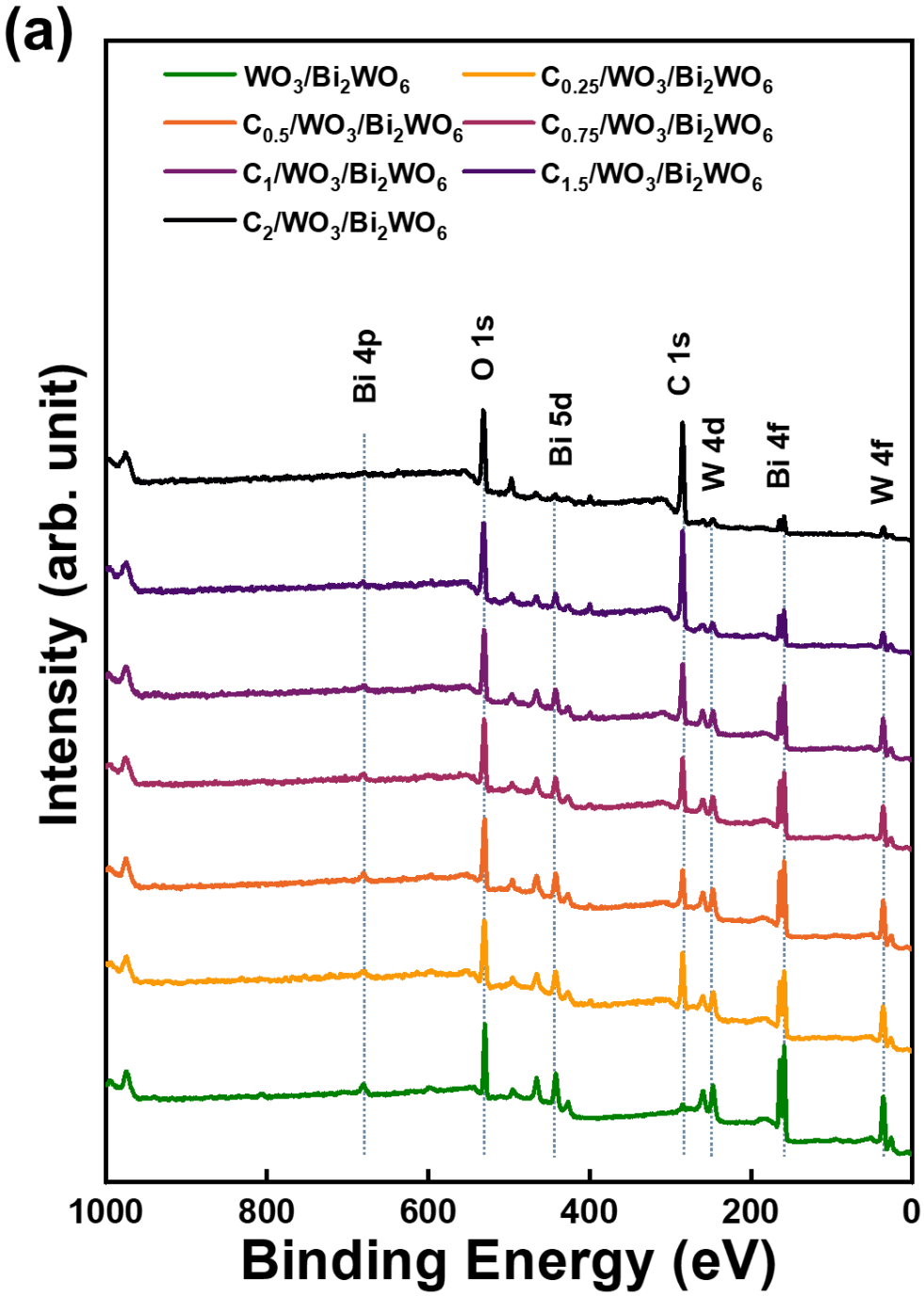

Figure 4-19 XPS spectra of the samples: (a) Low-resolution XPS spectrum.

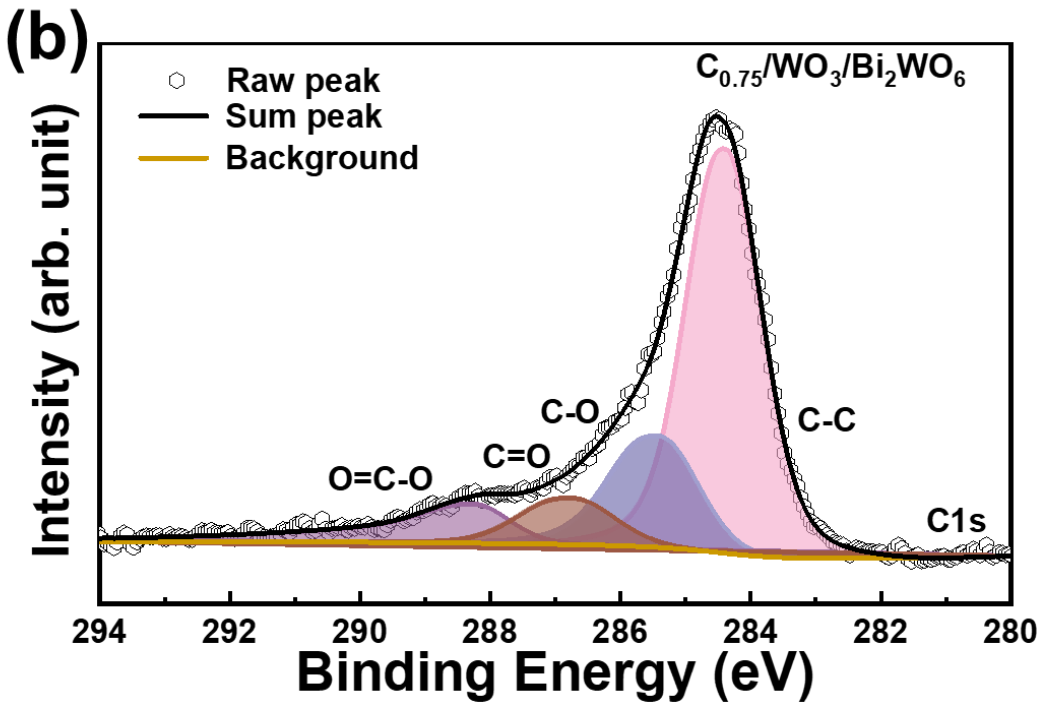

Figure 4-19 (b) High-resolution XPS spectrum for C 1s of $C_{0.75}/WO_3/Bi_2WO_6$.

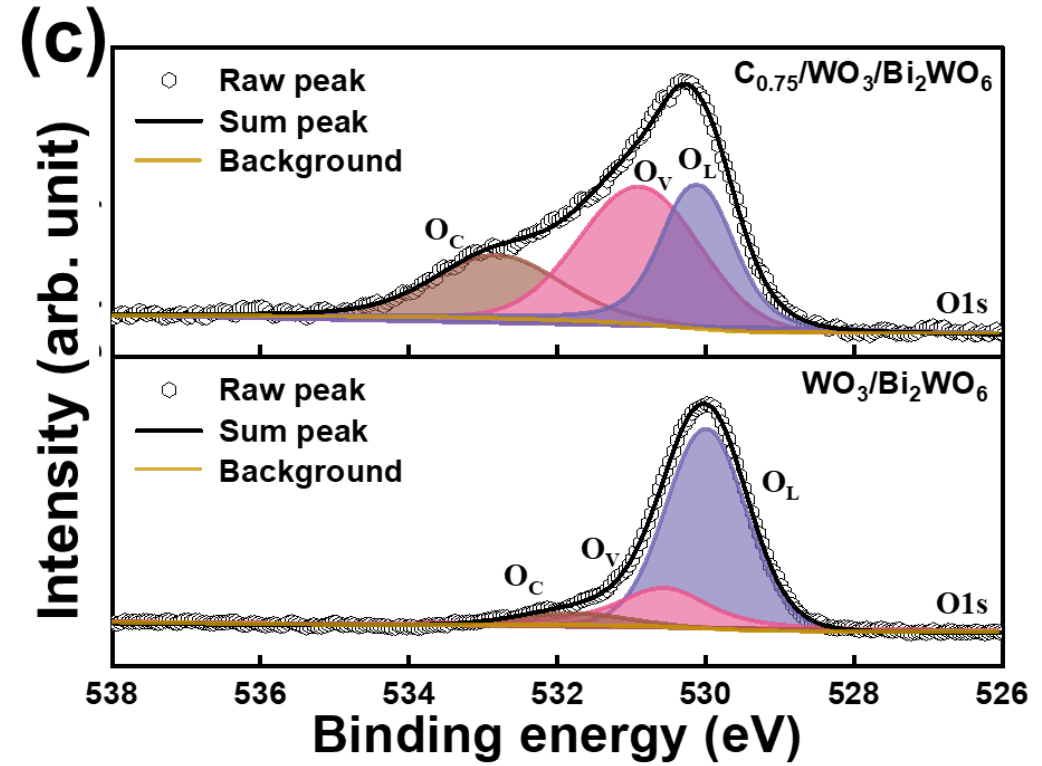

Figure 4-19 (c) High-resolution XPS spectrum for O 1s of $C_{0.75}/WO_3/Bi_2WO_6$ and pure WO_3/Bi_2WO_6.

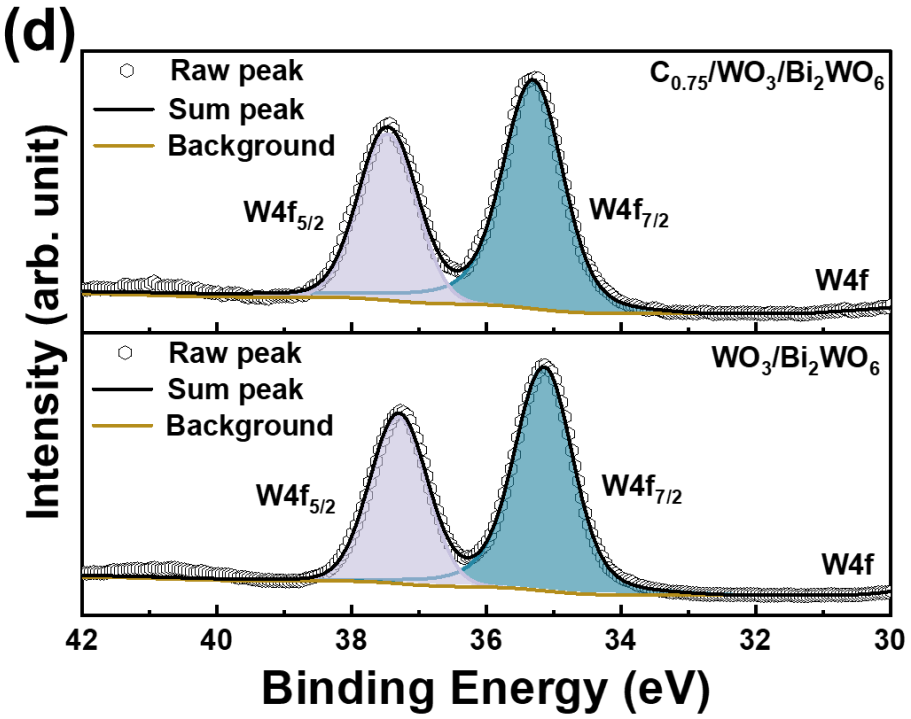

Figure 4-19 (d) High-resolution XPS spectrum for W 4f of $C_{0.75}/WO_3/Bi_2WO_6$ and pure WO_3/Bi_2WO_6.

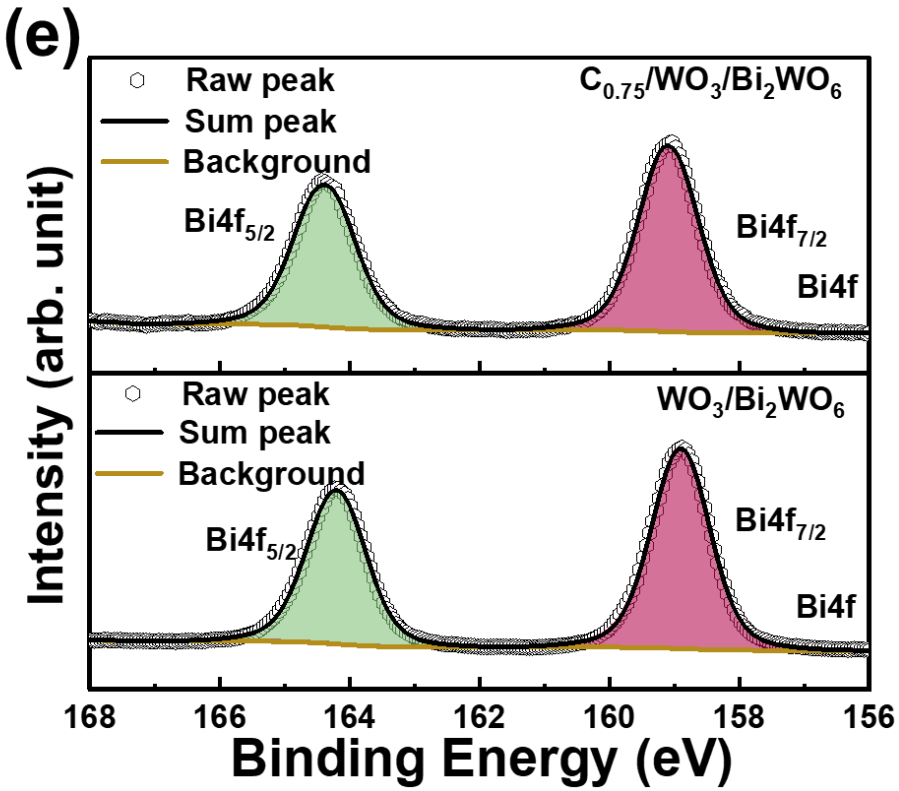

Figure 4-19 (e) High-resolution XPS spectrum for Bi 4f of $C_{0.75}/WO_3/Bi_2WO_6$ and pure WO_3/Bi_2WO_6.

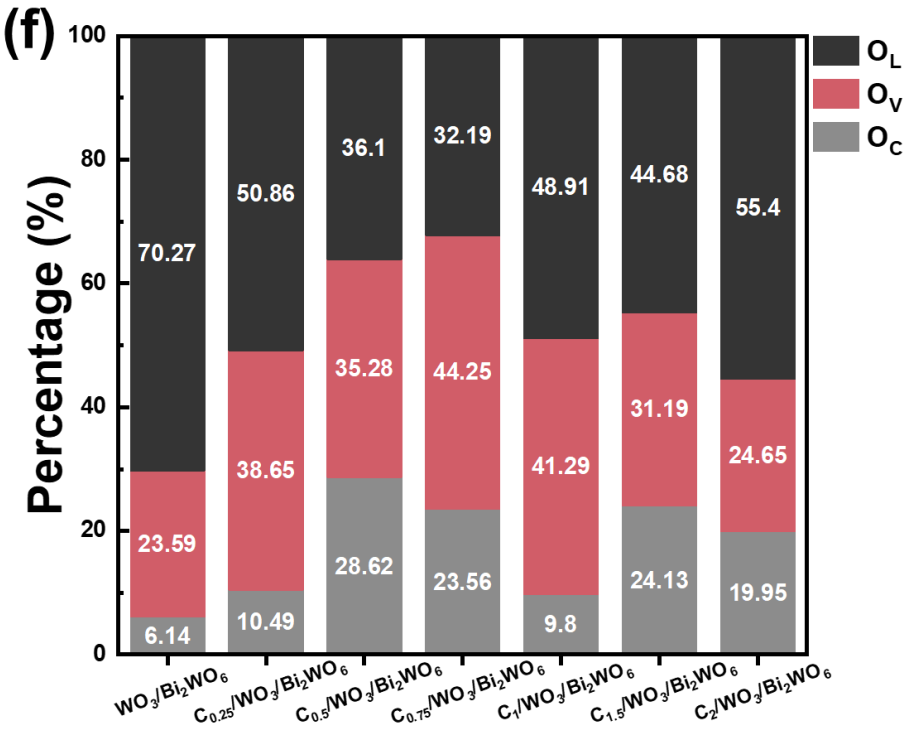

Figure 4-19 (f) Oxygen species proportion of all samples.

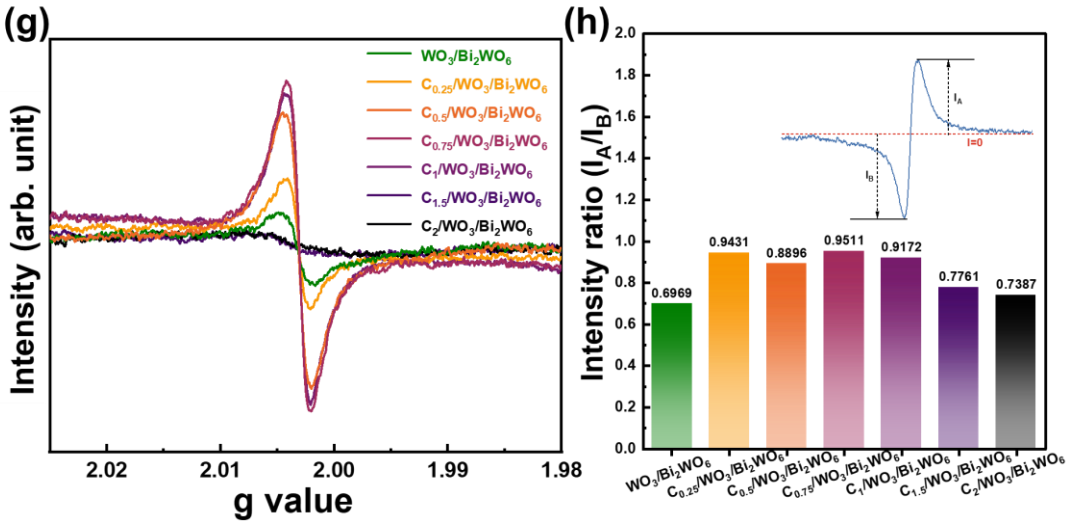

Figure 4-19 (g) EPR spectra of all samples, (h) Intensity ratio of symmetry parameters of defect signal. Inset: the ratio of symmetry coefficients is defined as I_A/I_B.

The UV-Vis absorption spectrum and bandgap value determined by the Tauc plot of all samples were shown in Figure 4-20a and Figure 4-20b, indicating a bandgap of ≈2.98 eV, 2.55 eV, 2.38 eV, 1.91 eV, 1.81 eV, 1.23 eV, and 1.13 eV of all samples (Figure 4-20c). This result illustrated that band gap narrowing was observed with increasing C

cladding content, making them advantageous for rapid carrier mobility and further enhancing sensitivity and exclusive detection at room temperature for gas sensors [281]. Carbon cladding reduces the bandgap for several reasons. Firstly, the carbon atoms introduce impurity energy levels into the material's band structure, typically located between the conduction band and valence band, serving as a transit station for electrons or holes, thereby reducing the bandgap. Secondly, the addition of carbon changes the material's symmetry, which in turn leads to changes in the band structure, including a decrease in the bandgap. Thirdly, the introduction of carbon atoms enhances electron-electron interactions in $C_x/WO_3/Bi_2WO_6$, especially in regions of high electron density, which may narrow the bandgap. We synchronously analyzed the BET surface areas and porosities of all as-prepared samples from N_2 adsorption-desorption isotherms recorded at 77 K (Figure 4-20d to Figure 4-20f). The isotherms of $C_{0.75}/WO_3/Bi_2WO_6$ and WO_3/Bi_2WO_6 were classified as type-IV, indicating the presence of abundant pores. $C_{0.75}/WO_3/Bi_2WO_6$ owned the highest specific surface area of 67.897 $m^2.g^{-1}$ while the counterpart of WO_3/Bi_2WO_6 is just 31.980 $m^2.g^{-1}$. However, excessive use of D-(+)-Glucose anhydrous may degrade the sample microstructure (Figure 4-13), thereby decreasing the specific surface area, as listed in Table 4-2. The mesoporous feature of $C_{0.75}/WO_3/Bi_2WO_6$ was evident, and the relatively large average pore diameter (3.713 nm) further enhanced gas-molecule transport. Importantly, $C_{0.75}/WO_3/Bi_2WO_6$ exhibited a more evenly mesopore (2-50 nm) distribution as shown in Figure 4-20e. All these superior characteristics synergistically and effectively reduced the reaction energy barrier for gas molecules, while promoting the interaction between target gas molecules and the active sites on $C_{0.75}/WO_3/Bi_2WO_6$.

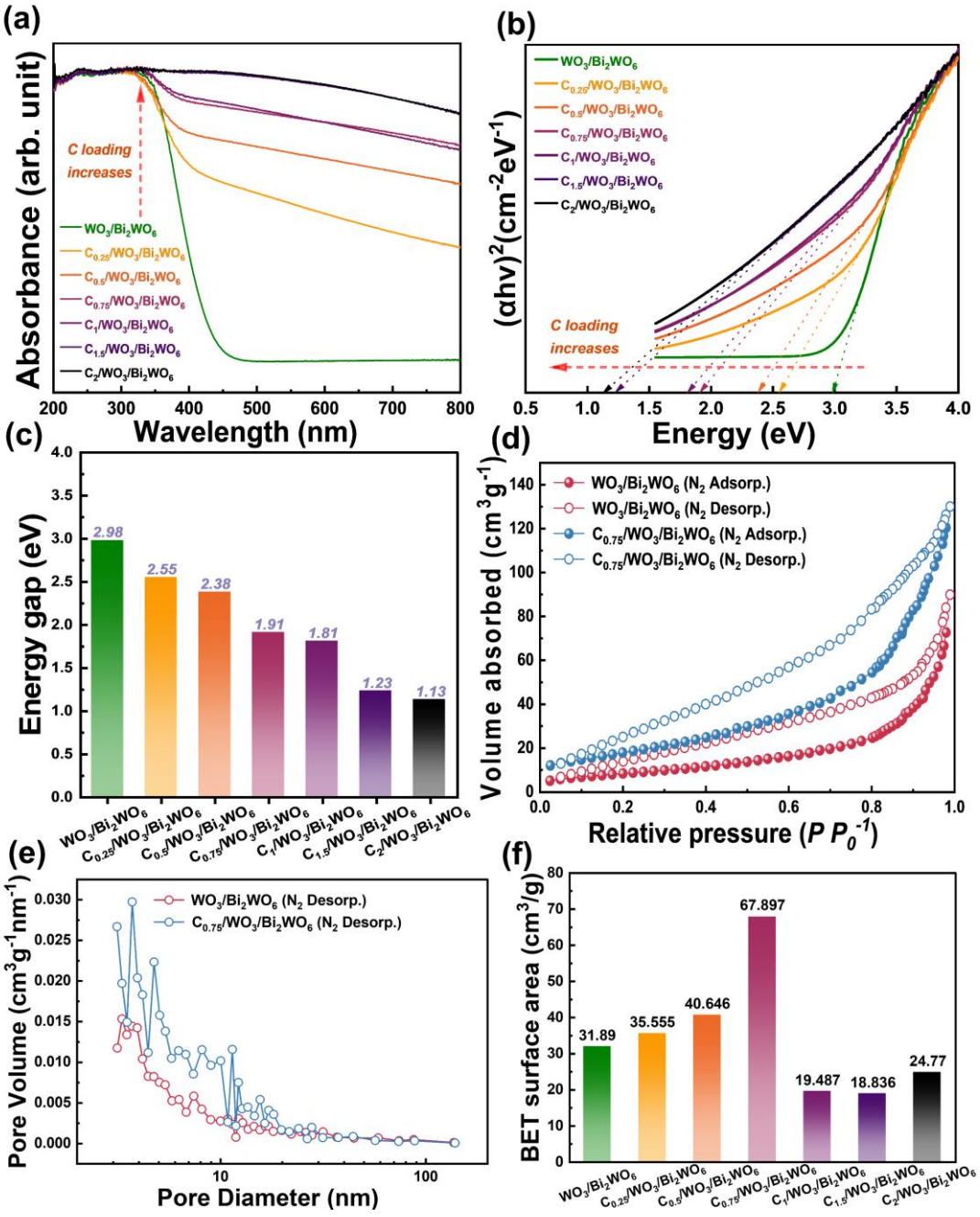

Figure 4-20 (a) UV-Vis absorption spectra, (b) Tauc plots and (c) band gap value of all samples, (d) Nitrogen adsorption-desorption isotherms, (e) Barrett-Joyner-Halenda pore-size distributions of $C_{0.75}/WO_3/Bi_2WO_6$ and pure WO_3/Bi_2WO_6 through fitting the desorption branch of isotherms and (f) the specific surface area value of all samples.

Table 4-2 BET results of as-synthesized samples.

Samples	S_{BET} ($m^2 \cdot g^{-1}$)	Average pore diameter (nm)	Total pore volume ($cm^3 \cdot g^{-1}$)
WO_3/Bi_2WO_6	31.980	3.312	0.130
$C_{0.25}/WO_3/Bi_2WO_6$	35.555	3.133	0.216
$C_{0.5}/WO_3/Bi_2WO_6$	40.646	3.937	0.184
$C_{0.75}/WO_3/Bi_2WO_6$	67.897	3.713	0.186
$C_1/WO_3/Bi_2WO_6$	19.487	3.505	0.090
$C_{1.5}/WO_3/Bi_2WO_6$	18.836	2.973	0.119
$C_2/WO_3/Bi_2WO_6$	24.770	3.139	0.197

4.2.2 Gas sensing properties

Due to the high photon energy of visible light, which produces more electron-hole pairs, degrading the sensing process [267]. The UV light (365 nm) was selected as the excitation source to facilitate charge modulation and to weaken excitonic effects [282]. We obtained the variation curves of the $C_{0.75}/WO_3/Bi_2WO_6$ gas sensor towards benzaldehyde (40 to 4 ppm) under UV light irradiation at an intensity of 1.0 mW/cm2 and in the dark (Figure 4-22). Compared with the two situations, $C_{0.75}/WO_3/Bi_2WO_6$ exhibited improved sensing performance while the response value was increased by more than 2 times, which was attributed to the increased generation of photocarriers facilitated by UV excitation in the $C_{0.75}/WO_3/Bi_2WO_6$ twisted micro-flowers, which in turn strengthen the density of electrons and active sites on the surface, allowing them to participate in the sensing reaction [283]. Furthermore, to assess the impact of photo-assisted activation on the gas-detection process, a comparative analysis of I-V characteristics for the $C_{0.75}/WO_3/Bi_2WO_6$ sensor was conducted under dark and UV-light conditions (Figure 4-23). The I-V curves of the samples were measured in a standard three-electrode electrochemical workstation. The three-electrode system consists of Pt film, FTO conductive glass (coated with 1 cm^2 of sensing films), and Ag/AgCl electrode. All experiments were measured in 0.5 M Na_2SO_4 solution. The

power of UV irradiated at the surface of the sensor is 10 mW/cm^2. Compared to the dark condition (e.g., 0.010 mA at 4 V), the current at 4 V increased to 0.034 mA under UV light irradiation, allowing the $C_{0.75}/WO_3/Bi_2WO_6$ sensor resistance to be measured easily. The triple augment observed upon UV light exposure clearly indicates the photo-induced generation of charge carriers within the $C_{0.75}/WO_3/Bi_2WO_6$ sensor [284]. Therefore, the following gas-sensing experiments were carried out under UV light excitation. The dynamic transient response curves of as-prepared samples toward 125-25 ppm benzaldehyde were obtained, while $C_{0.75}/WO_3/Bi_2WO_6$ exhibited the highest sensitivity (160.5@125 ppm) (Figure 4-21a). Furthermore, the $C_{0.75}/WO_3/Bi_2WO_6$ and $C_1/WO_3/Bi_2WO_6$ still exhibited the high response of 7.2 and 6.1 at a low benzaldehyde concentration of 25 ppm (Figure 4-21b). The response of the gas sensor first increased and then decreased with the increase in carbon cladding content, while the corresponding reference resistance consistently declined (Figure 4-21c), indicating that the formation of a narrowed bandgap and the reduction of impurity scattering. Also, based on Figure 4-21d, all the sensors exhibited outstanding linearity over a wide detection range. The profoundly reproducible sensing feature under repetitive thirty cycles of $C_{0.75}/WO_3/Bi_2WO_6$ sensor was obtained (Figure 4-21e), while the sensor platform also displayed excellently robust environmental long-term stability for 15 days (Figure 4-21f). The discriminative detection and analysis of benzaldehyde were meticulously presented in Figures 4-21g and 4-24. Firstly, the dynamic response curves of the $C_{0.75}/WO_3/Bi_2WO_6$ sensor to 8 diverse VOCs (25-125 ppm) were acquired, with the highest sensitivity to benzaldehyde discernible (Figure 4-21g). The specific response value and response time of the $C_{0.75}/WO_3/Bi_2WO_6$ sensor platform for discriminative detection were depicted on a radar map (Figures 4-24a and 4-24b). The Eley-Rideal model is used to investigate the kinetic properties involved in benzaldehyde and interfering-gas sensing, and the derived parameters can subsequently be employed to differentiate VOCs using principal component analysis (PCA) patterns [285]. We could obtain the sensitivity (η), kinetic reaction rate constant (k_r), β value, and activation energy (Ea) from Figures 4-24c to 4-24f and Tables 4-3 to 4-6.

Firstly, the sensitivity (η) of the $C_{0.75}/WO_3/Bi_2WO_6$ sensor was evaluated by the power law equation, which is shown in Equation (4-2) [286]:

$$\ln S = \eta \ln c + \ln A \quad (4\text{-}2)$$

where S refers to the response value, A represents a constant, and c is the concentration

of VOC vapor, in which the corresponding information can be obtained from Table 4-3. Thus, the plot of ln(response) versus ln(concentration) is shown in Figure 4-24c, while the η for diverse VOCs is shown in Table 4-6. Secondly, by combining the Eley-Rideal mechanism and conductance changing, which depends on VOCs interaction and adsorption/desorption course, the response time for different VOCs can be elaborated as Equation (4-3) [287-289]:

$$\tau_{res}=(\kappa_r c+\kappa_{-r})^{-1} \quad (4\text{-}3)$$

where τ_{res} is the response time for benzaldehyde adsorption at room temperature (Table 4-4), and κ_r and κ_{-r} refer to the kinetic reaction rate constant for the VOCs. Therefore, the κ_r values for diverse VOCs are shown in Figure 4-24e and listed in Table 4-6. Thirdly, based on the previous research [290], the relation between the τ_{res} with VOCs vapor concentration is illustrated in Equation (4-4):

$$\ln \tau_{res}=-\beta \ln c + \ln \gamma \quad (4\text{-}4)$$

where β and γ are constants. The β values for diverse VOCs are shown in Figure 4-24f and Table 4-6. At last, owning the response time is oriented by the VOCs sensing kinetics and operating temperature, the corresponding relation can be expressed as follows for fixing the concentration of VOCs at 25 ppm, [288, 290]:

$$\tau_{res}=\psi^{-1}\exp[\frac{E_a}{2kT}] \quad (4\text{-}5)$$

where ψ refers to the vibrational frequency of the interacting VOCs molecule, E_a represents the activation energy, k refers to the Boltzmann's constant (1.380649×10^{-23} J/K), and T is the operating temperature in Kelvin (298.15 K~398.15 K). The above equation can be rewritten as:

$$\ln \tau_{res}=\frac{E_a}{2kT} - ln\psi \quad (4\text{-}6)$$

Therefore, the plot for lnτres versus 1/(2kT) combined with Table 4-5 is shown in Figure 4-24d, and the slope represents the Ea values, which are displayed in Table 4-6.

As an extensively used statistical method, PCA can transform a collection of potentially interrelated variables into a set of linearly uncorrelated variables through an orthogonal transformation [291]. The kinetic parameters to diverse VOCs were set as input data. The resulting score plot displayed a beneficial separation and distinction of benzaldehyde point among 8 analytes, further confirming the excellent exclusive sensing performance of $C_{0.75}/WO_3/Bi_2WO_6$ sensor (Figure 4-21h).

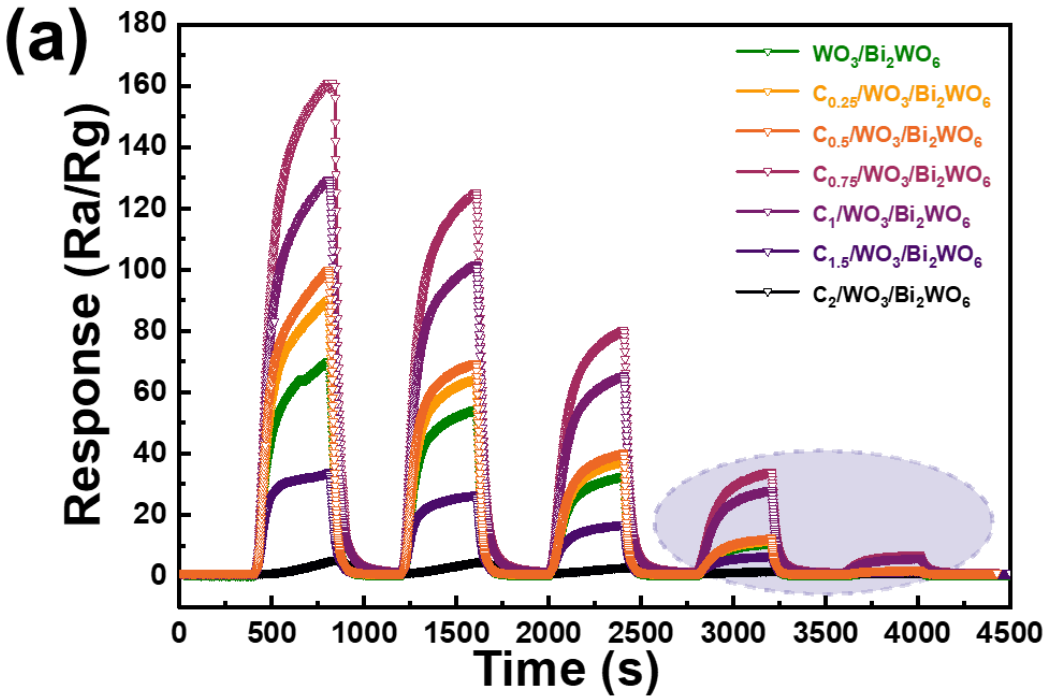

Figure 4-21 (a) Transient response of $C_x/WO_3/Bi_2WO_6$ film to benzaldehyde concentrations of 25-125 ppm.

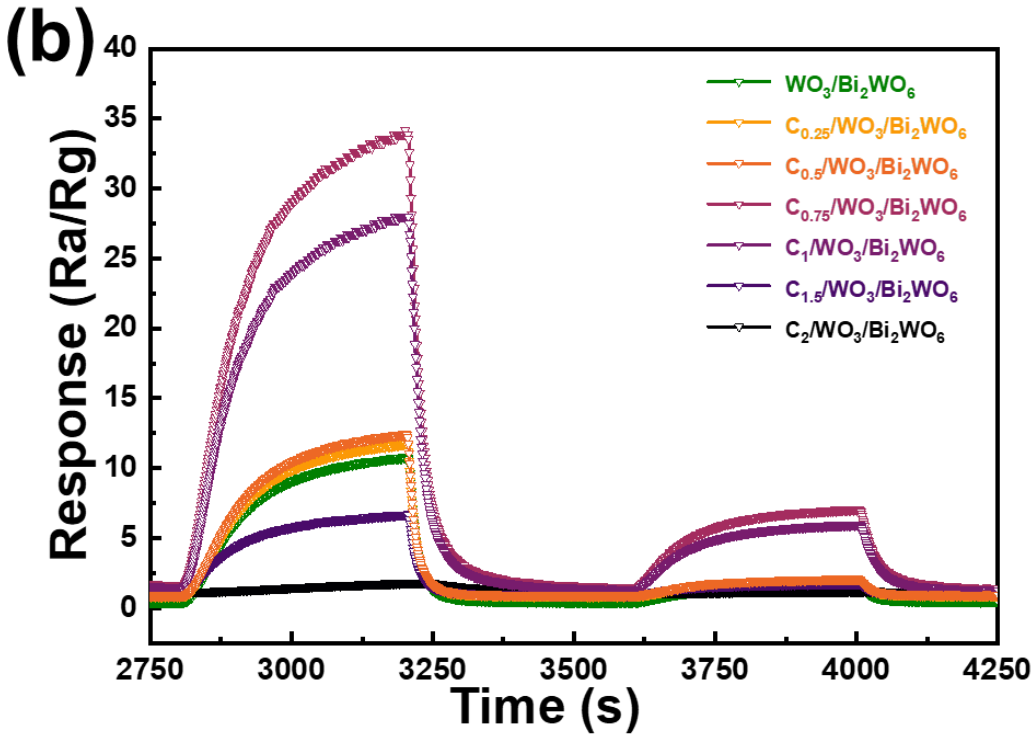

Figure 4-21 (b) Magnified area of Figure 4-21a

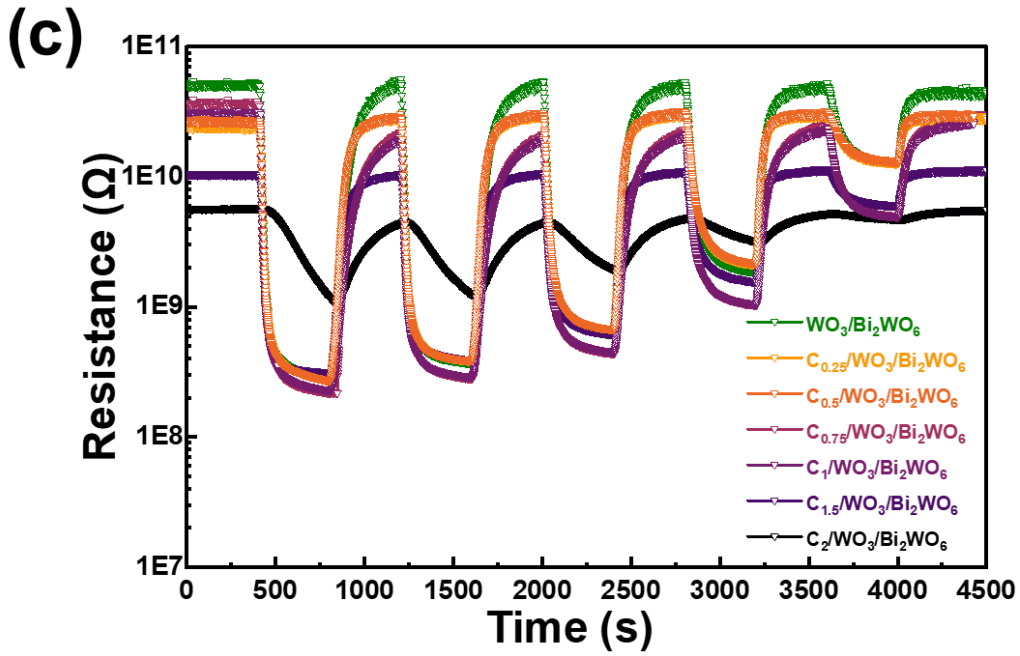

Figure 4-21 (c) Resistive response of $C_x/WO_3/Bi_2WO_6$ gas sensors toward exposure to 25-125 ppm of benzaldehyde.

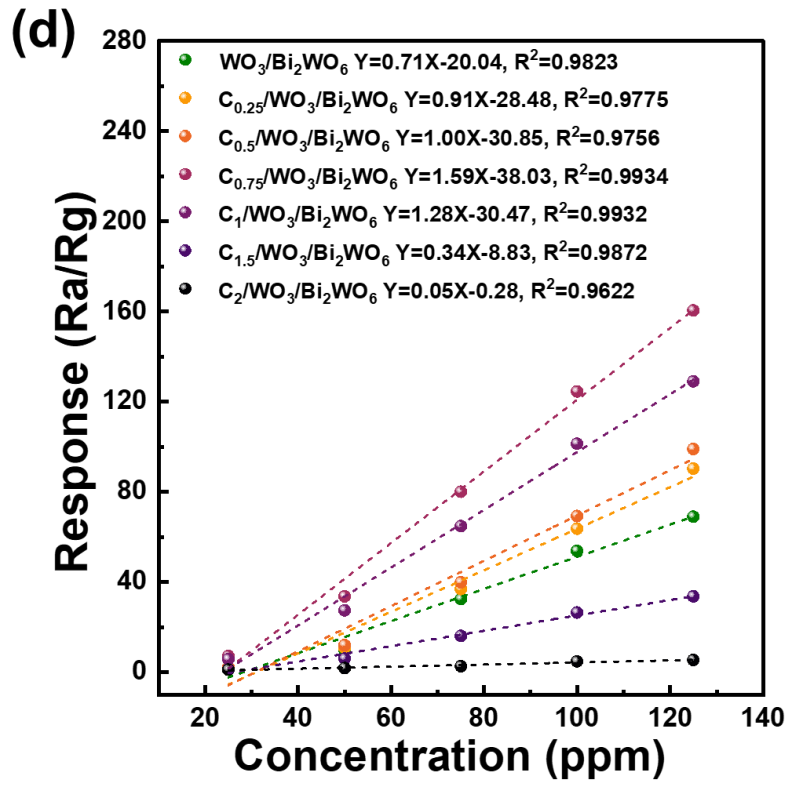

Figure 4-21 (d) Concentration-dependent response curves of the $C_x/WO_3/Bi_2WO_6$-based sensor for benzaldehyde.

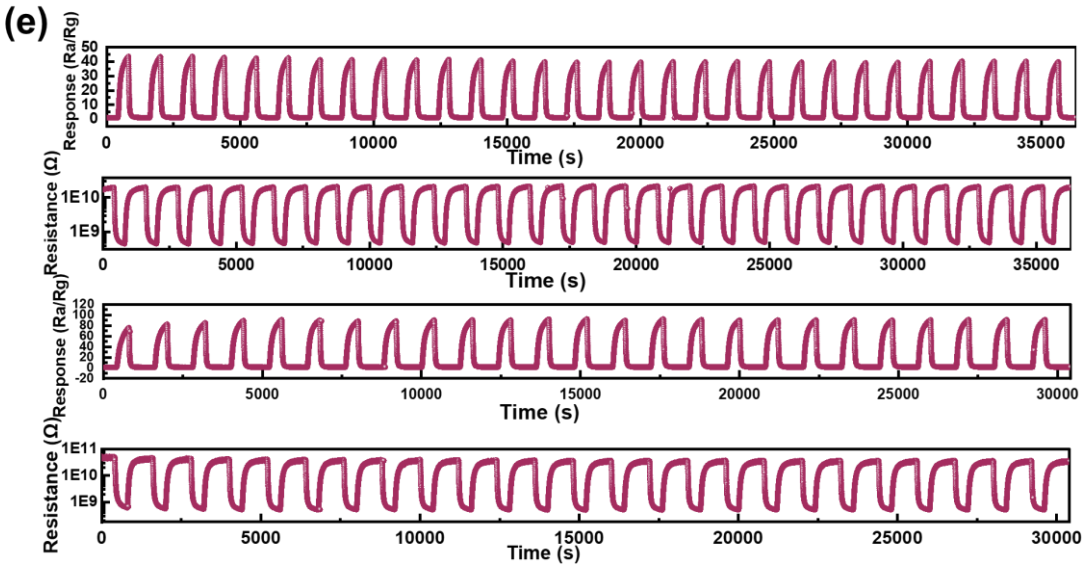

Figure 4-21 (e) Repeatability of the $C_{0.75}/WO_3/Bi_2WO_6$ sensor under 50 and 80 ppm benzaldehyde.

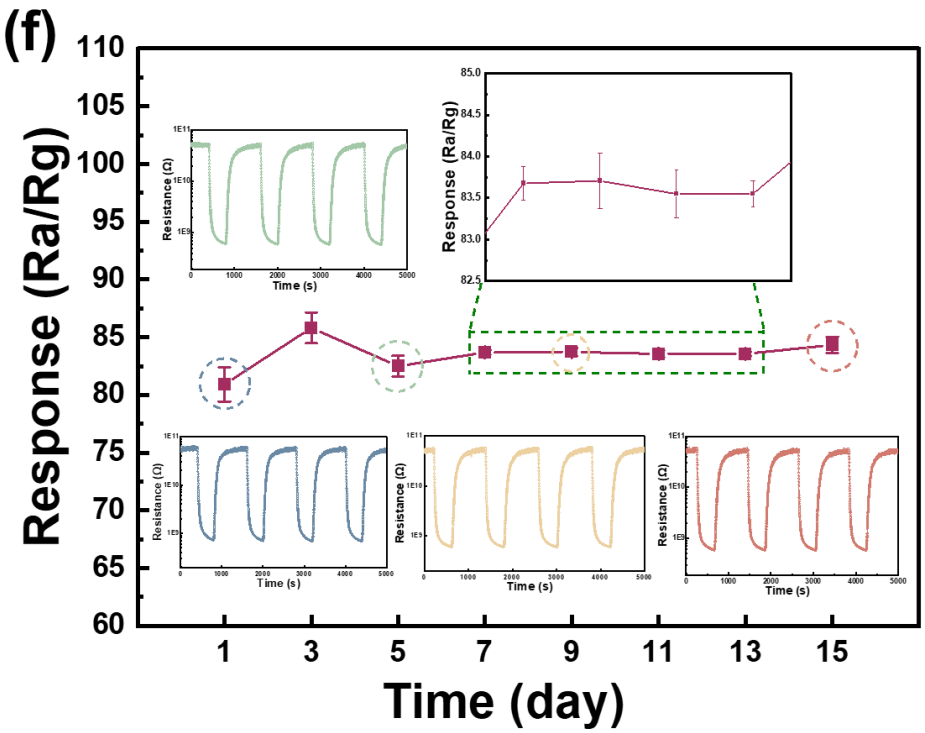

Figure 4-21 (f) Long-term stability of the $C_{0.75}/WO_3/Bi_2WO_6$ gas sensor to 75 ppm benzaldehyd

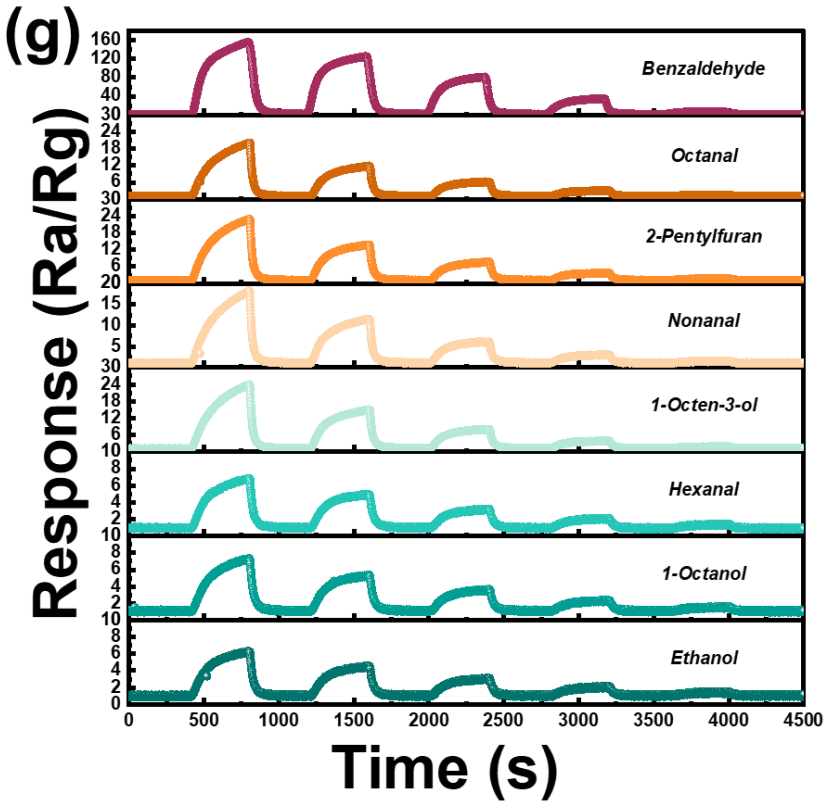

Figure 4-21 (g) The dynamic response curves of $C_{0.75}/WO_3/Bi_2WO_6$ sensor to 8 diverse VOCs (25-125 ppm).

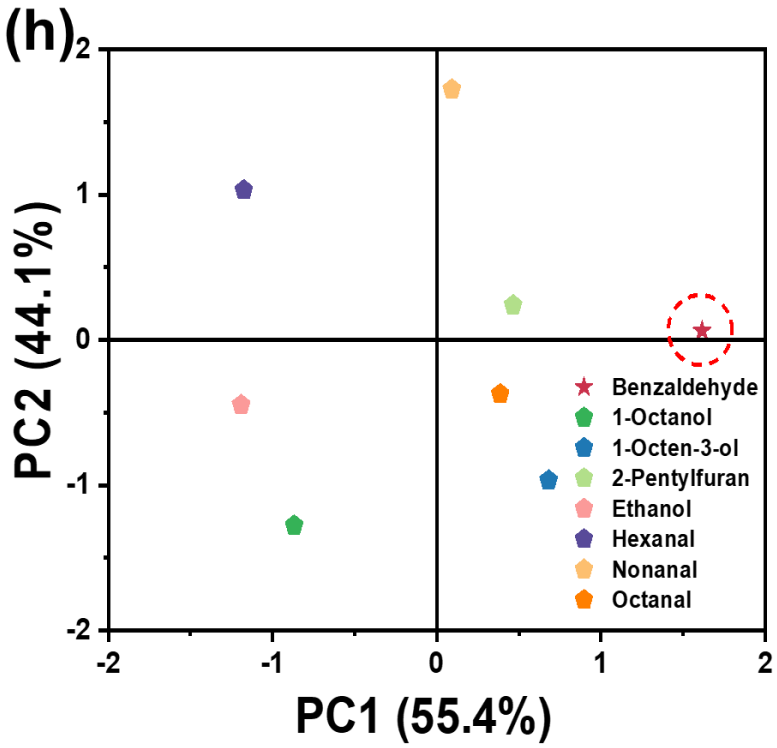

Figure 4-21 (h) Pattern recognition by the PCA method to analyze the selectivity of the $C_{0.75}/WO_3/Bi_2WO_6$-based sensor.

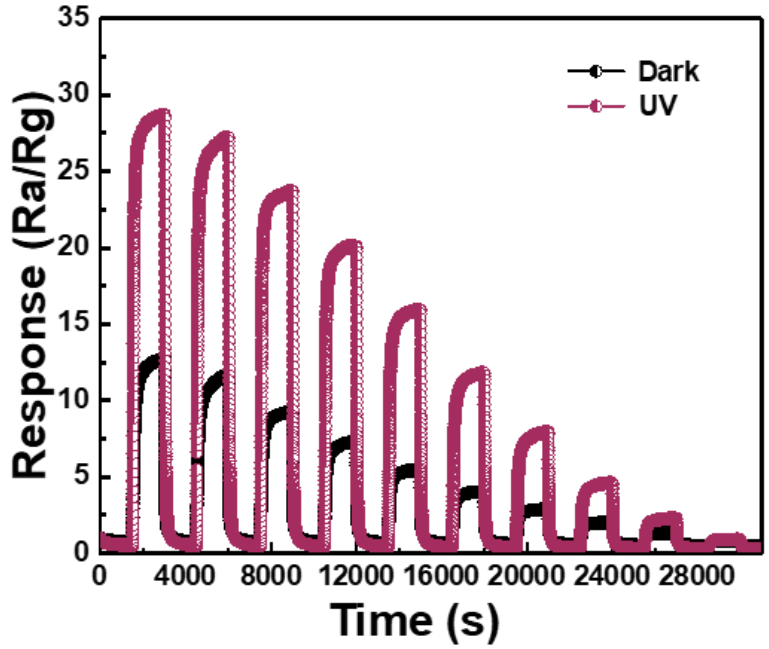

Figure 4-22 Responses variation versus benzaldehyde concentrations (40 ppm to 4 ppm) of $C_{0.75}/WO_3/Bi_2WO_6$-based sensor under UV light irradiation and dark conditions.

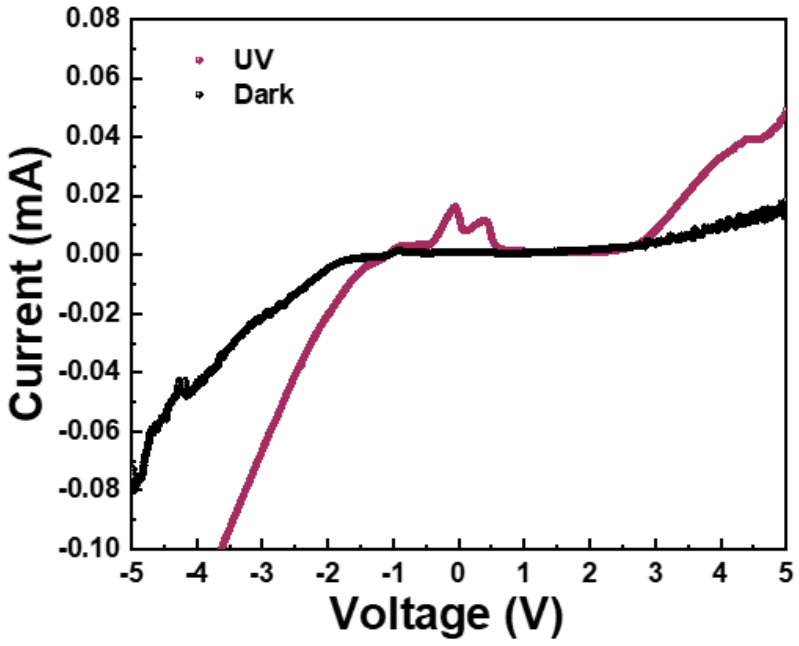

Figure 4-23 IV curve of $C_{0.75}/WO_3/Bi_2WO_6$ under 365 nm UV and in dark condition.

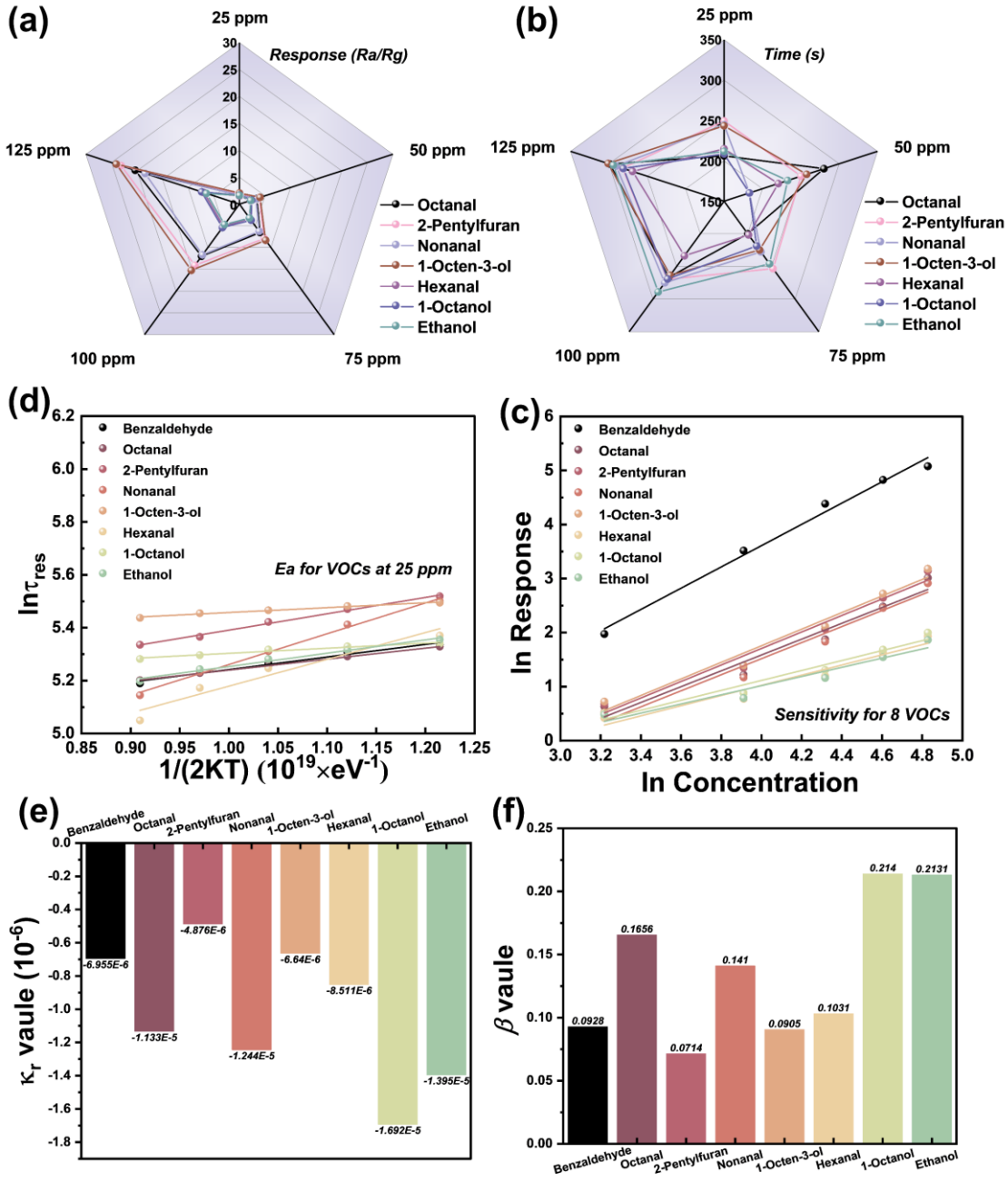

Figure 4-24 (a) response value and (b) response time of $C_{0.75}/WO_3/Bi_2WO_6$ film to various gases concentrations of 25-125 ppm and (c) sensitivity of the $C_{0.75}/WO_3/Bi_2WO_6$ sensor for the tested gases at room temperature (25 ± 2°C), (d) $1/\tau_{res}$ verse concentration plot to obtain the kinetic rate constant for tested gases, (e) kinetic reaction rate constant for tested gases, (f) activation energy (E_a) values for tested gases.

Table 4-3 The response value and the corresponding VOCs concentration of $C_{0.75}/WO_3/Bi_2WO_6$ sensor at room temperature.

VOCs	25 ppm	50 ppm	75 ppm	100 ppm	125 ppm
Benzaldehyde	7.2	33.7	80.1	124.57	160.5
Octanal	1.88	3.38	6.52	11.96	20.36
2-Pentylfuran	1.97	3.85	7.88	14.07	23.12
Nonanal	1.69	3.22	6.25	11.66	18.42
1-Octen-3-ol	2.06	4.03	8.30	15.20	24.06
Hexanal	1.52	2.17	3.31	5.08	6.91
1-Octanol	1.67	2.41	3.70	5.39	7.38
Ethanol	1.62	2.20	3.19	4.69	6.44

Table 4-4 The response time for the VOCs detection (25-125 ppm) of $C_{0.75}/WO_3/Bi_2WO_6$ sensor at room temperature.

VOCs	response time (s)				
	25 ppm	50 ppm	75 ppm	100 ppm	125 ppm
Benzaldehyde	207.6	225.8	219.9	218.3	258.3
Octanal	206.1	280.1	199.9	266.7	298.9
2-Pentylfuran	249.4	250.4	253.3	269.6	282.3
Nonanal	244.8	183.1	227.6	274.9	290.5
1-Octen-3-ol	243.4	257.6	224.6	263.4	301.1
Hexanal	214.9	200.6	201.7	233.5	269.2
1-Octanol	208.5	182.9	218.6	269.1	281.2
Ethanol	211.7	232.8	245.9	289.0	294.3

Table 4-5 The response time for the VOCs detection (25 ppm) of $C_{0.75}/WO_3/Bi_2WO_6$ sensor at different operating temperature.

VOCs	response time (s)				
	25ºC	50ºC	75ºC	100ºC	125ºC
Benzaldehyde	207.6	201.7	193.6	187.3	179.4
Octanal	206.1	198.6	191.5	186.5	181.6
2-Pentylfuran	249.4	237.6	226.3	213.9	207.6
Nonanal	244.8	224.1	202.6	187.4	171.5
1-Octen-3-ol	243.4	240.3	236.5	233.9	229.8
Hexanal	214.9	203.6	189.9	176.3	155.9
1-Octanol	208.5	206.3	203.9	199.6	196.7
Ethanol	211.7	203.7	196.7	189.3	180.9

Table 4-6 Characteristic Kinetic Parameter Values for VOCs.

VOCs	Sensitivity (η)[a]	κ_r value[a]	β value[a]	E_a (eV)[b]
Benzaldehyde	1.96729	$-6.955*10^{-6}$	0.0928	0.47599
Octanal	1.46515	$-1.133*10^{-5}$	0.1656	0.41546
2-Pentylfuran	1.52711	$-4.876*10^{-6}$	0.0714	0.61881
Nonanal	1.48539	$-1.244*10^{-5}$	0.1410	1.16485
1-Octen-3-ol	1.53428	$-6.640*10^{-6}$	0.0905	0.18496
Hexanal	0.94108	$-8.511*10^{-6}$	0.1031	1.01293
1-Octanol	0.92014	$-1.692*10^{-5}$	0.2140	0.19352
Ethanol	0.84821	$-1.395*10^{-5}$	0.2131	0.50477

[a]Sensitivity (η), β values, and κ_r values are obtained at room temperature. [b]Ea values are for the concentration range of 25-125 ppm.

The carbon cladding functionalizing can incredibly alleviate the influence of ambient humidity on chem-resistive bismuth tungstate sensor operation, as the intrinsically hydrophobic nature of the C film, which can potentially reduce the reaction between the sensing layer and H_2O. The WCA of WO_3/Bi_2WO_6 and $C_x/WO_3/Bi_2WO_6$

films were illustrated (Figure 4-25a). The WCA of the WO_3/Bi_2WO_6 film is only 36.47°, indicating its hydrophilic nature. In particular, the addition of a small amount of D-(+)-Glucose anhydrous (0.25 g) will provide the $C_{0.25}/WO_3/Bi_2WO_6$ with a hydrophobic feature, and the corresponding WCA is 116.59°. Furthermore, the WCA of $C_x/WO_3/Bi_2WO_6$ (x = 0.5, 0.75, 1, 1.5, and 2) were all greater than 130°, which proved that the C cladding can serve as a hydrophobic film for humidity-alleviated benzaldehyde detection. The dynamic response curve of all samples to 100 ppm benzaldehyde under dry air conditions and RH in the range of 40-90% under UV light (365 nm) excitation is depicted in Figure 4-25b, while the relevant response values are consolidated in Figure 4-25c. The WO_3/Bi_2WO_6-based sensor's sensitivity was significantly affected by atmospheric humidity (green portion), resulting in substantial drift in the response value as humidity levels increased (Figure 4-25e). The concrete response value for the WO_3/Bi_2WO_6 sensor was 45.22% (40% RH~90 % RH), while the equivalent value for the $C_{0.75}/WO_3/Bi_2WO_6$ sensor was 5.49% under the same conditions. Furthermore, we applied the coefficient of variation (CV) to demonstrate the impact of humidity on responses (Figure 4-25d), which is defined as Equation (4-7) [292]:

$$CV=R_{SD}/R_{average}\times100\% \qquad (4\text{-}7)$$

where R_{SD} and $R_{average}$ represent the standard deviation (SD), while the average value of responses obtained under varying humidity conditions, respectively. The CVs of the WO_3/Bi_2WO_6 to $C_2/WO_3/Bi_2WO_6$ were 40.6, 12.3, 6.4, 3.8, 6.1, 22.2, and 20.1, respectively. As the CVs value was negatively correlated with the moisture resistance of the material, adding between 0.5 and 1 g of D-(+)-Glucose anhydrous can improve the anti-humidity ability of $C_x/WO_3/Bi_2WO_6$ to the maximum extent.

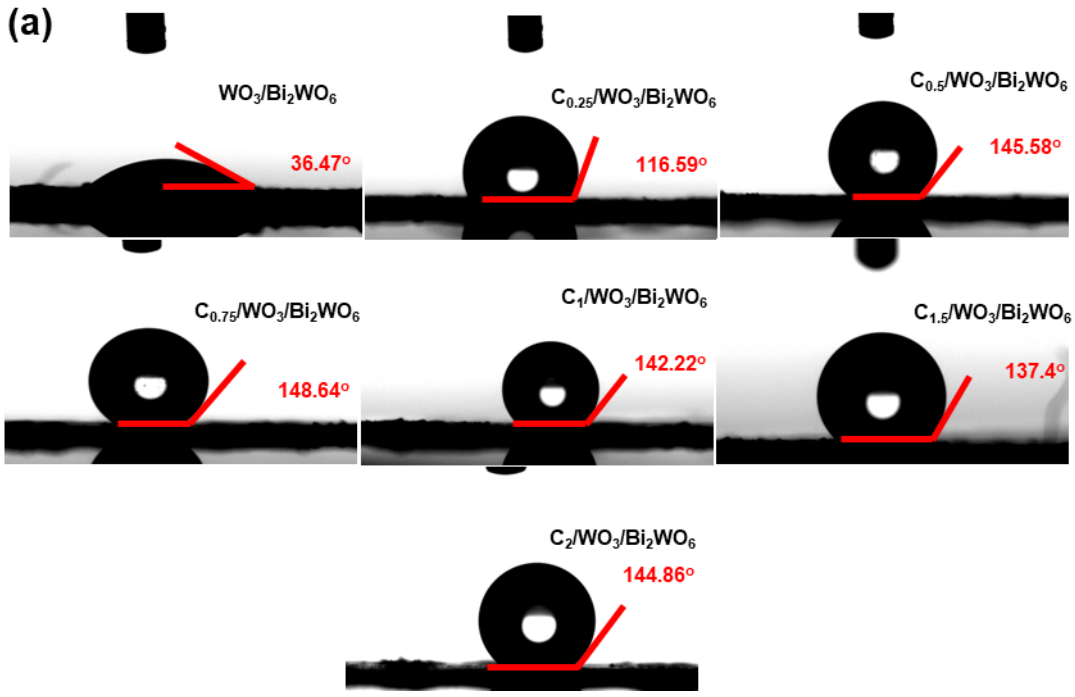

Figure 4-25 (a) Water contact angle of all sample films.

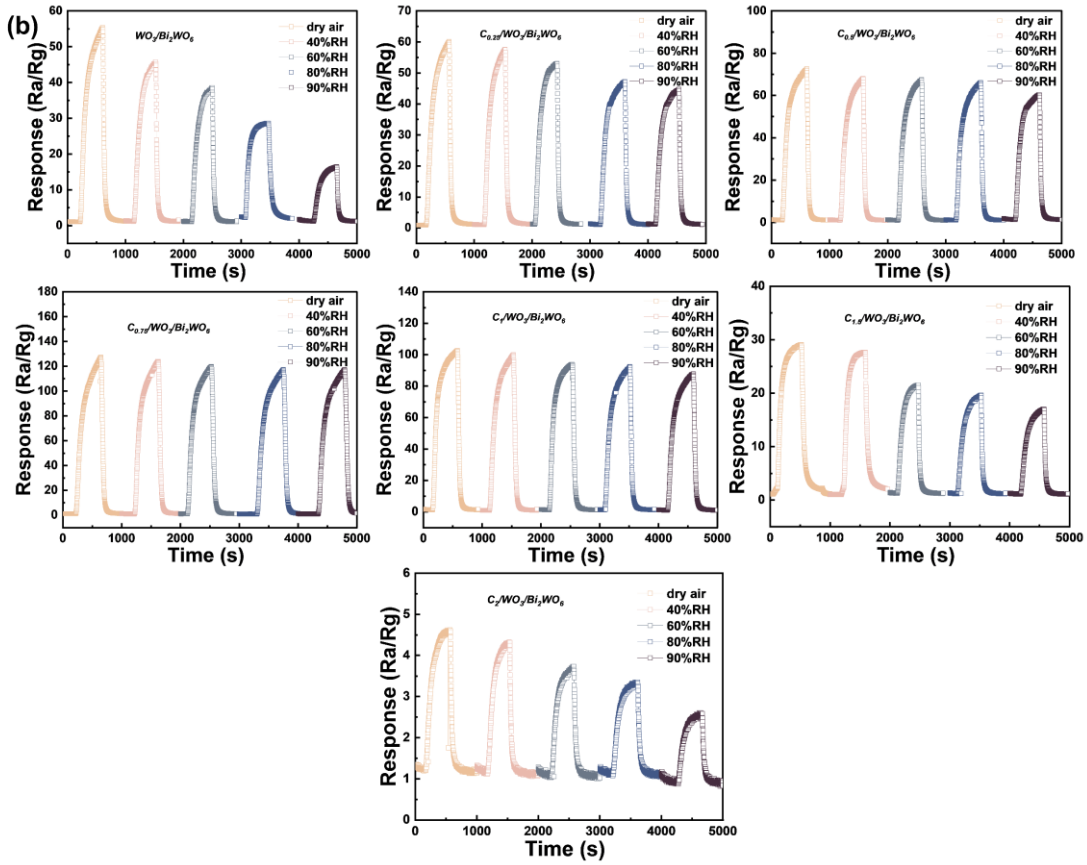

Figure 4-25 (b) Transient response of all sample films to benzaldehyde concentrations of 100 ppm under dry air circumstances, 40%RH, 60%RH, 80%RH, and 90%RH at room temperature (25 ± 2 °C).

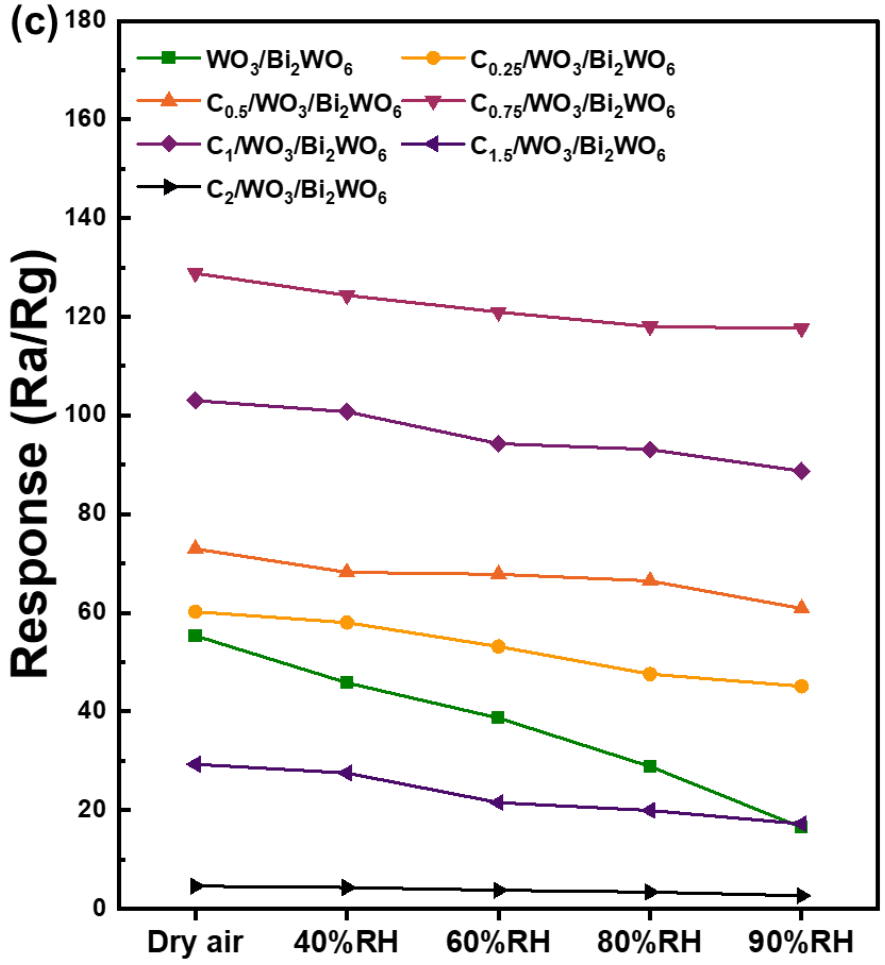

Figure 4-25 (c) Plots of response retentions for different sensors as a function of RH.

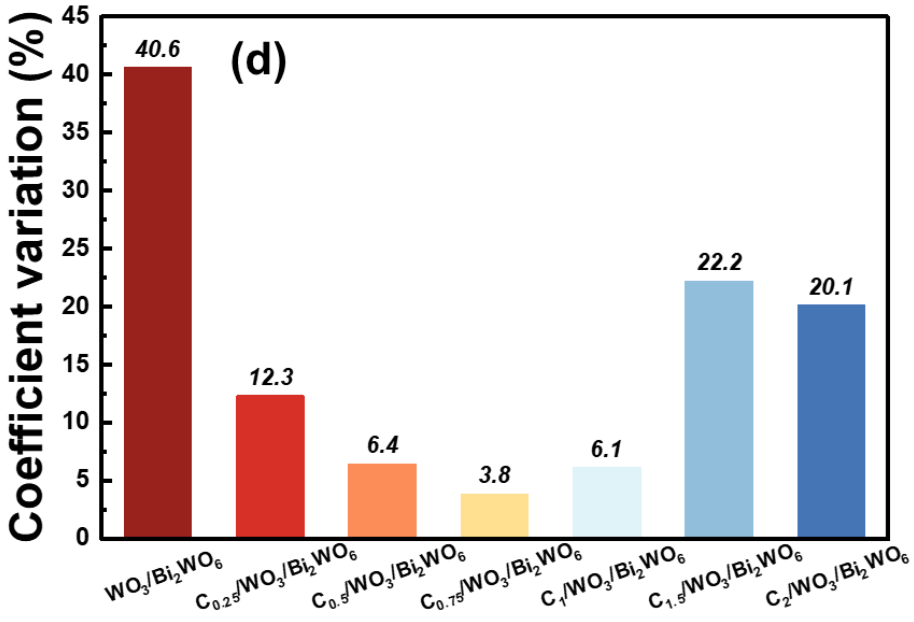

Figure 4-25 (d) CV values of different sensors.

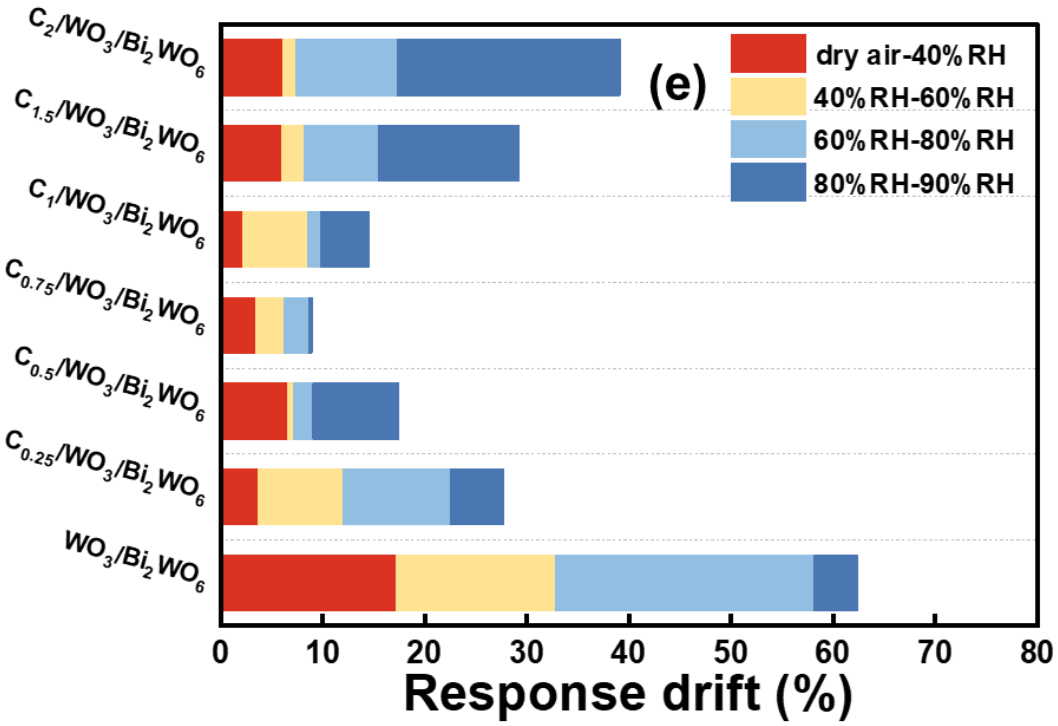

Figure 4-25 (e) Response drift of different sensors.

4.2.3 Gas sensing mechanism

At present, the VOC sensing mechanism has been comprehensively studied, and the fundamental benzaldehyde sensing process for $C_x/WO_3/Bi_2WO_6$ can be interpreted as the oxidation-reduction reaction between ionized oxygen species (O_2^-, O^-, and O^{2-}) and benzaldehyde molecules, which can be referred to our previous study [17, 115, 293]. Based on the above results, it was conjectured that the enhanced benzaldehyde sensing performance was attributed to the carbon-functionalized cladding, the n-n heterostructure setup, optical excitation, and the optimized twisted micro-flowers morphology. Firstly, the n-n heterojunction formed by tungsten oxide and bismuth tungstate generates an internal electric field, thereby reducing the reference resistance and decreasing power consumption. Secondly, the band structure of $C_{0.75}/WO_3/Bi_2WO_6$ and WO_3/Bi_2WO_6 can be obtained by VB-XPS and Tauc plots (Figure 4-26a to Figure 4-26c). The conduction band potential (E_{CB}) of the samples is calculated below, and the valence band potential can be obtained by the VB-XPS technique (Figure 4-26a). The $E_{VB,\ XPS}$ of WO_3/Bi_2WO_6 and $C_{0.75}/WO_3/Bi_2WO_6$ is measured to be 1.58 and 1.69 eV, respectively.

$$E_{VB,\,NHE}=\varphi+E_{VB,\,XPS}-4.44 \quad (4\text{-}8)$$

where φ is the work function of the instrument (4.52 eV) and $E_{VB,\,XPS}$ refers to the valence band potential. Therefore, the standard hydrogen electrode for the valence band potential ($E_{VB,\,NHE}$) of WO_3/Bi_2WO_6 and $C_{0.75}/WO_3/Bi_2WO_6$ is calculated to be 1.66 and 1.77 eV by Equation (2-8). Furthermore, the work function in actual VOCs detection (Φ) and the contact potential difference (ΔV) have the relationship below [294]:

$$\Delta V=\Phi-\varphi \quad (4\text{-}9)$$

The distance between the two inflection points (IP) of the plot is defined as ΔV (Figure 4-26b). Thus, the Φ for WO_3/Bi_2WO_6 and $C_{0.75}/WO_3/Bi_2WO_6$ are 5.93 eV and 5.70 eV, respectively, and the band structure can be obtained (Figure 4-26c).

As shown in Figure 4-26a, there exists a characteristic peak of O_V near the valence band, verifying the higher concentration of O_V in $C_{0.75}/WO_3/Bi_2WO_6$, which is consistent with the EPR and O 1s results [294]. Furthermore, the higher work function of $C_{0.75}/WO_3/Bi_2WO_6$ is evident (Figure 4-26c), indicating lower baseline resistance, a stronger built-in electric field, and faster reactive electron transfer. Thirdly, the reason for the enhanced sensitivity of $C_x/WO_3/Bi_2WO_6$ sensor from UV light excitation is the chemically adsorbed oxygen ions ($O_2^-{}_{(ads)}$) on the surface of $C_x/WO_3/Bi_2WO_6$ is greatly stable under dark conditions while the larger adsorption energy between $C_x/WO_3/Bi_2WO_6$ and $O_2^-{}_{(ads)}$ will result in the nonspontaneous O_2^- desorption. However, the electrons induced by photo-excitation will continue to react with O_2 to form more oxygen species ($O_2^-{}_{(photo\text{-}ads)}$) under ultraviolet light, making its desorption process easier above $C_x/WO_3/Bi_2WO_6$ surface (Figure 4-26d). Unlike $O_2^-{}_{(ads)}$, $O_2^-{}_{(photo\text{-}ads)}$ are relatively feeble, bound to the surface of $C_x/WO_3/Bi_2WO_6$, and can react with benzaldehyde molecules spontaneously, leading to a prominent resistance change (Figure 4-22) [284]. Following the successful incorporation of carbon, the gas sensing activity and stability for $C_x/WO_3/Bi_2WO_6$ have been improved as the excitons have been dissociated into free carriers, alleviating the side effects of photoexcitation [279]. Meanwhile, carbon could facilitate carrier mobility, while the existing electron transfer procedure (Bi/W→C sub Bi over W →C sub O →O) may provide novel carrier

transport channels, thereby enabling greater reactivity and rapid reactions. Furthermore, the concrete reaction of the benzaldehyde molecule was illustrated in Figure 4-26e and equations (4-10 to 4-12):

$$O_{2(gas)} \leftrightarrow O_{2(ads)} \quad (4\text{-}10)$$

$$O_{2(ads)} + e^- \leftrightarrow O^-_{2(ads)} (T<150^oC) \quad (4\text{-}11)$$

$$2C_6H_5CHO_{(gas)} + O^-_{2(ads)} \rightarrow 2C_6H_4CHO_{(gas)} + 2H_2O + e^- \quad (4\text{-}12)$$

For DFT calculation, the generalized gradient approximation (GGA) with Perdew-Burke-Ernzerhof (PBE) exchange-correlation functional was used to describe the exchange-correlation term. Grimme's empirical dispersion-corrected density functional theory (DFT-D) was employed to explain the interaction of the noncovalent chemical functionalization by gas molecules. The energy cutoff was set as 480 eV. The Monkhorst-Pack k-point mesh was selected rationally for the geometry optimization. The Brillouin zone integration was performed at fine quality. The convergence threshold in geometry optimization was set as 10^{-6} eV for energy. For the construction of surface models, a vacuum layer was used to eliminate interactions between periodic structures. The DFT results confirmed that the adsorption energy of benzaldehyde on carbon is higher (-1.795 eV) (Figure 4-26g), which is about three times that of the adsorption energy on the surface of WO_3/Bi_2WO_6 (-0.614 eV) (Figure 4-26f), proving that C cladding is beneficial to the improvement of the sensitivity of the sensor. Furthermore, the adsorption energy of a water molecule on the optimized geometric construction of $C_x/WO_3/Bi_2WO_6$ and WO_3/Bi_2WO_6 was -0.256 eV and -0.793 eV, respectively (Figures 4-26h and 4-26i), which is consistent with the experimental sensing results. On the whole, carbon materials (such as graphene, carbon nanotubes, activated carbon, etc.) typically possess high specific surface area, adequate electrical conductivity, and hydrophobic properties. The addition of D-(+)-Glucose anhydrous to the hydrothermal process can attach carbon to the surface of WO_3/Bi_2WO_6, forming a stable hydrophobic layer that blocks the adsorption and penetration of water molecules during the sensing process. The improved electrical conductivity after C cladding can enhance signal transmission efficiency and response speed, thereby maintaining the sensor's performance in a high-humidity environment.

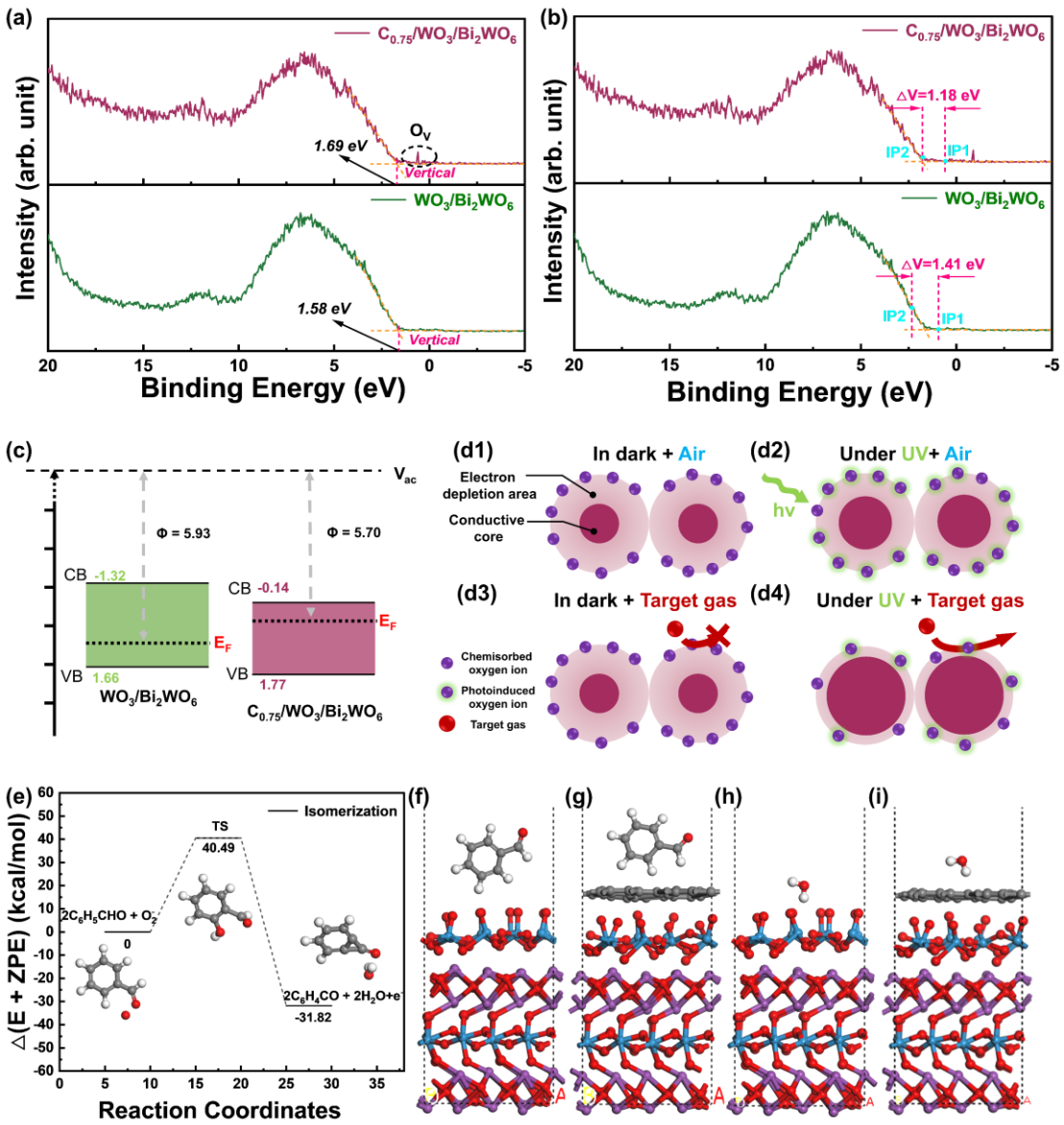

Figure 4-26 (a) VB-XPS, (b) work functions and (c) band structure of $C_{0.75}/WO_3/Bi_2WO_6$ and WO_3/Bi_2WO_6, (d1-d4) Schematic illustration of mechanism of photo-assisted gas sensing under UV excitation, (e) the reaction path of benzaldehyde during sensing, optimized structures for benzaldehyde adsorption in (f) WO_3/Bi_2WO_6 and (g) $C_{0.75}/WO_3/Bi_2WO_6$, Optimized structures for H_2O adsorption in (h) WO_3/Bi_2WO_6 and (i) $C_{0.75}/WO_3/Bi_2WO_6$.

4.3 Practical detection scenario

To assess the potential of the $C_{0.75}/WO_3/Bi_2WO_6$ sensor for evaluating the quality of agricultural products, we studied changes in benzaldehyde concentration emitted from diverse cooked rice (uncooked rice with different storage times) of similar weight (≈20 g). Firstly, we verified the presence of benzaldehyde molecules in VOCs released from cooked rice (raw materials: fresh uncooked rice and uncooked rice stored for six

months) by carrying out HS-SPME combined with GC-MS (Figure 4-27a to Figure 4-27f). Secondly, VOC detection on cooked rice prepared from coarse rice with different storage times (0, 1, 2, 3, 4, 5, 6, 7, and 8 weeks) was performed using homemade equipment with a $C_{0.75}/WO_3/Bi_2WO_6$ sensor (Figure 4-27g). Apparently, as the storage time of fresh rice brought from the supermarket gradually increases, the response of the $C_{0.75}/WO_3/Bi_2WO_6$ sensor to the corresponding cooked rice gradually increases, which was consistent with the slowly increasing benzaldehyde concentration in the coarse rice during storage (Figure 4-27h to Figure 4-27p) [295]. This observation further corroborates the potential of the developed devices for evaluating the quality of agricultural products. Finally, we applied two dimensionality reduction methods (PCA and linear discriminant analysis (LDA)) to visualize the dynamic loop data for cooked rice detection obtained above (Figures 4-27h to 4-27p), while the response and reaction times were extracted as a standardized dataset. As shown in Figure 4-28a, it can be observed that there is a large range of duplication between the data point regions of cooked rice made from raw rice stored for 0 to 3 weeks, while no correlation between the corresponding data point area of cooked rice prepared from fresh rice and stored for nearly 2 months was discerned. Similar analysis results were obtained in Figure 4-28b while the three groups (fresh group (0-2 weeks), mild group (3-5 weeks), moderate group (6-7 weeks)) were almost separate. The VOCs detection data of cooked rice made from rice with different storage times showed a specific pattern and rule, and the datasets for different storage times can be clearly distinguished, which provides an original strategy and idea for the detection of grain and other agricultural products.

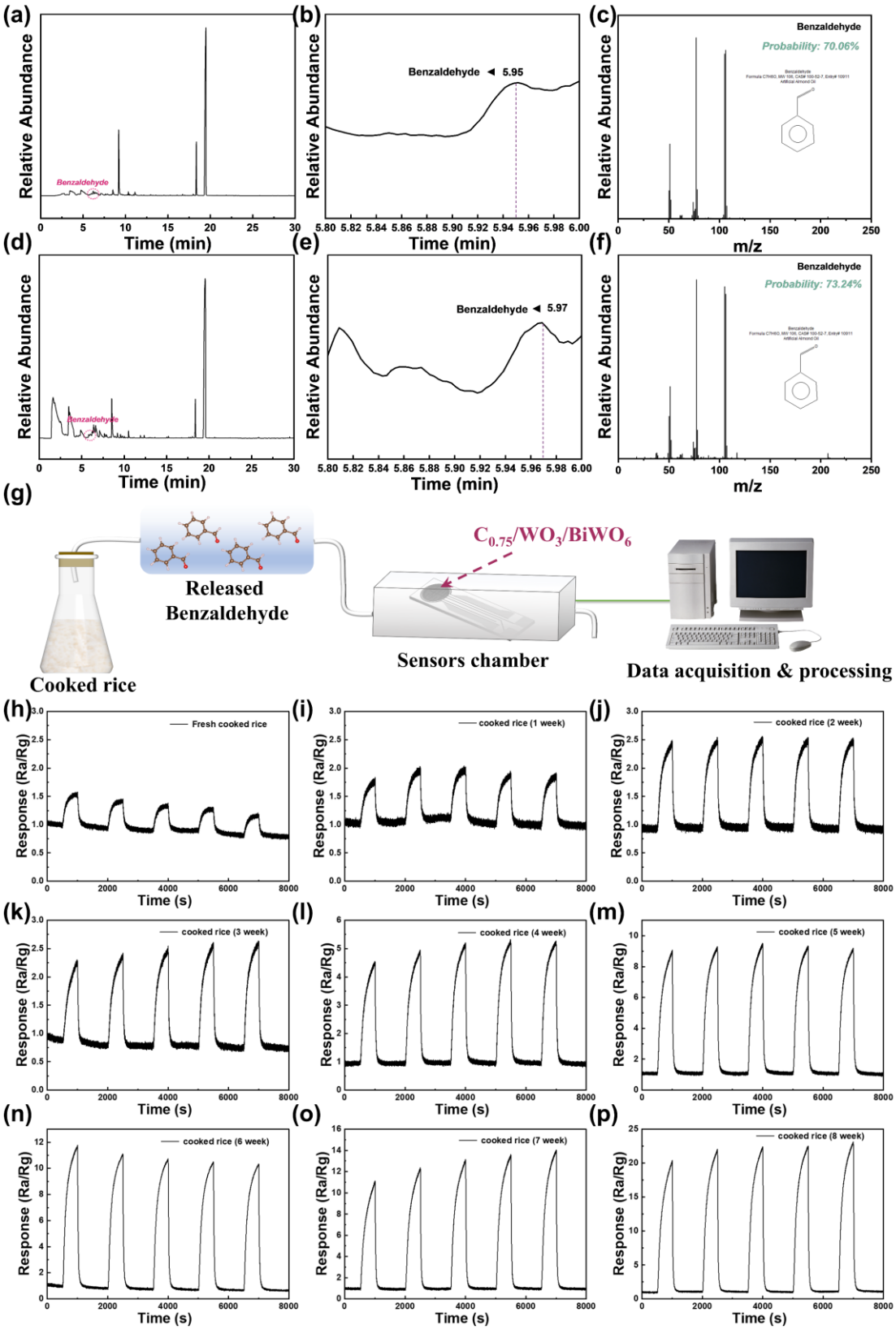

Figure 4-27 (a) Chromatogram of representative and (b) magnified chromatogram of the benzaldehyde region of cooked rice cooked from grains under fresh condition, (c) mass spectra of the benzaldehyde in cooked rice cooked from grains under fresh condition, (d) chromatogram of representative and (e) magnified chromatogram of the benzaldehyde region of cooked rice cooked from grains stored for six months, (f) mass spectra of the benzaldehyde in cooked rice cooked from

grains stored for six months, (g) schematic diagram of the stored cooked rice assessment system, five repetitive response curves of volatile gas detection on cooked rice cooked from (h) fresh rice and rice stored for (i) 1, (j) 2, (k) 3, (l) 4, (m) 5, (n) 6, (o) 7 and (p) 8 weeks using $C_{0.75}/WO_3/Bi_2WO_6$ sensor.

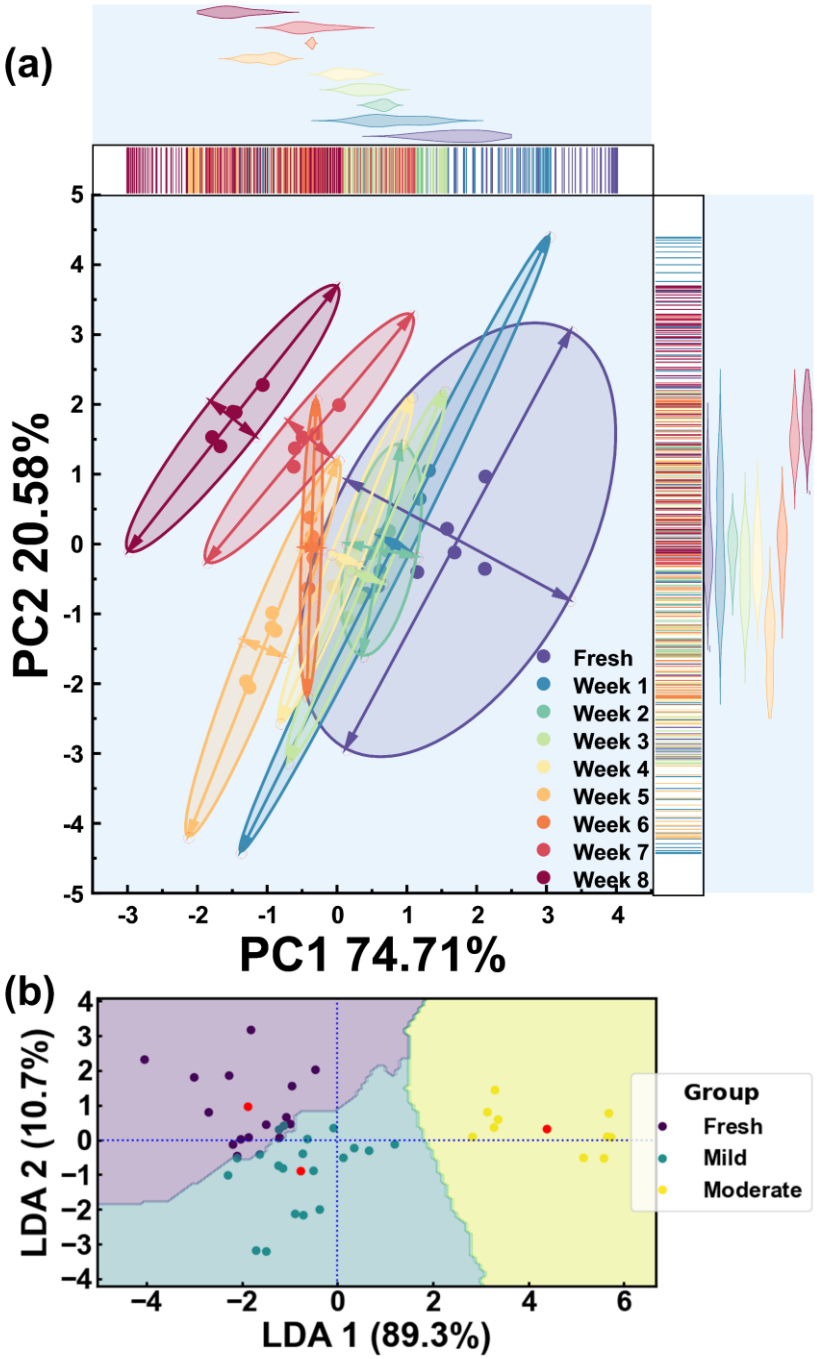

Figure 4-28 (a) Two-dimensional score plots of the first principal components derived from response curves for volatile gas detection on cooked rice cooked from fresh grains and grains stored for different weeks using $C_{0.75}/WO_3/Bi_2WO_6$ sensor, (b) LDA pattern recognition of volatile gas detection on cooked rice cooked from fresh grains and grains stored for different weeks (classified as fresh, mild and moderate groups) using $C_{0.75}/WO_3/Bi_2WO_6$ sensor.

4.4 Conclusions

In summary, we engineered carbon-cladded bismuth tungstate-based three-dimensional twisted micro-flowers and constructed a $C_{0.75}/WO_3/Bi_2WO_6$ heterojunction, thereby enabling outstanding benzaldehyde sensing performance. The optimized sensor exhibited high sensitivity (33.7 @ 50 ppm), excellent selectivity, long-term stability over 15 days (average response of 83.5 @ 75 ppm), and pronounced anti-humidity characteristics (CV = 3.8). Even at 90% relative humidity, the response of the $C_{0.75}/WO_3/Bi_2WO_6$ sensor decreased by only 8.96% compared with the dry condition. Under UV illumination, the device further benefited from enhanced charge carrier mobility, a low initial carrier concentration, and a reduced operating temperature. The origin of the high sensitivity and humidity tolerance was elucidated by correlating the carbon cladding-SMOX nanostructure interaction (DFT calculations), the carbon-modified band structure, and the photoactivated gas-sensing reactions. Finally, the practical applicability of the as-fabricated benzaldehyde chemiresistive sensor was demonstrated. To the best of our knowledge, this chapter represents the first study on carbon-clad TSMOX for benzaldehyde detection, with an explicit analysis of anti-humidity sensing, highlighting the versatility and application potential of this SMOX sensor platform.

Chapter 5: Defect-Engineered Nickel Tungstate Micro-flowers for 1-Octen-3-ol Detection

In this chapter, we report the successful synthesis of $NiWO_4$ micro-flowers subjected to varying H_2 treatment times. Hydrogen treatment increases the concentration of oxygen vacancies, significantly enhancing the structural characteristics of the H_2-treated $NiWO_4$ micro-flowered active layer and improving its sensing properties toward 1-octen-3-ol. We observed that the optimal sensing material exhibited a low LoD of 0.373 ppm, a superior response value of 20.6, and an excellent response time of 22 s for 40 ppm of 1-octen-3-ol. Furthermore, the optimal sensor demonstrated exceptional selective detection performance in agricultural product quality scenarios. To address the primary challenges associated with room-temperature gas sensors for 1-octen-3-ol, we significantly improved the anti-humidity performance of the optimal sensor, with only 19.7% response drift observed from 20% to 80% relative humidity (RH) when detecting 40 ppm 1-octen-3-ol. Furthermore, molecular dynamics (MD) simulations at 298 K were conducted to investigate the adsorption and diffusion characteristics of 1-octen-3-ol and oxygen on the $NiWO_4$ and O_V-$NiWO_4$ surfaces.

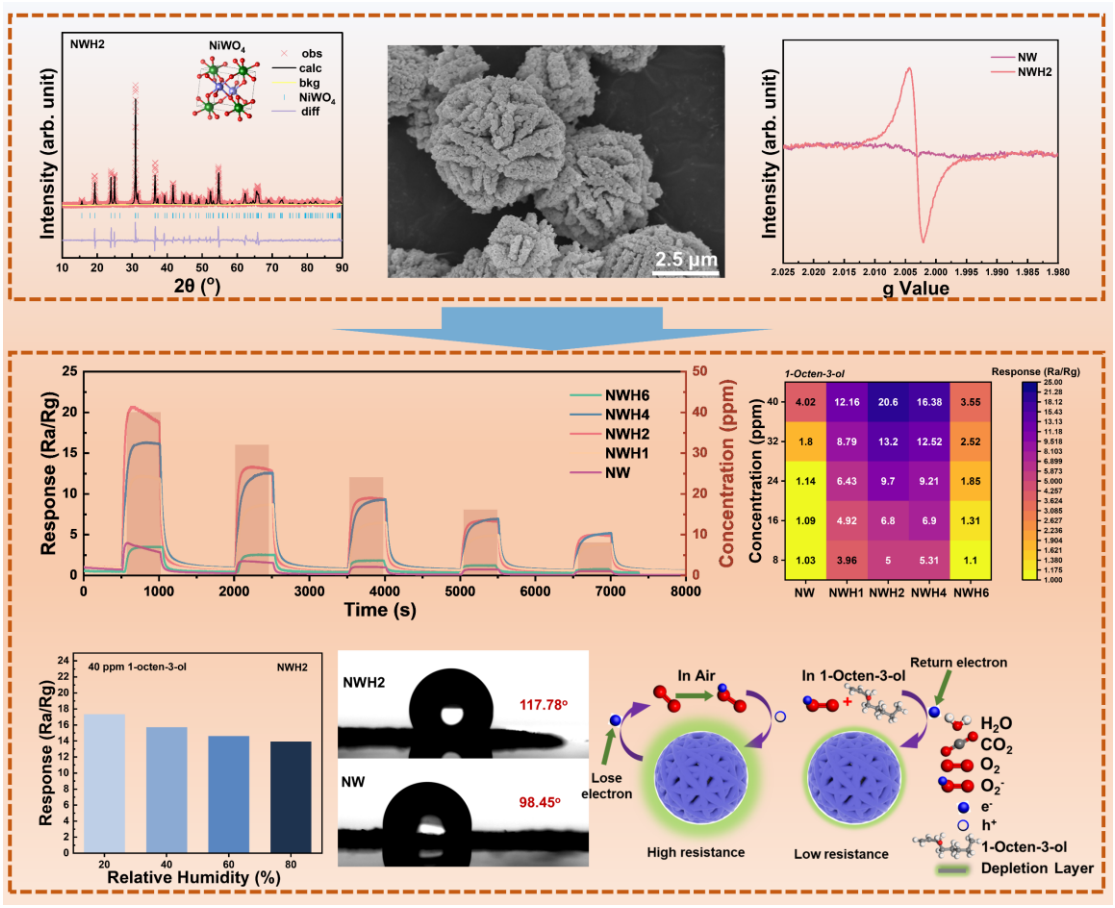

Schematic diagram chapter 5-1 Graphical abstract of this chapter.

In agricultural contexts, 1-octen-3-ol acts as a critical VOC key indicator in products like rice [23], grass carp fillets [296], and sorghum [297], influencing product quality and spoilage dynamics. It is commonly referred to as mushroom alcohol [298] and is recognized as a flavor compound derived from fungi, notable for its remarkably low odor detection threshold [299-301]. This VOC exhibits multifaceted biological and ecological roles. In medical contexts, 1-octen-3-ol has been identified as a potential biomarker for liver cancer through blood-based volatile analysis [302]. Additionally, exposure to this compound has been associated with dopaminergic neuron degeneration, suggesting its role as an environmental risk factor linked to the pathogenesis of Parkinson's disease [303]. Furthermore, 1-octen-3-ol serves as an attractant for hematophagous insects, such as mosquitoes, because it is present in human breath and sweat. This behavioral modulation has generated interest in disrupting insect olfactory receptors, with studies indicating that N,N-diethyl-3-methylbenzamide (DEET) reduces mosquito responsiveness to 1-octen-3-ol [280, 304-306]. Its detection in plant-

pathogen interactions highlights its broader significance in postharvest monitoring and food safety. Consequently, the development of a high-performance gas sensor for detecting 1-octen-3-ol is of paramount significance, as such sensors would enhance accurate assessments of cooked rice quality, the potential hazards associated with 1-octen-3-ol exposure, and non-invasive medical diagnostic methodologies.

Nickel tungstate ($NiWO_4$), a wolframite-type SMOX, demonstrates particular promise through its good electrical conductivity mediated by tungsten incorporation [307-309], providing a strong basis for developing high-response gas sensors. Despite this advantageous property, $NiWO_4$ has been underutilized in gas sensing applications, remaining primarily employed in hydrodesulfurization, biosensors, supercapacitors, and photocatalytic/electrocatalytic systems [308, 310-313]. Three fundamental limitations constrain its gas-detection implementation: insufficient active sites for target-molecule adsorption, high activation-energy barriers for surface redox reactions, and poor humidity resistance under ambient conditions. Conventional performance-enhancement strategies employing microheaters [314, 315] may introduce critical trade-offs and high operational costs. Elevated operational temperatures accelerate material degradation through irreversible phase transitions and can simultaneously increase cross-sensitivity to humidity and cross-interference with competing VOCs. These factors adversely affect the detection accuracy and long-term stability of chemical sensors. To address these challenges in $NiWO_4$ sensors, we used a hydrogen thermal treatment protocol that induces controlled oxygen vacancy (O_V) formation through selective removal of lattice oxygen (O_L) via H_2-O_L interactions, as described by [280, 316]: $NiWO_4 + xH_2 \rightarrow NiWO_{4-x} + xH_2O \uparrow (0 < x < 0.25)$. This procedure exploits the intrinsic oxygen deficiency in molten metal oxides, where the rates of oxygen loss exceed those of metal-atom loss during rapid cooling, thereby generating a thermodynamic driving force for the formation of oxygen vacancies. The increase in oxygen vacancy density creates adsorption centers (active sites), while vacancy-induced electron depletion reduces the energy barrier for redox reactions and accelerates reaction kinetics [317, 318]. Collectively, these modifications were reported to enable superior gas detection performance with achieved operational stability [319-321].

5.1 Synthesis of defect-rich $NiWO_4$ micro-flowers

All chemicals were of analytical grade and used without further purification. Nickel sulfate hexahydrate ($NiSO_4 \cdot 6H_2O$) (AR grade, CAS: 10101-97-0), hydrazine monohydrate ($N_2H_4 \cdot H_2O$) (CAS: 7803-57-8), anhydrous ethanol (AR grade, CAS: 64-17-5), and 1-octen-3-ol ($C_8H_{16}O$) (CAS: 3391-86-4) were procured from Aladdin Biochemical Technology Co., Ltd. in China. Sodium tungstate dihydrate ($Na_2WO_4 \cdot 2H_2O$) (AR grade, CAS: 10213-10-2) was supplied by Sinopharm Chemical Reagent Co., Ltd. The synthesis of defect-rich $NiWO_4$ followed a two-step protocol, as illustrated in Figure 5-1a to Figure 5-1c. Stage 1 involved preparing $NiWO_4$ through a modified coprecipitation method adapted from Yang et al. [322]. Specifically, 0.6 mmol of $NiSO_4 \cdot 6H_2O$ was dissolved in 60 mL of distilled water and maintained at 60°C under continuous stirring for 45 minutes. Subsequently, 0.6 mmol of $Na_2WO_4 \cdot 2H_2O$ was introduced, and the mixture was vigorously stirred (450 rpm) until a uniformly transparent green solution was achieved. The gradual addition of 1 mL of $N_2H_4 \cdot H_2O$ then triggered chromatic evolution from clear green to gray-blue colloidal suspension. Post-reaction stirring continued for 2 hours to ensure completion, followed by four centrifugation cycles using an ethanol-water solution (1:1 v/v). Following vacuum drying at 60°C for 24 hours, the purified precipitate was obtained. Subsequently, the sample was subjected to an immediate heat treatment in a box furnace at 800°C for 2 hours under an ambient atmosphere, with a heating rate of 10°C per minute. The furnace was then allowed to cool naturally, yielding $NiWO_4$ powder samples referred to as NW.

The second-stage processing involved controlled hydrogenation of the $NiWO_4$ samples under regulated conditions. The samples were loaded into alumina crucibles and subjected to H_2 treatment in a tubular furnace. Thermal processing parameters included linear temperature ramping (10°C/min) to target 500°C, followed by variable isothermal durations (1-6 h) under continuous H_2 flow (50 sccm). A systematic nomenclature protocol was implemented in which hydrogenation duration directly determined the material designation: NWH1 (1 h exposure), NWH2 (2 h), NWH4 (4 h), and NWH6 (6 h). Post-treatment cooling occurred naturally under H_2 purge environment to preserve defect architecture. This temporal series enabled a controlled comparison of the effects of reduction duration on crystallographic defects and surface

properties. The full gas sensor equipment of the sensor instrumentation is schematically illustrated in Figure 5-1d.

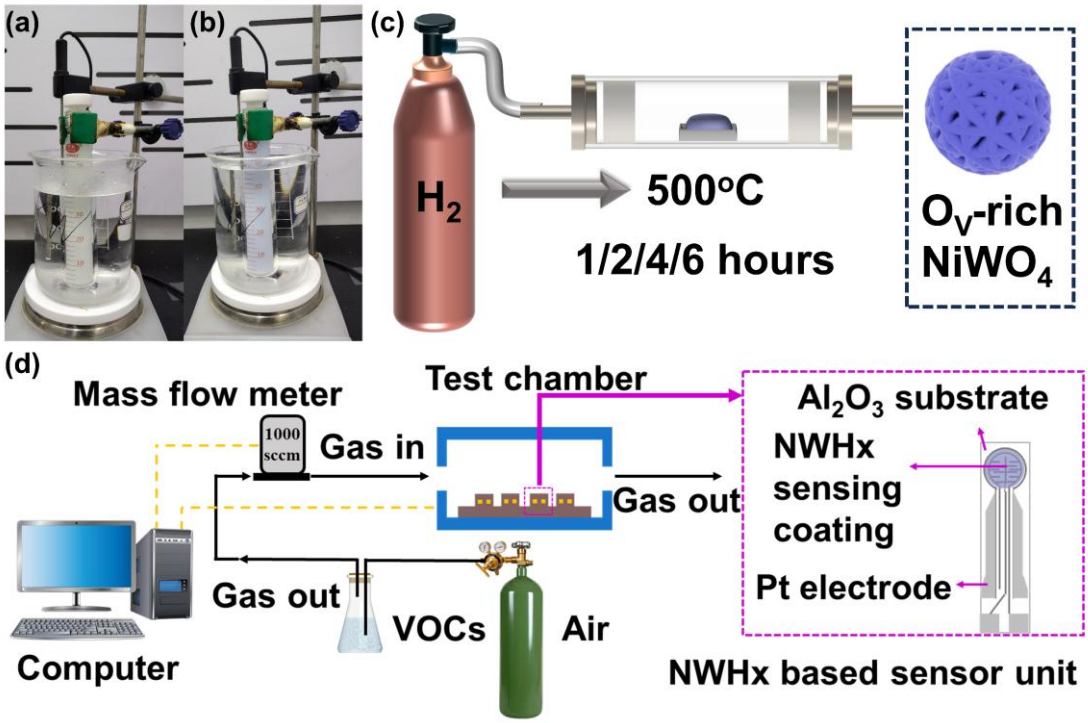

Figure 5-1 (a-c) Schematic illustration for fabricating O_V-rich $NiWO_4$ micro-flowers and (d) the setup for gas sensing tests.

5.2 Results and discussion

5.2.1 Characterization results

The crystallographic structure of the as-prepared sample was characterized using XRD. As illustrated in Figure 5-2a, the XRD patterns were analyzed to verify the phase composition and structural characteristics of the samples. For all samples, the XRD patterns match the standard reference pattern specified in ICDD #00-015-0755, indicating crystallization in the monoclinic P2/c space group [323]. Amplified XRD patterns of all samples at the (-111) plane are presented in Figure 5-2b, revealing that the NWH2 sample exhibits the smallest full width at half maximum (FWHM), indicating that it has high crystallinity (86.5%) and high purity, along with a more complete and orderly crystal structure, and fewer impurities. This is further confirmed

by specific crystallinity calculations (Figure 5-2c). The crystallinity was determined using the following equation [324, 325]:

$$\text{Crystallinity} = \frac{Area\ of\ crystalline\ peaks}{Area\ of\ all\ peaks\ (crystalline+Amorphous)} \times 100\% \qquad (5\text{-}1)$$

However, prolonged H_2 reduction time decreased the material's crystallinity. Additionally, the crystallite size for all samples was calculated using the Scherrer equation:

$$D = K\lambda/\beta \cos\theta \qquad (5\text{-}2)$$

where D, K λ, β and θ represent crystallite size (nm), Scherrer constant (0.9), wavelength of x-ray sources (0.15406 nm), FWHM (full width at half maxima, radians), and peak position (radians), respectively. It is noteworthy that both the crystallite size and crystallinity increased initially with hydrogen treatment, reaching a maximum at 2 hours. However, further prolonging the reduction time (4 h and 6 h) decreased both parameters. This phenomenon may result from excessive hydrogen-induced fragmentation or re-nucleation of grains at the nanoscale. The formation of high-density oxygen vacancies and increased lattice distortion during extended H_2 exposure could suppress crystal growth and induce disorder, leading to refined crystallite domains and reduced long-range order. Therefore, while crystallite size and crystallinity are generally correlated during moderate annealing, they may diverge under over-reduction conditions due to competing mechanisms of grain refinement and structural disorder.

To further explore the complexity of the crystal structure, a detailed XRD Rietveld refinement analysis of NWH2 was performed, as shown in Figure 5-2d. This analysis yielded a weighted residual (R_{wp}) of 14.34%, indicating a significant correlation with the original XRD data. This comprehensive analysis confirmed that the NWH2 sample has a monoclinic crystal structure, classified as P2/c. The accurately measured lattice parameters are: a = 4.582 Å, b = 5.661 Å, and c = 4.919 Å.

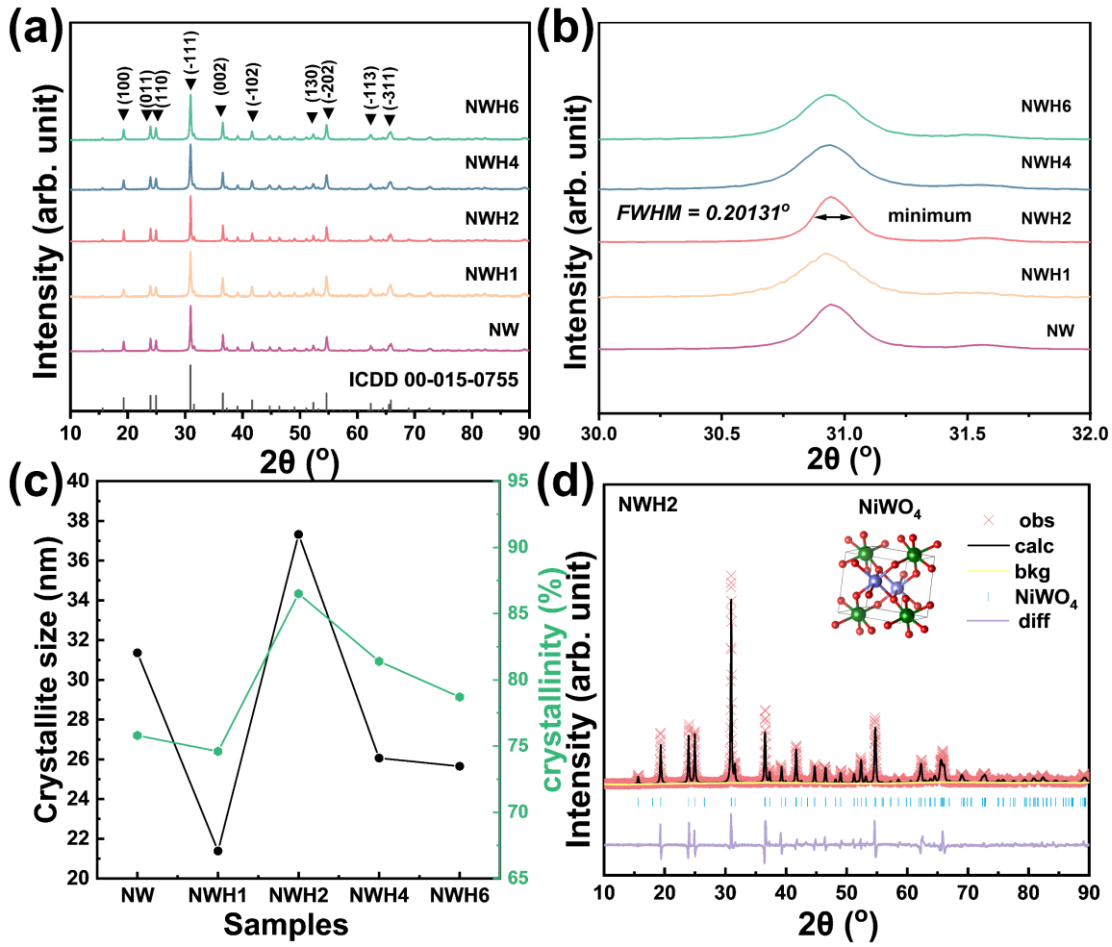

Figure 5-2 (a) Full and (b) partial enlarged XRD for all samples. (c) Calculated grain size and crystallinity. (d) Rietveld refinement of the XRD pattern for the NWH2 sample.

SEM images were obtained to investigate the morphological changes of $NiWO_4$ during air calcination and subsequent H_2 treatment. Following vacuum drying, as shown in Figure 5-3a, Figure 5-3c, and Figure 5-3e, it is evident that nickel tungstate micro-flowers are formed through the cross-stacking of numerous prism-like structures, each exhibiting a smooth surface. After air calcination and H_2 heat treatment, as demonstrated in Figure 5-3b, Figure 5-3d, and Figure 5-3f, the diameter of the typical NWH2 micro-flowers remained unchanged; however, their surface changed from smooth to coarse granular, significantly increasing the specific surface area. The presence of surface particles provides additional adsorption sites, enhancing the adsorption capacity of gas molecules and thus improving sensor sensitivity.

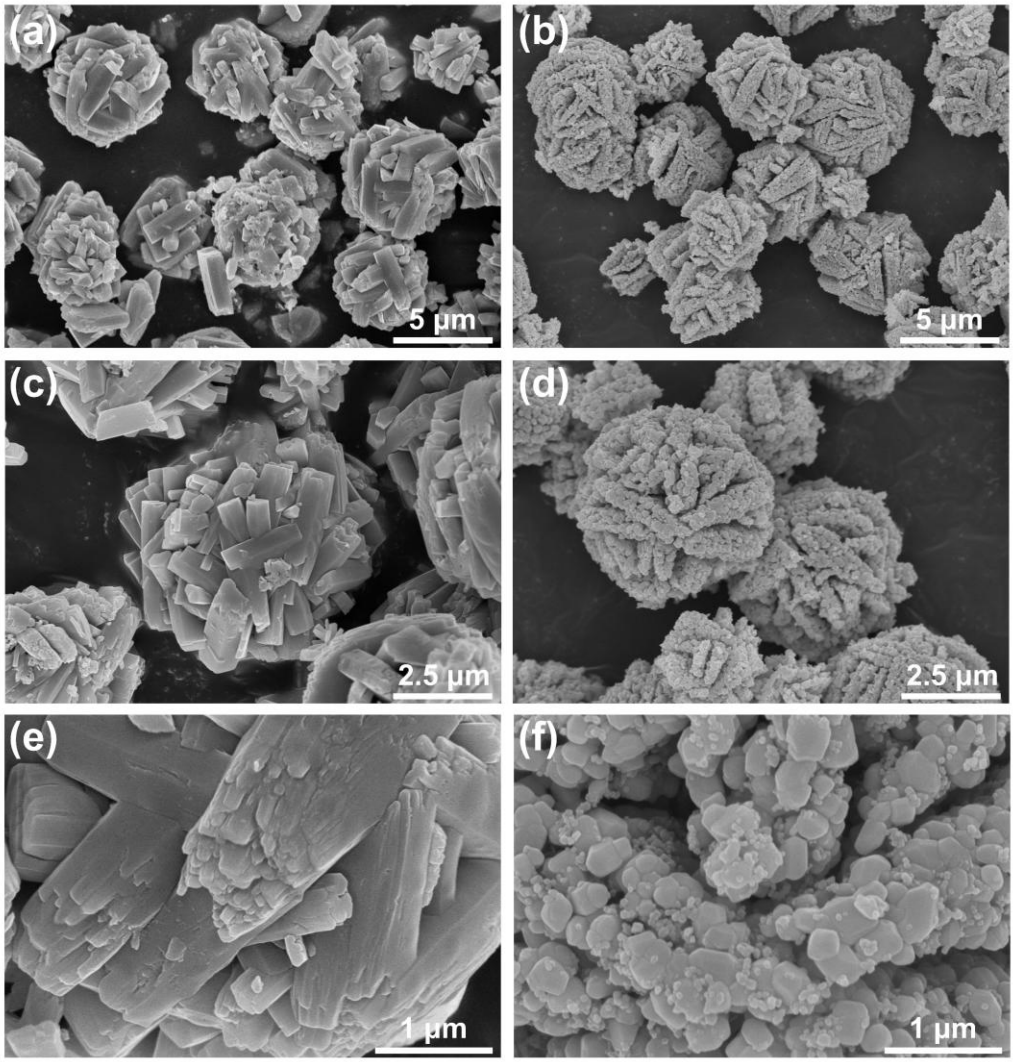

Figure 5-3 FESEM images of (a, c, and e) sample powder without processing heat treatment at 800ºC for 2 h and (b, d, and f) NWH2 sample.

In Figures 5-4a to 5-4e, the NWH2 sample exhibits uniform micrometer-sized flower-like structures with a particle-rich surface. The HRTEM image of the NWH2 sample reveals a crystal plane distance of 0.370 nm (Figure 5-4f), corresponding to the (011) crystal plane of $NiWO_4$.The SAED patterns of the NWH2 sample indicate the formation of polycrystalline nickel tungsten oxide micrometer flowers composed of multiple surface particles (Figure 5-5). Furthermore, the high-angle annular dark field scanning transmission electron microscopy (HAADF-STEM) images in Figure 5-4g further elucidate the multiparticle characteristics on the surface of the nickel tungsten oxide micrometer flowers. The EDX mapping results shown in Figures 5-4h-5-4j demonstrate a uniform distribution of Ni, W, and O across the NWH2 sample.

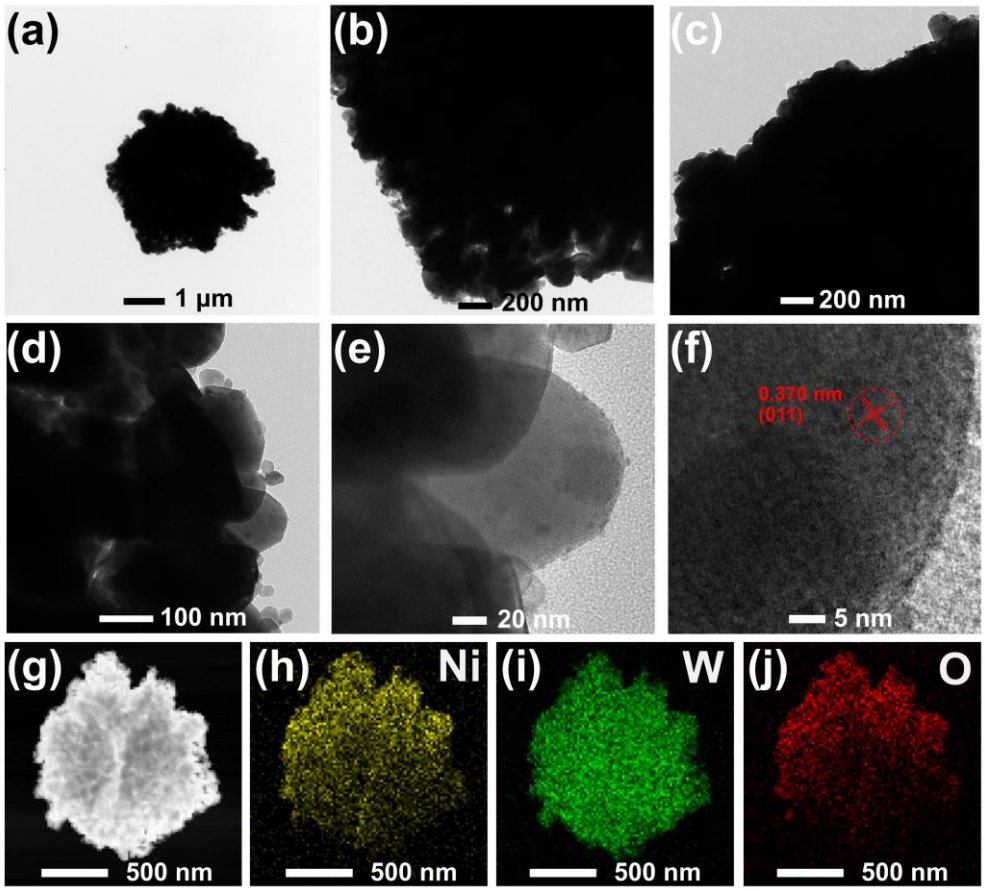

Figure 5-4 (a-e) TEM images of NWH2, (f) HRTEM images of NWH2, (g) HAADF-STEM image of NWH2, (h-j) EDX mapping of Ni, W, and O of NWH2.

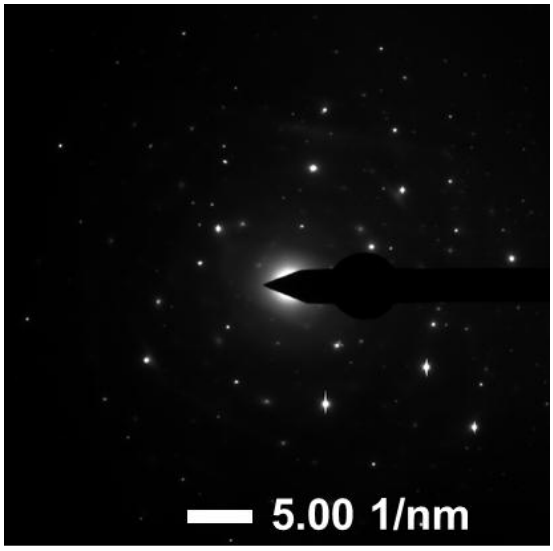

Figure 5-5 SAED pattern of NWH2.

The XPS analysis of the NW and the NWH2 samples provides essential insights into their elemental composition and chemical states. The XPS survey spectrum (Figure

5-6a) reveals the presence of nickel (Ni), tungsten (W), and oxygen (O) with characteristic peaks, thereby confirming the successful synthesis of $NiWO_4$. The Ni 2p spectrum of the NWH2 sample is characterized by two $2p_{3/2}$ and $2p_{1/2}$ doublets, as shown in Figure 5-6b, indicating the existence of two oxidation states of nickel: Ni^{2+} and $Ni^{\delta+}$ ($\delta<2$). Additionally, two peaks centered at 879.8 eV and 861.7 eV correspond well to satellite peaks [326, 327]. In comparison, the binding energies of the Ni 2p doublets for the NW sample are slightly shifted to lower binding energies than those observed for the NWH2 sample. This shift indicates that the increase in electron density around Ni may reduce effective shielding, thereby enhancing the reactivity of Ni on the sample surface and improving its capacity for gas-molecule adsorption. Furthermore, the W 4f spectrum for both NW and NWH2 samples exhibits the W4f doublet (Figure 5-6c), which is attributed to the W^{6+} oxidation state, confirming the presence of tungsten in its most common oxidation state in tungsten oxides. The XPS analysis of the O 1s peak for all the samples reveals distinct contributions from various oxygen species, as shown in Figure 5-6d and Table 5-1. In the NW sample, the O 1s spectrum is decomposed into three main components: chemisorbed oxygen species (O_C) centered at 531.1 eV, O_V at 530.4 eV, and lattice oxygen (O_L) near 529.9 eV. The relative intensity ratios indicate that O_C, O_V, and O_L account for 17.2%, 28.5%, and 54.3% of the total O1s peak, respectively. For NWH2, the components for O_C, O_V, and O_L are observed at 531.3 eV, 530.5 eV, and 529.9 eV, respectively. However, due to hydrogen reduction treatment, the proportion of O_V increased to 40.3%. In the reduced hydrogen state, the chemical environment of oxygen changes, leading to the release of more oxygen atoms from the crystal lattice and the formation of O_V. Concurrently, during the calcination process, the material's crystal structure reorganizes, contributing to the rearrangement of atoms in the crystal lattice and the formation of additional O_V. Moreover, the binding energies of the O_V and O_C species also show slight positive shifts (~0.1-0.2 eV), indicating changes in the local electronic environment and enhanced surface reactivity. These findings confirm that the improved gas-sensing performance of NWH2 arises from tailored oxygen-defect density and surface chemical states. As for charge balance, the removal of lattice oxygen leads to the partial reduction of nearby metal cations, which is evidenced by the shift in Ni 2p peaks in XPS (Figure 5-6b), suggesting an increase in local electron density and thus supporting a dynamic charge redistribution to compensate for the missing oxygen anions.

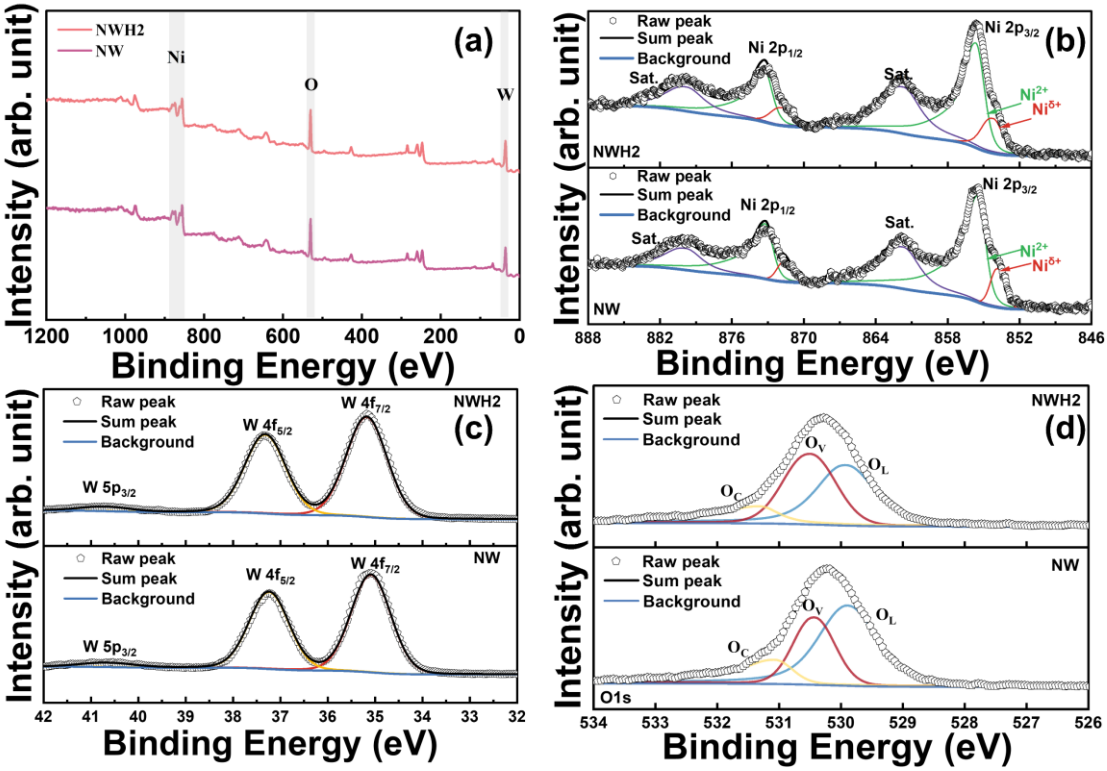

Figure 5-6 (a) Full XPS spectra of NW and NWH2, high-resolution XPS spectra of NW and NWH2 for (b) Ni 2p, (c) W 4f, and (d) O 1s.

Table 5-1 Oxygen species of as-synthesized samples obtained by XPS analysis.

Samples	Oxygen species	Binding energy (eV)	Fraction (%)
NW	O_L	529.9	54.3%
	O_V	530.4	28.5%
	O_C	531.1	17.2%
NWH1	O_L	530.2	55.0%
	O_V	530.8	27.5%
	O_C	531.7	17.5%
NWH2	O_L	529.9	45.2%
	O_V	530.5	40.3%
	O_C	531.3	14.5%
NWH4	O_L	530.1	50.8%
	O_V	530.7	26.4%
	O_C	531.5	22.8%

Samples	Oxygen species	Binding energy (eV)	Fraction (%)
NWH6	O_L	530.1	53.5%
	O_V	530.7	31.6%
	O_C	532.1	14.9%

Raman spectroscopy analysis reveals distinct vibrational modes, as displayed in Figure 5-7a. The prominent peaks detected at approximately 886 cm^{-1} are attributed to the symmetric and asymmetric stretching vibrations of the bridging WO_6 octahedra, indicative of the presence of W-O bonds within the crystal lattice. Low-intensity bands observed at 698 cm^{-1} are ascribed to the asymmetric stretching of O-W-O bonds [328]. Additionally, the peak centered around 421 cm^{-1} indicates lattice vibrations, which can be attributed to distortions within the NiO_6 octahedra that accommodate local structural variations in the nickel tungsten oxide matrix [329]. In detail, the Raman spectra of the H_2-treated samples do not exhibit major peak shifts or new vibrational modes, which is primarily due to the nature of O_V in transition metal oxides, while it significantly alters electronic and surface properties, it does not drastically distort the long-range crystal symmetry that Raman spectroscopy primarily probes. The consistent Raman features thus confirm that the bulk crystal framework remains largely intact, even as local defect environments evolve.

The UV-Vis absorption spectra of the NW sample and its hydrogen-reduced variant reveal significant differences in optical properties, which substantially influence their electronic behavior (Figure 5-7b). The H_2 reduction process modifies the electronic structure of $NiWO_4$, thereby enhancing light absorption in the visible region. This alteration is primarily attributed to the introduction of O_V and modifications in the valence band, which facilitate electronic transitions that were forbidden. To quantitatively assess these changes, the band gap energies were determined using the Tauc plot method, where the indirect band gap was calculated by plotting $(\alpha h\nu)^{1/2}$ against photon energy ($h\nu$), with the absorption coefficients (α) extracted from the UV-Vis spectra [220, 330]. The resulting plot showed a notably lower band gap for the NWH2 sample (2.09 eV) than for the NW sample (2.57 eV), as illustrated in Figure 5-7c. This reduction in band gap energy indicates increased electron mobility, thereby enhancing

sensor sensitivity and reducing operating temperature. This characteristic renders the gas-sensitive material more responsive at lower gas concentrations while minimizing energy consumption.

The EPR spectroscopy study of the NWH2 and NW samples provides valuable insights into the electronic structure and local symmetry of the transition metal sites within the material, as shown in Figure 5-7d. The EPR spectrum of the NW sample reveals a minimal characteristic signature of unpaired electrons, indicative of the presence of Ni^{2+} ions substituting for W^{6+} in the tungsten oxide structure. The EPR signal of the NWH2 sample is significantly enhanced following hydrogen reduction, primarily due to the formation of O_V and the consequent promotion of the electron transfer process. The reduction treatment results in a higher density of oxygen defects that serve as local charge carriers, thereby increasing the concentration of unpaired electrons in the crystal lattice. This increased density of unpaired electrons leads to an enhanced EPR signal, reflecting the sample's increased paramagnetic behavior. Furthermore, O_V may generate new electronic states within the band gap, promote electron delocalization, and enhance the overall electronic conductivity of the material [212]. Thus, the interplay between reduced structural defects and electronic properties underscores the potential of hydrogen reduction as a strategy to modulate the electronic properties of $NiWO_4$, paving the way for applications in advanced sensing systems.

The comparative analysis of the specific surface area of the NW sample and the hydrogen-treated samples revealed significant changes in its textural characteristics, which are crucial for gas sensing applications (Figure 5-7e to Figure 5-7f and Figure 5-8, Table 5-2). BET surface area measurements indicate that H_2 reduction leads to a substantial increase in specific surface area (NWH2: 27.789 m^2/g; NW: 10.707 m^2/g), attributed to the additional surface defects and microstructural changes introduced by O_V during the reduction process. The synergistic effect of the increase in specific surface area, coupled with alterations in electronic properties, highlights the promising potential of hydrogen-reduced $NiWO_4$ for gas-sensing applications.

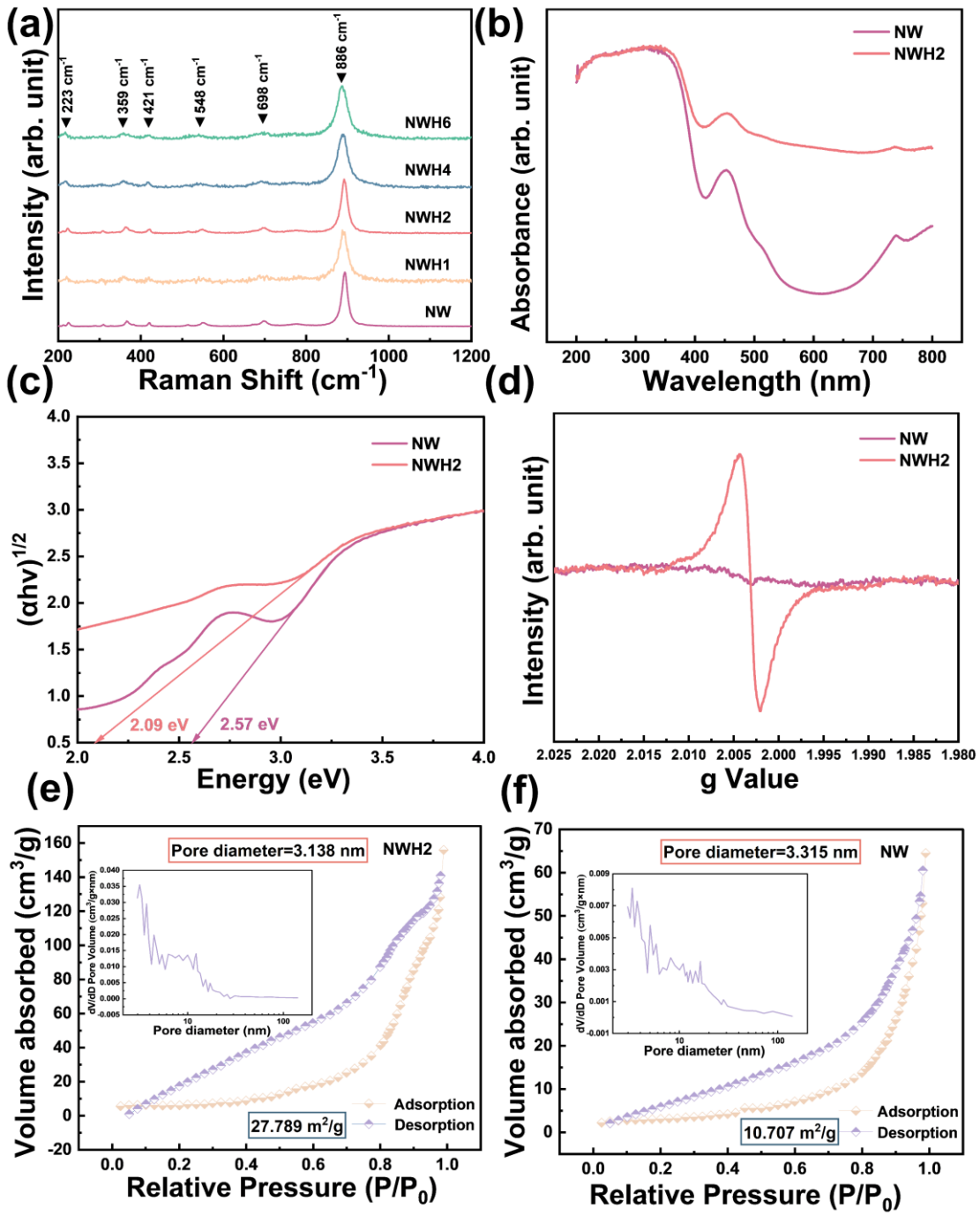

Figure 5-7 (a) Raman spectra of all samples, (b) the UV-Vis absorption spectrum of NW and NWH2 with (c) the corresponding Tauc plot, (d) EPR spectra of all samples, nitrogen sorption isotherms of the (e) NWH2 and (f) NW.

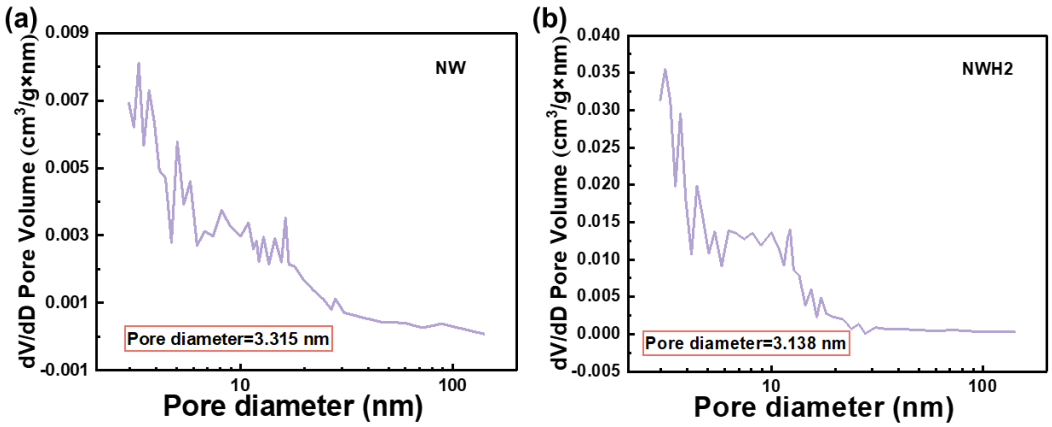

Figure 5-8 Pore size distributions of the (a) NW and (b) NWH2.

Table 5-2 BET results of as-synthesized samples.

Samples	S_{BET} ($m^2 \cdot g^{-1}$)	Average pore diameter (nm)	Total pore volume ($cm^3 \cdot g^{-1}$)
NW	10.707	3.315	0.09977
NWH1	16.628	3.610	0.1336
NWH2	27.789	3.138	0.2412
NWH4	18.046	3.709	0.1145
NWH6	9.910	3.134	0.1084

5.2.2 Gas sensing performance

To investigate the feasibility of $NiWO_4$-related materials for gas sensing, we examined the gas-sensing performances of NW, NWH1, NWH2, NWH4, and NWH6 samples, which correspond to different hydrogen reduction times at room temperature (25 °C ± 2 °C). The sensor response can be calculated as $S = R_a/R_g$, where R_a and R_g are the sensor resistances in ambient air and in the presence of the target analyte, respectively. All sensors exhibited a significant increase in response to 1-octen-3-ol concentrations ranging from 8 ppm to 40 ppm (Figure 5-9a) while the corresponding resistance were shown in Figure 5-10. Notably, the NWH2 sensor demonstrated the highest response (20.6) and fast response time (22 s) at 40 ppm (Figure 5-9b and Figure

5-9e), indicating that an optimal hydrogen reduction time enhances gas-sensing performance. The appropriate duration of hydrogen annealing is crucial for improving the gas-sensing performance of $NiWO_4$. This treatment enhances the material's crystallinity and structural stability, increases the number of vacancies, and optimizes electrical conductivity, thereby enhancing response time and sensitivity. Hydrogen also facilitates the partial reduction of certain metal ions within $NiWO_4$, rendering it more reactive. However, insufficient annealing time may result in inadequate reduction and a lack of active sites. In contrast, excessive annealing can lead to over-reduction or structural damage, negatively impacting gas-sensing capabilities. Thus, identifying the optimal hydrogen reduction time is essential for maximizing the gas-sensing performance of SMOX. The response of hydrogen-reduced $NiWO_4$ sensors to varying concentrations of 1-octen-3-ol was systematically analyzed to evaluate their linearity (Figure 5-9c). As the concentration of 1-octen-3-ol increased, the sensor exhibited a correspondingly higher response signal, demonstrating a clear linear relationship within a specific concentration range. This linearity indicates that the sensor effectively detects changes in analyte concentration, which is attributed to the enhanced surface properties and active sites provided by the hydrogen reduction process. The calibration curve constructed from the response data shows a strong correlation, underscoring the sensor's reliability in practical applications. Furthermore, this linear response suggests potential for quantitative analysis of 1-octen-3-ol in various environments, highlighting the effectiveness of hydrogen-reduced $NiWO_4$ as a viable sensing material for VOCs. Additionally, the NWH2 sensor's response to 1-octen-3-ol showed a closer fit to the exponential function (Figure 5-9d). As the concentration of 1-octen-3-ol increased, the sensor output exhibited a rapid initial increase, followed by a gradual slowing at higher concentrations, reflecting the saturation behavior common to gas sensors. This behavior suggests that as the analyte concentration increases, the active sites on the sensor surface become more occupied, resulting in a diminishing marginal benefit to the response. The exponential fit showed that at lower concentrations, small changes in 1-octen-3-ol concentration led to significant changes in the sensor response, which is critical for high-sensitivity detection. In comparison, at higher concentrations, the response tended to stabilize due to saturation effects. This exponential correlation highlights the effective sensing capability of hydrogen-reduced $NiWO_4$ for the detection of 1-octen-3-ol, especially in applications requiring high sensitivity at low

concentrations. Therefore, we calculated the LoD of the NWH2 sensor, which determines the lowest gas concentration the sensor can reliably detect. A lower detection limit is crucial for ensuring safety, environmental monitoring, and sensor performance. For the specific calculation, the signal is considered valid if the signal-to-noise ratio is 3. Therefore, the theoretical LoD can be calculated as [331]:

$$LOD(ppm)=3\frac{\sigma}{k} \tag{5-3}$$

$$\sigma=\sqrt{\frac{\sum (y-y_i)^2}{N}} \tag{5-4}$$

where k is the slope of the linear calibration curve of response value vs. gas concentration (ppm), and σ is the sensor noise. y, y_i, and N represent the baseline data point, the average, and the number of data points, respectively. Specifically, the σ of the NWH2 sensor was calculated to be 0.0584, and k is 0.47. Consequently, the LoD of the NWH2 sensor is 0.373 ppm. Based on the detection of 1-octen-3-ol (1-5 ppm) within the lower concentration range, as shown in Figure 5-11, we can estimate the actual lowest detection limit at approximately 1 ppm. Based on various VOCs in the quality detection of cooked rice [23, 332, 333], selectivity tests revealed that the NWH2 sensor showed a pronounced preference for 1-octen-3-ol over other common gases, indicating its potential for use in complex environments (Figure 5-9f). Furthermore, the impact of humidity on the gas response of the NWH2 sensor was also evaluated (Figure 5-9g). Under varying humidity conditions (from 20% to 80% RH), only 19.7% response drift was observed (40 ppm 1-octen-3-ol), with the response decreasing as water molecules occupied the adsorption sites on the sensor surface. Excellent moisture resistance is evidenced by the increased water contact angle (WCA) (Figure 5-9h), as the WCA for NW and NWH2 is 98.45° and 117.78°, respectively. Hydrogen annealing enhances the material's hydrophobicity and WCA, which can be attributed to several key factors. First, the reduction reaction during hydrogen exposure may alter surface chemistry, increasing the proportion of hydrophobic functional groups while decreasing the proportion of hydrophilic functional groups. Additionally, hydrogen annealing can trigger structural rearrangement or phase transitions, promoting a more hydrophobic structure. Finally, hydrogen exposure can alleviate the internal stress within the material

and further improve its wetting behavior. Taken together, these effects highlight the potential of hydrogen annealing to optimize material properties for gas sensing detection in humid environments. To evaluate the long-term stability of the fabricated NWH2 gas sensor for practical applications, the tests were conducted over three consecutive weeks under ambient conditions, with a target analyte concentration of 24 ppm 1-octen-3-ol. As shown in Figure 5-12, the sensor responses in week 1, week 2, and week 3 were basically maintained at around 10, indicating minimal fluctuation. These results demonstrate that the NWH2 sensor maintains a consistent and stable response over time, with no significant degradation observed throughout the testing period.

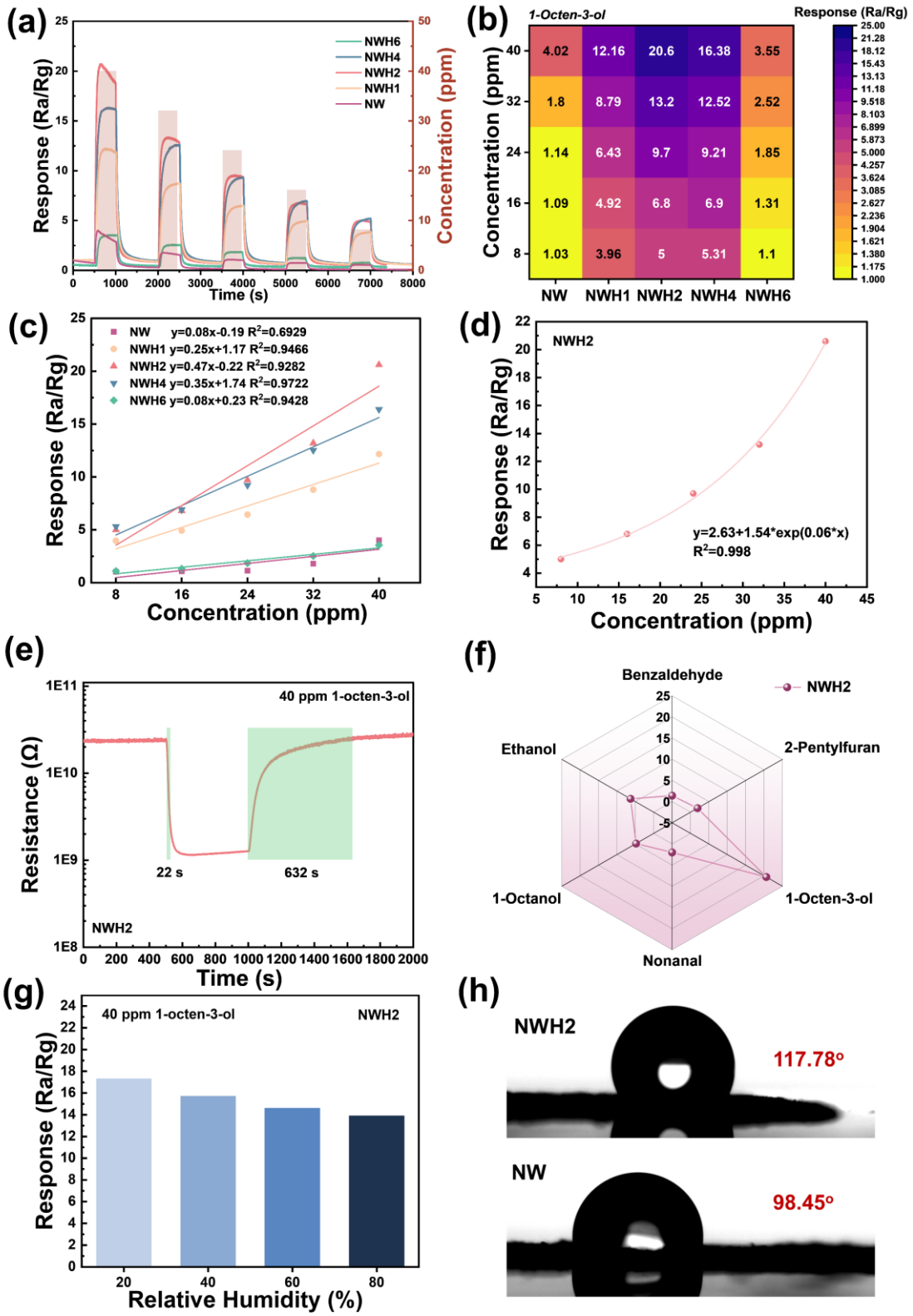

Figure 5-9 (a) Response of fabricated sensors to varying concentrations of 1-octen-3-ol at room temperature, specifically at ppm-levels of 40, 32, 24, 16, and 8 ppm; (b) response values of fabricated sensors to different concentrations 1-octen-3-ol at room temperature (40, 32, 24, 16 and 8 ppm); (c) linear correlation between sensor response and 1-octen-3-ol concentrations (40, 32, 24, 16 and 8 ppm); (d) concentration-dependent response curves of the NWH2 based sensor for 1-octen-3-ol; (e) single transient response curve of NWH2 based sensor to 40 ppm 1-octen-3-ol; (f) gas

response of NWH2 based sensor towards various target gases at 40 ppm; (g) response value of NWH2 sensors to 40 ppm 1-octen-3-ol at different RH; (h) WCA of NWH2 and NW sensors active layer.

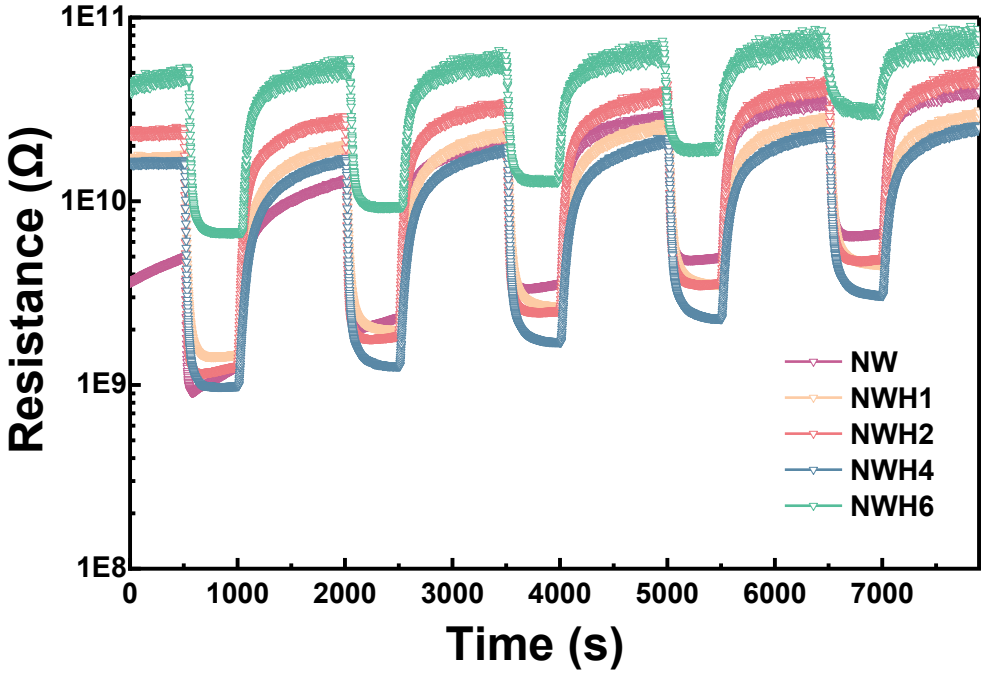

Figure 5-10 Resistive response of fabricated sensors to varying concentrations of 1-octen-3-ol at room temperature, specifically at ppm-levels of 40, 32, 24, 16, and 8 ppm.

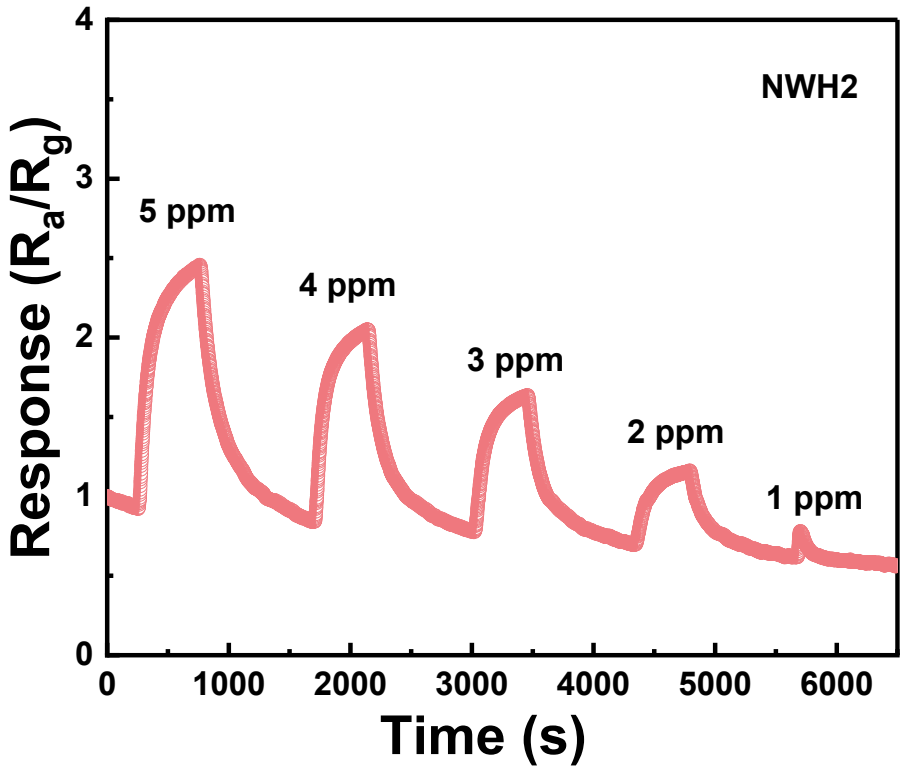

Figure 5-11 Response of NWH2 sensor to varying concentrations of 1-octen-3-ol at room

temperature, specifically at ppm-levels of 5, 4, 3, 2, and 1 ppm.

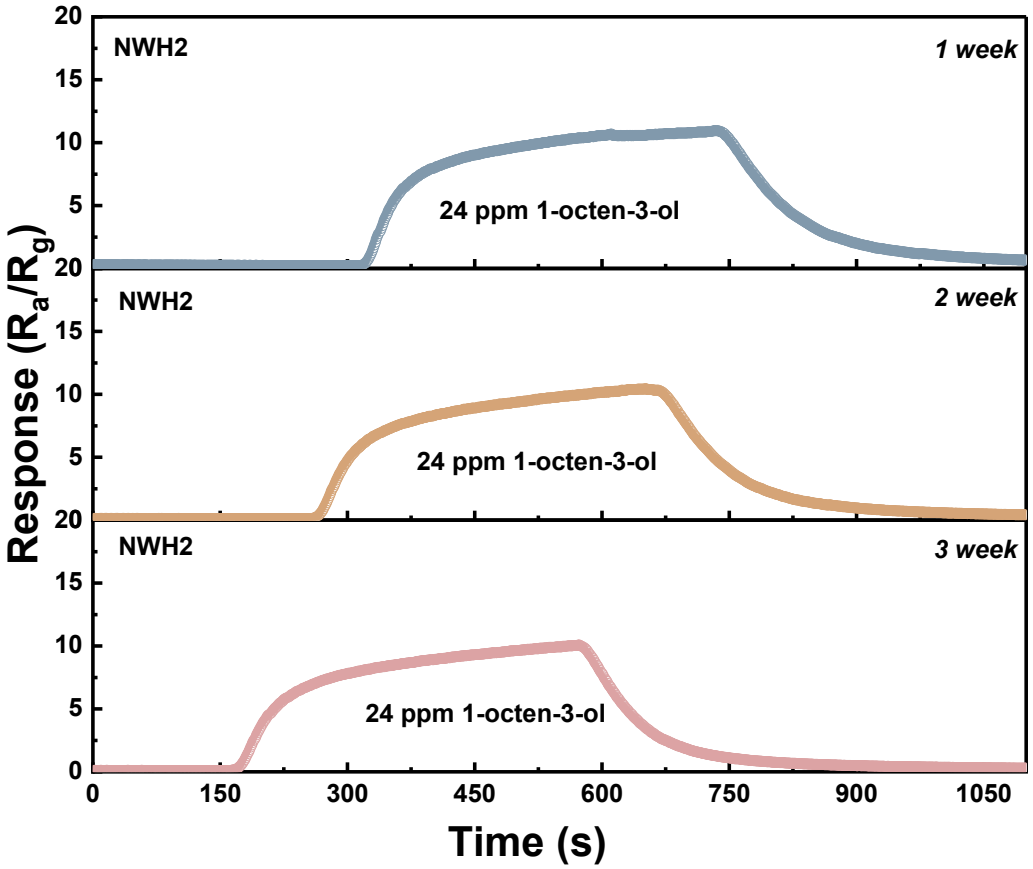

Figure 5-12 Long-term stability of the NWH2 gas sensor to 24 ppm 1-octen-3-ol at room temperature.

5.2.3 Gas sensing mechanism

The enhancement of the gas-sensing properties of $NiWO_4$ through hydrogen reduction primarily involves the formation of O_V, which significantly facilitates the adsorption of oxygen and its subsequent interaction with 1-octen-3-ol. The following presents a detailed analysis of the oxygen adsorption model mechanism that underpins the improved sensitivity of hydrogen-reduced $NiWO_4$ toward 1-octen-3-ol (Figure 5-13).

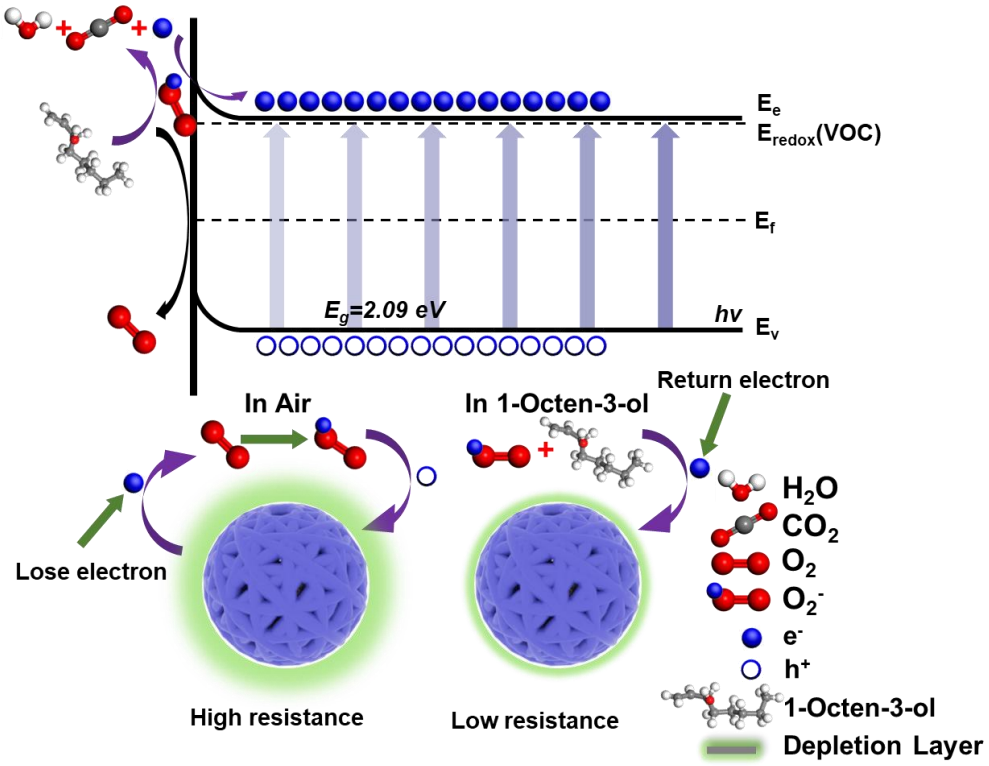

Figure 5-13 Schematic illustration of the sensing mechanism when the NWH2-based sensor is exposed to air and 1-octen-3-ol.

Formation of O_V: Hydrogen reduction of $NiWO_4$ removes lattice oxygen, resulting in the formation of O_V. These defects serve as active sites that alter the material's electronic properties, increasing its overall conductivity and promoting electron migration.

Enhanced oxygen adsorption: the presence of O_V significantly increases the adsorption capacity of the reduced $NiWO_4$ for molecular oxygen (O_2). These vacancies create localized states in the material's electronic structure that react with O_2 molecules, facilitating their adsorption onto the surface. The adsorbed oxygen will exist as O2- at temperatures below 150°C, enhancing surface reactivity while increasing the sensor's resistance. The reaction processes are as follows (Equation (5-5) and (5-6)) [334, 335]:

$$O_2(gas) \rightarrow O_2\ (ads) \qquad (5\text{-}5)$$

$$O_2(ads) + e^- \rightarrow O_2^-\ (ads) \qquad (5\text{-}6)$$

Reaction with 1-octen-3-ol: when 1-octen-3-ol interacts with the oxygen-adsorbed

$NiWO_4$ surface, it undergoes redox reactions facilitated by the O_2^-. The created O_V will enhance the material's surface activity, making it easier to react with 1-octen-3-ol. The 1-octen-3-ol molecules interact with the negatively charged adsorbed oxygen. This interaction leads to the removal of hydrogen atoms from alcohol, producing intermediate species as follows: Equations (5-7) and (5-8):

$$C_8H_{16}O(g) \rightarrow C_8H_{16}O\ (ads) \qquad (5\text{-}7)$$

$$2C_8H_{16}O(ads) + O_2^-(ads) \rightarrow 2C_8H_{14}O(ads) + 2H_2O(g) + e^- \qquad (5\text{-}8)$$

The oxidation of 1-octen-3-ol generates reactive intermediates that further react with additional adsorbed O_2 molecules. This process may create more radical species that enhance the reactivity of the sensor interface and reduce the sensor resistance. Ultimately, the reaction may generate carbon dioxide and water molecules [232, 336, 337]. As the reaction progresses, electrons are transferred between the gas molecules and the $NiWO_4$ surface, leading to a measurable change in electrical resistance. The enhanced oxygen adsorption, combined with the high density of O_V, facilitates rapid electron transfer, contributing to faster response times and higher sensitivity. The unique interaction between the modified $NiWO_4$ and 1-octen-3-ol, in the presence of adsorbed oxygen species, results in a specific change in electrical properties that is distinct from other VOCs. This selectivity is attributed to the structural alignment of the O_V and to the electronic effects it induces.

To evaluate the structural and chemical stability of the sensing material, XPS analysis was conducted on NWH2 after long-term stability testing of 1-octen-3-ol (Figure 5-14). The high-resolution spectra of Ni 2p, W 4f, and O 1s showed no noticeable shifts, and the O_V peak at ~530.5 eV remained at ~40.3%, comparable to the fresh sample, indicating preserved O_V structure. This stability is attributed to the energetically stabilized O_V within the dense monoclinic structure, which resists migration or recombination. The redox-inert behavior of Ni^{2+} and W^{6+} toward the target gas at room temperature also enhanced the robustness of NWH2. These results confirm the long-term reliability of NWH_2.

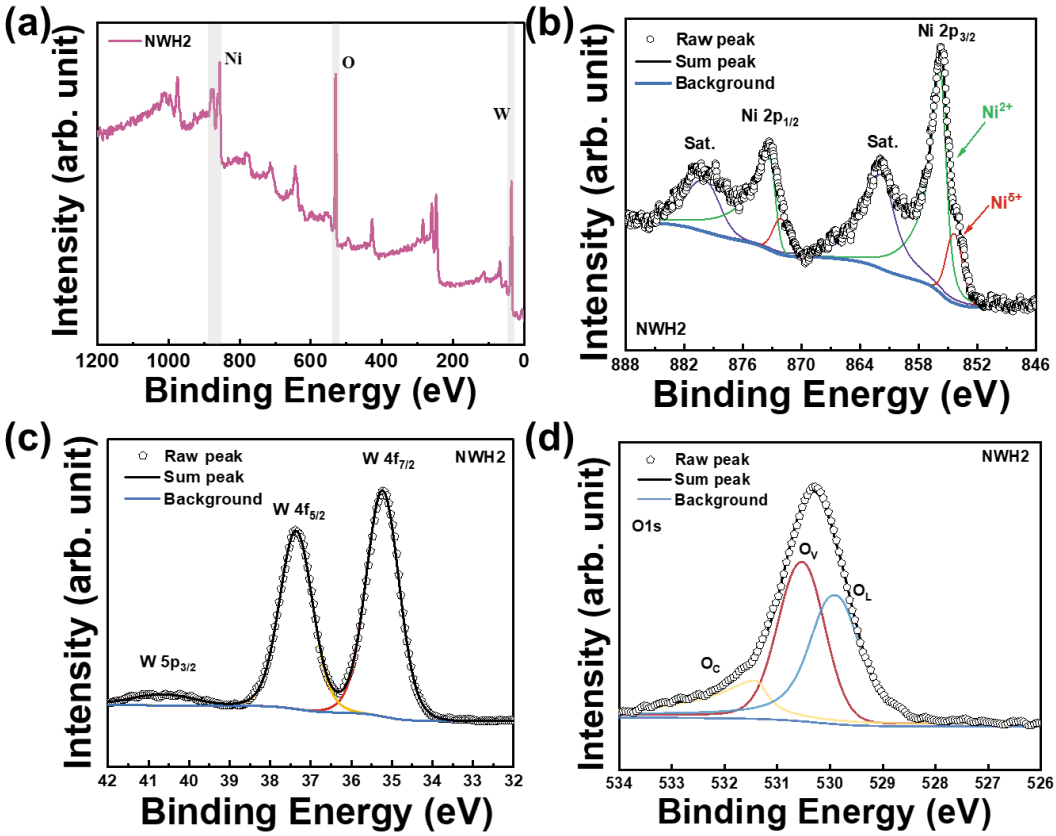

Figure 5-14 (a) Full XPS spectra of NWH2, high-resolution XPS spectra of NWH2 for (b) Ni 2p, (c) W 4f, and (d) O 1s after long-term stability testing to 24 ppm 1-octen-3-ol at room temperature.

In Figure 5-15a to Figure 5-15c, the geometry structures of $NiWO_4$ and O_V-$NiWO_4$ were acquired following the construction of 3×3×1 supercells of the (010) surface $NiWO_4$. MD simulation details are shown below. Force field used: [COMPASS]; Simulation Time: [500 ps]; Time Step: [1.0 fs]; System Size: [3 × 3 × 1 supercell of $NiWO_4$]; Temperature Control Method: [Nose-Hoover thermostat at 298.0 K]; Boundary Conditions: Periodic boundary conditions were applied in all three dimensions. As shown in Figure 5-15d to Figure 5-15e, with the gradual approach of 1-octen-3-ol toward the material surface and the simultaneous diffusion of O_2 molecules, a shift in adsorption kinetics is observed. This transition aligns well with the previously proposed oxygen adsorption model. As depicted in Figure 5-15f, between 1 ps and 50 ps, the interaction energy (E_{int}) in both M1 and M2 systems decreases significantly, indicating that 1-octen-3-ol is approaching the surface and entering the attractive interaction region. This phenomenon is primarily driven by van der Waals forces. In the M1 system, E_{int} gradually stabilizes during the 50-500 ps interval. In the M2 system, E_{int} reaches a relatively stable state during the 50-200 ps period, suggesting the

formation of a strong, stable adsorption complex between 1-octen-3-ol and surface-active sites. This process is mainly driven by polarity enhancement induced by O_V and hydrogen bonding interactions. However, during the 200-500 ps period, E_{int} exhibits noticeable fluctuations, which may result from transitions of the adsorbed molecule between different active sites, microscopic surface reconstruction, or a dynamic equilibrium between adsorption and desorption. This adsorption behavior reflects moderate binding strength and good dynamic response of the material toward 1-octen-3-ol, thereby enhancing the sensitivity, reversibility, and selectivity and optimizing its overall performance in VOC detection. To quantitatively analyze the interactions between gas-phase molecules and the sensing material, the mean-square displacement (MSD) was calculated, as shown in Figures 5-15g and 5-15h. In both M1 and M2 adsorption systems, O_2 molecules exhibit relatively high diffusion coefficients (D), measured at $3.06*10^{-4}$ cm^2/s and $4.33*10^{-4}$ cm^2/s, respectively. In contrast, the diffusion of 1-octen-3-ol is significantly hindered due to adsorption constraints, with D values of $1.73*10^{-4}$ cm^2/s in M1 and $1.58*10^{-4}$ cm^2/s in M2. Additionally, the MSD curve in M2 shows a more pronounced linear relationship, indicating a more stable adsorption-desorption process, further highlighting the critical role of O_V modulation in optimizing surface interactions and stabilizing the sensing mechanism. The simulation results also reveal that oxygen-deficient surfaces exhibit enhanced binding affinity for 1-octen-3-ol through strong hydrogen bonding and dipole interactions near vacancy sites. Notably, the molecular orientation favors electron donation from the hydroxyl group of 1-octen-3-ol to the electron-deficient vacancy environment, accompanied by local structural distortion and electron density redistribution. This suggests that O_V not only promote the adsorption and activation of oxygen molecules, as depicted in the classical surface redox pathway (Figure 5-13), but may also directly participate in charge transfer processes at the analyte interface. Therefore, a synergistic dual-pathway mechanism is also possible: (i) chemisorbed oxygen species (O_2^-) react with 1-octen-3-ol to generate electrons and modulate the resistance; (ii) concurrently, O_V act as electron acceptors and polarization centers, directly contributing to conductivity modulation, especially under room temperature conditions. This explains the sharp performance enhancement observed in O_V-rich samples (e.g., NWH2), and suggests that the sensing process is not exclusively reliant on oxygen molecule activation. These findings bridge the microscopic insights from MD simulations (Figure 5-15) with the macroscopic redox

model (Figure 5-13), providing a more comprehensive mechanistic understanding of the enhanced gas-sensing behavior.

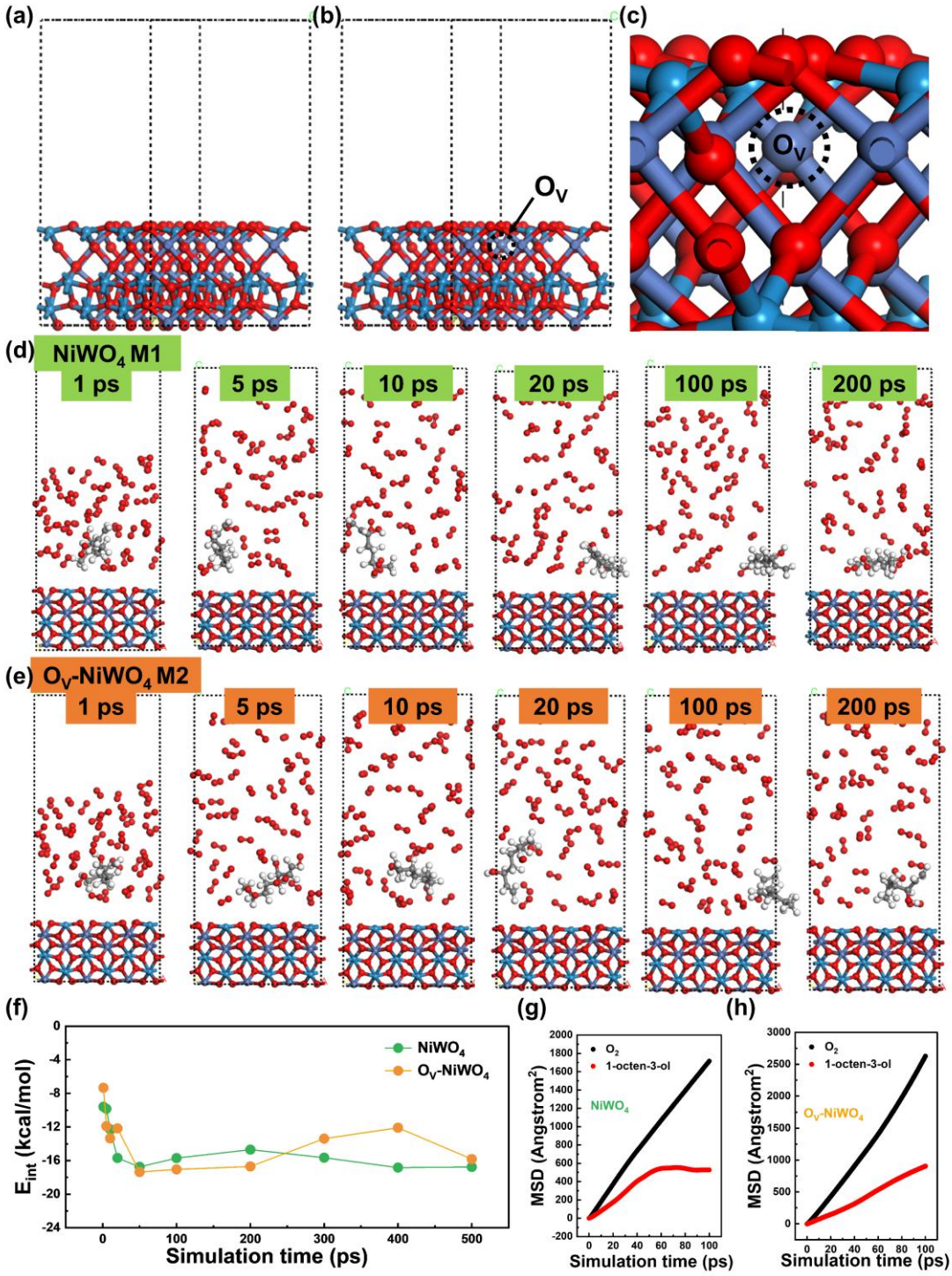

Figure 5-15 Geometry structures of (a) $NiWO_4$ and (b-c) O_V-$NiWO_4$. MD simulation snapshots of (d) $NiWO_4$ and (e) O_V-$NiWO_4$, (f) E_{int} for the dynamic process of 1-octen-3-ol and oxygen diffusion on $NiWO_4$ and O_V-$NiWO_4$. MSD of 1-octen-3-ol and oxygen diffusion on (g) $NiWO_4$ and (g) O_V-$NiWO_4$.

5.3 Conclusions

The investigation into the sensing properties of $NiWO_4$ micro-flowers, both in their untreated state and post-hydrogen treatment, provides key insights into the detection of 1-octen-3-ol. The use of hydrogen thermal treatment significantly enhances the concentration of O_V within the $NiWO_4$ micro-flowers, as confirmed by comprehensive surface analysis techniques. The O_V facilitated superior adsorption and interaction with 1-octen-3-ol molecules, which were identified as the key factors enhancing the gas-sensing performance. XPS analysis confirmed a significant increase in O_V content (from 28.5% to 40.3%), while EPR and UV-Vis results revealed an increase in unpaired electrons and a reduced band gap, indicative of improved surface reactivity and conductivity. The O_V act as active adsorption sites for oxygen species (e.g., O_2^-), facilitating their interaction with 1-octen-3-ol molecules through surface redox reactions. Consequently, the electron transfer process is accelerated, leading to faster response dynamics and higher sensitivity. Furthermore, the presence of abundant O_V enhances humidity resistance by modifying the surface energy and wettability of the sensing layer. The hydrogen reduction process not only generates essential O_V but also optimizes the gas-sensing capabilities of $NiWO_4$ towards this specific analyte. Our proposed model of oxygen adsorption, characterized by enhanced oxygen uptake and improved reaction kinetics, elucidates the fundamental mechanisms underlying the sensing process. This study highlights the transformative potential of modifying $NiWO_4$ through hydrogen reduction, paving the way for the development of high-performance gas sensors. Such advancements hold significant promise for applications in environmental monitoring and various industrial sectors, where precise detection of VOC is critical.

Chapter 6: CuO-Decorated Bismuth Subcarbonate Gas Sensor Arrays for Cooked Rice Quality Assessment

In this chapter, the single $CuO_x/Bi_2O_2CO_3$ (Cu_x-BC) (where x = 0, 10, 20, 30, and 40) gas sensor was employed to detect nonanal, benzaldehyde, and 1-octen-3-ol individually, which are the predominant VOCs released from various types of cooked rice, thereby validating its initial sensing capabilities for VOCs. Then, we established a gas-sensing array consisting of a printed circuit board (PCB) equipped with a 4 × 1 array of data acquisition units, each featuring voltage conversion and a microcontroller unit, for efficient detection of cooked rice quality. This array was based on the synthesized Cu_x-BC materials. The integration of a Cux-BC-based sensor array with embedded electronics presents a promising platform for intelligent monitoring of cooked rice quality.

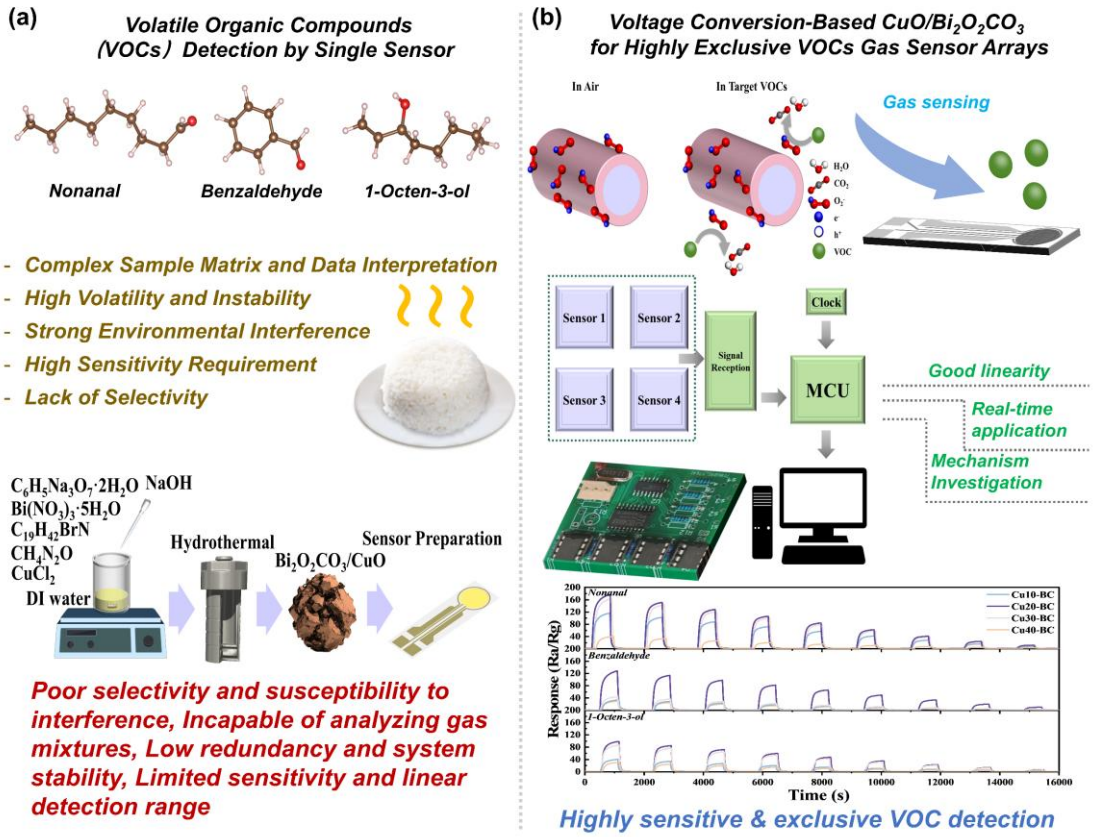

Schematic diagram 6-1 Graphical abstract of this chapter.

Bismuth subcarbonate ($Bi_2O_2CO_3$) is a notable n-type semiconductor characterized by its Aurivillius/Sillén-related structure, formed by alternating layers of $Bi_2O_2^{2+}$ and CO_3^{2-} [212]. This material has been systematically used in energy storage [338], photocatalysis [339], cancer treatment [340], and gas sensing [200] due to its unique physical and chemical properties. However, sensors that rely exclusively on bismuth subcarbonate $Bi_2O_2CO_3$ (BC) often struggle to achieve high sensitivity, robust stability, and selective detection simultaneously. To address these limitations, we can use the surface depletion mechanism. Specifically, creating an additional electron-depletion layer at the interface of heterostructured TSMOX cores can significantly enhance the gas-sensing response compared to a single TSMOX [341]. In this context, we aimed to enhance the VOCs sensing capabilities by forming $CuO/Bi_2O_2CO_3$ (Cu-BC) heterostructures. This was accomplished by adding $CuCl_2$ with a metal basis grade during the synthesis process. The use of chemical reagents with a metal basis grade optimizes the electrical and chemical properties of Cu-BC, reduces side reactions during synthesis, and enhances the stability of BC-based materials. This approach facilitates a more controlled preparation of materials. Nevertheless, individual gas sensors continue to encounter several practical challenges, including poor selectivity, limited sensitivity, and susceptibility to environmental influences. Consequently, assembling gas sensors into an array is a more effective strategy for practical detection [342, 343]. For instance, Jiang et al. proposed a framework for optimizing gas sensor arrays by considering factors such as material composition, morphology, metal doping, and operating temperature. They established a database using 32 SMOX sensors, including SnO_2, In_2O_3, and WO_3, with varying morphologies, dopants (such as Pd, Pt, Ce, Ru, and Rb), and operating temperatures ranging from 250° to 370°C. This database recorded the sensor array responses to six gases at low-ppm concentrations. From a total of 10,518,300 possible material-temperature combinations, an optimized sensor array was constructed, demonstrating enhanced selectivity. Notably, the integrated chip successfully identified all target gases and their mixtures after applying a linear discriminant analysis transformation [344]. Similarly, Yang et al. developed a six-sensor micro-electromechanical systems (MEMS) microarray, along with a wireless, battery-free flexible e-nose controlled by a smartphone. By applying ensemble models (MLP, RF, XGBoost, and LGBM), they achieved high classification accuracy for VOCs

and precise predictions of their concentrations. This flexible e-nose offers promising applications in monitoring vehicle and indoor air quality [345].

6.1 Synthesis of CuOx-BC Micro-structures

The reagents were used without further purification. Bismuth nitrate pentahydrate ($Bi(NO_3)_3 \cdot 5H_2O$) (AR grade, CAS: 10035-06-0), copper(II) chloride ($CuCl_2$) (99.99% metals basis, CAS: 7447-39-4), urea (CH_4N_2O) (AR grade, CAS: 57-13-6), trisodium citrate dihydrate ($C_6H_5Na_3O_7 \cdot 2H_2O$) (AR grade, CAS: 6132-04-3), hexadecyl trimethyl ammonium bromide ($C_{19}H_{42}BrN$) (AR grade, CAS: 57-09-0), sodium hydroxide (NaOH) (AR grade, CAS: 1310-73-2), nitric acid (HNO_3) (ACS, 70%, CAS: 7697-37-2), 1-octen-3-ol ($C_8H_{16}O$) (CAS: 3391-86-4), nonanal ($C_9H_{18}O$) (AR grade, CAS: 124-19-6) and benzaldehyde (C_7H_6O) (AR grade, CAS: 100-52-7) were purchased from Aladdin Biochemical Technology Co., Ltd., China. The synthetic route of heterostructured $CuO/Bi_2O_2CO_3$ micro-flowers is illustrated in Figure 6-1. Typically, 1.94 g of $Bi(NO_3)_3 \cdot 5H_2O$ and varying quantities of $CuCl_2$ (0 mg, 200 mg, 400 mg, 600 mg, and 800 mg) were uniformly dispersed in 50 mL of deionized water. The mass ratios of $CuCl_2$ to $Bi(NO_3)_3 \cdot 5H_2O$ were adjusted to around 0%, 10%, 20%, 30%, and 40%. Subsequently, 0.48 g of CH_4N_2O, 2.35 g of $C_6H_5Na_3O_7 \cdot 2H_2O$, and 0.4 g of $C_{19}H_{42}BrN$ were added to the mixture. The resulting solution was stirred for 30 minutes, and the pH was adjusted to 7 using a NaOH and HNO_3 solution under stirring. The homogeneous mixture was then transferred into a Teflon-lined stainless-steel autoclave (100 mL capacity) and maintained at 200°C for 24 hours. After the reaction, the products were recovered through centrifugation and washed several times with absolute ethanol and deionized water. The purified products were subsequently dried at 60°C for 12 hours. The dried precursor was calcined in a muffle furnace at 250°C for 1 hour. The final products, namely pristine BC and CuO/BC, were designated as BC, Cu10-BC, Cu20-BC, Cu30-BC, and Cu40-BC, respectively.

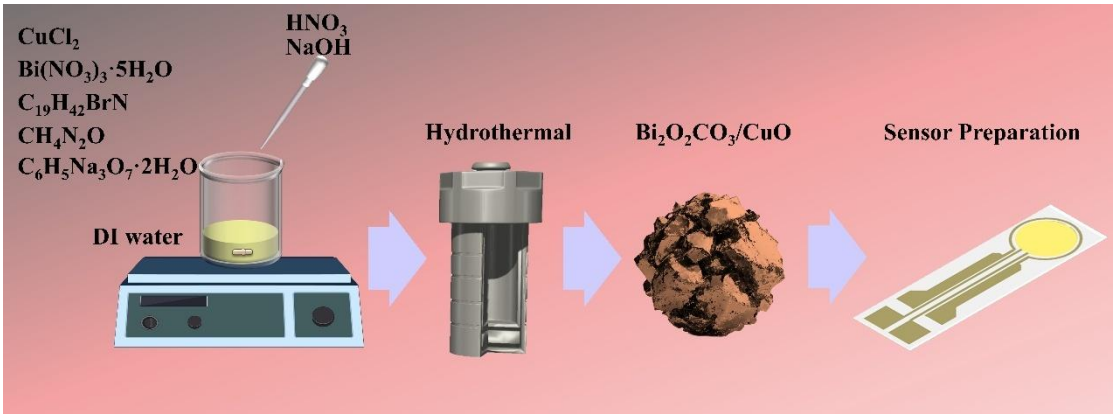

Figure 6-1 Schematic illustrations of the fabrication process of Cux-BC microstructure.

6.2 Results and discussion

6.2.1 Characterization results

XRD analysis was performed to determine the composition and structural properties of the synthesized products and to evaluate compositional changes under varying synthesis conditions. As shown in Figure 6-2a, the pristine BC sample exhibits a crystalline phase consistent with orthorhombic $Bi_2O_2CO_3$ (JCPDS No. 84-1752), characterized by three prominent diffraction peaks at 23.9°, 30.3°, and 32.7°, corresponding to the (121), (161), and (002) crystal planes, respectively. Following the addition of $CuCl_2$ at the metal basis grade during the synthesis process, two additional peaks emerged in the XRD diffractogram of the resultant sample, located approximately 36.6° and 43.6°, which are attributable to the (111) and (200) crystal planes of the cubic CuO structure (JCPDS No. 78-0428). Notably, the peak corresponding to the (200) crystal plane of the CuO phase has shifted to a higher angle compared to the standard PDF card. This shift indicates lattice compression, suggesting that CuO has a smaller lattice constant (a = b = c = 4.245 Å) compared to the substrate material, BC, which has lattice constants of a = c = 5.468 Å and b = 27.320 Å. As the amount of $CuCl_2$ in the synthesis gradually increases from 200 mg to 800 mg, the intensity of the peak corresponding to the CuO (200) crystal also increases, confirming the successful formation of the CuO/BC p-n heterostructure.

The morphology of the Cu20-BC sample was examined using scanning electron microscopy (SEM) and transmission electron microscopy (TEM) techniques. As

illustrated in Figure 6-2b, Cu20-BC exhibits a micro-flower structure with semi-hollow characteristics, which is further confirmed by the TEM images (Figure 6-2c to Figure 6-2e). Additionally, defects within the Cu20-BC structure are clearly visible in the high-resolution transmission electron microscopy (HRTEM) lattice fringe image (Figure 6-2f), verifying the presence of defects in the structure of the Cu20-BC sample. The selected area electron diffraction (SAED) pattern (Figure 6-2g) indicates the single-crystalline nature of the Cu20-BC sample. Furthermore, as shown in Figure 6-2h to Figure 6-2n, the energy-dispersive X-ray spectroscopy (EDS) elemental mapping reveals a uniform distribution of Bi, C, O, and Cu elements throughout the Cu20-BC micro-flower sample.

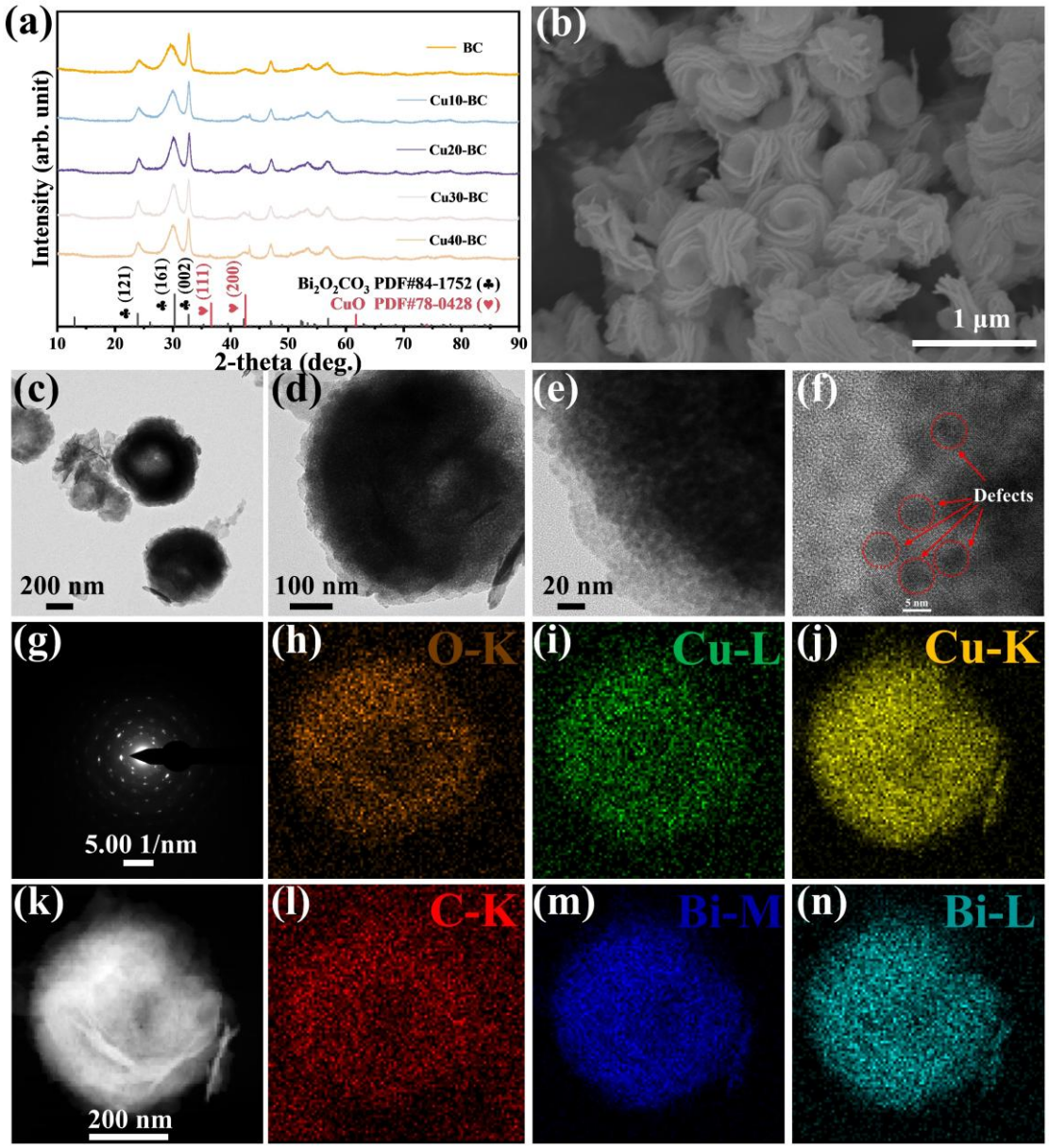

Figure 6-2 (a) XRD patterns of BC, Cu10-BC, Cu20-BC, Cu30-BC, and Cu40-BC samples, (b) SEM images of the Cu20-BC sample, (c-e) TEM images of the Cu20-BC sample, (f) HRTEM image of defective sites of Cu single atom in the Cu20-BC sample, (g) SAED pattern of the Cu20-BC sample, (h-j, l-n) EDS elemental mapping images of O, Cu, C, and Bi, (k) HAADF-STEM image of the Cu20-BC sample.

The XPS analysis was conducted to investigate the surface chemical composition and elemental states, as shown in Figure 6-3. The presence of Bi, C, Cu, and O in the samples was confirmed (Figure 6-3a). The O 1s spectrum of Cu20-BC, shown in Figure 6-3b, reveals three components centered at 528.9 eV (O_L), 529.9 eV (O_V), and 531.6

eV (O_C) [346]. Comparative analysis of the O_V component derived from the deconvolution of the O 1s spectra indicates a significantly higher concentration of O_V (53.8%) in Cu20-BC compared to pristine BC (42.3%). This increase in O_V suggests that lattice mismatch induces alterations in the spatial distribution of electrons or ions within Cu20-BC, leading to the formation of excess O_V. And the formation of a p-n heterostructure may enhance sensing properties, as vacancy sites could facilitate oxygen adsorption [320, 347]. Additionally, a comparison of the Bi 4f peak in Cu20-BC shows a narrowing effect relative to pure BC samples (Figure 6-3c). This phenomenon can be attributed to the reorganization of electronic states at the CuO-BC interface, leading to increased electron localization within the valence and conduction bands. The C 1s spectrum of Cu20-BC (Figure 6-3d) was deconvoluted into two distinct components: one centered at 284.1 eV corresponds to adventitious carbon (AC) species, while the one centered at 287.9 eV is associated with ester groups. These observations are consistent with the C 1s spectrum recorded for the BC sample [220, 221]. The Cu 2p spectrum indicates the presence of the Cu^{2+} oxidation state, as confirmed by Figure 6-3e. The presence of Cu^{+} $2p_{3/2}$ and Cu^{+} $2p_{1/2}$ peaks suggests that Cu^{2+} is partially reduced to Cu^{+} due to the presence of O_V in the samples. In a related study, Wang et al. demonstrated that the addition of $CuCl_2$ during material modification successfully stabilized single-atom Cu on ultrathin $WO_{2.72}$ nanowires, achieving high-sensitivity detection of toluene [32], as we have successfully loaded CuO, primarily due to the differences in the properties of the support and the varying amounts of copper loaded.

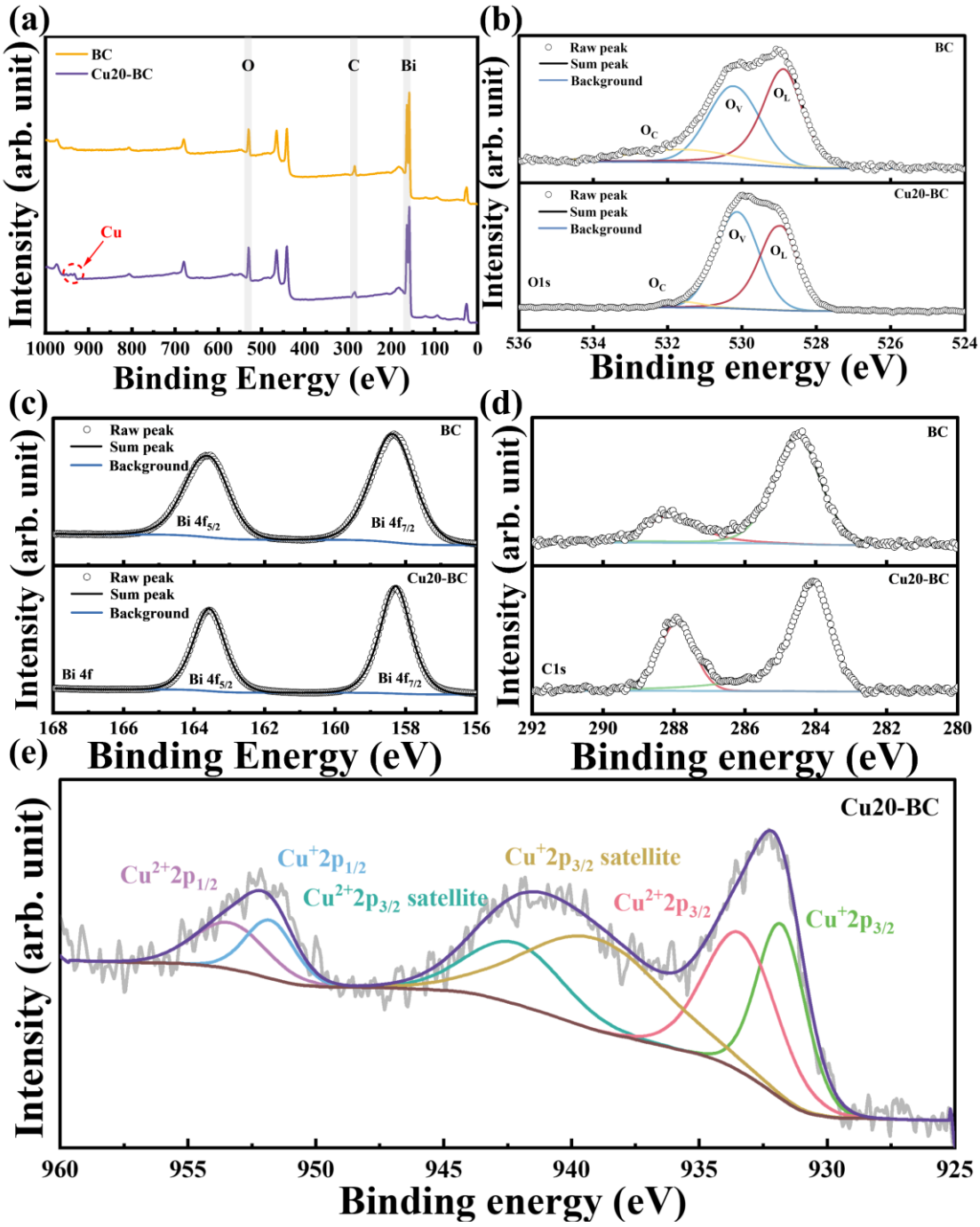

Figure 6-3 (a) XPS survey scan and core-level spectra of (b) O 1s, (c) Bi 4f, (d) C 1s, and (e) Cu 2p regions.

FT-IR spectroscopy was employed to examine the structural bonding associated with functional groups. As illustrated in Figure 6-4a, the absorption band at 851 cm^{-1} corresponds to the out-of-plane bending modes of CO_3^{2-}. Additionally, the bands at 1386 cm^{-1} and 1532 cm^{-1} are assigned to the antisymmetric vibrational modes of CO_3^{2-} [348]. To further investigate and confirm the presence of O_V, EPR spectra were

conducted on the as-prepared samples. The EPR signal can be attributed to paramagnetic O_V, which creates intermediary energy levels within the band gap. As illustrated in Figure 6-4b, the EPR signal at a g factor of 2.003 is detected in the as-prepared samples, corresponding to unpaired electrons in O_V sites, thereby confirming the existence of O_V. Furthermore, the signal intensity increased in the following order: Cu20-BC > Cu30-BC > Cu10-BC > Cu40-BC > BC, with Cu20-BC exhibiting the highest content of O_V. Additionally, the calculated intensity signal in Figure 6-4c exhibits asymmetric characteristics, which are related to the localization of the defect center on the surface. The UV-Vis absorption spectra of all samples were obtained, as shown in Figure 6-4d. The bandgap of the BC and Cu20-BC was calculated to be 2.79 eV and 2.47 eV, respectively, according to the Tauc equation (Figure 6-4e). A reduced band gap indicates that it is easier to excite electrons into the conduction band, thereby enhancing the conductivity of the material and improving the responsiveness to gas molecules. The thermal stability of Cu20-BC was investigated using thermogravimetric analysis (TGA) (Figure 6-4f and Figure 6-4g), which shows two stages of large mass losses corresponding to the evaporation of adsorbed water (1.01 wt%) and the release of CO_2 during decomposition (8.93 wt%) of the sample, respectively. The BET results for BC and Cu20-BC are shown in Figure 6-4h and Figure 6-4i. The successful formation of a heterostructure in Cu20-BC, characterized by a greater abundance of Ov, leads to an increased BET surface area (76.667 $m^2 \cdot g^{-1}$), compared to the BC sample (BET surface area: 13.069 $m^2 \cdot g^{-1}$). Specifically, the loading of CuO induces the reorganization of the BC framework, resulting in the formation of a hollow structure and an increase in the specific surface area. Furthermore, the loaded CuO provides more active sites, significantly enhancing the material's adsorption capacity for gases and effectively increasing the utilization of the surface area. During CuO loading, BC particle growth is promoted, leading to aggregation into smaller units that further increase the material's specific surface area.

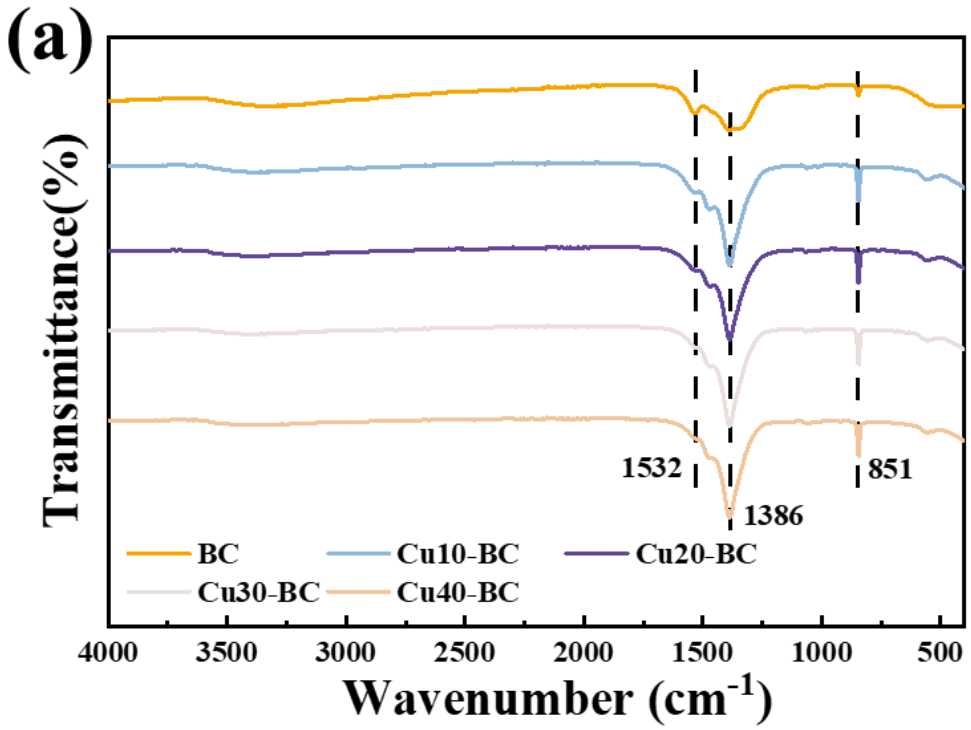

Figure 6-4 (a) FT-IR spectrum of all samples.

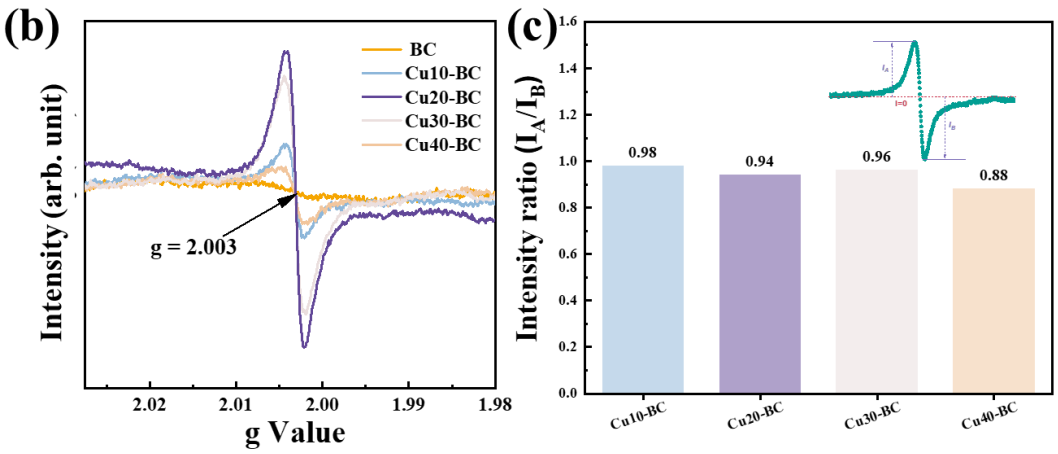

Figure 6-4 (b) EPR spectra of all samples, (c) intensity ratio of symmetry parameters of defect signal. The ratio of symmetry coefficients is defined as I_A/I_B.

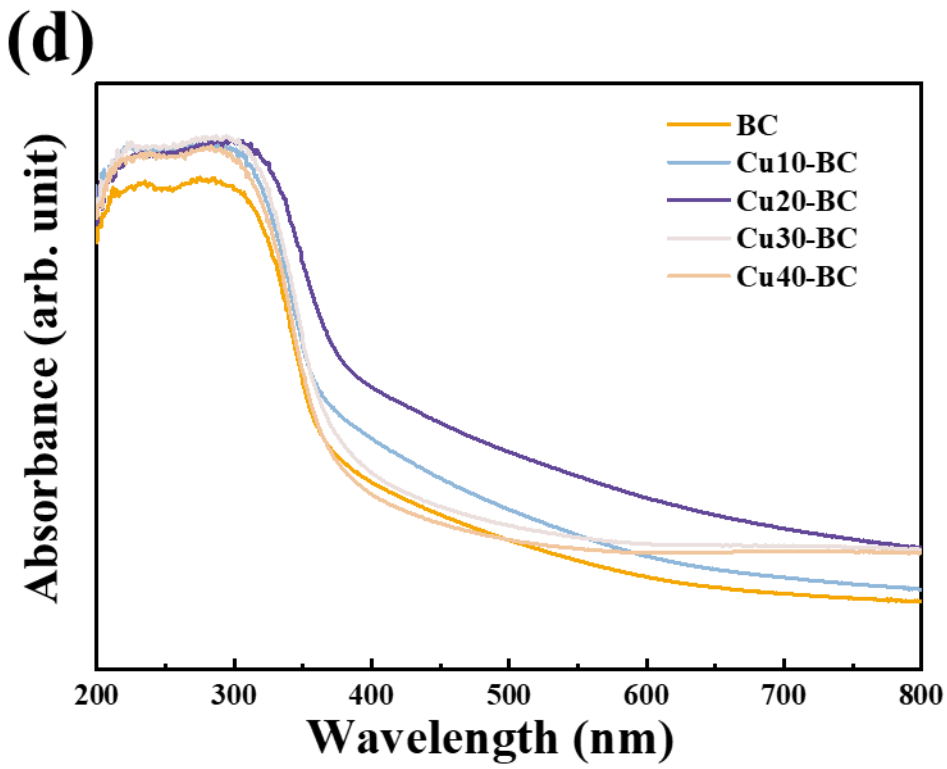

Figure 6-4 (d) UV-Vis absorption spectra of all samples.

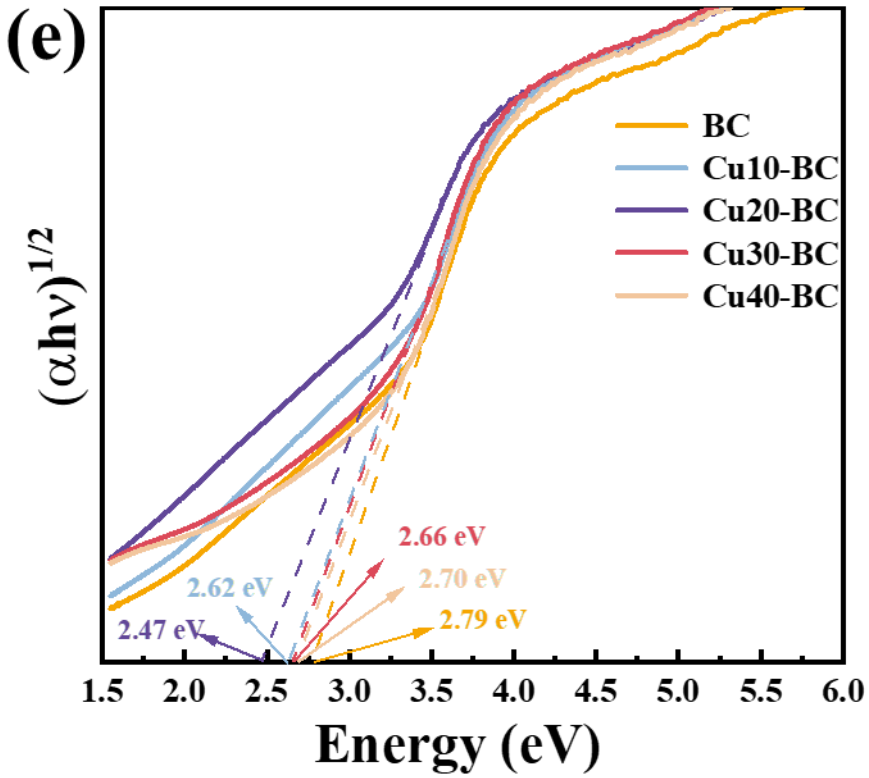

Figure 6-4 (e) Tauc plots of all samples.

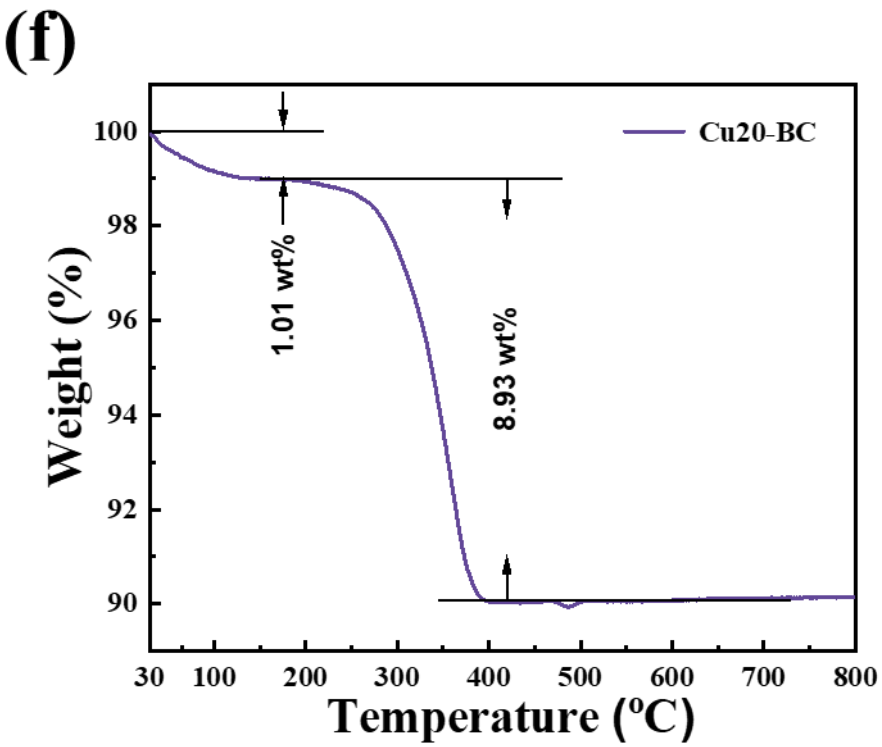

Figure 6-4 (f) TGA curves for Cu20-BC.

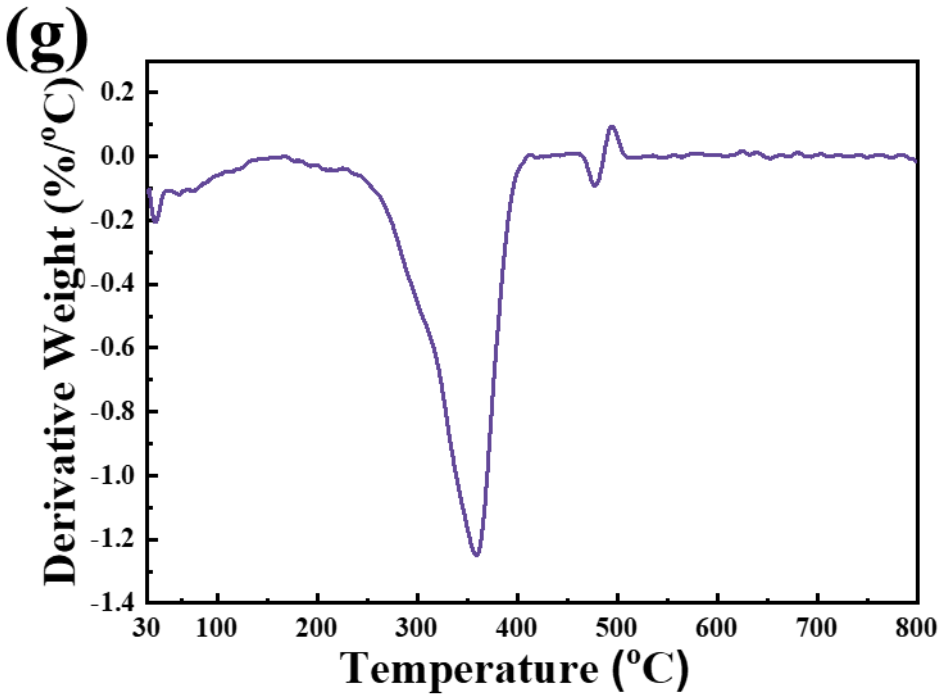

Figure 6-4 (g) Derivatives of the TGA curves for Cu20-BC.

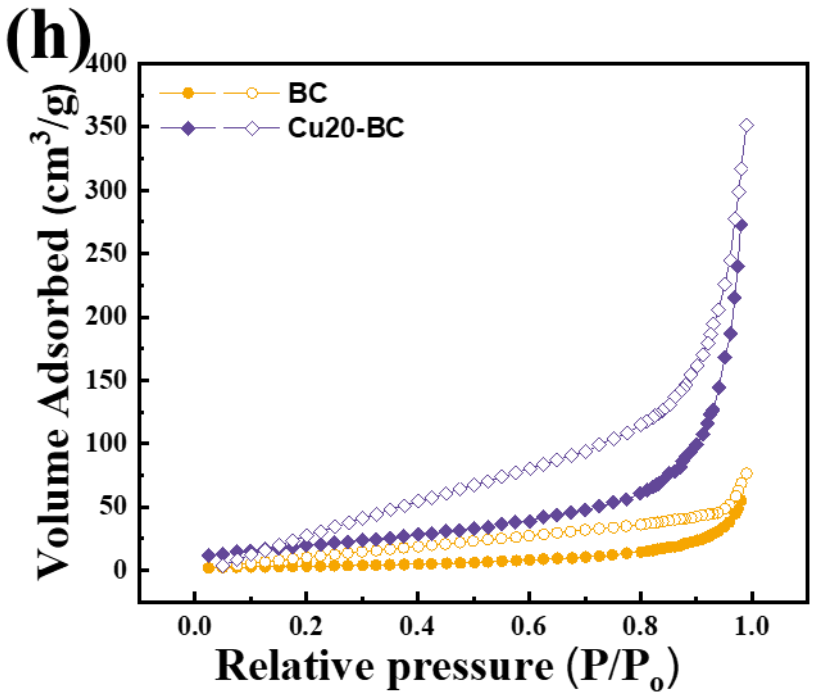

Figure 6-4 (h) N_2 adsorption-desorption isotherms of BC and Cu20-BC.

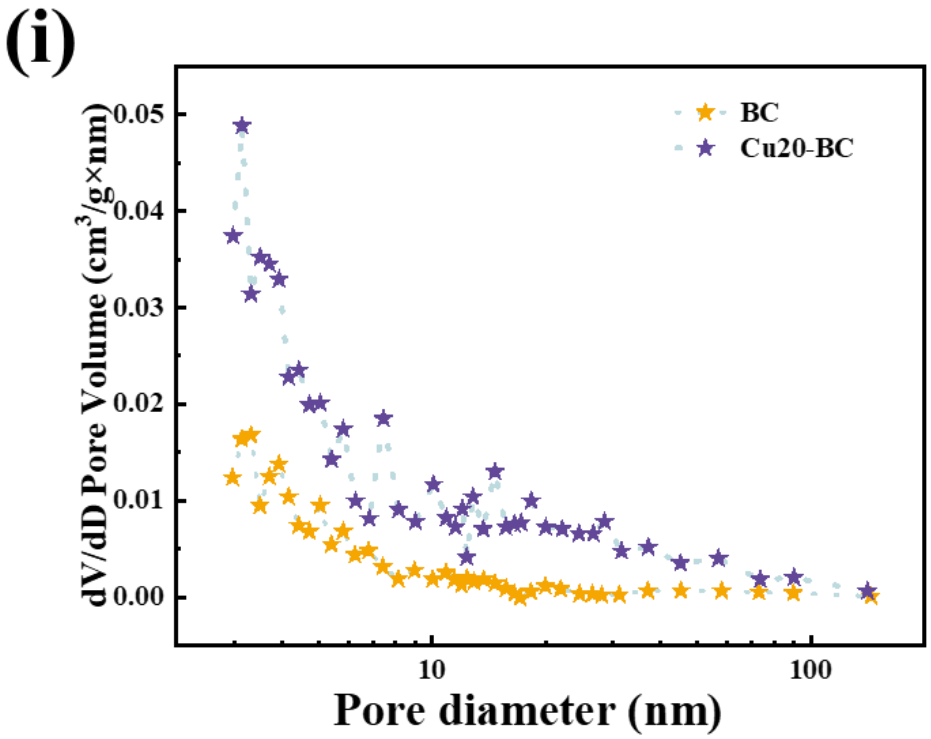

Figure 6-4 (i) Pore-size distributions of BC and Cu20-BC.

6.2.2 Gas sensing performance

To assess the potential of the as-fabricated sensor array for evaluating the quality of cooked rice, we first verified the presence of VOCs released from cooked rice (raw materials, including fresh uncooked rice and uncooked rice stored for six months) using headspace solid-phase microextraction (HS-SPME) combined with GC-MS. As shown in Figure 6-5a, the presence of benzaldehyde and nonanal was confirmed in cooked rice prepared from grains under fresh conditions, while benzaldehyde, nonanal, and 1-octen-3-ol were detected in cooked rice prepared from grains stored for six months. Additionally, the mass spectra of the benzaldehyde, nonanal, and 1-octen-3-ol in cooked rice made from grains stored for six months are depicted in Figure 6-5b.

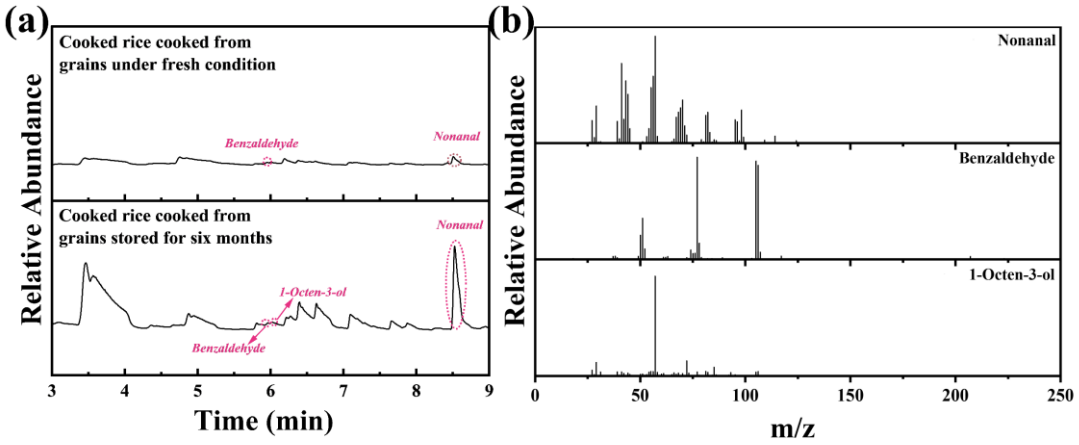

Figure 6-5 (a) Chromatogram of a representative cooked rice cooked from grains under fresh conditions and cooked rice prepared from grains stored for six months, (b) mass spectra of the benzaldehyde, nonanal, and 1-octen-3-ol in cooked rice prepared from grains stored for six months.

For the specific VOC sensing process, we initially employed a single sensor (Cux-BC, x = 10, 20, 30, and 40) to detect benzaldehyde, nonanal, and 1-octen-3-ol. The transient response features for VOCs were observed in all sensors, as shown in Figure 6-6a. A good linear correlation was established between the sensor response and the concentration of the detected gas, demonstrating its practical applicability (Figure 6-6b to Figure 6-6d). Among the response values, Cu20-BC exhibited the highest response for the three gases, with the order being Cu20-BC > Cu30-BC > Cu10-BC > Cu40-BC (Figure 6-6e to Figure 6-6g). In the Cu-BC heterostructure, moderate loading of CuO enhances the gas sensing response of the material. This improvement is primarily

achieved through promoting interface contact, improving electrical conductivity, increasing surface activity, and forming an appropriate conductive network. An optimal amount of copper oxide can modulate the surface electronic structure, thus enhancing the responsiveness to three VOCs. Conversely, excessive loading may lead to adverse effects. Therefore, optimizing the loading of copper oxide is crucial for enhancing gas-sensing performance, with Cu20-BC identified as the optimal sensing material in this study. In Figures 6-6h to 6-6k, the pattern recognition treated by principal component analysis (PCA) demonstrated the exclusive detection of all three sensors for benzaldehyde, nonanal, and 1-octen-3-ol.

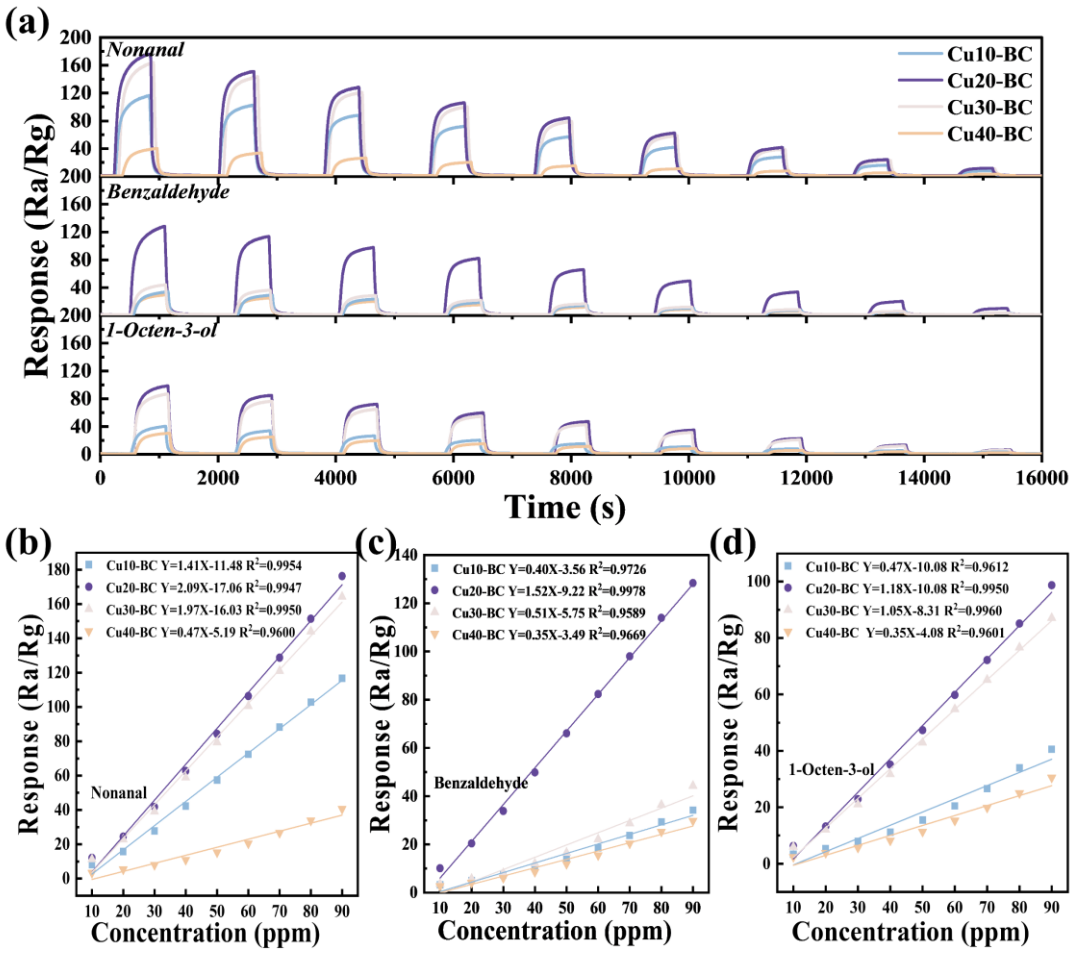

Figure 6-6 (a) Transient response of Cux-BC (x = 10, 20, 30, and 40) film to nonanal, benzaldehyde, and 1-octen-3-ol (10-90 ppm) at room temperature, concentration-dependent response curves of the fabricated sensors for (b) nonanal, (c) benzaldehyde, and (d) 1-octen-3-ol.

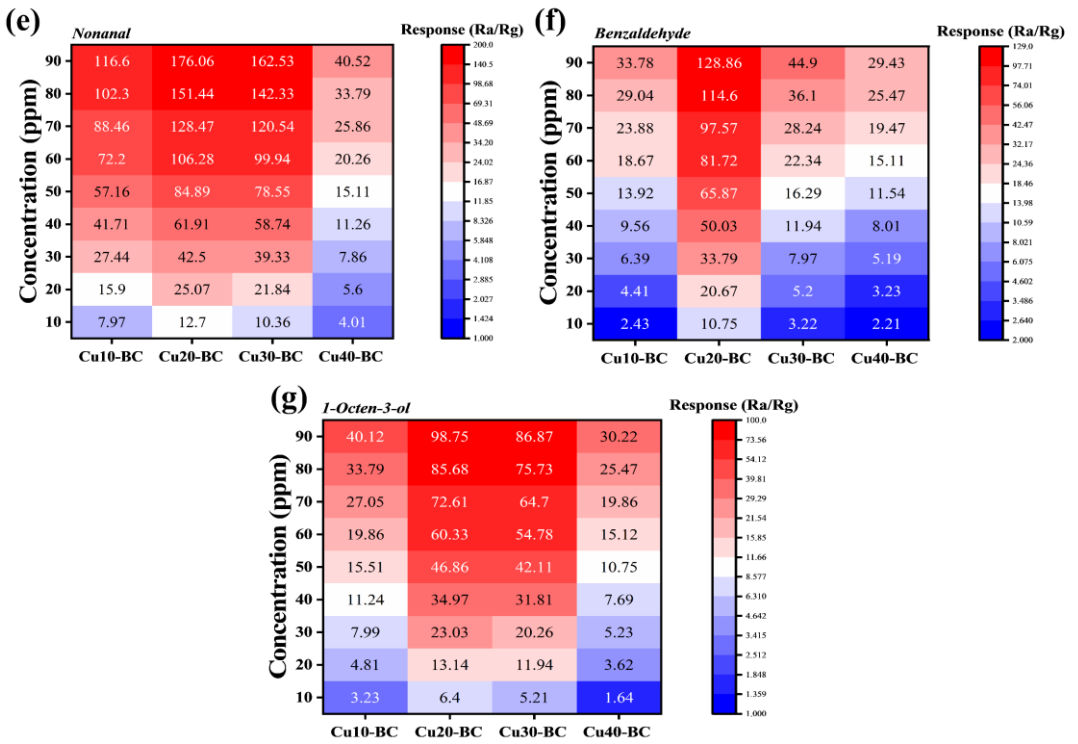

Figure 6-6 Response values of fabricated sensors to different concentrations of (e) nonanal, (f) benzaldehyde, and (g) 1-octen-3-ol at room temperature (10-90 ppm).

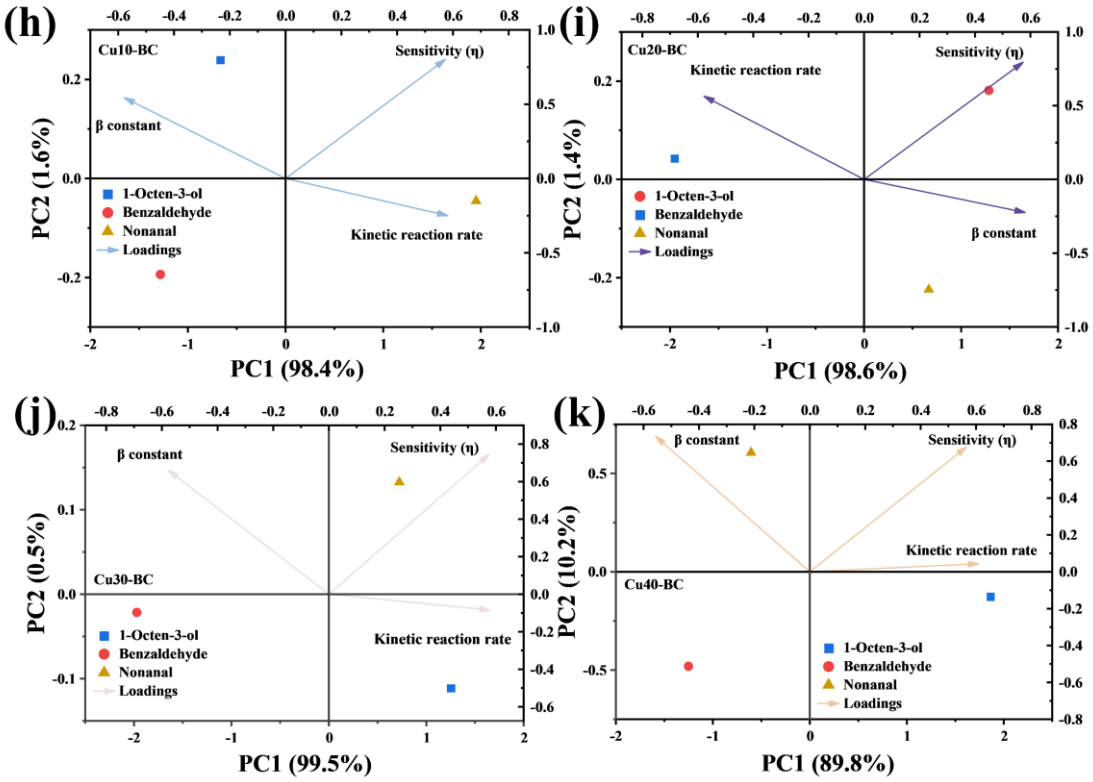

Figure 6-6 Pattern recognition by the PCA method to analyze the exclusive detection of the (h) Cu10-BC, (i) Cu20-BC, (j) Cu30-BC, and (k) Cu40-BC sensors, respectively.

6.2.3 Gas sensing mechanism

To investigate the enhanced sensing mechanism, we construct the band structures of BC and Cu20-BC using the following procedure. Firstly, the valence band potentials (E_{VB}) for BC and Cu20-BC were determined to be 0.69 eV and 1.00 eV, respectively, using the valence band X-ray photoelectron spectroscopy (VB-XPS) technique (Figure 6-7a). By applying Equation (4-1), the valence band potential relative to the standard hydrogen electrode ($E_{VB, NHE}$) of BC and Cu20-BC is 0.77 eV and 1.08 eV, respectively [115, 294],

$$E_{VB, NHE}=\varphi+E_{VB, XPS}-4.44 \quad (6\text{-}1)$$

where φ is the instrument work function (4.52 eV), and $E_{VB, XPS}$ is the valence band potential. Secondly, the correlation between the work function in the actual sensing process (Φ) and the contact potential discrepancy (ΔV) is based on Equation (6-2) [294],

$$\Delta V=\Phi-\varphi \quad (6\text{-}2)$$

where ΔV represents the interval between two different inflection points (IP) on the graph, as depicted in Figure 6-8 and Figure 6-9. Consequently, the Φ for BC and Cu20-BC were obtained to be 5.59 eV and 5.17 eV, respectively. Finally, the band structure can be obtained, as shown in Figure 6-7b. The lower work function facilitates electron transfer from VOC molecules to the Cu20-BC sensor surface, thereby increasing the sensor's sensitivity to lower VOC concentrations. Sensors with lower work functions require less energy to initiate sensing, enabling more energy-efficient operation and making room-temperature sensing possible, which is important for portable and wearable sensor applications.

The heterostructure formed by BC and CuO exhibits significantly enhanced performance in VOC gas sensing. Its primary mechanisms can be summarized as follows (Figure 6-7c). First, the formation of the heterostructure increases interfacial contact between the two materials and promotes the effective separation and migration of charge carriers, allowing photogenerated electrons and holes to be separated at the interface, thereby reducing carrier recombination and improving conductivity. Secondly, the structure significantly increases the number of surface-active sites, thereby enhancing contact between gas molecules and the sensing materials, thereby improving the adsorption capacity and reactivity of VOCs. Furthermore, the band structure of the

heterostructure is adjusted, reducing the energy barrier for gas-molecule reaction, thereby enhancing sensitivity to VOCs. Additionally, the catalytic properties of CuO are crucial, accelerating chemical reactions and enhancing sensor response speed. Collectively, these factors highlight the advantages of the Cu-BC heterostructure for gas-sensing detection.

To further investigate the adsorption and diffusion mechanisms of the target gas molecules and oxygen on the surface of materials, MD simulations were employed. The geometric structures of BC were acquired following the construction of the (020) $Bi_2O_2CO_3$ surface with a 25 Å thick vacuum layer. The geometric structures of Cu-BC were acquired following the construction of the (020) $Bi_2O_2CO_3$ surface and (100) CuO surface with a 25 Å thick vacuum layer. In Figures 6-7e and 6-7f, as nonanal gradually approaches the material surface and O2 molecules diffuse simultaneously, a shift in adsorption kinetics is observed in both the BC and Cu-BC systems. This transition aligns well with the previously proposed model of oxygen adsorption. As depicted in Figure 6-7d, between 1 ps and 25 ps, the interaction energy (E_{int}) in both BC and Cu-BC systems decreases significantly, indicating that nonanal is approaching the surface and entering the attractive interaction region, primarily driven by van der Waals forces. Interestingly, after 50 ps, although the calculated E_{int} of nonanal and O_2 molecules on the CuO-loaded $Bi_2O_2CO_3$ heterojunction are slightly lower in absolute value compared to pristine $Bi_2O_2CO_3$, the gas-sensing response is significantly enhanced, as depicted in Figure 6-6a. This seemingly counterintuitive result can be attributed to several factors. Firstly, the formation of a p-n heterojunction between p-type CuO and n-type $Bi_2O_2CO_3$ facilitates efficient charge separation and modulates the width of the depletion layer, thereby amplifying the surface potential change upon gas exposure. Secondly, moderate adsorption strength is more favorable for reversible gas adsorption-desorption dynamics, ensuring faster response and recovery. Finally, the CuO domains provide additional active sites for oxygen activation and catalytic oxidation of nonanal, thereby enhancing electron transfer and signal output. These synergistic effects highlight the critical role of interface engineering in modulating both adsorption thermodynamics and charge-transport behavior, thereby providing a rational approach to designing high-performance gas sensors.

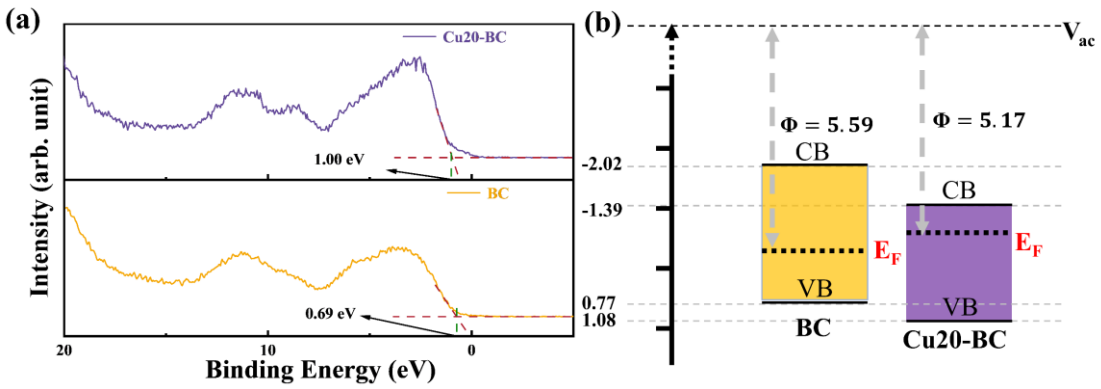

Figure 6-7 (a) VB-XPS and (b) band structure of Cu20-BC and BC.

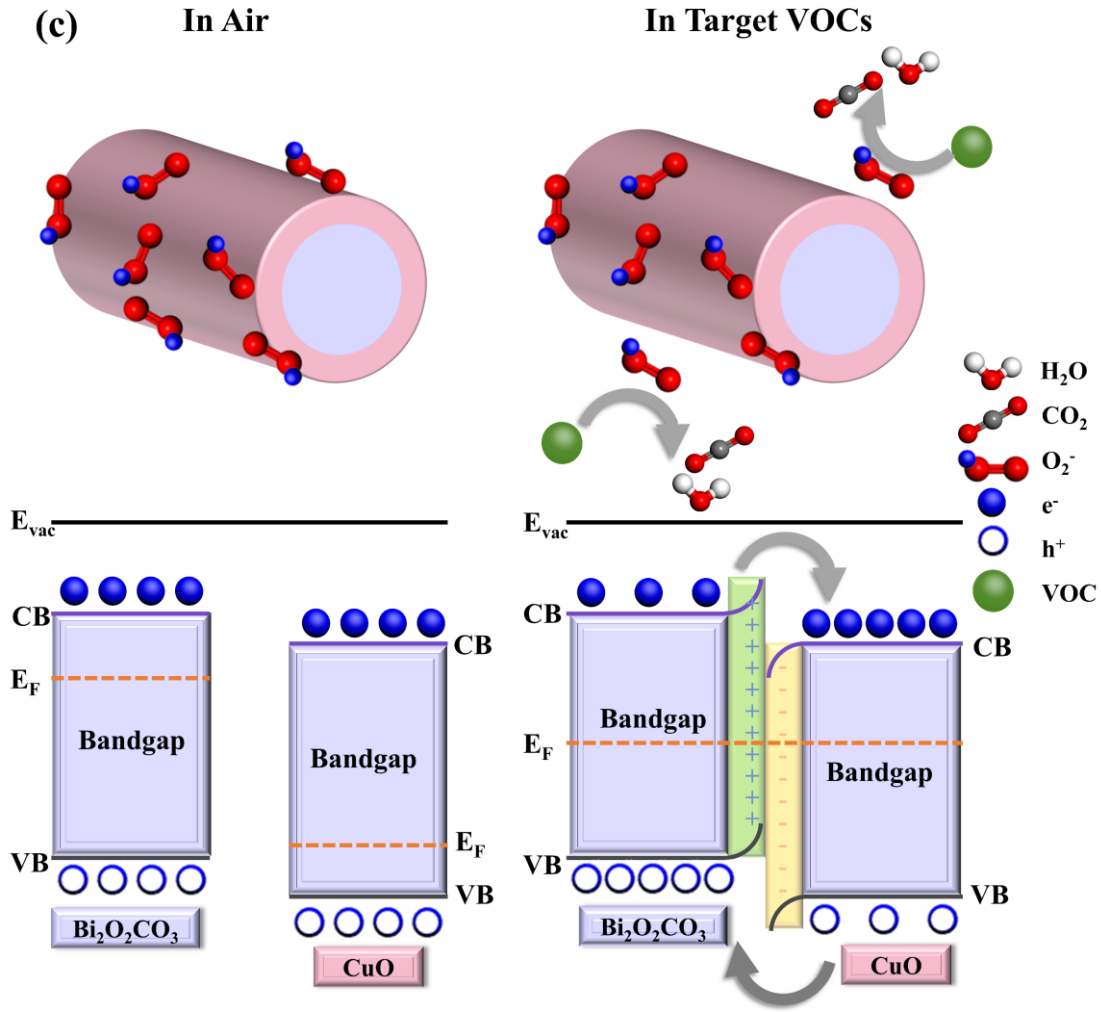

Figure 6-7 (c) Schematic illustration of the nonanal, benzaldehyde, and 1-octen-3-ol sensing mechanism of CuO-loaded $Bi_2O_2CO_3$ micro-flowers at room temperature.

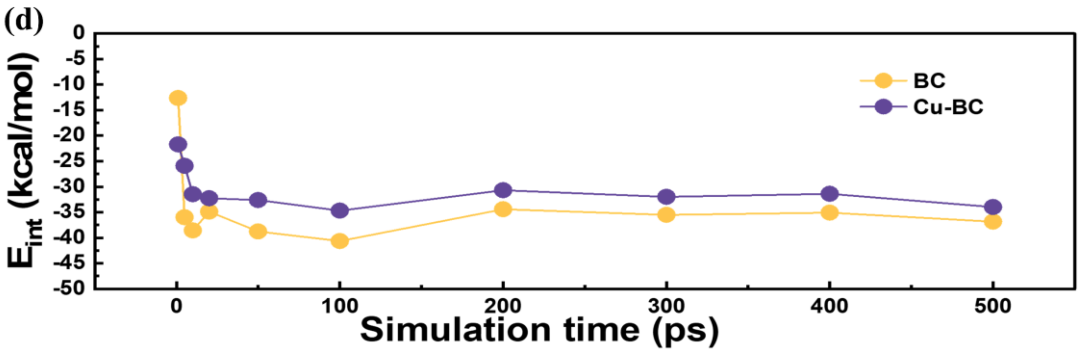

Figure 6-7 (d) E_{int} for the dynamic process of nonanal and oxygen diffusion on BC and Cu-BC.

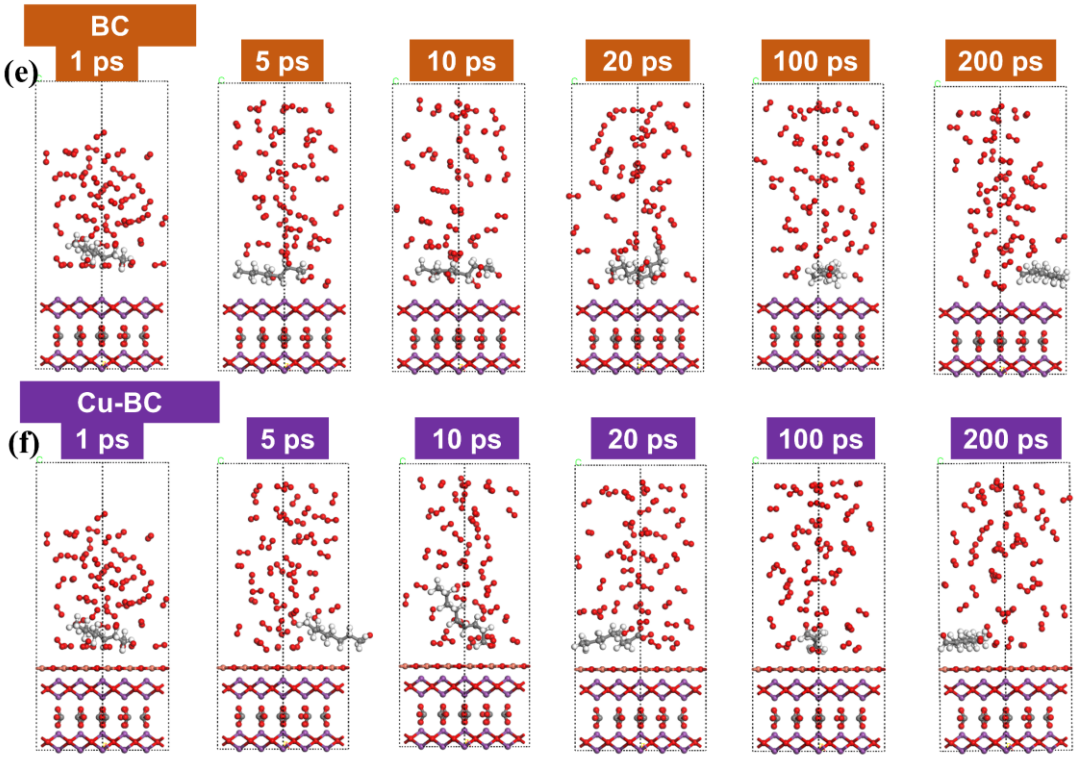

Figure 6-7 The corresponding MD simulation snapshots of (e) BC and (f) Cu-BC related to the Figure 6-7 (d) above.

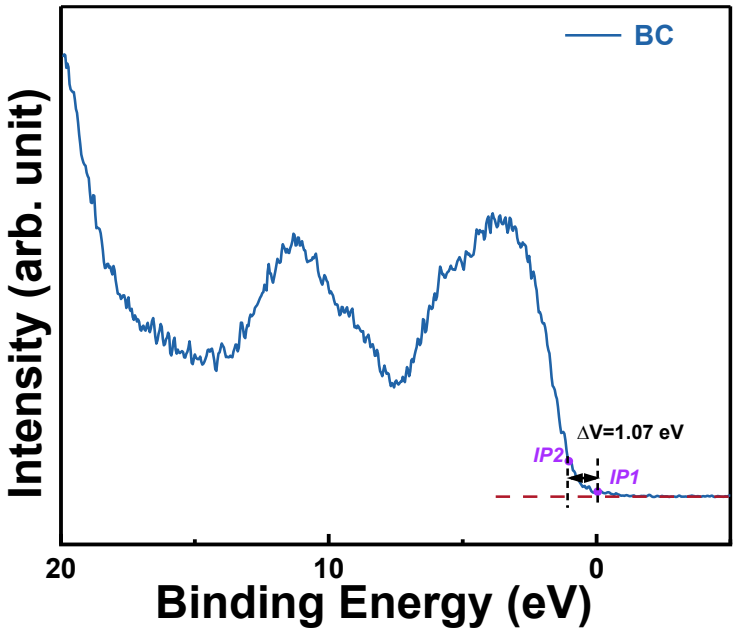

Figure 6-8 Work functions of BC.

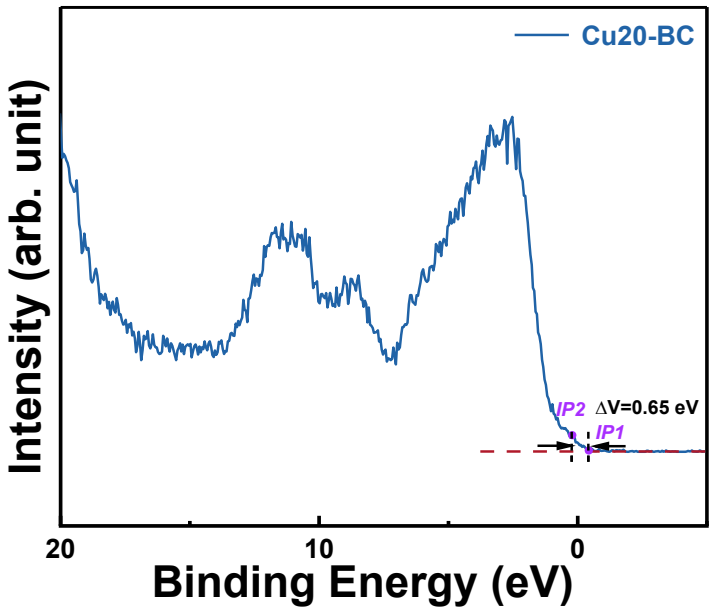

Figure 6-9 Work functions of Cu20-BC.

6.2.4 Sensor arrays detection

Figure 6-10 illustrates the overall construction of a real-time gas sensor array and the evaluation of cooked rice quality performance. A schematic diagram of the system

structure, which includes a circuit board, a microcontroller unit (MCU), and a data transmission module, enables an integrated, portable gas-detection function, as shown in Figure 6-10a. The MCU sequentially reads the real-time signal from the four channels based on Cu10-BC, Cu20-BC, Cu30-BC, and Cu40-BC materials reported above. A physical photograph of the sensor circuit board in the system, as shown in Figure 6-10b, displays the layout and compact design of the multi-channel gas sensor module. The correlation curves between voltage and resistance in one sensing channel is demonstrated in Figure 6-10c, reflecting the correlation between voltage and resistance in each channel, which indicates the stability of the sensing system. To assess the potential of the gas sensor array for evaluating the quality of agricultural products, we studied changes in VOC concentrations emitted from various cooked rice samples (uncooked rice with different storage times) of similar weight (≈20 g). VOCs detection on cooked rice prepared from coarse rice with different storage times (0, 1, 2, 3, 4, 5, and 6 weeks) was performed using homemade equipment with a real-time gas sensor array. The data were obtained, and we employed two dimensionality reduction methods (PCA and linear discriminant analysis (LDA)) to visualize the dynamic loop data for cooked rice detection. It can be observed that there is considerable overlap among the data point regions of cooked rice made from raw rice stored for 0 to 2 weeks (Figure 6-10d). Similar analysis results were obtained in Figure 6-10e. In comparison, the three groups (fresh group (0-2 weeks), mild group (3-4 weeks), and moderate group (5-6 weeks)) were almost distinct. The VOCs detection data for cooked rice made from rice with different storage times exhibited specific patterns and trends, allowing clear differentiation of the datasets across varying storage durations, thereby providing an innovative strategy for detecting grain and other agricultural products.

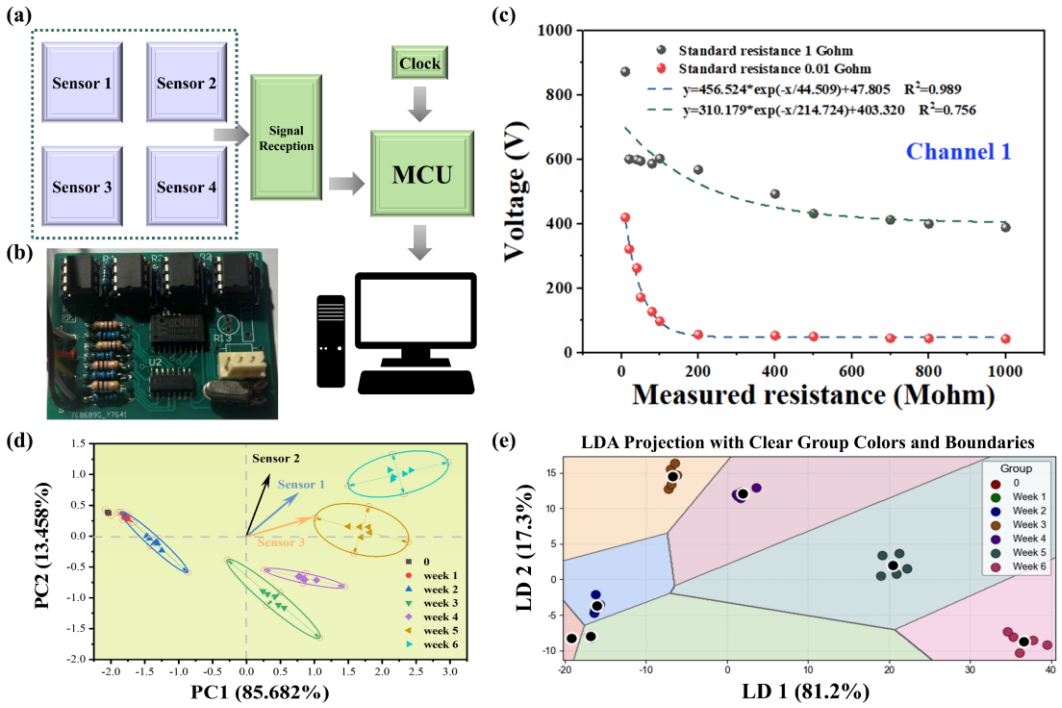

Figure 6-10 (a) Schematic of the real-time gas sensor array. (b) Photograph of the sensor PCB of the real-time gas sensor array. (c) The relationship between voltage and measured resistance for the four channels in the gas sensor array. (d) Two-dimensional score plots of the first principal components derived from response curves for volatile gas detection on cooked rice cooked from fresh grains and grains stored for different weeks using a real-time gas sensor array, (e) LDA pattern recognition of volatile gas detection on cooked rice cooked from fresh grains and grains stored for different weeks using a real-time gas sensor array.

6.3 Conclusions

In conclusion, this chapter presents a one-step hydrothermal method for the synthesis of heterostructured Cu-BC nanomaterials. This synthesis route aims to create functional sensing materials and sensor array systems with significantly enhanced selectivity. A systematic investigation was conducted to evaluate the composition of the heterogeneous structure of Cu-BC materials as a function of CuO loading. This variation directly influenced the sensing performance for VOCs, specifically nonanal, benzaldehyde, and 1-octen-3-ol. Notably, the VOC sensitivity of the Cu20-BC sample was markedly enhanced, attributed to its relatively high specific surface area and increased oxygen vacancy content. Additionally, a sensor array capable of detecting VOCs at ppm levels was successfully constructed, using a specially designed TSMOX-based voltage conversion circuit, demonstrating significant potential for real-time environmental monitoring of cooked rice quality. Future research should focus on improving sensor selectivity through strategies such as molecular imprinting or surface

functionalization, thereby facilitating discrimination among structurally similar VOCs in complex food matrices. Moreover, integrating machine learning algorithms for pattern recognition could further enhance the precision and adaptability of the sensing system. Beyond applications in cooked rice, the platform has considerable potential for broader uses in food spoilage detection, shelf-life prediction, and quality control across various agricultural and consumer products. Ultimately, this work paves the way for advancements in smart packaging and Internet of Things (IoT)-enabled food safety monitoring.

Chapter 7: Conclusions And Perspectives

This thesis focuses on the non-destructive evaluation of cooked rice quality at room temperature. To achieve this, high-performance ternary semiconductor metal oxide gas sensors and a multi-channel sensor array were developed. Based on the changes in rice aroma during storage, three typical VOCs were chosen as key indicators: nonanal, benzaldehyde, and 1-octen-3-ol. A comprehensive research process was then developed, covering indicator selection, material design, analysis of sensing mechanisms, and system-level pattern recognition.

For nonanal detection, La-modified $Bi_2O_2CO_3$ microspheres were designed to address the limitation that traditional metal oxide sensors typically require high operating temperatures. After La modification, more O_V-related active sites were formed, and gas adsorption was enhanced. As a result, the sensor showed a high response of 174.6 to 30 ppm nonanal at room temperature, a fast response time of 36 s at 18 ppm, and good long-term stability.

For benzaldehyde detection, carbon-modified WO_3/Bi_2WO_6 twisted micro-flowers were prepared by a one-pot hydrothermal method. In this material, the carbon coating, the n-n heterojunction, and UV light together improved charge transport and surface reaction activity. The optimized $C_{0.75}/WO_3/Bi_2WO_6$ sensor exhibited a sensitivity of 33.7-50 ppm benzaldehyde at room temperature, remained stable for more than 15 days, and showed good resistance to humidity. Under humid conditions, the response decreased by only 8.96% compared with dry air, and the humidity-caused drift was much smaller than that of uncoated WO_3/Bi_2WO_6. Density functional theory calculations further explained this result. They showed that benzaldehyde adsorbed more strongly on the carbon-coated surface, while water adsorbed more weakly, which agrees well with the improved moisture resistance seen in the experiments.

For 1-octen-3-ol detection, a defect-engineering method based on controlled hydrogen reduction was used to prepare $NiWO_4$ micro-flowers. This method adjusted both the bulk conductivity and the surface activity by introducing oxygen vacancies. The optimized sensor showed a response of 20.6 to 40 ppm 1-octen-3-ol and a fast response time of 22 s at room temperature. It also performed well under different humidity levels, with only 19.7% response drift from 20% to 80% relative humidity. This improvement was supported by an oxygen adsorption model and molecular

dynamics simulations, which helped explain how oxygen and target gas molecules adsorb and diffuse on vacancy-rich surfaces.

Finally, these material-level improvements were applied to a practical sensing system. $CuO/Bi_2O_2CO_3$ p-n heterostructure micro-flowers were integrated into a four-channel sensor array. Combined with principal component analysis and linear discriminant analysis, the array successfully distinguished cooked rice samples ranging from freshly prepared rice to rice stored for 1 to 6 weeks.

Beyond the performance of the individual sensors, this thesis also offers a useful general approach to room-temperature chemiresistive sensing. A key point is that sensor performance at room temperature can be improved more effectively when O_V and interfacial charge transfer are treated as the main design factors. These factors directly affect gas adsorption, the role of ionized oxygen, and carrier transport, rather than relying solely on trial-and-error material replacement. Based on this idea, three main and experimentally verified strategies were developed: first, creating defects in ternary oxide materials to increase active sites and speed up surface reactions; second, forming heterojunctions to adjust the depletion layer and improve electron transport; third, using hydrophobic carbon coatings together with optical excitation to keep good sensing activity while reducing humidity interference.

By combining sensing experiments with theoretical calculations and molecular simulations, this thesis also improves the understanding of the sensing mechanism. The increase in sensitivity and the better humidity resistance were linked to adsorption energy and to a clearer physical picture of adsorption and diffusion. This makes it easier to compare not only the performance of different materials, but also the interfacial processes behind that performance. At the system level, the work also shows that, for complex food-odor analysis, higher accuracy is more realistically achieved with sensor arrays and pattern recognition, as a single sensor is often not enough.

At the same time, some limitations remain, and these also point to future research directions. In the short term, long-term stability under realistic humidity changes should be further improved. This is important because baseline drift and weaker responses may appear over time due to surface contamination, changes in oxygen vacancy states, and competition between water and target gases for adsorption sites. A practical solution, consistent with the findings of this thesis, is to further optimize protective and hydrophobic interfacial layers, especially carbon-based coatings with naturally weaker

water adsorption. At the same time, defect states should be carefully controlled so that oxygen vacancies improve sensing performance without causing faster aging. Future evaluation should include repeated humidity cycling tests, drift measurement, and recovery analysis, so that humidity resistance can be shown as a stable property rather than a one-time result.

In the medium term, selectivity in mixed-gas environments should be improved by further developing the array design demonstrated in this work. This means designing sensing elements with different defect densities, heterojunction types, and surface wettability, so that the response patterns become more diverse. The current statistical methods, such as principal component analysis and linear discriminant analysis, can continue to be used as a basic framework, but future studies should test more demanding tasks, including more storage periods, more rice varieties, and more realistic headspace conditions. Evaluation should gradually move from single-gas testing to mixed-gas testing and repeated sampling experiments, while keeping the same resistance-based readout and pattern-recognition method for better comparison.

In the long term, the framework developed in this thesis can also be extended to food systems beyond cooked rice. The same workflow can still be used: first identify the main volatile markers of a food product, then design room temperature sensing materials with suitable defect and interface properties for those targets, and finally build multi-channel sensor arrays for overall quality evaluation. To make this extension reliable, more attention should be paid to measurement consistency, including sensor-to-sensor reproducibility, batch-to-batch stability in microstructure and defect states, and proper calibration methods that link voltage signals and resistance outputs to stable evaluation standards across devices and over time. Possible risks include the sensitivity of optical excitation to power changes and device differences, as well as the limited long-term stability of highly defective surfaces. These risks may be reduced by comparing different excitation methods and interfacial protection strategies, while keeping the array-based recognition approach, which can still work even if some channels partially degrade because it relies on signal patterns rather than on a single sensing element.

APPENDICES

Appendix A1: Cooked rice quality evaluation

For this study, Wuchang rice was prepared according to the GB/T 19266 standard, using a standard domestic rice cooker under specific stages [79], was monitored at room temperature at different storage conditions. The cooking process follows the four steps: (I) around 25 min from the beginning of heating until steam comes out; (II) the steam starts to come out of the pot and ends 13 min later; (III) the remaining steam overflows from the rice cooker until it stops automatically 10 min of heating; (IV) 30 min of heat preservation starting from automatic stop heating. In detail, 20 g of cooked rice was weighed and sealed in a 100 mL sample container. High-purity mixed air (Nanjing Special Gas Factory Co., Ltd.) blew through the sample. The produced VOCs were further diluted before being exposed to the surface of the sensing material, as shown in Figure A1-1. The variation of electrical resistance at different storage stages was recorded, and PCA and LDA were used to assess and classify the cooked rice quality.

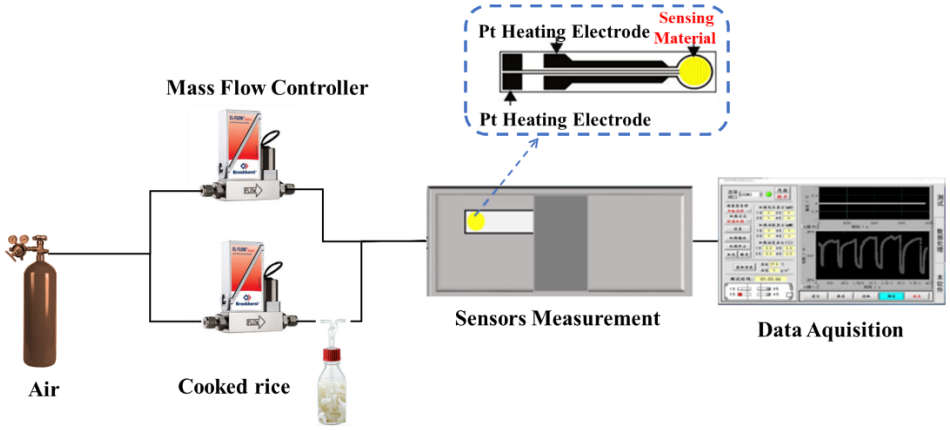

Figure A1-1 The schematic diagram of the gas sensing test systems.

Appendix A2: Specific description of the representation characterization methods.

In detail, the content below describes the characterization methods used in this thesis. It introduces the working principle, the type of information obtainable, key steps for data treatment, and the typical conditions employed here.

XRD identifies crystal structures and phase composition. When incident X-rays interact with lattice planes, the Bragg law n lambda equals two d sine theta is satisfied, and the diffraction peak positions yield interplanar spacings and lattice parameters, while peak profiles carry information on average crystallite size and micro-strain. Powder patterns are matched to standard databases for phase identification, and full pattern fitting with Rietveld refinement provides cell constants and microstructural parameters [349]. Reliable analysis requires background subtraction, removal of K alpha two contributions, correction of the zero shift, instrumental broadening, and the use of appropriate peak shape functions. In this work, a Cu K alpha source with a wavelength of 0.15406 nm was used at 40 kV and 40 mA, and the scan rate was 5 degrees per minute on a Bruker D8 Advance instrument.

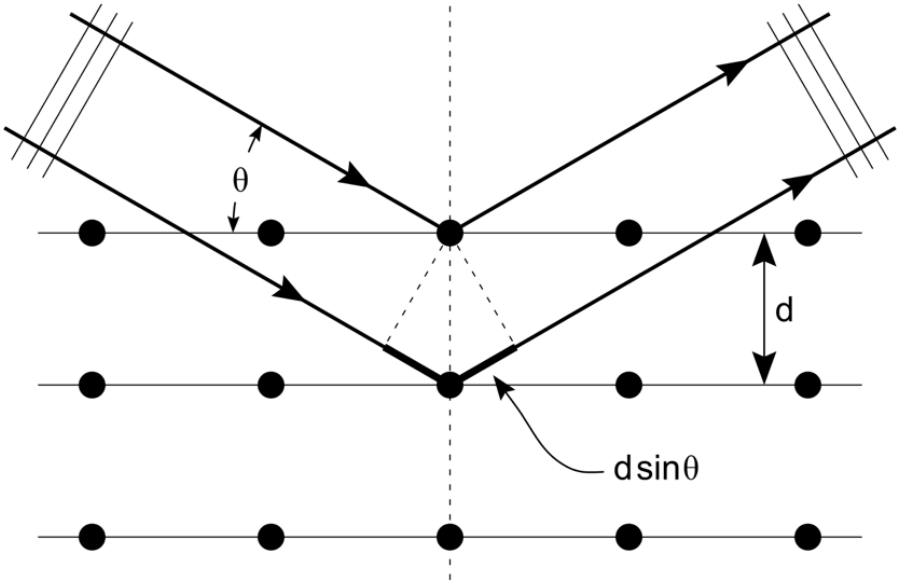

Figure A2-1 Schematic representation of Bragg diffraction.

Field emission scanning electron microscopy visualizes surface morphology and composition contrast at high spatial resolution. A focused electron beam induces secondary electrons that emphasize topography and backscattered electrons that

correlate with the average atomic number, enabling the imaging of surface features, grains, fractures, and porosity with clarity. Image treatment involves consistent brightness and contrast settings and particle statistics based on thresholding while conductive coatings are used to reduce charging on insulating samples. In this work, morphology was examined using an S4800 field-emission scanning electron microscope [350].

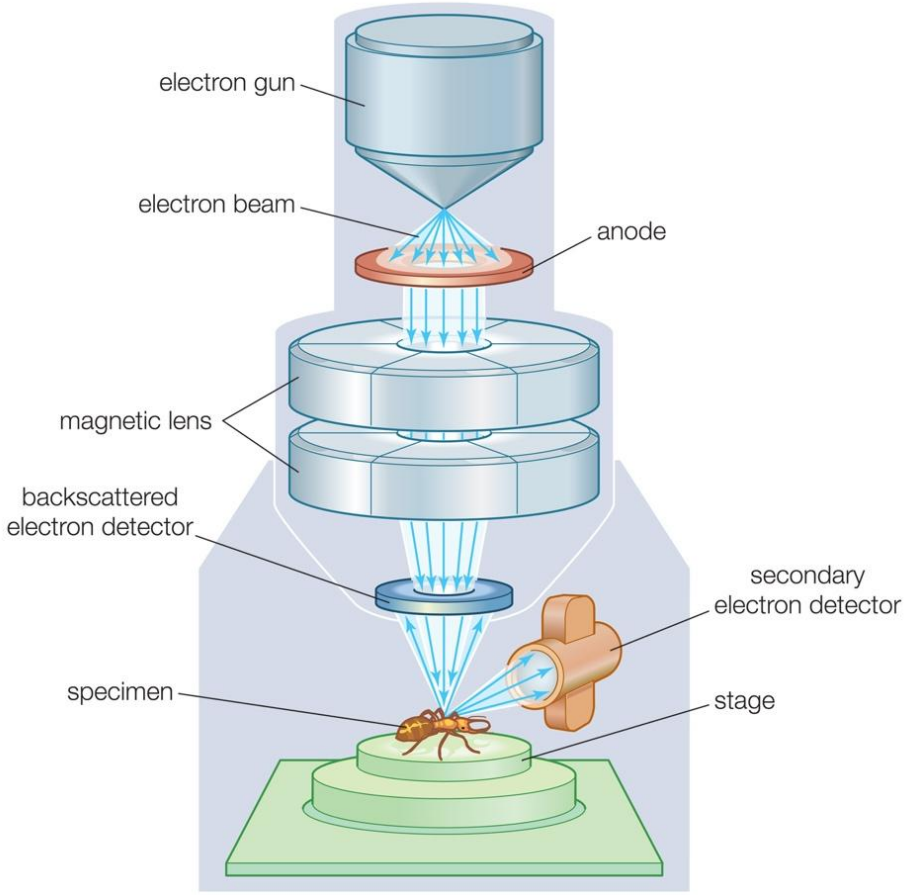

Figure A2-2 Schematic representation of a scanning electron microscope.

Transmission electron microscopy, including high-resolution imaging and selected area electron diffraction probe internal structure and interfaces. High-energy electrons pass through thin specimens and form contrast from phase and amplitude variations, while electron diffraction patterns in reciprocal space allow indexing of planes and measurement of interplanar spacings. High-resolution imaging can resolve lattice fringes under suitable defocus and aberration conditions, and fast Fourier transforms and inverse filtering help isolate specific plane information. Accurate analysis requires scale calibration, determination of the camera constant, and comparison with standard

cards. In this work, a Tecnai instrument operated at 200 kV was used, and Gatan Digital Micrograph was used for fringe and Fourier analyses [351].

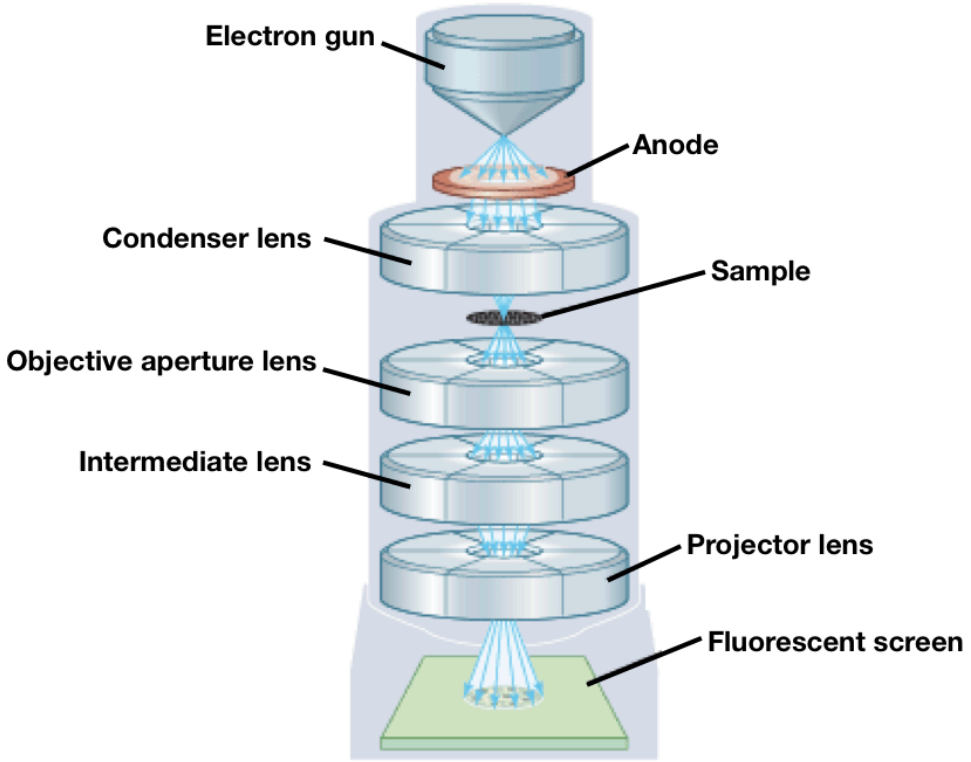

Figure A2-3 Schematic representation of a transmission electron microscope.

FTIR assigns molecular vibrations and coordination modes. A Michelson interferometer converts the time-domain interferogram into a frequency-domain spectrum, and the resulting absorption bands correspond to stretching and bending motions, so that functional groups, hydrogen-bonding strength, and metal-oxygen modes can be identified. Proper processing uses baseline correction, smoothing, and peak fitting, and removes water and carbon dioxide background. In this work, KBr pellet spectra were recorded from four thousand to four hundred inverse centimeters at zero point one inverse centimeter resolution on an Agilent 660 IR spectrometer [352].

Ultraviolet-visible near-infrared diffuse reflectance spectroscopy, combined with Tauc analysis, estimates optical band gaps and reveals defect absorption. Diffuse reflectance of powders is converted to an approximate absorption coefficient with the Kubelka Munk function, and a suitable Tauc plot is constructed based on the assumed transition type, then the linear region near the absorption edge is extrapolated to obtain the bandgap. White reference calibration and baseline treatment improve accuracy, and the Urbach tail width can be compared to assess disorder. In this work, a Cary 5000

spectrophotometer with an integrating sphere was used, and band gaps were derived with Kubelka Munk and Tauc methods [353].

XPS determines surface elemental states and coordination environments. Monochromatic Al K alpha photons eject core electrons, and energy conservation relates the measured kinetic energy to the binding energy, which shifts with chemical environment, while satellite features and spin-orbit splitting assist in assignment. The probing depth is on the nanometer scale, so X-ray photoelectron spectroscopy is surface sensitive. Reliable quantification uses the C 1s peak at 284.8 eV for charge correction, appropriate background functions, peak shapes, and relative sensitivity factors for atomic ratios. In this work, a Thermo Fisher ESCALAB 250Xi with monochromatic Al K alpha radiation was used, and all spectra were referenced to C 1s at 284.8 eV [354-356].

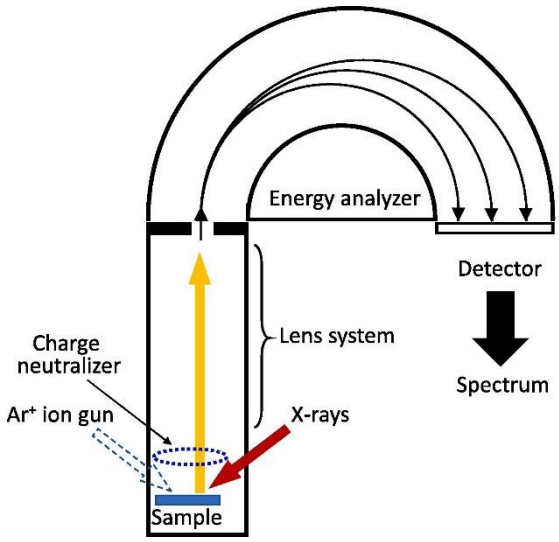

Figure A2-4 The schematic view of the photoelectron spectrometer with a hemispherical electron energy analyzer [357].

High-angle annular dark-field scanning transmission electron microscopy, combined with energy-dispersive X-ray spectroscopy, maps elemental distributions and interfaces. High-angle scattered electrons collected by an annular detector produce an intensity that scales approximately with the atomic number, yielding strong Z contrast, while energy-dispersive spectroscopy detects characteristic X rays for elemental identification and mapping. Data treatment includes deconvolution of overlapping peaks, background subtraction, and drift correction, and thin specimen approximations or standards are used for quantification. In this work, HAADF-STEM imaging and EDS mapping were used to assess uniformity and enrichment of elements across interfaces

[358].

Electron paramagnetic resonance detects unpaired electrons and defect centers. An external magnetic field splits energy levels, and resonance occurs when the microwave frequency matches the Zeeman splitting described by h nu equals g mu B times B. Signals near g equal to two are often associated with oxygen vacancies and related centers in metal oxides, and line width and double integration intensity provide relative measures of concentration and exchange interactions. Processing requires baseline correction and double integration, and low-temperature acquisition enhances sensitivity and resolution. In this work, a Bruker A300 10 12 spectrometer was used to verify the presence and relative evolution of surface oxygen vacancies [359, 360].

Raman spectroscopy and microscopic Raman mapping analyze molecular vibrations and lattice phonons, providing spatially resolved chemical imaging. Inelastic scattering shifts encode specific vibrational modes, so functional groups, crystal structure, disorder, and strain can be identified, and point-by-point spectral acquisition enables two- or three-dimensional maps of peak positions and intensities. Processing includes fluorescence background removal, peak fitting, and wavenumber calibration, and laser heating should be minimized to avoid spectral drift. In this work, spectra and maps were recorded on a Renishaw in Via system and a Thermo Fisher DXRxi microscopic Raman imaging spectrometer [361, 362].

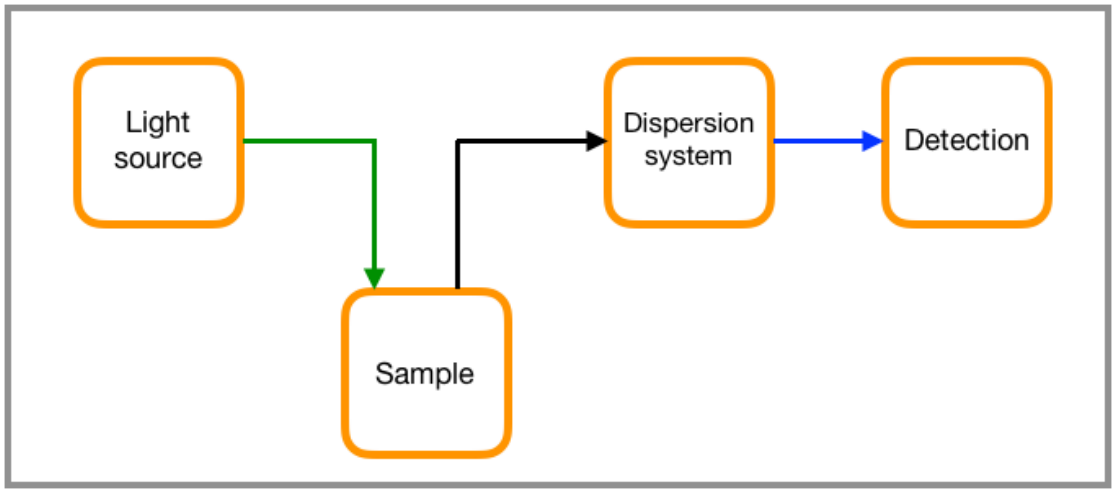

Figure A2-5 Diagram of a typical Raman spectrometer.

Nitrogen adsorption and desorption at liquid nitrogen temperature provide specific surface area and pore size distribution. Multilayer physisorption is described by the

Brunauer, Emmett, and Teller theory, and the linear region of the isotherm at low relative pressure yields the surface area. Mesopore size distributions are commonly calculated from the desorption branch using the Barrett, Joyner, and Halenda method, and micropores can be evaluated by t-plot analysis or models based on nonlocal density functional theory. Treatment includes checking the linear region and the physical meaning of the C constant and comparing the adsorption and desorption branches. In this work, isotherms were collected at 77 Kelvin on an Autosorb IQ3 analyzer, and surface area and pore structure parameters were calculated accordingly [363, 364].

Thermogravimetric analysis monitors mass changes during controlled heating in a controlled gas environment to assess thermal stability and composition. Distinct mass loss steps correspond to desorption of physisorbed species, removal of crystal water, decomposition of organic components, and redox processes of inorganic phases, and the derivative thermogravimetric curve helps resolve overlapping events. Processing requires baseline and buoyancy correction, and interpretation distinguishes processes in inert and oxidizing atmospheres. In this work, a Pyris 1 TGA was used from thirty to eight hundred degrees Celsius in nitrogen at a heating rate of ten degrees per minute [365, 366].

Static water contact angle measurements evaluate surface wettability and relative surface energy. The equilibrium shape of a sessile droplet on an ideal, smooth surface is described by the Young equation, whereas rough or chemically heterogeneous surfaces are described by the Wenzel and Cassie-Baxter models. Analysis uses baseline fitting and Young Laplace fitting of the droplet shape and advancing and receding angles are reported to quantify hysteresis. In this work, static contact angles were recorded on a LAUDA OSA 100 system to assess surface hydrophobicity [367, 368].

Inductively coupled plasma mass spectrometry and flame atomic absorption spectrometry quantify elemental contents. In inductively coupled plasma mass spectrometry, the plasma ionizes species, and a mass analyzer separates ions by mass-to-charge ratio, enabling multi-element detection at trace levels and isotope ratio work. In flame atomic absorption spectrometry, the flame atomizes elements, and the ground state atoms absorb element-specific lines with absorbance proportional to concentration, so single-element determinations are simple and robust. Quality control uses internal standards or standard addition to correct matrix effects, blanks, and method detection limits, and certified reference materials. In this work an Optima 7300 DV inductively

coupled plasma system and a PinAAcle 900F atomic absorption instrument were used for elemental analysis [369, 370].

In situ Fourier transform infrared spectroscopy tracks adsorbed species and reaction intermediates under controlled temperature and atmosphere, clarifying adsorption configurations and reaction pathways. Differential spectra highlight dynamic changes, and a liquid nitrogen-cooled MCT detector provides higher sensitivity, while a DTGS detector offers a stable response. Processing follows the evolution of characteristic band positions and areas over time and links them to kinetic models. In this work, a Bruker INVENIO S was used with zero-point four inverse centimeter resolution, equipped with DTGS and liquid nitrogen cooled MCT detectors [371-373].

Headspace solid phase microextraction coupled with gas chromatography and mass spectrometry quantifies volatile and semivolatile compounds. Under isothermal conditions, analytes distribute between the headspace and the coated fiber, and after thermal desorption at the injector, they are separated by capillary gas chromatography and detected by electron ionization mass spectrometry. Identification combines library matching with the calculation of linear retention indices using n-alkane standards. In this work twenty gram cooked rice samples were sealed in twenty milliliter headspace vials at fifty degrees Celsius for sixty minutes to allow extraction by a DVB CAR PDMS fiber then the fiber was desorbed at two hundred fifty degrees Celsius for five minutes in splitless mode and separation used a DB 5MS column with the specified temperature program and electron ionization at seventy electronvolt and the NIST and WILEY libraries were used for matching and linear retention indices were referenced to C7 to C40 n alkanes [374, 375].

REFERENCES

[1] J.-l. Bian, G.-l. Ren, C. Han, F.-f. Xu, S. Qiu, J.-h. Tang, H.-c. Zhang, H.-y. Wei, H. Gao, Comparative analysis on grain quality and yield of different panicle weight indica-japonica hybrid rice (Oryza sativa L.) cultivars, Journal of Integrative Agriculture 19 (2020) 999-1009, https://doi.org/10.1016/S2095-3119(19)62798-X.

[2] S.G. Park, H.S. Park, M.K. Baek, J.M. Jeong, Y.C. Cho, G.M. Lee, C.M. Lee, J.P. Suh, C.S. Kim, S.M. Kim, Improving the Glossiness of Cooked Rice, an Important Component of Visual Rice Grain Quality, Rice 12 (2019), https://doi.org/10.1186/s12284-019-0348-0.

[3] K. Liu, C. Zhang, J. Xu, Q. Liu, Research advance in gas detection of volatile organic compounds released in rice quality deterioration process, Compr Rev Food Sci Food Saf 20 (2021) 5802-5828, https://doi.org/10.1111/1541-4337.12846.

[4] K. Timsorn, Y. Lorjaroenphon, C. Wongchoosuk, Identification of adulteration in uncooked Jasmine rice by a portable low-cost artificial olfactory system, Measurement 108 (2017) 67-76, https://doi.org/10.1016/j.measurement.2017.05.035.

[5] R.G. Buttery, L.C. Ling, B.O. Juliano, J.G. Turnbaugh, Cooked rice aroma and 2-acetyl-1-pyrroline, Journal of Agricultural and Food Chemistry 31 (1983) 823-826, https://doi.org/10.1021/jf00118a036.

[6] G. Lina, Z. Min, Formation and release of cooked rice aroma, Journal of Cereal Science 107 (2022) 103523, https://doi.org/10.1016/j.jcs.2022.103523.

[7] R. Ma, Y. Tian, L. Chen, Z. Jin, Impact of cooling rates on the flavor of cooked rice during storage, Food Bioscience 35 (2020) 100563, https://doi.org/10.1016/j.fbio.2020.100563.

[8] D. Xu, Y. Hong, Z. Gu, L. Cheng, Z. Li, C. Li, Effect of high pressure steam on the eating quality of cooked rice, Lwt 104 (2019) 100-108, https://doi.org/10.1016/j.lwt.2019.01.043.

[9] Z.Y. Wang, H.M. Su, X. Bi, M. Zhang, Effect of fragmentation degree on sensory and texture attributes of cooked rice, Journal of Food Processing and Preservation 43

(2019), https://doi.org/10.1111/jfpp.13920.

[10] K. Wakte, R. Zanan, V. Hinge, K. Khandagale, A. Nadaf, R. Henry, Thirty-three years of 2-acetyl-1-pyrroline, a principal basmati aroma compound in scented rice (Oryza sativa L.): a status review, J Sci Food Agric 97 (2017) 384-395, https://doi.org/10.1002/jsfa.7875.

[11] D.K. Berner, B.J. Hoff, Inheritance of Scent in American Long Grain Rice, Crop Science 26 (1986) 876-878, https://doi.org/10.2135/cropsci1986.0011183X002600050008x.

[12] J.S. Bijral, B.B. Gupta, Inheritance of aroma in Saanwal Basmati, Indian Journal of Genetics and Plant Breeding 58 (1998) 117-119,

[13] K. Wimonmuang, Y.-S. Lee, Absolute contents of aroma-affecting volatiles in cooked rice determined by one-step rice cooking and volatile extraction coupled with standard-addition calibration using HS-SPME/GC-MS, FOOD CHEMISTRY 440 (2024), https://doi.org/10.1016/j.foodchem.2023.138271.

[14] S.Y. Jeong, Y.K. Moon, T.H. Kim, S.W. Park, K.B. Kim, Y.C. Kang, J.H. Lee, A New Strategy for Detecting Plant Hormone Ethylene Using Oxide Semiconductor Chemiresistors: Exceptional Gas Selectivity and Response Tailored by Nanoscale Cr_2O_3 Catalytic Overlayer, Adv Sci (Weinh) 7 (2020) 1903093, https://doi.org/10.1002/advs.201903093.

[15] X. Geng, S. Li, L. Mawella-Vithanage, T. Ma, M. Kilani, B. Wang, L. Ma, C.C. Hewa-Rahinduwage, A. Shafikova, E. Nikolla, G. Mao, S.L. Brock, L. Zhang, L. Luo, Atomically dispersed Pb ionic sites in PbCdSe quantum dot gels enhance room-temperature NO_2 sensing, Nat Commun 12 (2021) 4895, https://doi.org/10.1038/s41467-021-25192-4.

[16] Y.K. Jo, S.Y. Jeong, Y.K. Moon, Y.M. Jo, J.W. Yoon, J.H. Lee, Exclusive and ultrasensitive detection of formaldehyde at room temperature using a flexible and monolithic chemiresistive sensor, Nat Commun 12 (2021) 4955, https://doi.org/10.1038/s41467-021-25290-3.

[17] X.-X. He, H.-F. Chai, Y.-W. Zhou, K.-W. Liu, Z.-X. Yu, C. Zhang, Sensing

properties and mechanisms of LaF_3–Co_3O_4 nanorods for low-concentration methanol detection, Rare Metals 43 (2024) 2193-2204, https://doi.org/10.1007/s12598-023-02593-6.

[18] K. Xu, M. Han, Z. Zheng, Z. Yu, H. Liao, H. Sun, C. Zhang, Well-designed g-C_3N_4 nanosheet incorporated Ag loaded $Er_{0.05}La_{0.95}FeO_3$ heterojunctions for isoamyl alcohol detection, Journal of Advanced Ceramics 13 (2024) 736-745, https://doi.org/10.26599/JAC.2024.9220892.

[19] S. Neogi, R. Ghosh, Influence of dipole moment on the VOC sensing properties of $BiFeO_3$ microspheres: Addressing the selectivity towards acetone, Sensors and Actuators B: Chemical 415 (2024) 135980, https://doi.org/10.1016/j.snb.2024.135980.

[20] M. Souri, H. Salar Amoli, Y. Yamini, Three-dimensionally ordered porous In-doped $SmFeO_3$ perovskite gas sensor for highly sensitive and selective detection of formaldehyde, Sensors and Actuators B: Chemical 404 (2024) 135213, https://doi.org/10.1016/j.snb.2023.135213.

[21] W. Li, X. Li, Y. Zong, L. Kong, W. Zhu, M. Xu, H. Liu, Detection of n-Propanol Down to the Sub-ppm Level Using p-Type Delafossite $AgCrO_2$ Nanoparticles, ACS Sensors 8 (2023) 289-296, https://doi.org/10.1021/acssensors.2c02182.

[22] X. Li, W. Zeng, S. Zhuo, B. Qian, Q. Chen, Q. Luo, R. Qian, Highly Sensitive Room-Temperature Detection of Ammonia in the Breath of Kidney Disease Patients Using $Fe_2Mo_3O_8$/MoO_2@MoS_2 Nanocomposite Gas Sensor, Advanced Science 11 (2024) 2405942, https://doi.org/10.1002/advs.202405942.

[23] K. Liu, Z. Zheng, M. Debliquy, C. Zhang, Highly-sensitive volatile organic compounds evaluation by three-dimensional $ZnFe_2O_4$/$ZnSnO_3$ heterostructures and their predictive grain quality monitoring, Chemical Engineering Journal 453 (2023) 139824, https://doi.org/10.1016/j.cej.2022.139824.

[24] A. Bag, M. Kumar, D.-B. Moon, A. Hanif, M.J. Sultan, D.H. Yoon, N.-E. Lee, A room-temperature operable and stretchable NO_2 gas sensor composed of reduced graphene oxide anchored with MOF-derived $ZnFe_2O_4$ hollow octahedron, Sensors and Actuators B: Chemical 346 (2021) 130463, https://doi.org/10.1016/j.snb.2021.130463.

[25] F.S.G. Hashemi, M.Y. Rafii, M.R. Ismail, T.M.M. Mahmud, H.A. Rahim, R. Asfaliza, M.A. Malek, M.A. Latif, Biochemical, Genetic and Molecular Advances of Fragrance Characteristics in Rice, Critical Reviews in Plant Sciences 32 (2013) 445-457, https://doi.org/10.1080/07352689.2013.807716.

[26] R.G. Buttery, J.G. Turnbaugh, L.C. Ling, Contribution of volatiles to rice aroma, Journal of Agricultural and Food Chemistry 36 (1988) 1006-1009, https://doi.org/10.1021/jf00083a025.

[27] M.-R. Yoon, S.-C. Lee, M.-Y. Kang, The lipid composition of rice cultivars with different eating qualities, Journal of the Korean Society for Applied Biological Chemistry 55 (2012) 291-295, https://doi.org/10.1007/s13765-012-1095-8.

[28] L. Amagliani, J. O'Regan, A.L. Kelly, J.A. O'Mahony, The composition, extraction, functionality and applications of rice proteins: A review, Trends in Food Science & Technology 64 (2017) 1-12, https://doi.org/10.1016/j.tifs.2017.01.008.

[29] M.E.A.S. Oliveira, P.P.S. Coimbra, M.C. Galdeano, C.W.P. Carvalho, C.Y. Takeiti, How does germinated rice impact starch structure, products and nutrional evidences? – A review, Trends in Food Science & Technology 122 (2022) 13-23, https://doi.org/10.1016/j.tifs.2022.02.015.

[30] B. Zhang, D. Qiao, S. Zhao, Q. Lin, J. Wang, F. Xie, Starch-based food matrices containing protein: Recent understanding of morphology, structure, and properties, Trends in Food Science & Technology 114 (2021) 212-231, https://doi.org/10.1016/j.tifs.2021.05.033.

[31] M.A. Monsoor, A. Proctor, Volatile component analysis of commercially milled head and broken rice, Journal of Food Science 69 (2004) C632-C636, https://doi.org/10.1111/j.1365-2621.2004.tb09911.x.

[32] R.J. Bryant, A.M. McClung, Volatile profiles of aromatic and non-aromatic rice cultivars using SPME/GC–MS, Food Chemistry 124 (2011) 501-513, https://doi.org/10.1016/j.foodchem.2010.06.061.

[33] D.S. Yang, K.S. Lee, O.Y. Jeong, K.J. Kim, S.J. Kays, Characterization of volatile aroma compounds in cooked black rice, Journal of Agricultural and Food Chemistry 56

(2008) 235-240, https://doi.org/10.1021/jf072360c.

[34] C.C. Grimm, E.T. Champagne, S.W. Lloyd, M. Easson, B. Condon, A. McClung, Analysis of 2-Acetyl-1-Pyrroline in Rice by HSSE/GC/MS, Cereal Chemistry 88 (2011) 271-277, https://doi.org/10.1094/cchem-09-10-0136.

[35] M. Jezussek, B.O. Juliano, P. Schieberle, Comparison of key aroma compounds in cooked brown rice varieties based on aroma extract dilution analyses, Journal of Agricultural and Food Chemistry 50 (2002) 1101-1105, https://doi.org/10.1021/jf0108720.

[36] H.J. McKerchar, S. Clerens, R.C.J. Dobson, J.M. Dyer, E. Maes, J.A. Gerrard, Protein-protein crosslinking in food: Proteomic characterisation methods, consequences and applications, Trends in Food Science & Technology 86 (2019) 217-229, https://doi.org/https://doi.org/10.1016/j.tifs.2019.02.005.

[37] E.I. Champagne, Rice aroma and flavor: A literature review, Cereal Chemistry 85 (2008) 447-456, https://doi.org/10.1094/cchem-85-4-0445.

[38] J.S. Park, K.-Y. Kim, H.H. Baek, Potent aroma-active compounds of cooked Korean non-aromatic rice, Food Science and Biotechnology 19 (2010) 1403-1407, https://doi.org/10.1007/s10068-010-0200-1.

[39] K. Mahattanatawee, R.L. Rouseff, Comparison of aroma active and sulfur volatiles in three fragrant rice cultivars using GC-olfactometry and GC-PFPD, Food Chem 154 (2014) 1-6, https://doi.org/10.1016/j.foodchem.2013.12.105.

[40] Q. Zhao, J. Xi, D. Xu, Y. Jin, F. Wu, Q. Tong, X. Xu, Effect of optimal-water boiling cooking on the volatile compounds in 26 Japonica rice varieties from China, Food Res Int 155 (2022) 111078, https://doi.org/10.1016/j.foodres.2022.111078.

[41] D. Kasote, V.K. Singh, H. Bollinedi, A.K. Singh, N. Sreenivasulu, A. Regina, Profiling of 2-Acetyl-1-Pyrroline and Other Volatile Compounds in Raw and Cooked Rice of Traditional and Improved Varieties of India, Foods 10 (2021), https://doi.org/10.3390/foods10081917.

[42] Q. Zhao, J. Xi, D. Xu, Y. Jin, F. Wu, Q. Tong, Y. Yin, X. Xu, A comparative HS-SPME/GC-MS-based metabolomics approach for discriminating selected japonica rice

varieties from different regions of China in raw and cooked form, Food Chemistry 385 (2022) 132701, https://doi.org/10.1016/j.foodchem.2022.132701.

[43] D.K. Verma, P.P. Srivastav, A paradigm of volatile aroma compounds in rice and their product with extraction and identification methods: A comprehensive review, Food Research International 130 (2020) 108924, https://doi.org/10.1016/j.foodres.2019.108924.

[44] D.S. Yang, R.L. Shewfelt, K.-S. Lee, S.J. Kays, Comparison of Odor-Active Compounds from Six Distinctly Different Rice Flavor Types, Journal of Agricultural and Food Chemistry 56 (2008) 2780-2787, https://doi.org/10.1021/jf072685t.

[45] N. Tsuchida, K. Kuwahara, Chemical Analyses to Examine the Smell of Cooked Rice and the Effect of Bamboo Charcoal on the Improvement of Smell, Nippon Shokuhin Kagaku Kogaku Kaishi 66 (2019) 1-8, https://doi.org/10.3136/nskkk.66.1.

[46] S. Arsa, C. Theerakulkait, K.R. Cadwallader, Quantitation of Three Strecker Aldehydes from Enzymatic Hydrolyzed Rice Bran Protein Concentrates as Prepared by Various Conditions, Journal of Agricultural and Food Chemistry 67 (2019) 8205-8211, https://doi.org/10.1021/acs.jafc.9b02025.

[47] J. Pico, Å.S. Hansen, M.A. Petersen, Comparison of the volatile profiles of the crumb of gluten-free breads by DHE-GC/MS, Journal of Cereal Science 76 (2017) 280-288, https://doi.org/10.1016/j.jcs.2017.07.004.

[48] J. Demyttenaere, K.A. Tehrani, N. De Kimpe, The Chemistry of the Most Important Maillard Flavor Compounds of Bread and Cooked Rice, Heteroatomic Aroma Compounds, American Chemical Society2002, pp. 150-165.

[49] J.F. Hoffmann, P.Z. Bassinello, J.M. Colombari Filho, I.d.S. Lindemann, M.C. Elias, G.R. Takeoka, N.L. Vanier, Volatile compounds profile of Brazilian aromatic brown rice genotypes and its cooking quality characteristics, Cereal Chemistry 96 (2019) 292-301, https://doi.org/10.1002/cche.10121.

[50] Z. Zeng, H. Zhang, T. Zhang, S. Tamogami, J.Y. Chen, Analysis of flavor volatiles of glutinous rice during cooking by combined gas chromatography–mass spectrometry with modified headspace solid-phase microextraction method, Journal of Food

Composition and Analysis 22 (2009) 347-353, https://doi.org/10.1016/j.jfca.2008.11.020.

[51] N. Frank, M. Dubois, J.F. Huertas Pérez, Detection of Furan and five Alkylfurans, including 2-Pentylfuran, in various Food Matrices, Journal of Chromatography A 1622 (2020), https://doi.org/10.1016/j.chroma.2020.461119.

[52] K. Wilkie, M. Wootton, J.E. Paton, Sensory Testing of Australian Fragrant, Imported Fragrant, and Non-fragrant Rice Aroma, International Journal of Food Properties 7 (2004) 27-36, https://doi.org/10.1081/jfp-120022493.

[53] R. Lapchareonsuk, P. Sirisomboon, Sensory Quality Evaluation of Rice Using Visible and Shortwave Near-Infrared Spectroscopy, International Journal of Food Properties 18 (2014) 1128-1138, https://doi.org/10.1080/10942912.2013.870572.

[54] M. Limpawattana, R.L. Shewfelt, Flavor Lexicon for Sensory Descriptive Profiling of Different Rice Types, Journal of Food Science 75 (2010) S199-S205, https://doi.org/10.1111/j.1750-3841.2010.01577.x.

[55] Z.X. Han, M.M. Rana, G.F. Liu, M.J. Gao, D.X. Li, F.G. Wu, X.B. Li, X.C. Wan, S. Wei, Green tea flavour determinants and their changes over manufacturing processes, Food Chem 212 (2016) 739-48, https://doi.org/10.1016/j.foodchem.2016.06.049.

[56] I. Honma, A. Ito, R. Ueda, F. Hayakawa, K. Maruyama, Sensory Characterization of Cooked Brown Rice Using Quantitative Descriptive Analysis (QDA), Nippon Shokuhin Kagaku Kogaku Kaishi 66 (2019) 33-40, https://doi.org/10.3136/nskkk.66.33.

[57] W. Routray, K. Rayaguru, 2-Acetyl-1-pyrroline: A key aroma component of aromatic rice and other food products, Food Reviews International 34 (2018) 539-565, https://doi.org/10.1080/87559129.2017.1347672.

[58] K.-S. Youn, H.-S. Chung, Optimization of the roasting temperature and time for preparation of coffee-like maize beverage using the response surface methodology, LWT - Food Science and Technology 46 (2012) 305-310, https://doi.org/10.1016/j.lwt.2011.09.014.

[59] Y. Shi, L. Wang, Y. Fang, H. Wang, H. Tao, F. Pei, P. Li, B. Xu, Q. Hu, A comprehensive analysis of aroma compounds and microstructure changes in brown rice

during roasting process, Lwt 98 (2018) 613-621, https://doi.org/10.1016/j.lwt.2018.09.018.

[60] X. Qi, L. Cheng, X. Li, D. Zhang, G. Wu, H. Zhang, L. Wang, H. Qian, Y.n. Wang, Effect of cooking methods on solubility and nutrition quality of brown rice powder, Food Chemistry 274 (2019) 444-451, https://doi.org/10.1016/j.foodchem.2018.07.164.

[61] L.G. Dias, A. Hacke, S.F. Bergara, O.V. Villela, L.R.B. Mariutti, N. Bragagnolo, Identification of volatiles and odor-active compounds of aromatic rice by OSME analysis and SPME/GC-MS, Food Res Int 142 (2021) 110206, https://doi.org/10.1016/j.foodres.2021.110206.

[62] F. Utz, A. Spaccasassi, J. Kreissl, T.D. Stark, C. Tanger, U. Kulozik, T. Hofmann, C. Dawid, Sensomics-Assisted Aroma Decoding of Pea Protein Isolates (Pisum sativum L.), Foods 11 (2022), https://doi.org/10.3390/foods11030412.

[63] I. López-Galilea, N. Fournier, C. Cid, E. Guichard, Changes in Headspace Volatile Concentrations of Coffee Brews Caused by the Roasting Process and the Brewing Procedure, Journal of Agricultural and Food Chemistry 54 (2006) 8560-8566, https://doi.org/10.1021/jf061178t.

[64] M.A. Pozo-Bayón, A. Ruíz-Rodríguez, K. Pernin, N. Cayot, Influence of Eggs on the Aroma Composition of a Sponge Cake and on the Aroma Release in Model Studies on Flavored Sponge Cakes, Journal of Agricultural and Food Chemistry 55 (2007) 1418-1426, https://doi.org/10.1021/jf062203y.

[65] I. Maraval, C. Mestres, K. Pernin, F. Ribeyre, R. Boulanger, E. Guichard, Z. Gunata, Odor-Active Compounds in Cooked Rice Cultivars from Camargue (France) Analyzed by GC−O and GC−MS, Journal of Agricultural and Food Chemistry 56 (2008) 5291-5298, https://doi.org/10.1021/jf7037373.

[66] W. Wardencki, T. Chmiel, T. Dymerski, 7 - Gas chromatography-olfactometry (GC-O), electronic noses (e-noses) and electronic tongues (e-tongues) for in vivo food flavour measurement, in: D. Kilcast (Ed.), Instrumental Assessment of Food Sensory Quality, Woodhead Publishing2013, pp. 195-229.

[67] Z. Guo, S. Huang, M. Chen, Y. Ni, X. Hu, N. Sun, Identification and quantitative

determination of 2-acetyl-1-pyrroline using GC-TOF MS combined with HS and HS-SPME pretreatment, Journal of Cereal Science 93 (2020), https://doi.org/10.1016/j.jcs.2020.102975.

[68] H.S. Kwak, M. Kim, Y. Lee, Y. Jeong, Identification of key sensory attributes for consumer acceptance and instrumental quality of aseptic-packaged cooked rice, International Journal of Food Science & Technology 50 (2015) 691-699, https://doi.org/10.1111/ijfs.12684.

[69] Y.S. Lee, Y. Oh, T.H. Kim, Y.H. Cho, Quantitation of 2-acetyl-1-pyrroline in aseptic-packaged cooked fragrant rice by HS-SPME/GC-MS, Food Sci Nutr 7 (2019) 266-272, https://doi.org/10.1002/fsn3.879.

[70] J.W. Gardner, P.N. Bartlett, A brief history of electronic noses, Sensors and Actuators B: Chemical 18 (1994) 210-211, https://doi.org/10.1016/0925-4005(94)87085-3.

[71] Y. Li, Z. Wang, T. Zhao, H. Li, J. Jiang, J. Ye, Electronic nose for the detection and discrimination of volatile organic compounds: Application, challenges, and perspectives, TrAC Trends in Analytical Chemistry 180 (2024) 117958, https://doi.org/10.1016/j.trac.2024.117958.

[72] T. Feng, H. Zhuang, R. Ye, Z. Jin, X. Xu, Z. Xie, Analysis of volatile compounds of Mesona Blumes gum/rice extrudates via GC-MS and electronic nose, Sensors and Actuators B: Chemical 160 (2011) 964-973, https://doi.org/10.1016/j.snb.2011.09.013.

[73] S. Jiang, J. Wang, Y. Wang, S. Cheng, A novel framework for analyzing MOS E-nose data based on voting theory: Application to evaluate the internal quality of Chinese pecans, Sensors and Actuators B: Chemical 242 (2017) 511-521, https://doi.org/10.1016/j.snb.2016.11.074.

[74] A. Jana, N. Bhattacharyya, R. Bandyopadhyay, B. Tudu, S. Mukherjee, D. Ghosh, J.K. Roy, Fragrance Measurement of Scented Rice using Electronic Nose, International Journal on Smart Sensing and Intelligent Systems 8 (2015) 1730-1747, https://doi.org/10.21307/ijssis-2017-827.

[75] N. Sinelli, S. Benedetti, G. Bottega, M. Riva, S. Buratti, Evaluation of the optimal

cooking time of rice by using FT-NIR spectroscopy and an electronic nose, Journal of Cereal Science 44 (2006) 137-143, https://doi.org/10.1016/j.jcs.2006.05.002.

[76] J. Song, J.R. Son, N.K. Park, H.Y. Cho, K.S. Chang, Classification of Japonica Varieties by Volatile Component Patterns of Milled and Cooked Rice Using Electronic Nose, 50 (2005),

[77] C. Yu, L. Zhu, H. Zhang, S. Bi, G. Wu, X. Qi, H. Zhang, L. Wang, H. Qian, L. Zhou, Effect of cooking pressure on phenolic compounds, gamma-aminobutyric acid, antioxidant activity and volatile compounds of brown rice, Journal of Cereal Science 97 (2021), https://doi.org/10.1016/j.jcs.2020.103127.

[78] S.H. Kim, B.R. Yu, I.M. Chung, Changes in the contents and profiles of selected phenolics, soyasapogenols, tocopherols, and amino acids during soybean-rice mixture cooking: Electric rice cooker vs electric pressure rice cooker, Food Chem 176 (2015) 45-53, https://doi.org/10.1016/j.foodchem.2014.12.024.

[79] Z. Zeng, H. Zhang, J.Y. Chen, T. Zhang, R. Matsunaga, Flavor Volatiles of Rice During Cooking Analyzed by Modified Headspace SPME/GC-MS, Cereal Chemistry 85 (2008) 140-145, https://doi.org/10.1094/CCHEM-85-2-0140.

[80] Z. Zeng, H. Zhang, J.Y. Chen, T. Zhang, R. Matsunaga, Direct Extraction of Volatiles of Rice During Cooking Using Solid-Phase Microextraction, Cereal Chemistry 84 (2007) 423-427, https://doi.org/10.1094/CCHEM-84-5-0423.

[81] T. Tsugita, T. Ohta, H. Kato, Cooking Flavor and Texture of Rice Stored under Different Conditions, Agricultural and Biological Chemistry 47 (1983) 543-549, https://doi.org/10.1080/00021369.1983.10865684.

[82] B. Gruber, F. David, P. Sandra, Capillary gas chromatography-mass spectrometry: Current trends and perspectives, TrAC Trends in Analytical Chemistry 124 (2020), https://doi.org/10.1016/j.trac.2019.04.007.

[83] C.A. Valdez, Gas Chromatography-Mass Spectrometry Analysis of Synthetic Opioids Belonging to the Fentanyl Class: A Review, Crit Rev Anal Chem (2021) 1-31, https://doi.org/10.1080/10408347.2021.1927668.

[84] N. De Giovanni, D. Marchetti, A Systematic Review of Solid-Phase

Microextraction Applications in the Forensic Context, J Anal Toxicol 44 (2020) 268-297, https://doi.org/10.1093/jat/bkz077.

[85] W.S. Al-Dayyeni, S. Al-Yousif, M.M. Taher, A.W. Al-Faouri, N.M. Tahir, M.M. Jaber, F. Ghabban, I.A. Najm, I.M. Alfadli, O.Z. Ameerbakhsh, M.J. Mnati, N.A. Al-Shareefi, A.H. Saleh, A Review on Electronic Nose: Coherent Taxonomy, Classification, Motivations, Challenges, Recommendations and Datasets, IEEE Access 9 (2021) 88535-88551, https://doi.org/10.1109/access.2021.3090165.

[86] Z. Lei, D. Zhang, Domain Adaptation Extreme Learning Machines for Drift Compensation in E-Nose Systems, IEEE Transactions on Instrumentation and Measurement 64 (2015) 1790-1801, https://doi.org/10.1109/tim.2014.2367775.

[87] J. Chen, L. Tao, T. Zhang, J. Zhang, T. Wu, D. Luan, L. Ni, X. Wang, J. Zhong, Effect of four types of thermal processing methods on the aroma profiles of acidity regulator-treated tilapia muscles using E-nose, HS-SPME-GC-MS, and HS-GC-IMS, Lwt 147 (2021), https://doi.org/10.1016/j.lwt.2021.111585.

[88] H. Song, J. Liu, GC-O-MS technique and its applications in food flavor analysis, Food Res Int 114 (2018) 187-198, https://doi.org/10.1016/j.foodres.2018.07.037.

[89] Y. Huan, K. Wu, C. Li, H. Liao, M. Debliquy, C. Zhang, Micro-nano structured functional coatings deposited by liquid plasma spraying, Journal of Advanced Ceramics 9 (2020) 517-534, https://doi.org/10.1007/s40145-020-0402-9.

[90] T.B. Bagchi, K. Chattopadhyay, M. Sivashankari, S. Roy, A. Kumar, T. Biswas, S. Pal, Effect of different processing technologies on phenolic acids, flavonoids and other antioxidants content in pigmented rice, Journal of Cereal Science 100 (2021), https://doi.org/10.1016/j.jcs.2021.103263.

[91] Z. Yin, W. Xinhui, W. Wei, Z. Jiaming, Effect of boiling and frying on nutritional value and in vitro digestibility of rabbit meat, African Journal of Food Science 8 (2014) 92-103, https://doi.org/10.5897/ajfs2013.1114.

[92] K.L. Liu, J.B. Zheng, F.S. Chen, Effects of washing, soaking and domestic cooking on cadmium, arsenic and lead bioaccessibilities in rice, Journal of the Science of Food and Agriculture 98 (2018) 3829-3835, https://doi.org/10.1002/jsfa.8897.

[93] M. Menon, W.R. Dong, X.M. Chen, J. Hufton, E.J. Rhodes, Improved rice cooking approach to maximise arsenic removal while preserving nutrient elements, Science of the Total Environment 755 (2021), https://doi.org/10.1016/j.scitotenv.2020.143341.

[94] L. Yu, M.S. Turner, M. Fitzgerald, J.R. Stokes, T. Witt, Review of the effects of different processing technologies on cooked and convenience rice quality, Trends in Food Science & Technology 59 (2017) 124-138, https://doi.org/https://doi.org/10.1016/j.tifs.2016.11.009.

[95] M.O. Bello, M.A. Loubes, R.J. Aguerre, M.P. Tolaba, Hydrothermal treatment of rough rice: effect of processing conditions on product attributes, J Food Sci Technol 52 (2015) 5156-63, https://doi.org/10.1007/s13197-014-1534-0.

[96] C. Seki, Y. Kainuma, A study of rice cooking (Part 2): Soaking time as a factor controlling rice cooking, Journal of Home Economics of Japan 33 (1982) 228-234,

[97] L.H. Xie, S.Q. Tang, X.J. Wei, G.A. Jiao, Z.H. Sheng, P.S. Hu, An optimized analysis of 2-acetyl-1-pyrroline content diversity in the core collection of aromatic rice germplasm (Oryza sativa L.), Cereal Chemistry 96 (2019) 698-707, https://doi.org/10.1002/cche.10166.

[98] M.N. Calingacion, C. Boualaphanh, V.D. Daygon, R. Anacleto, R. Sackville Hamilton, B. Biais, C. Deborde, M. Maucourt, A. Moing, R. Mumm, R.C.H. de Vos, A. Erban, J. Kopka, T.H. Hansen, K.H. Laursen, J.K. Schjoerring, R.D. Hall, M.A. Fitzgerald, A genomics and multi-platform metabolomics approach to identify new traits of rice quality in traditional and improved varieties, Metabolomics 8 (2012) 771-783, https://doi.org/10.1007/s11306-011-0374-4.

[99] E.D. Wahengbam, A.J. Das, B.D. Green, M.K. Hazarika, Studies on in vitro bioavailability and starch hydrolysis in zinc fortified ready-to-eat parboiled rice (komal chawal), J Food Sci Technol 56 (2019) 3399-3407, https://doi.org/10.1007/s13197-019-03824-4.

[100] E.D. Wahengbam, T. Tongbram, M.K. Hazarika, Drying characteristics of ready-to-eat komal chawal rice: processing and modeling, J Food Sci Technol 57 (2020) 1698-1709, https://doi.org/10.1007/s13197-019-04203-9.

[101] S. Yu, Y. Ma, T. Liu, L. Menager, D.-W. Sun, Impact of cooling rates on the staling behavior of cooked rice during storage, Journal of Food Engineering 96 (2010) 416-420, https://doi.org/10.1016/j.jfoodeng.2009.08.019.

[102] V. Rocha-Villarreal, S.O. Serna-Saldivar, S. García-Lara, Effects of parboiling and other hydrothermal treatments on the physical, functional, and nutritional properties of rice and other cereals, Cereal Chemistry 95 (2018) 79-91, https://doi.org/10.1002/cche.10010.

[103] S. Li, H. Li, L. Lu, G. Shao, Z. Guo, Y. He, Y. Wang, X. Yang, M. Chen, X. Hu, Analysis of rice characteristic volatiles and their influence on rice aroma, Current Research in Food Science 9 (2024) 100794, https://doi.org/10.1016/j.crfs.2024.100794.

[104] Z. Zheng, C. Zhang, K. Liu, Q. Liu, Volatile Organic Compounds, Evaluation Methods and Processing Properties for Cooked Rice Flavor, Rice 15 (2022) 53, https://doi.org/10.1186/s12284-022-00602-3.

[105] L. Guan, Y. Mi, M. Zhang, S. Li, G. Ye, Construction of aroma association network of cooked rice based on gas chromatography–mass spectrometry (GC–MS) and sensory analysis, Flavour and Fragrance Journal 39 (2024) 45-57, https://doi.org/10.1002/ffj.3765.

[106] D.S. Yang, K.-S. Lee, O.Y. Jeong, K.-J. Kim, S.J. Kays, Characterization of Volatile Aroma Compounds in Cooked Black Rice, Journal of Agricultural and Food Chemistry 56 (2008) 235-240, https://doi.org/10.1021/jf072360c.

[107] S. Ye, Q. Gao, D. Shi, A.W. Zongo, J. He, B. Li, Influence of Gradient Milling on Cooking and Sensory Attributes of Chinese Black Rice: Insights into Volatile Flavor Compounds, Foods, 2024.

[108] A. Aznan, C. Gonzalez Viejo, A. Pang, S. Fuentes, Rapid Assessment of Rice Quality Traits Using Low-Cost Digital Technologies, Foods 11 (2022), https://doi.org/10.3390/foods11091181.

[109] J. Xu, K. Liu, C. Zhang, Electronic nose for volatile organic compounds analysis in rice aging, Trends in Food Science & Technology 109 (2021) 83-93, https://doi.org/10.1016/j.tifs.2021.01.027.

[110] L.L. SONG Wei, ZHI Yong-hai, CHEN Rui, Discriminating the Quality of Brown Rice Stored at Different Conditions by Electronic Nose, FOOD SCIENCE 31 (2010) 360-365, https://doi.org/10.7506/spkx1002-6630-201024079.

[111] S. Cui, H. Pu, S.A. Wells, Z. Wen, S. Mao, J. Chang, M.C. Hersam, J. Chen, Ultrahigh sensitivity and layer-dependent sensing performance of phosphorene-based gas sensors, Nature Communications 6 (2015) 8632, https://doi.org/10.1038/ncomms9632.

[112] S. Li, Z. Ma, Z. Cao, L. Pan, Y. Shi, Advanced Wearable Microfluidic Sensors for Healthcare Monitoring, Small 16 (2020) 1903822, https://doi.org/10.1002/smll.201903822.

[113] S. Panda, S. Mehlawat, N. Dhariwal, A. Kumar, A. Sanger, Comprehensive review on gas sensors: Unveiling recent developments and addressing challenges, Materials Science and Engineering: B 308 (2024) 117616, https://doi.org/10.1016/j.mseb.2024.117616.

[114] Y.K. Lee, S. Jang, H.J. Koh, Identification of volatile organic compounds related to the eating quality of cooked japonica rice, Sci Rep 12 (2022) 18133, https://doi.org/10.1038/s41598-022-21863-4.

[115] Z. Zheng, K. Liu, Y. Zhou, M. Debliquy, C. Zhang, Ultrasensitive room-temperature geranyl acetone detection based on Fe@WO3−x nanoparticles in cooked rice flavor analysis, Journal of Advanced Ceramics 12 (2023) 1547-1561, https://doi.org/10.26599/JAC.2023.9220771.

[116] N.-S. Mohammad Sabri, N.A. Mahyudin, M.S. Abdullah Sani, M.G. Han, K.H. Chong, K. Padmanabhan, J. Shan, N.K. Mahmud Ab Rashid, Microbial populations, sensory, and volatile compounds profiling of local cooked rice, Food Quality and Safety 8 (2024) fyad065, https://doi.org/10.1093/fqsafe/fyad065.

[117] H. Jayan, R. Zhou, C. Sun, C. Wang, L. Yin, X. Zou, Z. Guo, Intelligent Gas Sensors for Food Safety and Quality Monitoring: Advances, Applications, and Future Directions, Foods, 2025.

[118] S.J. Park, S.M. Lee, M.-H. Oh, Y.S. Huh, H.W. Jang, Food quality assessment

using chemoresistive gas sensors: achievements and future perspectives, Sustainable Food Technology 2 (2024) 266-280, https://doi.org/10.1039/D3FB00196B.

[119] P. Jun-Cheol, Y. Yeonji, L. Sanghan, Recent Trends in Gas Sensors for Food Spoilage Monitoring, JOURNAL OF SENSOR SCIENCE AND TECHNOLOGY 33 (2024) 412-418, https://doi.org/10.46670/JSST.2024.33.6.412.

[120] S. Dhall, B.R. Mehta, A.K. Tyagi, K. Sood, A review on environmental gas sensors: Materials and technologies, Sensors International 2 (2021) 100116, https://doi.org/10.1016/j.sintl.2021.100116.

[121] A.G. Patil, B. Pramanick, A. Madhukar, MOS-Based Gas Sensors for Monitoring of Air Pollution: A Review, IEEE Sensors Journal 25 (2025) 9250-9262, https://doi.org/10.1109/JSEN.2025.3531888.

[122] H.-T. Jung, The Present and Future of Gas Sensors, ACS Sensors 7 (2022) 912-913, https://doi.org/10.1021/acssensors.2c00688.

[123] Y. Gu, B. Huang, H. Zhu, Smart Gas Sensors Toward Signal and Data Processing: A Review, IEEE Sensors Journal 25 (2025) 2125-2140, https://doi.org/10.1109/JSEN.2024.3507195.

[124] K. Choi, R.-H. Koo, J. Park, D. Kim, J. Kim, H. Shin, G. Jung, J.-H. Lee, Novel Gas Sensor Signal Acquisition Method: Amplifying Sensor Signals and Enabling Efficient Gas Identification, Advanced Science 12 (2025) 2415104, https://doi.org/10.1002/advs.202415104.

[125] N. Goel, K. Kunal, A. Kushwaha, M. Kumar, Metal oxide semiconductors for gas sensing, Engineering Reports 5 (2023) e12604, https://doi.org/https://doi.org/10.1002/eng2.12604.

[126] A. Dey, Semiconductor metal oxide gas sensors: A review, Materials Science and Engineering: B 229 (2018) 206-217, https://doi.org/10.1016/j.mseb.2017.12.036.

[127] S. Ma, J. Xu, Nanostructured metal oxide heterojunctions for chemiresistive gas sensors, Journal of Materials Chemistry A 11 (2023) 23742-23771, https://doi.org/10.1039/D3TA04953A.

[128] Z. Cai, J. Park, S. Park, Synthesis of Flower-like ZnO and Its Enhanced

Sensitivity towards NO_2 Gas Detection at Room Temperature, Chemosensors, 2023.

[129] C.-H. Jiang, C.-B. Yao, L.-Y. Wang, X. Wang, Z.-M. Wang, H.-T. Yin, Interface engineering of modified ZnO@MoS_2 heterostructure to enhance charge transfers and carrier regulation efficiently, Journal of Luminescence 255 (2023) 119546, https://doi.org/10.1016/j.jlumin.2022.119546.

[130] J. Rodrigues, S. Jain, A. Shah, N. Shimpi, Chapter 6 - Improving the parameters of metal oxide gas sensors through doping, in: B.C. Yadav, P. Kumar (Eds.), Complex and Composite Metal Oxides for Gas, VOC and Humidity Sensors, Elsevier2024, pp. 159-188.

[131] A. Sagitova, M. Markelova, A. Nikolaeva, S. Polomoshnov, S. Generalov, N. Khmelevskiy, Y. Grigoriev, E. Konstantinova, V. Krivetskiy, Restraining SnO_2 gas sensor response degradation through heterovalent doping, Sensors and Actuators B: Chemical 429 (2025) 137345, https://doi.org/10.1016/j.snb.2025.137345.

[132] Z. Zheng, K. Liu, K. Xu, C. Zhang, Investigation on microstructure and nonanal sensing properties of hierarchical Sb_2WO_6 microspheres, Ceramics International 48 (2022) 30249-30259, https://doi.org/10.1016/j.ceramint.2022.06.298.

[133] S. Yi, W. Shi, X. Yang, Z. Yao, Engineering sensitive gas sensor based on MOF-derived hollow metal-oxide semiconductor heterostructures, Talanta 258 (2023) 124442, https://doi.org/10.1016/j.talanta.2023.124442.

[134] H. Yuan, N. Li, W. Fan, H. Cai, D. Zhao, Metal-Organic Framework Based Gas Sensors, Advanced Science 9 (2022) 2104374, https://doi.org/10.1002/advs.202104374.

[135] J. Han, H. Li, J. Cheng, X. Ma, Y. Fu, Advances in metal oxide semiconductor gas sensor arrays based on machine learning algorithms, Journal of Materials Chemistry C 13 (2025) 4285-4303, https://doi.org/10.1039/D4TC05220J.

[136] C. Zhang, L. Qian, W. Zeng, MOS based gas sensor in detection of volatile organic compounds: A review, Sensors and Actuators A: Physical 393 (2025) 116818, https://doi.org/10.1016/j.sna.2025.116818.

[137] S. Uma, M.K. Shobana, Metal oxide semiconductor gas sensors in clinical diagnosis and environmental monitoring, Sensors and Actuators A: Physical 349 (2023)

114044, https://doi.org/10.1016/j.sna.2022.114044.

[138] Z. Zhang, Z. Zheng, X. He, K. Liu, M. Debliquy, Y. Zhou, C. Zhang, Electronic nose based on metal oxide semiconductor sensors for medical diagnosis, Progress in Natural Science: Materials International 34 (2024) 74-88, https://doi.org/10.1016/j.pnsc.2024.01.018.

[139] Z. Zheng, C. Zhang, Electronic noses based on metal oxide semiconductor sensors for detecting crop diseases and insect pests, Computers and Electronics in Agriculture 197 (2022) 106988, https://doi.org/10.1016/j.compag.2022.106988.

[140] X. He, H. Chai, Y. Luo, L. Min, M. Debliquy, C. Zhang, Metal oxide semiconductor gas sensing materials for early lung cancer diagnosis, Journal of Advanced Ceramics 12 (2023) 207-227, https://doi.org/10.26599/JAC.2023.9220694.

[141] J. Wawrzyniak, Advancements in Improving Selectivity of Metal Oxide Semiconductor Gas Sensors Opening New Perspectives for Their Application in Food Industry, Sensors, 2023.

[142] Y. Xiao, H. Li, C. Wang, S. Pan, J. He, A. Liu, J. Wang, P. Sun, F. Liu, G. Lu, Room Temperature Wearable Gas Sensors for Fabrication and Applications, Advanced Sensor Research 3 (2024) 2300035, https://doi.org/10.1002/adsr.202300035.

[143] L.-X. Ou, M.-Y. Liu, L.-Y. Zhu, D.W. Zhang, H.-L. Lu, Recent Progress on Flexible Room-Temperature Gas Sensors Based on Metal Oxide Semiconductor, Nano-Micro Letters 14 (2022) 206, https://doi.org/10.1007/s40820-022-00956-9.

[144] G. Liu, E. Froudarakis, J.M. Patel, M.Y. Kochukov, B. Pekarek, P.J. Hunt, M. Patel, K. Ung, C.H. Fu, J. Jo, H.K. Lee, A.S. Tolias, B.R. Arenkiel, Target specific functions of EPL interneurons in olfactory circuits, Nature Communications 10 (2019) 3369, https://doi.org/10.1038/s41467-019-11354-y.

[145] V. Kumar, C.R. Mariappan, Characterization of mesoporous Zn doped $NiCo_2O_4$ rods produced by hydrothermal method for NO_x gas sensing application, Journal of Alloys and Compounds 773 (2019) 158-167, https://doi.org/10.1016/j.jallcom.2018.09.264.

[146] J. Liu, L. Zhang, B. Cheng, J. Fan, J. Yu, A high-response formaldehyde sensor

based on fibrous Ag-ZnO/In_2O_3 with multi-level heterojunctions, Journal of Hazardous Materials 413 (2021) 125352, https://doi.org/10.1016/j.jhazmat.2021.125352.

[147] K. Izawa, H. Ulmer, A. Staerz, U. Weimar, N. Barsan, 5 - Application of SMOX-based sensors, in: N. Barsan, K. Schierbaum (Eds.), Gas Sensors Based on Conducting Metal Oxides, Elsevier2019, pp. 217-257.

[148] B. Saruhan, R. Lontio Fomekong, S. Nahirniak, Review: Influences of Semiconductor Metal Oxide Properties on Gas Sensing Characteristics, Volume 2 - 2021 (2021), https://doi.org/10.3389/fsens.2021.657931.

[149] J. Huang, Q. Wan, Gas Sensors Based on Semiconducting Metal Oxide One-Dimensional Nanostructures, Sensors, 2009, pp. 9903-9924.

[150] C. Wang, L. Yin, L. Zhang, D. Xiang, R. Gao, Metal Oxide Gas Sensors: Sensitivity and Influencing Factors, Sensors, 2010, pp. 2088-2106.

[151] N. Dufour, Y. Veyrac, P. Menini, F. Blanc, C. Talhi, B. Franc, C. Ganibal, N. Dufour, C. Wartelle, K. Aguir, Increasing the sensitivity and selectivity of Metal Oxide gas sensors by controlling the sensitive layer polarization, SENSORS, 2012 IEEE, 2012, pp. 1-4.

[152] J.-K. Choi, I.-S. Hwang, S.-J. Kim, J.-S. Park, S.-S. Park, U. Jeong, Y.C. Kang, J.-H. Lee, Design of selective gas sensors using electrospun Pd-doped SnO_2 hollow nanofibers, Sensors and Actuators B: Chemical 150 (2010) 191-199, https://doi.org/10.1016/j.snb.2010.07.013.

[153] V. Bochenkov, G. Sergeev, Sensitivity, selectivity, and stability of gas-sensitive metal-oxide nanostructures, Metal oxide nanostructures and their applications2010, pp. 31-52.

[154] S. Acharyya, S. Nag, S. Kimbahune, A. Ghose, A. Pal, P.K. Guha, Selective Discrimination of VOCs Applying Gas Sensing Kinetic Analysis over a Metal Oxide-Based Chemiresistive Gas Sensor, ACS Sensors 6 (2021) 2218-2224, https://doi.org/10.1021/acssensors.1c00115.

[155] W. Zhang, Z. Yuan, H. Zhu, S. Zhang, F. Meng, Kinetic Modeling in Temperature-Modulated Semiconductor Gas Sensor Utilizing Eley–Rideal Mechanism and Its

Application in Discriminative Detection of VOCs, ACS Sensors 9 (2024) 6460-6470, https://doi.org/10.1021/acssensors.4c01835.

[156] H. He, C. Zhao, J. Xu, K. Qu, Z. Jiang, Z. Gao, Y.Y. Song, Exploiting Free-Standing p-CuO/n-TiO_2 Nanochannels as a Flexible Gas Sensor with High Sensitivity for H_2S at Room Temperature, ACS Sens 6 (2021) 3387-3397, https://doi.org/10.1021/acssensors.1c01256.

[157] Z. Liu, X. Mo, S. Tian, J. Chen, Y. Liu, H. Wu, Y. Zhao, Y. Wang, S. Peng, Low-temperature gas sensor with good long-term stability based on $Co_3O_4/Ti_3C_2T_x$ heterojunction, Sensors and Actuators B: Chemical 400 (2024) 134853, https://doi.org/10.1016/j.snb.2023.134853.

[158] Y. Wang, Y. Zhou, Recent Progress on Anti-Humidity Strategies of Chemiresistive Gas Sensors, Materials, 2022.

[159] H. Liu, B. Liu, P. Li, W. Kang, Y. Zhang, High sensitivity and anti-humidity gas sensor for nitrogen dioxide based on Ce/SnO_2 nanomaterials, Sensors and Actuators A: Physical 344 (2022) 113717, https://doi.org/10.1016/j.sna.2022.113717.

[160] N. Barsan, U. Weimar, Conduction Model of Metal Oxide Gas Sensors, Journal of Electroceramics 7 (2001) 143-167, https://doi.org/10.1023/A:1014405811371.

[161] Y. Ou, G. Zhu, P. Liu, Y. Jia, L. Zhu, J. Nie, S. Zhang, W. Zhang, J. Gao, H. Lu, Y. Huang, X. Shi, M. Hojamberdiev, Anchoring Platinum Clusters onto Oxygen Vacancy-Modified In_2O_3 for Ultraefficient, Low-Temperature, Highly Sensitive, and Stable Detection of Formaldehyde, ACS Sens 7 (2022) 1201-1212, https://doi.org/10.1021/acssensors.2c00334.

[162] H. Ji, W. Zeng, Y. Li, Gas sensing mechanisms of metal oxide semiconductors: a focus review, Nanoscale 11 (2019) 22664-22684, https://doi.org/10.1039/C9NR07699A.

[163] Z. Li, H. Li, Z. Wu, M. Wang, J. Luo, H. Torun, P. Hu, C. Yang, M. Grundmann, X. Liu, Y. Fu, Advances in designs and mechanisms of semiconducting metal oxide nanostructures for high-precision gas sensors operated at room temperature, Materials Horizons 6 (2019) 470-506, https://doi.org/10.1039/c8mh01365a.

[164] D. Meena, M. Jain, M.C. Bhatnagar, Resistive gas sensors based on nanostructured ternary metal oxide: a review, Journal of Materials Science 59 (2024) 12177-12218, https://doi.org/10.1007/s10853-024-09903-y.

[165] K. Sivaperuman, A. Thomas, R. Thangavel, L. Thirumalaisamy, S. Palanivel, S. Pitchaimuthu, N. Ahsan, Y. Okada, Binary and ternary metal oxide semiconductor thin films for effective gas sensing applications: A comprehensive review and future prospects, Progress in Materials Science 142 (2024) 101222, https://doi.org/10.1016/j.pmatsci.2023.101222.

[166] J.W. Fergus, Perovskite oxides for semiconductor-based gas sensors, Sensors and Actuators B: Chemical 123 (2007) 1169-1179, https://doi.org/10.1016/j.snb.2006.10.051.

[167] W. Ding, D. Liu, J. Liu, J. Zhang, Oxygen Defects in Nanostructured Metal-Oxide Gas Sensors: Recent Advances and Challenges†, Chinese Journal of Chemistry 38 (2020) 1832-1846, https://doi.org/10.1002/cjoc.202000341.

[168] C. Balamurugan, S.-J. Song, H.-S. Kim, Enhancing Gas Response Characteristics of Mixed Metal Oxide Gas Sensors, J. Korean Ceram. Soc 55 (2018) 1-20, https://doi.org/10.4191/kcers.2018.55.1.10.

[169] D.R. Miller, S.A. Akbar, P.A. Morris, Nanoscale metal oxide-based heterojunctions for gas sensing: A review, Sensors and Actuators B: Chemical 204 (2014) 250-272, https://doi.org/10.1016/j.snb.2014.07.074.

[170] S. Yang, G. Lei, H. Xu, Z. Lan, Z. Wang, H. Gu, Metal Oxide Based Heterojunctions for Gas Sensors: A Review, Nanomaterials (Basel, Switzerland) 11 (2021), https://doi.org/10.3390/nano11041026.

[171] Y. Qian, G. Zhao, C. Zhang, S. Yin, J. Chen, Y. Luo, Z. Huang, B. Liu, G. Duan, Hydrogen sensing with high-performance via O^- ion spillover at Pd single atoms stabilized SnO_2 interface, Communications Materials 6 (2025) 137, https://doi.org/10.1038/s43246-025-00865-5.

[172] S. Navale, M. Shahbaz, A. Mirzaei, S.S. Kim, H.W. Kim, Effect of Ag Addition on the Gas-Sensing Properties of Nanostructured Resistive-Based Gas Sensors: An

Overview, Sensors, 2021.

[173] Y. Shi, X. Li, X.F. Sun, X. Shao, H.Y. Wang, Strategies for improving the sensing performance of In_2O_3-based gas sensors for ethanol detection, Journal of Alloys and Compounds 963 (2023) 171190, https://doi.org/10.1016/j.jallcom.2023.171190.

[174] D.K. Singh, V. Ganesan, D.K. Yadav, M. Yadav, Metal (Mn, Fe, Co, Ni, Cu, and Zn) Phthalocyanine-Immobilized Mesoporous Carbon Nitride Materials as Durable Electrode Modifiers for the Oxygen Reduction Reaction, Langmuir 36 (2020) 12202-12212, https://doi.org/10.1021/acs.langmuir.0c01822.

[175] S. Sahoo, K.Y. Wickramathilaka, E. Njeri, D. Silva, S.L. Suib, A review on transition metal oxides in catalysis, Volume 12 - 2024 (2024), https://doi.org/10.3389/fchem.2024.1374878.

[176] M. Tomić, M. Šetka, L. Vojkůvka, S. Vallejos, VOCs Sensing by Metal Oxides, Conductive Polymers, and Carbon-Based Materials, Nanomaterials (Basel, Switzerland) 11 (2021), https://doi.org/10.3390/nano11020552.

[177] N. Barrow, J. Bradley, B. Corrie, Y. Cui, T.D. Tran, T.E. Erden, A. Fish, M. Garcia, P. Glen, N. Mistry, M. Nicholson, S. Roloff-Standring, D. Sheldon, T. Smith, A. Summer, K.U. Din, N. Macleod, Doubling the life of Cu/ZnO methanol synthesis catalysts via use of Si as a structural promoter to inhibit sintering, Science Advances 10 eadk2081, https://doi.org/10.1126/sciadv.adk2081.

[178] X. Gao, Z. Wang, J. Ashok, S. Kawi, A comprehensive review of anti-coking, anti-poisoning and anti-sintering catalysts for biomass tar reforming reaction, Chemical Engineering Science: X 7 (2020) 100065, https://doi.org/10.1016/j.cesx.2020.100065.

[179] S.S. Patil, B.M. Babar, D.Y. Nadargi, F.I. Shaikh, J.D. Nadargi, B.R. Sankapal, I.S. Mulla, M.S. Tamboli, N.T. Nguyen Truong, S.S. Suryavanshi, La-Fe-O Perovskite Based Gas Sensors: Recent Advances and Future Challenges, ACS Omega 9 (2024) 29994-30014, https://doi.org/10.1021/acsomega.4c00334.

[180] J.P. Morán-Lázaro, M. Courel, A. Guillén-Bonilla, F. López-Urías, H. Guillén-Bonilla, V. Soto, A. Palafox Corona, D. Hernández-Poot, A Novel Sensor for the Detection of n-Butanol Based on $CoMn_2O_4$ Nanoparticles, Electronic Materials Letters

20 (2024), https://doi.org/10.1007/s13391-024-00498-9.

[181] S. Wang, J. Cao, W. Cui, L. Fan, X. Li, D. Li, Oxygen vacancies and grain boundaries potential barriers modulation facilitated formaldehyde gas sensing performances for In_2O_3 hierarchical architectures, Sensors and Actuators B: Chemical 255 (2018) 159-165, https://doi.org/10.1016/j.snb.2017.08.054.

[182] B. Han, T.H. Rupam, A. Chakraborty, B.B. Saha, A comprehensive review on VOCs sensing using different functional materials: Mechanisms, modifications, challenges and opportunities, Renewable and Sustainable Energy Reviews 196 (2024) 114365, https://doi.org/10.1016/j.rser.2024.114365.

[183] C. Xiao, Z. Tang, Z. Ma, X. Gao, H. Wang, L. Jia, High performance porous $LaFeO_3$ gas sensor with embedded p-n junctions enabling ppb-level formaldehyde detection, Sensors and Actuators B: Chemical 397 (2023) 134670, https://doi.org/10.1016/j.snb.2023.134670.

[184] D. Zhang, T. Wang, L. Huo, S. Gao, B. Li, C. Guo, H. Yu, Z. Major, X. Zhang, X. Cheng, Y. Xu, Small size porous $NiO/NiFe_2O_4$ nanocubes derived from Ni-Fe bimetallic metal–organic frameworks for fast volatile organic compounds detection, Applied Surface Science 623 (2023) 157075, https://doi.org/10.1016/j.apsusc.2023.157075.

[185] S.J.A. Zaidi, J.C. Park, J.W. Han, J.H. Choi, M.A. Ali, M.A. Basit, T.J. Park, Interfaces in Atomic Layer Deposited Films: Opportunities and Challenges, Small Science 3 (2023) 2300060, https://doi.org/10.1002/smsc.202300060.

[186] R. Zhao, P. Mao, J. Lv, P.-C. Yang, M. Li, B. Wang, W. Bi, S. Xing, Y. Zhong, Z. Zou, Atomic layer deposition processed interlayers in photovoltaics: applications, challenges and perspectives, Journal of Energy Chemistry 109 (2025) 702-725, https://doi.org/10.1016/j.jechem.2025.06.013.

[187] M. Ma, L. Chen, L. Peng, Y. Peng, J. Bi, D. Gao, J. Wu, Carrier and oxygen vacancy engineering of aliovalent ion modified $BiFeO_3$ and their gas sensing properties, Sensors and Actuators B: Chemical 370 (2022) 132400, https://doi.org/10.1016/j.snb.2022.132400.

[188] H. Cheng, Y. Wang, Y. Jin, B. Zhou, D. Li, S. Mo, X. Liu, W. Si, J. Li, Oxygen vacancy engineering through equivalent and aliovalent doping on $LaCoO_3$, Separation and Purification Technology 351 (2024) 128078, https://doi.org/10.1016/j.seppur.2024.128078.

[189] F. Tang, Y. Cai, X. Tang, M. Zhang, Rich surface oxygen vacancies $SmFeO_3$ for acetylene gas sensor with ppb-level detection, Sensors and Actuators B: Chemical 422 (2025) 136708, https://doi.org/10.1016/j.snb.2024.136708.

[190] L. Guo, S. Zhao, G. Yang, L. Gao, Y. Wu, X. Zhang, Oxygen vacancies assisted $LaFeO_3$ derived from metal organic frameworks endows a practical HCHO sensor with excellent sensing characteristics, Journal of Industrial and Engineering Chemistry 126 (2023) 501-509, https://doi.org/10.1016/j.jiec.2023.06.038.

[191] Y. Ma, Y. Lu, H. Gou, W. Zhang, S. Yan, X. Xu, Octahedral $NiFe_2O_4$ for high-performance gas sensor with low working temperature, Ceramics International 44 (2018) 2620-2625, https://doi.org/10.1016/j.ceramint.2017.11.008.

[192] X. Wang, X. Li, G. Zhang, Z. Wang, X.Z. Song, Z. Tan, Surface Structure Engineering of Nanosheet-Assembled $NiFe_2O_4$ Fluffy Flowers for Gas Sensing, Nanomaterials (Basel, Switzerland) 11 (2021), https://doi.org/10.3390/nano11020297.

[193] Y. Yang, W. Si, Y. Peng, Y. Wang, H. Liu, Z. Su, J. Li, Defect Engineering on $CuMn_2O_4$ Spinel Surface: A New Path to High-Performance Oxidation Catalysts, Environmental Science & Technology 56 (2022) 16249-16258, https://doi.org/10.1021/acs.est.2c04858.

[194] M.M. Torres, M.L. Martínez, D.M. Maestri, A multivariate study of the relationship between fatty acids and volatile flavor components in olive and walnut oils, Journal of the American Oil Chemists' Society 82 (2005) 105-110, https://doi.org/10.1007/s11746-005-1050-0.

[195] I. Thaveesangsakulthai, J. Jongkhumkrong, K. Chatdarong, P. Torvorapanit, W. Sukbangnop, T. Sooksimuang, C. Kulsing, B. Tomapatanaget, A fluorescence-based sweat test sensor in a proof-of-concept clinical study for COVID-19 screening diagnosis, Analyst 148 (2023) 2956-2964, https://doi.org/10.1039/d3an00429e.

[196] M. Tsujiguchi, Y. Kii, T. Aitoku, M. Iwao, Y.Y. Maruo, Nonanal Gas Sensors Using Porous Glass as a Reaction Field for Ammonia-Catalyzed Aldol Condensation, ACS Omega 8 (2023) 7874-7882, https://doi.org/10.1021/acsomega.2c07622.

[197] P. Fuchs, C. Loeseken, J.K. Schubert, W. Miekisch, Breath gas aldehydes as biomarkers of lung cancer, International Journal of Cancer 126 (2010) 2663-2670, https://doi.org/10.1002/ijc.24970.

[198] T. Itoh, T. Nakashima, N. Izu, W. Shin, Y. Setoguchi, K. Kato, M. Toyota, 6.3. 4 Noble Metal Added Tin Oxide VOC Sensors as Nonanal Detection for Exhaled Breath Air Monitoring, 14th International Meeting on Chemical Sensors - IMCS 2012, 2012, pp. 547-550.

[199] S. Janfaza, M. Banan Nojavani, B. Khorsand, M. Nikkhah, J.J.D. Zahiri, Cancer Odor Database (COD): a critical databank for cancer diagnosis research, Database 2017 (2017),

[200] X.-Y. Huang, Z.-T. Chi, W. Yang, Y. Deng, W.-F. Xie, Synthesis of $Bi_2O_2CO_3$/$In(OH)_3 \cdot xH_2O$ nanocomposites for isopropanol sensor with excellent performances at low temperature, Sensors and Actuators B: Chemical 361 (2022) 131715, https://doi.org/10.1016/j.snb.2022.131715.

[201] P. Chen, H. Liu, Y. Sun, J. Li, W. Cui, L.a. Wang, W. Zhang, X. Yuan, Z. Wang, Y. Zhang, F. Dong, Bi metal prevents the deactivation of oxygen vacancies in $Bi_2O_2CO_3$ for stable and efficient photocatalytic NO abatement, Applied Catalysis B: Environmental 264 (2020) 118545, https://doi.org/10.1016/j.apcatb.2019.118545.

[202] J. Zai, F. Cao, N. Liang, K. Yu, Y. Tian, H. Sun, X. Qian, Rose-like I-doped $Bi_2O_2CO_3$ microspheres with enhanced visible light response: DFT calculation, synthesis and photocatalytic performance, Journal of Hazardous Materials 321 (2017) 464-472, https://doi.org/10.1016/j.jhazmat.2016.09.034.

[203] J.-h. Li, J. Ren, Y.-j. Hao, E.-p. Zhou, Y. Wang, X.-j. Wang, R. Su, Y. Liu, X.-h. Qi, F.-t. Li, Construction of β-Bi_2O_3/$Bi_2O_2CO_3$ heterojunction photocatalyst for deep understanding the importance of separation efficiency and valence band position, Journal of Hazardous Materials 401 (2021) 123262,

https://doi.org/10.1016/j.jhazmat.2020.123262.

[204] X. Zu, Y. Zhao, X. Li, R. Chen, W. Shao, Z. Wang, J. Hu, J. Zhu, Y. Pan, Y. Sun, Y. Xie, Ultrastable and Efficient Visible-light-driven CO_2 Reduction Triggered by Regenerative Oxygen-Vacancies in $Bi_2O_2CO_3$ Nanosheets, Angewandte Chemie International Edition 60 (2021) 13840-13846, https://doi.org/10.1002/anie.202101894.

[205] P. Wang, S. Guo, Z. Hu, L. Zhou, T. Li, S. Pu, H. Mao, H. Cai, Z. Zhu, B. Chen, H.Y. Li, H. Liu, Single-Atom Cu Stabilized on Ultrathin $WO_{2.72}$ Nanowire for Highly Selective and Ultrasensitive ppb-Level Toluene Detection, Adv Sci (Weinh) 10 (2023) e2302778, https://doi.org/10.1002/advs.202302778.

[206] E. Grabowska, Selected perovskite oxides: Characterization, preparation and photocatalytic properties-A review, Applied Catalysis B: Environmental 186 (2016) 97-126, https://doi.org/10.1016/j.apcatb.2015.12.035.

[207] P. Li, X. Xu, J. Zhao, P. Awasthi, X. Qiao, J. Du, X. Fan, G. Qian, Lanthanide doped fluorosilicate glass-ceramics: A review on experimental and theoretical progresses, Journal of Rare Earths 40 (2022) 169-192, https://doi.org/10.1016/j.jre.2021.09.014.

[208] Y. Gao, X. Wang, Q. Zhang, H. Wang, G. Xu, X. Wang, Influence of La doping on the ethanol gas sensing properties of $CdSnO_3$ micro-cubes, Sensors and Actuators B: Chemical 394 (2023) 134447, https://doi.org/10.1016/j.snb.2023.134447.

[209] K. Shingange, H.C. Swart, G.H. Mhlongo, H_2S detection capabilities with fibrous-like La-doped ZnO nanostructures: A comparative study on the combined effects of La-doping and post-annealing, Journal of Alloys and Compounds 797 (2019) 284-301, https://doi.org/10.1016/j.jallcom.2019.05.060.

[210] X.-d. Wang, N.-l. Zhou, W.-y. Wang, Y.-d. Tang, J. Zhang, J. Shen, The antimicrobial properties of carboxylated graphene oxide decorated with La particles, Carbon 52 (2013) 625, https://doi.org/10.1016/j.carbon.2012.10.026.

[211] N. Yuksel, A. Kose, D. Düzenli, M.F. Fellah, Hydrogen molecule adsorption and sensing on lanthanide (La) doped/decorated carbon nanotube and graphene structures, Journal of Vacuum Science & Technology A 41 (2023),

https://doi.org/10.1116/6.0002229.

[212] X.-Y. Huang, K. Chen, W. Xie, Y. Li, F. Yang, Y. Deng, J. Li, F. Jiang, Y. Shu, L. Wu, W.-F. Xie, Y. Deng, Chemiresistive Gas Sensors Based on Highly Permeable Sn-Doped Bismuth Subcarbonate Microspheres: Facile Synthesis, Sensing Performance, and Mechanism Study, Advanced Functional Materials 33 (2023) 2304718, https://doi.org/10.1002/adfm.202304718.

[213] C. Greaves, S.K. Blower, Structural relationships between $Bi_2O_2CO_3$ and β-Bi_2O_3, Materials Research Bulletin 23 (1988) 1001-1008, https://doi.org/10.1016/0025-5408(88)90055-4.

[214] T. Onishi, Chapter 2 - Quantum Chemistry in Functional Inorganic Materials, in: J.R. Sabin, E.J. Brändas (Eds.), Advances in Quantum Chemistry, Academic Press2012, pp. 31-81.

[215] L. Chen, R. Mao, Lattice oxygen behaviors of Mn-based catalytic oxygen carriers and sustainable oxidative coupling of methane in chemical-looping scheme, Fuel 371 (2024) 131910, https://doi.org/10.1016/j.fuel.2024.131910.

[216] Y. Wang, L. Zhu, J. Li, W. Zhang, X. Shi, Y. Huang, M. Hojamberdiev, G. Zhu, Metal support interaction of defective-rich CuO and Au with enhanced CO low-temperature catalytic oxidation and moisture resistance, Advanced Powder Materials 2 (2023) 100119, https://doi.org/10.1016/j.apmate.2023.100119.

[217] H. Idriss, On the wrong assignment of the XPS O1s signal at 531–532 eV attributed to oxygen vacancies in photo- and electro-catalysts for water splitting and other materials applications, Surface Science 712 (2021) 121894, https://doi.org/10.1016/j.susc.2021.121894.

[218] L. Jiang, Z. Chen, Y. Xu, R. Zhang, C. Yang, F. Tang, Oxygen Vacancies Induced Performance Enhancement of Sensitivity to Acetone Using La-Doped $ZnSnO_3$ Nanosheets: Experimental and DFT-D3 Study, IEEE Sensors Journal 24 (2024) 2388-2395, https://doi.org/10.1109/JSEN.2023.3340671.

[219] J. Li, X. Wu, Z. Wan, H. Chen, G. Zhang, Full spectrum light driven photocatalytic in-situ epitaxy of one-unit-cell $Bi_2O_2CO_3$ layers on Bi_2O_4 nanocrystals

for highly efficient photocatalysis and mechanism unveiling, Applied Catalysis B: Environmental 243 (2019) 667-677, https://doi.org/10.1016/j.apcatb.2018.10.067.

[220] H. Huang, X. Li, J. Wang, F. Dong, P.K. Chu, T. Zhang, Y. Zhang, Anionic Group Self-Doping as a Promising Strategy: Band-Gap Engineering and Multi-Functional Applications of High-Performance CO_3^{2-}-Doped $Bi_2O_2CO_3$, ACS Catalysis 5 (2015) 4094-4103, https://doi.org/10.1021/acscatal.5b00444.

[221] B. Yang, K. Lv, Q. Li, J. Fan, M.J.A.S.S. Li, Photosensitization of $Bi_2O_2CO_3$ nanoplates with amorphous Bi_2S_3 to improve the visible photoreactivity towards NO oxidation, Applied Surface Science 495 (2019) 143561, https://doi.org/10.1016/j.apsusc.2019.143561.

[222] X. Hu, X. Li, H. Yang, C. Xu, W. Xiong, X. Guo, C. Xie, D. Zeng, Active W Sites Promoted by Defect Engineering Enhanced $C_2H_6S_3$ Sensing Performance of WO_3 Nanosheets, ACS Sensors 7 (2022) 1894-1902, https://doi.org/10.1021/acssensors.2c00487.

[223] H. Yin, Z. Chen, Y. Peng, S. Xiong, Y. Li, H. Yamashita, J. Li, Dual Active Centers Bridged by Oxygen Vacancies of Ruthenium Single-Atom Hybrids Supported on Molybdenum Oxide for Photocatalytic Ammonia Synthesis, Angewandte Chemie International Edition 61 (2022) e202114242, https://doi.org/10.1002/anie.202114242.

[224] M. Sun, Y. Zhang, W. Liu, X. Zhao, H. Luo, G. Miao, Z. Wang, S. Li, L. Kong, Synergy of metallic Pt and oxygen vacancy sites in Pt–WO_{3-x} catalysts for efficiently promoting vanillin hydrodeoxygenation to methylcyclohexane, Green Chemistry 24 (2022) 9489-9495, https://doi.org/10.1039/D2GC03144B.

[225] Y. Cai, D. Chen, N. Li, Q. Xu, H. Li, J. He, J. Lu, A Self-Cleaning Heterostructured Membrane for Efficient Oil-in-Water Emulsion Separation with Stable Flux, Advanced materials (Deerfield Beach, Fla.) 32 (2020) e2001265, https://doi.org/10.1002/adma.202001265.

[226] Y. Lan, Z. Li, W. Xie, D. Li, G. Yan, S. Guo, C. Pan, J. Wu, In situ fabrication of I-doped $Bi_2O_2CO_3$/g-C_3N_4 heterojunctions for enhanced photodegradation activity under visible light, Journal Of Hazardous Materials 385 (2020) 121622,

https://doi.org/10.1016/j.jhazmat.2019.121622.

[227] C. Wang, T. Hosomi, K. Nagashima, T. Takahashi, G. Zhang, M. Kanai, H. Yoshida, T. Yanagida, Phosphonic acid modified ZnO nanowire sensors: directing reaction pathway of volatile carbonyl compounds, ACS Appl Mater Interfaces 12 (2020) 44265-44272, https://doi.org/10.1021/acsami.0c10332.

[228] A. Daneshkhah, S. Vij, A.P. Siegel, M. Agarwal, Polyetherimide/carbon black composite sensors demonstrate selective detection of medium-chain aldehydes including nonanal, Chemical Engineering Journal 383 (2020) 123104, https://doi.org/10.1016/j.cej.2019.123104.

[229] J.A. Herron, P. Ferrin, M. Mavrikakis, First-Principles Mechanistic Analysis of Dimethyl Ether Electro-Oxidation on Monometallic Single-Crystal Surfaces, The Journal of Physical Chemistry C 118 (2014) 24199-24211, https://doi.org/10.1021/jp505919x.

[230] C. Sunli, S. Jun, M. Hanping, W. Xiaohong, W. Pei, Z. Xiaodong, Non-destructive detection for mold colonies in rice based on hyperspectra and GWO-SVR, Journal of the Science of Food and Agriculture 98 (2018) 1453-1459, https://doi.org/10.1002/jsfa.8613.

[231] C. Zhang, J. Xu, H. Li, H. Liao, Role of ruthenium incorporation on room-temperature nonanal sensing properties of Ru-loaded urchin-like $W_{18}O_{49}$ hierarchical nanostructure, Sensors and Actuators B: Chemical 353 (2022) 131096, https://doi.org/10.1016/j.snb.2021.131096.

[232] D. Meena, B. Singh, A. Anand, M. Singh, M.C. Bhatnagar, Phase dependent selectivity shifting behavior of Cd_2SnO_4 nanoparticles based gas sensor towards volatile organic compounds (VOC) at low operating temperature, Journal of Alloys and Compounds 820 (2020) 153117, https://doi.org/10.1016/j.jallcom.2019.153117.

[233] H. Gao, Y. Ma, P. Song, Z. Yang, Q. Wang, Three-dimensional reduced graphene oxide/cobaltosic oxide as a high-response sensor for triethylamine gas at room temperature, Materials Science in Semiconductor Processing 133 (2021) 105904, https://doi.org/10.1016/j.mssp.2021.105904.

[234] Y. Masuda, T. Itoh, W. Shin, K. Kato, SnO_2 Nanosheet/Nanoparticle Detector for the Sensing of 1-Nonanal Gas Produced by Lung Cancer, Sci Rep 5 (2015) 10122, https://doi.org/10.1038/srep10122.

[235] P.G. Choi, N. Shirahata, Y. Masuda, Tin oxide nanosheet thin film with bridge type structure for gas sensing, Thin Solid Films 698 (2020) 137845, https://doi.org/10.1016/j.tsf.2020.137845.

[236] H. Wang, H. Zhu, Y. Zhang, J.J.I.J.o.H.E. Pu, Highly active Ni/CeO_2 for the steam reforming of acetic acid using CTAB as surfactant template, International Journal of Hydrogen Energy 47 (2022) 27493-27507,

[237] X. Qiao, D. Li, L. Cheng, B. Jin, Mechanism of electrochemical capture of CO_2 via redox cycle of chlorinated 1,4-naphthoquinone in BMIMBF4: An in-situ FT-IR spectroelectrochemical approach, Journal of Electroanalytical Chemistry 845 (2019) 126-136, https://doi.org/10.1016/j.jelechem.2019.05.057.

[238] T. Shinkai, K. Masumoto, M. Iwai, Y. Inomata, T. Kida, Study on Sensing Mechanism of Volatile Organic Compounds Using Pt-Loaded ZnO Nanocrystals, Sensors (Basel) 22 (2022), https://doi.org/10.3390/s22166277.

[239] F. Kobayashi, Y. Narahara, K. Ohmori, H. Ikeura, Y. Hayata, T. Itani, Effects of Storage with a Deoxygenating Agent and a Nitrogen-atmosphere Package on the Quality, Especially Flavor, of Cooked Stored Rice, Food Science and Technology Research 16 (2010) 175-178, https://doi.org/10.3136/fstr.16.175.

[240] A. Andersen, Final report on the safety assessment of benzaldehyde, International journal of toxicology 25 (2006) 11-27, https://doi.org/10.1080/10915810600716612.

[241] Y. Li, X. Liu, Q. Wu, J. Yi, G. Zhang, Discrimination and detection of benzaldehyde derivatives using sensor array based on fluorescent carbon nanodots, Sensors and Actuators B: Chemical 261 (2018) 271-278, https://doi.org/10.1016/j.snb.2018.01.160.

[242] C. Wang, J. Sun, Y. Sun, Z. Tan, X. Xu, Y. Fu, Z. Feng, J. Zhu, Fabrication of cubic Co_3O_4-hexagonal ZnO disk/rGO as a two-phase benzaldehyde sensor via a sequential nucleation strategy, Sensors and Actuators B: Chemical 330 (2021) 129384,

https://doi.org/10.1016/j.snb.2020.129384.

[243] Y. Wu, S. Zhang, X. Wang, N. Na, Z. Zhang, Development of a benzaldehyde sensor utilizing chemiluminescence on nanosized Y_2O_3, Luminescence 23 (2008) 376-80, https://doi.org/10.1002/bio.1047.

[244] P.Y. Du, W. Gu, X. Liu, Highly selective luminescence sensing of nitrite and benzaldehyde based on 3d-4f heterometallic metal-organic frameworks, Dalton Transactions 45 (2016) 8700-8704, https://doi.org/10.1039/c6dt01360k.

[245] C. Fang, S. Wang, Q. Wang, J. Liu, B. Geng, Coralloid SnO_2 with hierarchical structure and their application as recoverable gas sensors for the detection of benzaldehyde/acetone, Materials Chemistry and Physics 122 (2010) 30-34, https://doi.org/10.1016/j.matchemphys.2010.03.005.

[246] F. Yang, Z. Guo, Engineering NiO sensitive materials and its ultra-selective detection of benzaldehyde, Journal of Colloid and Interface Science 467 (2016) 192-202, https://doi.org/10.1016/j.jcis.2016.01.033.

[247] K.V. Gobi, K. Matsumoto, K. Toko, H. Ikezaki, N. Miura, Enhanced sensitivity of self-assembled-monolayer-based SPR immunosensor for detection of benzaldehyde using a single-step multi-sandwich immunoassay, Analytical and Bioanalytical Chemistry 387 (2007) 2727-2735, https://doi.org/10.1007/s00216-007-1159-5.

[248] H. Zhang, Z. Zhang, Z. Li, H. Han, W. Song, J. Yi, A chemiresistive-potentiometric multivariate sensor for discriminative gas detection, Nature Communications 14 (2023) 3495, https://doi.org/10.1038/s41467-023-39213-x.

[249] K. Großmann, S. Wicker, U. Weimar, N. Barsan, Impact of Pt additives on the surface reactions between SnO_2, water vapour, CO and H_2; an operando investigation, Physical Chemistry Chemical Physics 15 (2013) 19151-19158, https://doi.org/10.1039/C3CP52782D.

[250] D. Zhang, J. Tong, B. Xia, Humidity-sensing properties of chemically reduced graphene oxide/polymer nanocomposite film sensor based on layer-by-layer nano self-assembly, Sensors and Actuators B: Chemical 197 (2014) 66-72, https://doi.org/10.1016/j.snb.2014.02.078.

[251] H. Bi, K. Yin, X. Xie, J. Ji, S. Wan, L. Sun, M. Terrones, M.S. Dresselhaus, Ultrahigh humidity sensitivity of graphene oxide, Scientific Reports 3 (2013) 2714, https://doi.org/10.1038/srep02714.

[252] Y. Wang, Y. Zhou, G. Xie, J. Li, Y. Wang, X. Liu, Z. Zang, Dual Resistance and Impedance Investigation: Ultrasensitive and Stable Humidity Detection of Molybdenum Disulfide Nanosheet-Polyethylene Oxide Hybrids, ACS Applied Materials & Interfaces 13 (2021) 25250-25259, https://doi.org/10.1021/acsami.1c02119.

[253] Y. Zhou, Y. Wang, Y. Wang, H. Yu, R. Zhang, J. Li, Z. Zang, X. Li, MXene $Ti_3C_2T_x$-Derived Nitrogen-Functionalized Heterophase TiO_2 Homojunctions for Room-Temperature Trace Ammonia Gas Sensing, ACS Applied Materials & Interfaces 13 (2021) 56485-56497, https://doi.org/10.1021/acsami.1c17429.

[254] Y. Byoun, S.-W. Choi, Y. Tae Byun, Realisation of highly sensitive and selective NO_2 detection at room temperature utilizing defect-induced single-walled carbon nanotubes combined with Pt functionalisation, Applied Surface Science 590 (2022) 153068, https://doi.org/10.1016/j.apsusc.2022.153068.

[255] N. Liu, Y. Li, Y. Li, L. Cao, N. Nan, C. Li, L. Yu, Tunable NH_4F-Assisted Synthesis of 3D Porous In_2O_3 Microcubes for Outstanding NO_2 Gas-Sensing Performance: Fast Equilibrium at High Temperature and Resistant to Humidity at Room Temperature, ACS Applied Materials & Interfaces 13 (2021) 14355-14364, https://doi.org/10.1021/acsami.0c22987.

[256] Z. Wang, C. Xie, B. Liu, Y. Jiang, Z. Li, H. Tai, X. Li, Self-adaptive temperature and humidity compensation based on improved deep BP neural network for NO_2 detection in complex environment, Sensors and Actuators B: Chemical 362 (2022) 131812, https://doi.org/10.1016/j.snb.2022.131812.

[257] X. Chen, J. Hu, P. Chen, M. Yin, F. Meng, Y. Zhang, UV-light-assisted NO_2 gas sensor based on WS_2/PbS heterostructures with full recoverability and reliable anti-humidity ability, Sensors and Actuators B: Chemical 339 (2021) 129902, https://doi.org/10.1016/j.snb.2021.129902.

[258] J.-S. Kim, K.B. Kim, H.-Y. Li, C.W. Na, K. Lim, Y.K. Moon, J.W. Yoon, J.-H. Lee, Pure and Pr-doped $Ce_4W_9O_{33}$ with superior hydroxyl scavenging ability: humidity-independent oxide chemiresistors, Journal of Materials Chemistry A 9 (2021) 16359-16369, https://doi.org/10.1039/D1TA02618F.

[259] Y. Sun, Z. Zhao, K. Suematsu, P. Li, Z. Yu, W. Zhang, J. Hu, K. Shimanoe, Rapid and Stable Detection of Carbon Monoxide in Changing Humidity Atmospheres Using Clustered In_2O_3/CuO Nanospheres, ACS Sensors 5 (2020) 1040-1049, https://doi.org/10.1021/acssensors.9b02557.

[260] J. Wu, Z. Wu, H. Ding, Y. Wei, W. Huang, X. Yang, Z. Li, L. Qiu, X. Wang, Three-Dimensional Graphene Hydrogel Decorated with SnO_2 for High-Performance NO_2 Sensing with Enhanced Immunity to Humidity, ACS Applied Materials & Interfaces 12 (2020) 2634-2643, https://doi.org/10.1021/acsami.9b18098.

[261] W. Liu, L. Xu, K. Sheng, C. Chen, X. Zhou, B. Dong, X. Bai, S. Zhang, G. Lu, H. Song, APTES-functionalized thin-walled porous WO_3 nanotubes for highly selective sensing of NO_2 in a polluted environment, Journal of Materials Chemistry A 6 (2018) 10976-10989, https://doi.org/10.1039/C8TA02452A.

[262] H. Zhou, Z. Wen, J. Liu, J. Ke, X. Duan, S. Wang, Z-scheme plasmonic Ag decorated WO_3/Bi_2WO_6 hybrids for enhanced photocatalytic abatement of chlorinated-VOCs under solar light irradiation, Applied Catalysis B: Environmental 242 (2019) 76-84, https://doi.org/10.1016/j.apcatb.2018.09.090.

[263] W. Guo, L. Jian, X. Wang, W. Zeng, Hydrothermal synthesis of Ni-doped hydrangea-like Bi_2WO_6 and the enhanced gas sensing property to n-butanol, Sensors and Actuators B: Chemical 357 (2022) 131396, https://doi.org/10.1016/j.snb.2022.131396.

[264] A. Marikutsa, L. Yang, A.N. Kuznetsov, M. Rumyantseva, A. Gaskov, Effect of W–O bonding on gas sensitivity of nanocrystalline Bi_2WO_6 and WO_3, Journal of Alloys and Compounds 856 (2021) 158159, https://doi.org/10.1016/j.jallcom.2020.158159.

[265] Y. Li, X. Wang, G. Sun, J. Cao, Y. Wang, In situ modification of discoid α-Fe_2O_3 nanostructures with Bi_2WO_6 for high performance n-butanol sensor, Vacuum 216 (2023)

112478, https://doi.org/10.1016/j.vacuum.2023.112478.

[266] X. Qian, D. Yue, Z. Tian, M. Reng, Y. Zhu, M. Kan, T. Zhang, Y. Zhao, Carbon quantum dots decorated Bi_2WO_6 nanocomposite with enhanced photocatalytic oxidation activity for VOCs, Applied Catalysis B: Environmental 193 (2016) 16-21, https://doi.org/10.1016/j.apcatb.2016.04.009.

[267] P. Jineesh, T.C. Bhagya, R. Remya, S.M.A. Shibli, Photocatalytic hydrogen generation by WO_3 in synergism with hematite-anatase heterojunction, International Journal of Hydrogen Energy 45 (2020) 18946-18960, https://doi.org/10.1016/j.ijhydene.2020.05.043.

[268] T.H. Eom, S.H. Cho, J.M. Suh, T. Kim, J.W. Yang, T.H. Lee, S.E. Jun, S.J. Kim, J. Lee, S.-H. Hong, H.W. Jang, Visible Light Driven Ultrasensitive and Selective NO_2 Detection in Tin Oxide Nanoparticles with Sulfur Doping Assisted by l-Cysteine, Small 18 (2022) 2106613, https://doi.org/10.1002/smll.202106613.

[269] M.-S. Gui, W.-D. Zhang, Y.-Q. Chang, Y.-X. Yu, One-step hydrothermal preparation strategy for nanostructured WO_3/Bi_2WO_6 heterojunction with high visible light photocatalytic activity, Chemical Engineering Journal 197 (2012) 283-288, https://doi.org/10.1016/j.cej.2012.05.032.

[270] X. Wang, J. Lu, W. Han, P. Cheng, Y. Wang, J. Sun, J. Ma, P. Sun, H. Zhang, Y. Sun, G. Lu, Carbon modification endows WO_3 with anti-humidity property and long-term stability for ultrafast H_2S detection, Sensors and Actuators B: Chemical 350 (2022) 130884, https://doi.org/10.1016/j.snb.2021.130884.

[271] X. Chen, J. Li, F. Chen, Photocatalytic degradation of MB by novel and environmental ZnO/Bi_2WO_6-CC hierarchical heterostructures, Materials Characterization 189 (2022) 111961, https://doi.org/10.1016/j.matchar.2022.111961.

[272] G. Zhang, F. Lü, M. Li, J. Yang, X. Zhang, B. Huang, Synthesis of nanometer Bi_2WO_6 synthesized by sol–gel method and its visible-light photocatalytic activity for degradation of 4BS, Journal of Physics and Chemistry of Solids 71 (2010) 579-582, https://doi.org/10.1016/j.jpcs.2009.12.041.

[273] J. Yan, M.-T.F. Rodrigues, Z. Song, H. Li, H. Xu, H. Liu, J. Wu, Y. Xu, Y. Song,

Y. Liu, P. Yu, W. Yang, R. Vajtai, H. Li, S. Yuan, P.M. Ajayan, Reversible Formation of g-C_3N_4 3D Hydrogels through Ionic Liquid Activation: Gelation Behavior and Room-Temperature Gas-Sensing Properties, Advanced Functional Materials 27 (2017) 1700653, https://doi.org/10.1002/adfm.201700653.

[274] P.-F. Cao, S.-Y. Ma, R.-J. Fan, Carbon-doped porous hollow alpha-Fe_2O_3 microtubules controlled by absorbent cotton bio-template to detect acetic acid vapor, Ceramics International 48 (2022) 12729-12741, https://doi.org/10.1016/j.ceramint.2022.01.142.

[275] S. Laurenzi, S. Botti, A. Rufoloni, M.G. Santonicola, Mapping the residual strain of carbon nanotubes in DWCNT/epoxy nanocomposites after tensile load using Raman microscopy, Composites Communications 21 (2020) 100424, https://doi.org/10.1016/j.coco.2020.100424.

[276] J. Huang, Y. Xiao, Z. Peng, Y. Xu, L. Li, L. Tan, K. Yuan, Y. Chen, Co_3O_4 Supraparticle-Based Bubble Nanofiber and Bubble Nanosheet with Remarkable Electrochemical Performance, Advanced Science 6 (2019) 1900107, https://doi.org/10.1002/advs.201900107.

[277] D.-H. Kim, S. Chong, C. Park, J. Ahn, J.-S. Jang, J. Kim, I.-D. Kim, Oxide/ZIF-8 Hybrid Nanofiber Yarns: Heightened Surface Activity for Exceptional Chemiresistive Sensing, Advanced Materials 34 (2022) 2105869, https://doi.org/10.1002/adma.202105869.

[278] H. Pazniak, A.S. Varezhnikov, D.A. Kolosov, I.A. Plugin, A.D. Vito, O.E. Glukhova, P.M. Sheverdyaeva, M. Spasova, I. Kaikov, E.A. Kolesnikov, P. Moras, A.M. Bainyashev, M.A. Solomatin, I. Kiselev, U. Wiedwald, V.V. Sysoev, 2D Molybdenum Carbide MXenes for Enhanced Selective Detection of Humidity in Air, Advanced Materials 33 (2021) 2104878, https://doi.org/10.1002/adma.202104878.

[279] X. Wang, P. Ren, H. Tian, H. Fan, C. Cai, W. Liu, Enhanced gas sensing properties of SnO_2: The role of the oxygen defects induced by quenching, Journal of Alloys and Compounds 669 (2016) 29-37, https://doi.org/10.1016/j.jallcom.2016.01.225.

[280] C. Zhang, K. Liu, Z. Zheng, M. Debliquy, Defect engineering of nanostructured

$ZnSnO_3$ for conductometric room temperature CO_2 sensors, Sensors and Actuators B: Chemical 384 (2023) 133628, https://doi.org/10.1016/j.snb.2023.133628.

[281] B. Yu, Y. Li, Y. Wang, N. Li, P. Xiao, D. Liu, L. Geng, Stable Tunable Luminescence of Hetero-valent Eu Ion Activated Ba_2InTaO_6 Phosphors Synthesized by Defect-Induced Self-Reduction in the Molten-Salt Method, Inorg Chem 61 (2022) 2463-2475, https://doi.org/10.1021/acs.inorgchem.1c03312.

[282] Y. Qian, Y. Han, X. Zhang, G. Yang, G. Zhang, H.L. Jiang, Computation-based regulation of excitonic effects in donor-acceptor covalent organic frameworks for enhanced photocatalysis, Nat Commun 14 (2023) 3083, https://doi.org/10.1038/s41467-023-38884-w.

[283] H. Zhao, J. Sun, J. Liu, H. Zhang, H. He, X. Liu, D. Liao, Z. Tong, L. Sun, UV-triggered carrier transport regulation of fibrous NiO/SnO_2 heterostructures for triethylamine detection, Chemical Engineering Journal 476 (2023) 146687, https://doi.org/10.1016/j.cej.2023.146687.

[284] Y.K. Jo, S.-Y. Jeong, Y.K. Moon, Y.-M. Jo, J.-W. Yoon, J.-H. Lee, Exclusive and ultrasensitive detection of formaldehyde at room temperature using a flexible and monolithic chemiresistive sensor, Nature Communications 12 (2021) 4955, https://doi.org/10.1038/s41467-021-25290-3.

[285] A. Šetkus, Heterogeneous reaction rate based description of the response kinetics in metal oxide gas sensors, Sensors and Actuators B: Chemical 87 (2002) 346-357, https://doi.org/10.1016/S0925-4005(02)00269-1.

[286] N. Yamazoe, K. Shimanoe, Theory of power laws for semiconductor gas sensors, Sensors and Actuators B: Chemical 128 (2008) 566-573, https://doi.org/10.1016/j.snb.2007.07.036.

[287] D.R. Jones, T.G.G. Maffeïs, Analysis of the kinetics of surface reactions on a zinc oxide nanosheet-based carbon monoxide sensor using an Eley–Rideal model, Sensors and Actuators B: Chemical 218 (2015) 16-24, https://doi.org/10.1016/j.snb.2015.04.072.

[288] N.M. Vuong, D. Kim, H. Kim, Surface gas sensing kinetics of a WO_3 nanowire

sensor: Part 2—Reducing gases, Sensors and Actuators B: Chemical 224 (2016) 425-433, https://doi.org/10.1016/j.snb.2015.10.070.

[289] A. Fort, M. Mugnaini, S. Rocchi, M.B. Serrano-Santos, V. Vignoli, R. Spinicci, Simplified models for SnO_2 sensors during chemical and thermal transients in mixtures of inert, oxidizing and reducing gases, Sensors and Actuators B: Chemical 124 (2007) 245-259, https://doi.org/10.1016/j.snb.2006.12.030.

[290] H. Hu, M. Trejo, M.E. Nicho, J.M. Saniger, A. García-Valenzuela, Adsorption kinetics of optochemical NH_3 gas sensing with semiconductor polyaniline films, Sensors and Actuators B: Chemical 82 (2002) 14-23, https://doi.org/10.1016/S0925-4005(01)00984-4.

[291] S. Shao, C. Xie, L. Zhang, S. Wei, H.W. Kim, S.S. Kim, $CsPbI_3$NC-Sensitized SnO_2/Multiple-Walled Carbon Nanotube Self-Assembled Nanomaterials with Highly Selective and Sensitive NH_3 Sensing Performance at Room Temperature, ACS Applied Materials & Interfaces 13 (2021) 14447-14457, https://doi.org/10.1021/acsami.0c20566.

[292] M.-S. Yao, W.-X. Tang, G.-E. Wang, B. Nath, G. Xu, MOF Thin Film-Coated Metal Oxide Nanowire Array: Significantly Improved Chemiresistor Sensor Performance, Advanced Materials 28 (2016) 5229-5234, https://doi.org/10.1002/adma.201506457.

[293] C. Zhang, Z. Zheng, K. Liu, M. Debliquy, Q. Liu, Highly sensitive and selective Sb_2WO_6 microspheres in detecting VOC biomarkers in cooked rice: Experimental and density functional theory study, Food Chemistry 424 (2023) 136323, https://doi.org/10.1016/j.foodchem.2023.136323.

[294] X. Li, B. Kang, F. Dong, Z. Zhang, X. Luo, L. Han, J. Huang, Z. Feng, Z. Chen, J. Xu, B. Peng, Z.L. Wang, Enhanced photocatalytic degradation and H_2/H_2O_2 production performance of S-pCN/$WO_{2.72}$ S-scheme heterojunction with appropriate surface oxygen vacancies, Nano Energy 81 (2021) 105671, https://doi.org/10.1016/j.nanoen.2020.105671.

[295] B. Guan, J. Zhao, H. Jin, H. Lin, Determination of Rice Storage Time with

Colorimetric Sensor Array, Food Analytical Methods 10 (2016) 1054-1062, https://doi.org/10.1007/s12161-016-0664-6.

[296] W. Chen, Z. Wang, S. Gu, J. Wang, Y. Wang, Z. Wei, Detection of hexanal and 1-octen-3-ol in refrigerated grass carp fillets using a QCM gas sensor based on hydrophobic Cu(I)-Cys nanocomposite, Sensors and Actuators B: Chemical 305 (2020) 127476, https://doi.org/10.1016/j.snb.2019.127476.

[297] X. Fan, X. Jiao, J. Liu, M. Jia, C. Blanchard, Z. Zhou, Characterizing the volatile compounds of different sorghum cultivars by both GC-MS and HS-GC-IMS, Food Research International 140 (2021) 109975, https://doi.org/10.1016/j.foodres.2020.109975.

[298] T.H.M. Database, Showing metabocard for (R)-1-Octen-3-ol (HMDB0031299), in: T.H.M. Database (Ed.) 2019.

[299] R. Kataoka, T. Watanabe, S. Yano, O. Mizutani, O. Yamada, T. Kasumi, J. Ogihara, Aspergillus luchuensis fatty acid oxygenase ppoC is necessary for 1-octen-3-ol biosynthesis in rice koji, Journal of Bioscience and Bioengineering 129 (2020) 192-198, https://doi.org/10.1016/j.jbiosc.2019.08.010.

[300] F. Brodhun, I. Feussner, Oxylipins in fungi, The FEBS Journal 278 (2011) 1047-1063, https://doi.org/10.1111/j.1742-4658.2011.08027.x.

[301] Y. Duan, H. Lin, P. He, Q. Chen, Detection of volatile marker in the wheat infected with Aspergillus flavus by porous silica nanospheres doped Bodipy dyes, Sensors and Actuators B: Chemical 330 (2021) 129407, https://doi.org/10.1016/j.snb.2020.129407.

[302] R. Rahimi, M. Solimannejad, $B_3C_2N_3$ monolayer as a potential biosensor for the sensitive and selective detection of liver cancer biomarkers: A DFT study, Materials Science in Semiconductor Processing 186 (2025) 109025, https://doi.org/10.1016/j.mssp.2024.109025.

[303] A.A. Inamdar, M.M. Hossain, A.I. Bernstein, G.W. Miller, J.R. Richardson, J.W. Bennett, Fungal-derived semiochemical 1-octen-3-ol disrupts dopamine packaging and causes neurodegeneration, Proceedings of the National Academy of Sciences of the United States of America 110 (2013) 19561-6,

https://doi.org/10.1073/pnas.1318830110.

[304] A. Petherick, How DEET jams insects' smell sensors, Nature (2008), https://doi.org/10.1038/news.2008.672.

[305] M. Ditzen, M. Pellegrino, L.B. Vosshall, Insect Odorant Receptors Are Molecular Targets of the Insect Repellent DEET, Science 319 (2008) 1838-1842, https://doi.org/10.1126/science.1153121.

[306] Z. Syed, W.S. Leal, Mosquitoes smell and avoid the insect repellent DEET, Proceedings of the National Academy of Sciences 105 (2008) 13598-13603, https://doi.org/10.1073/pnas.0805312105.

[307] X. Guo, M. Li, Y. Liu, Y. Huang, S. Geng, W. Yang, Y. Yu, Hierarchical core-shell electrode with $NiWO_4$ nanoparticles wrapped $MnCo_2O_4$ nanowire arrays on Ni foam for high-performance asymmetric supercapacitors, Journal of Colloid and Interface Science 563 (2020) 405-413, https://doi.org/10.1016/j.jcis.2019.12.076.

[308] Y. Ji, L. Yang, X. Ren, G. Cui, X. Xiong, X. Sun, Full Water Splitting Electrocatalyzed by $NiWO_4$ Nanowire Array, ACS Sustainable Chemistry & Engineering 6 (2018) 9555-9559, https://doi.org/10.1021/acssuschemeng.8b01841.

[309] W. Miao, Q. Han, H. Zhang, K. Chen, L. Zhang, Y. Li, S. Han, Uniform phosphorus doped $CoWO_4$@$NiWO_4$ nanocomposites for asymmetric supercapacitors, Journal of Alloys and Compounds 877 (2021) 160301, https://doi.org/10.1016/j.jallcom.2021.160301.

[310] S. Huang, Y. Meng, Y. Cao, F. Yao, Z. He, X. Wang, H. Pan, M. Wu, Amorphous $NiWO_4$ nanoparticles boosting the alkaline hydrogen evolution performance of Ni_3S_2 electrocatalysts, Applied Catalysis B: Environmental 274 (2020) 119120, https://doi.org/10.1016/j.apcatb.2020.119120.

[311] T. Meng, Z. Kou, I.S. Amiinu, X. Hong, Q. Li, Y. Tang, Y. Zhao, S. Liu, L. Mai, S. Mu, Electronic Structure Control of Tungsten Oxide Activated by Ni for Ultrahigh-Performance Supercapacitors, Small 14 (2018) 1800381, https://doi.org/10.1002/smll.201800381.

[312] G. Nagaraju, R. Kakarla, S.M. Cha, J.S. Yu, Highly flexible conductive fabrics

with hierarchically nanostructured amorphous nickel tungsten tetraoxide for enhanced electrochemical energy storage, Nano Research 8 (2015) 3749-3763, https://doi.org/10.1007/s12274-015-0874-z.

[313] S. Mani, V. Vediyappan, S.-M. Chen, R. Madhu, V. Pitchaimani, J.-Y. Chang, S.-B. Liu, Hydrothermal synthesis of $NiWO_4$ crystals for high performance non-enzymatic glucose biosensors, Scientific Reports 6 (2016) 24128, https://doi.org/10.1038/srep24128.

[314] N. Yamazoe, G. Sakai, K. Shimanoe, Oxide Semiconductor Gas Sensors, Catalysis Surveys from Asia 7 (2003) 63-75, https://doi.org/10.1023/A:1023436725457.

[315] N. Yamazoe, Y. Kurokawa, T. Seiyama, Effects of additives on semiconductor gas sensors, Sensors and Actuators 4 (1983) 283-289, https://doi.org/10.1016/0250-6874(83)85034-3.

[316] V. Gurylev, T.P. Perng, Defect engineering of ZnO: Review on oxygen and zinc vacancies, Journal of the European Ceramic Society 41 (2021) 4977-4996, https://doi.org/10.1016/j.jeurceramsoc.2021.03.031.

[317] L. Zhang, H. Yu, L. Han, K. Tao, Vacancy engineering of metal–organic framework derivatives for supercapacitors and electrochemical water splitting, Chemical Communications 61 (2025) 8830-8842, https://doi.org/10.1039/D5CC01512J.

[318] Q. He, L. Han, C. Lin, K. Tao, A review on defect modulated electrocatalysts for the oxygen evolution reaction, Nanoscale 16 (2024) 12368-12379, https://doi.org/10.1039/D4NR01805B.

[319] N. Spataru, C. Anastasescu, M.M. Radu, I. Balint, C. Negrila, T. Spataru, A. Fujishima, The improvement of SiO_2 nanotubes electrochemical behavior by hydrogen atmosphere thermal treatment, Applied Surface Science 444 (2018) 216-223, https://doi.org/10.1016/j.apsusc.2018.03.074.

[320] M. Al-Hashem, S. Akbar, P. Morris, Role of Oxygen Vacancies in Nanostructured Metal-Oxide Gas Sensors: A Review, Sensors and Actuators B: Chemical 301 (2019) 126845, https://doi.org/10.1016/j.snb.2019.126845.

[321] Q. He, L. Han, K. Tao, Oxygen vacancy modulated Fe-doped Co_3O_4 hollow nanosheet arrays for efficient oxygen evolution reaction, Chemical Communications 60 (2024) 1116-1119, https://doi.org/10.1039/D3CC05581G.

[322] M. Yang, C. Au, G. Deng, S. Mathur, Q. Huang, X. Luo, G. Xie, H. Tai, Y. Jiang, C. Chen, Z. Cui, X. Liu, C. He, Y. Su, J. Chen, $NiWO_4$ Microflowers on Multi-Walled Carbon Nanotubes for High-Performance NH_3 Detection, ACS Applied Materials & Interfaces 13 (2021) 52850-52860, https://doi.org/10.1021/acsami.1c10805.

[323] M. Chatterjee, S. Saha, T. Chatterjee, S. Das, S.K. Pradhan, Mn-doped $NiWO_4$ quantum dots with superior electrochemical and conductivity performance for energy storage application, Journal of Energy Storage 56 (2022) 105946, https://doi.org/10.1016/j.est.2022.105946.

[324] İ. Uzun, Methods of determining the degree of crystallinity of polymers with X-ray diffraction: a review, Journal of Polymer Research 30 (2023) 394, https://doi.org/10.1007/s10965-023-03744-0.

[325] K. Liu, Z. Zheng, Y. Zhou, C. Bittencourt, M. Debliquy, Q. Liu, C. Zhang, Heterovalent-doping-induced ultrasensitive and highly exclusive ethylene sensor: Application to crop quality inspection, Chemical Engineering Journal 508 (2025) 161075, https://doi.org/10.1016/j.cej.2025.161075.

[326] W. Liu, M. Li, X. Feng, H. Yin, S. Gong, K. Yu, Z. Zhu, Microgram-Level Ta_4C_3 Nanosheets Decorated with $NiWO_4$ Nanoparticles as a High-Performance Humidity Sensor, ACS Applied Nano Materials 6 (2023) 20970-20981, https://doi.org/10.1021/acsanm.3c03964.

[327] A. Bhardwaj, I.-H. Kim, L. Mathur, J.-Y. Park, S.-J. Song, Ultrahigh-sensitive mixed-potential ammonia sensor using dual-functional $NiWO_4$ electrocatalyst for exhaust environment monitoring, Journal of Hazardous Materials 403 (2021) 123797, https://doi.org/10.1016/j.jhazmat.2020.123797.

[328] D. Komatireddy, S. Andem, P.P. Gotipamul, V.V. Rajankumar, S. Chidambaram, Harnessing the potential of transition metal tungstates (MWO_4, M = Ni, Co, Cu, and Zn) for high-performance asymmetric supercapacitors, Journal of Energy Storage 100

(2024) 113557, https://doi.org/10.1016/j.est.2024.113557.

[329] E.S. Babu, B.J. Rani, G. Ravi, R. Yuvakkumar, R.K. Guduru, V. Ganesh, S. Kim, Novel $NiWO_4$ nanoberries morphology effect on photoelectrochemical properties, Materials Letters 220 (2018) 209-212, https://doi.org/10.1016/j.matlet.2018.03.018.

[330] J. Park, Y. Kim, S.Y. Park, S.J. Sung, H.W. Jang, C.R. Park, Band gap engineering of graphene oxide for ultrasensitive NO_2 gas sensing, Carbon 159 (2020) 175-184, https://doi.org/10.1016/j.carbon.2019.11.063.

[331] N. Luo, H. Cai, B. Lu, Z. Xue, J. Xu, Pt-functionalized Amorphous RuO_x as Excellent Stability and High-activity Catalysts for Low Temperature MEMS Sensors, Small 19 (2023) 2300006, https://doi.org/10.1002/smll.202300006.

[332] W. Jin, Z. Zhang, S. Zhao, J. Liu, R. Gao, P. Jiang, Characterization of volatile organic compounds of different pigmented rice after puffing based on gas chromatography-ion migration spectrometry and chemometrics, Food Research International 169 (2023) 112879, https://doi.org/10.1016/j.foodres.2023.112879.

[333] W. Zhang, Y. Yang, J. Zhang, W. Zheng, Y. Du, B. Dang, Study of the effect of milling on nutritional and sensory quality and volatile flavor compounds of cooked highland barley rice, LWT 198 (2024) 115972, https://doi.org/10.1016/j.lwt.2024.115972.

[334] N. Barsan, U. Weimar, Conduction Model of Metal Oxide Gas Sensors, Journal of Electroceramics 7 (2001) 143-167, https://doi.org/10.1023/A:1014405811371.

[335] C. Blackman, Do We Need “Ionosorbed” Oxygen Species? (Or, “A Surface Conductivity Model of Gas Sensitivity in Metal Oxides Based on Variable Surface Oxygen Vacancy Concentration”), ACS Sensors 6 (2021) 3509-3516, https://doi.org/10.1021/acssensors.1c01727.

[336] Y. Masuda, T. Itoh, W. Shin, K. Kato, SnO2 Nanosheet/Nanoparticle Detector for the Sensing of 1-Nonanal Gas Produced by Lung Cancer, Scientific Reports 5 (2015) 10122, https://doi.org/10.1038/srep10122.

[337] Y. Zhou, Y. Luo, Z. Zheng, K. Liu, X. He, K. Wu, M. Debliquy, C. Zhang, Urchin-like Na-doped zinc oxide nanoneedles for low-concentration and exclusive VOC

detections, Journal of Advanced Ceramics 13 (2024) 507-517, https://doi.org/10.26599/JAC.2024.9220873.

[338] L. Wang, B. Zhang, B. Wang, S. Zeng, M. Zhao, X. Sun, Y. Zhai, L. Xu, In-situ Nano-Crystallization and Solvation Modulation to Promote Highly Stable Anode Involving Alloy/De-alloy for Potassium Ion Batteries, Angewandte Chemie International Edition 60 (2021) 15381-15389, https://doi.org/10.1002/anie.202100654.

[339] H. Lu, L. Xu, B. Wei, M. Zhang, H. Gao, W. Sun, Enhanced photosensitization process induced by the p–n junction of $Bi_2O_2CO_3$/BiOCl heterojunctions on the degradation of rhodamine B, Applied Surface Science 303 (2014) 360-366, https://doi.org/10.1016/j.apsusc.2014.03.006.

[340] Y. Yang, H. Wu, B. Liu, Z. Liu, Tumor microenvironment-responsive dynamic inorganic nanoassemblies for cancer imaging and treatment, Advanced Drug Delivery Reviews 179 (2021) 114004, https://doi.org/10.1016/j.addr.2021.114004.

[341] L.-Y. Zhu, K. Yuan, J.-G. Yang, H.-P. Ma, T. Wang, X.-M. Ji, J.-J. Feng, A. Devi, H.-L. Lu, Fabrication of heterostructured p-CuO/n-SnO_2 core-shell nanowires for enhanced sensitive and selective formaldehyde detection, Sensors and Actuators B: Chemical 290 (2019) 233-241, https://doi.org/10.1016/j.snb.2019.03.092.

[342] V. Krivetskiy, I. Malkov, A. Garshev, N. Mordvinova, O.I. Lebedev, S. Dolenko, A. Efitorov, T. Grigoriev, M. Rumyantseva, A. Gaskov, Chemically modified nanocrystalline SnO_2-based materials for nitrogen-containing gases detection using gas sensor array, Journal of Alloys and Compounds 691 (2017) 514-523, https://doi.org/10.1016/j.jallcom.2016.08.275.

[343] A. Hierlemann, R. Gutierrez-Osuna, Higher-Order Chemical Sensing, Chemical Reviews 108 (2008) 563-613, https://doi.org/10.1021/cr068116m.

[344] Y. Jiang, L. Yao, Y. Hu, X. Liu, L. Xu, C. Zheng, L. Chen, J. Yang, X. Gao, An on-chip microarray platform for material-temperature optimization and gas discrimination, Sensors and Actuators B: Chemical 409 (2024) 135633, https://doi.org/10.1016/j.snb.2024.135633.

[345] Z. Yang, Y. Liu, D. Chen, J. Miao, M. Chen, G. Liu, G. Gao, Y. Guo, D. Cui, Q.

Li, A battery-free, wireless, flexible bandlike e-nose based on MEMS gas sensors for precisely volatile organic compounds detection, Nano Energy 127 (2024) 109711, https://doi.org/10.1016/j.nanoen.2024.109711.

[346] L. Sun, R. Li, W. Zhan, Y. Yuan, X. Wang, X. Han, Y. Zhao, Double-shelled hollow rods assembled from nitrogen/sulfur-codoped carbon coated indium oxide nanoparticles as excellent photocatalysts, Nature Communications 10 (2019) 2270, https://doi.org/10.1038/s41467-019-10302-0.

[347] S. Park, M. Kim, Y. Lim, D. Oh, J. Ahn, C. Park, S. Woo, W. Jung, J. Kim, I.-D. Kim, Dual-Photosensitizer Synergy Empowers Ambient Light Photoactivation of Indium Oxide for High-Performance NO_2 Sensing, Advanced Materials 36 (2024) 2313731, https://doi.org/10.1002/adma.202313731.

[348] Y. Cai, D. Chen, N. Li, Q. Xu, H. Li, J. He, J. Lu, A Self-Cleaning Heterostructured Membrane for Efficient Oil-in-Water Emulsion Separation with Stable Flux, Adv. Mater. 32 (2020) 2001265, https://doi.org/10.1002/adma.202001265.

[349] H. Rietveld, A profile refinement method for nuclear and magnetic structures, Journal of Applied Crystallography 2 (1969) 65-71, https://doi.org/doi:10.1107/S0021889869006558.

[350] N. Ritchie, Scanning Electron Microscopy and X-Ray Microanalysis, Springer New York, NY2018, https://doi.org/10.1007/978-1-4939-6676-9.

[351] David B. Williams, C.B. Carter, Transmission Electron Microscopy, Springer New York, NY2009, https://doi.org/10.1007/978-0-387-76501-3.

[352] B.C. Smith, Fundamentals of Fourier Transform Infrared Spectroscopy (2nd ed.), CRC Press2011, https://doi.org/10.1201/b10777.

[353] J. Tauc, Optical properties and electronic structure of amorphous Ge and Si, Materials Research Bulletin 3 (1968) 37-46, https://doi.org/10.1016/0025-5408(68)90023-8.

[354] M.P. Seah, W.A. Dench, Quantitative electron spectroscopy of surfaces: A standard data base for electron inelastic mean free paths in solids, Surface and Interface Analysis 1 (1979) 2-11, https://doi.org/10.1002/sia.740010103.

[355] H. Shinotsuka, S. Tanuma, C.J. Powell, D.R. Penn, Calculations of electron inelastic mean free paths. XII. Data for 42 inorganic compounds over the 50 eV to 200 keV range with the full Penn algorithm, Surface and interface analysis : SIA 51 (2018) 427-457, https://doi.org/10.1002/sia.6598.

[356] N. Fairley, V. Fernandez, M. Richard-Plouet, C. Guillot-Deudon, J. Walton, E. Smith, D. Flahaut, M. Greiner, M. Biesinger, S. Tougaard, D. Morgan, J. Baltrusaitis, Systematic and collaborative approach to problem solving using X-ray photoelectron spectroscopy, Applied Surface Science Advances 5 (2021) 100112, https://doi.org/10.1016/j.apsadv.2021.100112.

[357] G. Greczynski, L. Hultman, X-ray photoelectron spectroscopy: Towards reliable binding energy referencing, Progress in Materials Science 107 (2020) 100591, https://doi.org/https://doi.org/10.1016/j.pmatsci.2019.100591.

[358] A. Pundt, R. Kirchheim, HYDROGEN IN METALS: Microstructural Aspects, 36 (2006) 555-608, https://doi.org/10.1146/annurev.matsci.36.090804.094451.

[359] C. Corvaja, Introduction to Electron Paramagnetic Resonance, Electron Paramagnetic Resonance2009, pp. 1-36.

[360] P. Höfer, Basic Experimental Methods in Continuous Wave Electron Paramagnetic Resonance, Electron Paramagnetic Resonance2009, pp. 37-82.

[361] The Theory of Raman Spectroscopy, Modern Raman Spectroscopy – A Practical Approach2004, pp. 71-92.

[362] A.C. Ferrari, J. Robertson, Interpretation of Raman spectra of disordered and amorphous carbon, Physical Review B 61 (2000) 14095-14107, https://doi.org/10.1103/PhysRevB.61.14095.

[363] S. Brunauer, P.H. Emmett, E. Teller, Adsorption of Gases in Multimolecular Layers, Journal of the American Chemical Society 60 (1938) 309-319, https://doi.org/10.1021/ja01269a023.

[364] E.P. Barrett, L.G. Joyner, P.P. Halenda, The Determination of Pore Volume and Area Distributions in Porous Substances. I. Computations from Nitrogen Isotherms, Journal of the American Chemical Society 73 (1951) 373-380,

https://doi.org/10.1021/ja01145a126.

[365] S. Vyazovkin, K. Chrissafis, M.L. Di Lorenzo, N. Koga, M. Pijolat, B. Roduit, N. Sbirrazzuoli, J.J. Suñol, ICTAC Kinetics Committee recommendations for collecting experimental thermal analysis data for kinetic computations, Thermochimica Acta 590 (2014) 1-23, https://doi.org/10.1016/j.tca.2014.05.036.

[366] H.E. Kissinger, Reaction Kinetics in Differential Thermal Analysis, Analytical Chemistry 29 (1957) 1702-1706, https://doi.org/10.1021/ac60131a045.

[367] R.N. Wenzel, RESISTANCE OF SOLID SURFACES TO WETTING BY WATER, Industrial & Engineering Chemistry 28 (1936) 988-994, https://doi.org/10.1021/ie50320a024.

[368] A.B.D. Cassie, S. Baxter, Wettability of porous surfaces, Transactions of the Faraday Society 40 (1944) 546-551, https://doi.org/10.1039/TF9444000546.

[369] R.S. Houk, Mass spectrometry of inductively coupled plasmas, Analytical Chemistry 58 (1986) 97A-105A, https://doi.org/10.1021/ac00292a003.

[370] The Techniques of Atomic Absorption Spectrometry, Atomic Absorption Spectrometry1998, pp. 335-475.

[371] J.F. Haw, Overview of In Situ Methods in Catalysis, In-Situ Spectroscopy in Heterogeneous Catalysis2002, pp. 1-14.

[372] Seyferth, Infrared and raman spectra of inorganic and coordination compounds, Wiley,

[373] R.F. Howe, In Situ Infrared Methods, In-Situ Spectroscopy in Heterogeneous Catalysis2002, pp. 139-177.

[374] C.L. Arthur, J. Pawliszyn, Solid phase microextraction with thermal desorption using fused silica optical fibers, Analytical Chemistry 62 (1990) 2145-2148, https://doi.org/10.1021/ac00218a019.

[375] H. van Den Dool, P. Dec. Kratz, A generalization of the retention index system including linear temperature programmed gas—liquid partition chromatography, Journal of Chromatography A 11 (1963) 463-471, https://doi.org/10.1016/S0021-9673(01)80947-X.

SCIENTIFIC CONTRIBUTIONS

Peer-reviewed publications

[1] **Z. Zheng**, K. Liu, Y. Zhou, K. Xu, Y. Luo, J. Ding, C. Bittencourt, M. Debliquy, C. Zhang*, Decorated-Induced Oxygen Vacancy Engineering for Ultra-low Concentration Nonanal Sensing: A Case Study of La-Decorated $Bi_2O_2CO_3$, *Advanced Science*, 11 (2024) 2408096.

[2] **Z. Zheng**, Y. Li, Y. Luo, M. Debliquy, C. Zhang*, Facile synthesis of bismuth ferrite nanoparticles for ppm-level isopropanol gas sensor, *Journal of Materials Science-Materials in Electronics*, 33 (2022) 18507-18521.

[3] **Z. Zheng**, C. Zhang*, K. Liu, Q. Liu, Volatile organic compounds, evaluation methods and processing properties for cooked rice flavor, *Rice*, 15 (2022) 53.

[4] **Z. Zheng**, K. Liu, Y. Zhou, M. Debliquy, C. Zhang*, Ultrasensitive Room-Temperature Geranyl Acetone Detection based on $Fe@WO_{3-x}$ Nanoparticles in Cooked Rice Flavor Analysis, *Journal of Advanced Ceramics*, 12 (2023) 1547-1561.

[5] **Z. Zheng**, K. Liu, Y. Zhou, Z. Zhang, H. Su, X. Nie, M. Debliquy, Z. Yu, C. Zhang*, Spinel Type MCo_2O_4 (M = Mn, Mg, Ni, Cu, Fe and Zn) for Chemoresistance Gas Sensors. *Materials Today Chemistry*, 36 (2024) 101928.

[6] **Z. Zheng**, K. Liu, M. Debliquy, C. Zhang*, Carbon functionalized cladding bismuth tungstate based 3D twisted micro-flowers for benzaldehyde detection under ultraviolet light excitation, *Sensors and Actuators B: Chemical*, 415 (2024) 135982.

[7] **Z. Zheng**, C. Zhang*, Electronic noses based on metal oxide semiconductor sensors for detecting crop diseases and insect pests, *Computers and Electronics in Agriculture*, 197 (2022) 106988.

[8] **Z. Zheng**, K. Liu, Y. Zhou, M. Debliquy, C. Bittencourt, C. Zhang*, A Comprehensive Overview of the Principles and Advances in Electronic Noses for the Detection of Alcoholic Beverages, *Trends in Food Science & Technology*, 156 (2025) 104862.

[9] **Z. Zheng**, K. Liu, Y. Zhou, Z. Zhang, Y. Qin, Y. Luo, K. Xu, L. Guo, M. Debliquy, C. Bittencourt, C. Zhang*, Sensing Mechanisms of Hierarchical Bismuth-Doped Antimony Tungstate Microspheres for CO_2 Detection at Ambient Temperatures, *Rare Metals*, (2025).

[10] **Z. Zheng**, K. Liu, Y. Zhou, K. Xu, L. Guo, M. Debliquy, C. Bittencourt, C. Zhang*, Rational design of defect-engineered $NiWO_4$ micro-flowers for chemiresistive gas detection: Synthesis, performance, and mechanistic understanding, *Chemical Engineering Journal*, 522 (2025) 168064.

[11]**Z. Zheng**, Kewei Liu, Yiwen Zhou, Kaichun Xu, Changlong Wang, Marc Debliquy, Carla Bittencourt, Chao Zhang*, CuO-decorated bismuth subcarbonate p-n heterostructured micro-flowers for high-selectivity VOC gas sensor arrays and cooked rice quality assessment, Journal of Advanced Ceramics, 15 (2026) 9221233.

[12]Y. Zhou, K. Xu, **Z. Zheng**, X. He, C. Zhang*, Quartz Crystal Microbalance Sensors Based On ZnO Nanofilms For Alcohol Detection, *IEEE Sensors Journal*, 24 (2024) 204-214.

[13]C. Zhang*, **Z. Zheng**, K. Liu, M. Debliquy, Q. Liu, Highly Sensitive and Selective Sb_2WO_6 Microspheres in Detecting VOC Biomarkers in Cooked Rice: Experimental and Density Functional Theory Study, *Food Chemistry*, 424 (2023) 136323.

[14]C. Zhang*, X. He, Y. Zhou, J. Xu, **Z. Zheng**, Y. Bian, M. Debliquy, Highly sensitive and stable yolk-shell Bi_2MoO_6 gas sensor for ppb-level isopropanol detection, *Sensors and Actuators B: Chemical*, 401 (2024) 135059.

[15]K. Xu, M. Han, J. Xu, **Z. Zheng**, K. Wu, Z. Yu, C. Zhang*, Highly sensitive $LaFeO_3$ coatings deposited by solution precursor plasma spraying for isoamyl alcohol detection, *Journal of Thermal Spray Technology*, 33 (2024) 1205-1219.

[16]K. Xu, Y. Luo, J. Xu, **Z. Zheng**, A. Ly, D. Lahem, M. Debliquy, C. Zhang*, MXene derived TiO_2-ZnO nanocomposites and well-defined n-n heterojunctions for highly efficient lung cancer biomarkers detection, *Ceramics International*, 50 (2024) 16155-16165.

[17]Z. Zhang, **Z. Zheng**, X. He, K. Liu, M. Debliquy, Y. Zhou, C. Zhang*, Electronic nose for medical diagnosis based on metal oxide semiconductor sensors, *Progress in Natural Science: Materials International*, 34 (2024) 74-88.

[18]Y. Zhou, Y. Luo, **Z. Zheng**, K. Liu, X. He, K. Wu, M. Debliquy, C. Zhang*, Urchin-like Na-doped zinc oxide nanoneedles for low concentration and exclusive VOCs detections, *Journal of Advanced Ceramics*, 13 (2024) 507-517.

[19]K. Xu, M. Han, **Z. Zheng**, Z. Yu, H. Liao, C. Zhang*, Well-designed g-C_3N_4 nanosheets incorporated Ag loaded $Er_{0.05}La_{0.95}FeO_3$ heterojunctions for isoamyl alcohol detection, *Journal of Advanced Ceramics*, 13 (2024) 736-745.

[20]K. Liu, **Z. Zheng**, M. Debliquy, C. Zhang*, Highly-sensitive volatile organic compounds evaluation by three-dimensional $ZnFe_2O_4$/$ZnSnO_3$ heterostructures and their predictive grain quality monitoring, *Chemical Engineering Journal*, 453 (2022) 139824.

[21]K. Liu, **Z. Zheng**, J. Xu, C. Zhang*, Enhanced visible light-excited $ZnSnO_3$ for room temperature ppm-level CO_2 detection, *Journal of Alloys and Compounds*, 907 (2022) 164440.

[22]K. Wu, W. Zhang, **Z. Zheng**, M. Debliquy, C. Zhang*, Room-temperature gas sensors based on titanium dioxide quantum dots for highly sensitive and selective H_2S detection, *Applied Surface Science*, 585 (2022) 152744.

[23]Y. Qin, Y. Jiang, **Z. Zheng**, G. Zhou, L. Zhang*, C. Wang*, Y. Bian*, A Highly Sensitive Electrochemical lmmunosensor Based on PET/GO/pPd/MAb Nanofber-Particles for Metolachlor Detection, *Electrochimica Acta*, 509 (2025) 145336.

[24]C. Zhang*, K. Liu, **Z. Zheng**, M. Debliquy, Defect engineering of nanostructured $ZnSnO_3$ for conductometric room temperature CO_2 sensors, *Sensors and Actuators B: Chemical*, 384 (2023) 133628.
[25]J. Ding, J. Qiao, **Z. Zheng**, Z. Song, S. Ding, J. Luo, F. Wang, F. Li, H. Li*, Assembling MOF on CNTs into 0D-1D heterostructures for enhanced volatile organic compounds detection, *Talanta*, 285 (2025) 127444.
[26]H. Chai, **Z. Zheng**, K. Liu, J. Xu, K. Wu, Y. Luo, H. Liao, M. Debliquy, C. Zhang*, Stability of Metal Oxide Semiconductor Gas Sensors: A Review, *IEEE Sensors Journal*, 22 (2022) 5470-5481.
[27]C. Zhang*, K. Xu, K. Liu, J. Xu, **Z. Zheng**, Metal oxide resistive sensors for carbon dioxide detection, *Coordination Chemistry Reviews*, 472 (2022) 214758.
[28]K. Liu, **Z. Zheng**, Y. Zhou, C. Bittencourt, M. Debliquy, Q. Liu, C. Zhang*, Heterovalent-doping-induced ultrasensitive and highly exclusive ethylene sensor: Application to crop quality inspection, *Chemical Engineering Journal*, 508 (2025) 161075.
[29]K. Xu, K. Wu, J. Xu, M. Han, **Z. Zheng**, M. Planche, S. Deng, H. Liao, C. Zhang*, Co-MOF-derived Co_3O_4 sensors for efficient 3-octanone biomarker monitoring in wheat mildew, *Talanta*, 291 (2025) 127892.
[30]Y. Qin, **Z. Zheng**, W. Gu, C. Bittencourt, Y. Jiang, L. Zhang*, Y. Bian*, A self-actuating and self-sensing microcantilever sensor modified by rGO-COOH@CuNPs@Ce-MOF nanocomposites for rapid detection of ALV-J, *Chemical Engineering Journal*, 513 (2025) 162755.
[31]K. Liu, **Z. Zheng**, Y. Zhou, C. Bittencourt, M. Debliquy, C. Zhang*, M. Debliquy, Probing the Challenge of P-Type Semiconductors in Long-Chain VOC Detection: 3D Micro-Flower Zinc Cobaltate Heterojunction Sensors, *Advanced Science*, (2025).
[32]J. Ding, **Z. Zheng**, Z. Song, S. Ding, J. Wen, K. Liu, C. Zhang*, H. Li*, Recent progress in chemiresistive gas sensors with 1D nanostructured sensing materials: Insights into the structure-morphology-performance relationship, *Materials & Design*, 234 (2023) 112360.
[33]K. Xu, M. Han, **Z. Zheng**, J. Xu, M. Debliquy, C. Zhang*, Role of Er doping on isoamyl alcohol sensing performance of $LaFeO_3$ microspheres and its prospect in wheat mildew detection, *Journal of Materials Chemistry A*, 11 (2023) 24939-24947.
[34]Y. Qin, J. Guan, D. Xu*, C. Wang*, J. Sun, **Z. Zheng**, W. Gu, K. Liu, C. Bittencourt, L. Zhang, Advanced electrochemical impedance immunosensor based on PS-b-PAA film architecture for sensitive alpha-fetoprotein detection, *Microchemical Journal*, (2025) 116234.
[35]K. Xu, K. Wu, **Z. Zheng**, Marie-Pierre Planche, S. Deng, H. Liao, C. Zhang*, Quantum Dot-Enhanced Co_3O_4/TiO_2 Type-II Heterojunction Chemiresistor for Efficient 3-Octanone Monitoring in Wheat Mildew Identification, Sensors and Actuators B: Chemical, 451 (2026) 139385.
[36]K. Xu, K. Wu, **Z. Zheng**, Marie-Pierre Planche, Sihao Deng, Hanlin Liao, Chao Zhang*, Hierarchical Core-shell Metal Hydroxide-derived $NiO/NiFe_2O_4$

Microflowers with Interior Heterojunction for Wheat Mildew biomarkers Detection, Journal of Colloid and Interface Science, 714 (2026) 140239.

[37]Yiwen Zhou, **Zichen Zheng**, Kewei Liu, Marc Debliquy, Carla Bittencourt, Chao Zhang*, Large-Surface-Area $Bi_2Sn_2O_7$ Quantum Dots for Room-Temperature 1-Octanol Sensing: A Combined Experimental and DFT Study, ACS Sensors, (2026).

Congress proceedings

1 oral presentation and 3 posters in European/international conferences, 5 oral presentations in national conferences

1. **Zichen Zheng**; The 11th Yangzhou University-Kyushu Institute of Technology Student Symposium (session chair), Yangzhou, China, 22-3-2022.
2. **Zichen Zheng**; The 12th Yangzhou University-Kyushu Institute of Technology Student Symposium, Yangzhou, China, 22-3-2023.
3. **Zichen Zheng**; Chao Zhang; The 15th National Symposium on Air-Humidity Sensitive Sensing Technology, Ningbo, China, 14-04-2023 to 16-04-2023.
4. **Zichen Zheng**; Jiangsu Graduate Students' Academic Innovation Forum on New Materials with "Double Carbon" Strategy (Winner Award), Yangzhou, China, 15-10-2022 to 16-10-2022.
5. **Zichen Zheng**; Jiangsu Province Graduate Academic Innovation Forum on High-End Equipment and Intelligent Manufacturing, Zhenjiang, China, 08-10-2022.
6. **Zichen Zheng**; Carla Bittencourt, Chao Zhang. Mardi des Chercheurs 2025, Valenciennes, France, 01-04-2025.
7. **Zichen Zheng**; Beilstein Nanotechnology Symposium 2025, Defect-mediated engineering of nanomaterials for energy and quantum applications; Rüdesheim, Germany, 13-05-2025 to 15-05-2025.
8. **Zichen Zheng**; 108th Iuvsta Workshop on Machine Learning in Nanoscience; Mons, Belgium, 22-07-2025 to 24-07-2025.
9. **Zichen Zheng**; 11th Asia-Pacific Drying Conference (ADC) 2023; Online; Kolkata, India,19-02-2023.

Project

1. 2020.5-2021.5 The "Graduate Student Research and Practice Innovation Program" of Jiangsu Province "Research on Metal Oxide Sensors for Crop Pest and Disease Detection", Project No. SJCX21_1605 (Hosted, Completed);

2. 2023.5-2024.5 The “Graduate Student Research and Practice Innovation Program” of Jiangsu Province “Research on Semiconductor Gas Sensor Array for Rice Quality Detection”, Project No. KYCX23_3551 (Hosted, Completed);

3. 2024.5-2026.5, presided over the 2023 National Construction of High-Level Universities Postgraduate Program, Admission Document Number: Liu Jin Xuan [2023] No. 49, Project No.: 202308320445 (Hosted, under research);

4. 2025.5, Beilstein Nanotechnology Symposium 2025 Conference Grant. (Hosted, Completed);

5. 2025.09.15-2025.09.24, Fonds de la Recherche Scientifique (FNRS) Mobility and Congress funding, Application followup V3, Accomplishment of a stay abroad [V3][40036258] Tarragona-Spain. (Hosted, under research).

6. 2021.7-2024.7, Jiangsu Province Basic Research Program (Natural Science Foundation) - Outstanding Youth Fund Project "Room Temperature Semiconductor Gas-Sensitive Layer Design and Plasma Spraying Manufacturing" Project No.: BK20211548 (Participated, Completed);

7. 2022.12-now, China Postdoctoral Science Foundation, the 72nd batch of surface funding second class, "Research on the coupling mechanism of room temperature gas sensor device based on amnesia effect and its accurate identification method of VOCs" Project No.: 2022M721185 (Participated, under research);

8. 2021.7-2023.6, 2021 Municipal Program - Municipal and University Cooperation Special Project "Research on Metal-Based Reinforced Coating on the Inner Wall of Cylinder Liner of Commercial Vehicle Engines", Project No.: YZ2021153 (Participated, Completed);

Awards

- National Scholarships (The highest scholarship, doctoral, twice);
- Top Ten Graduate Student Academic Stars of the University (Yangzhou University).